FINAL TECHNICAL REPORT

Report No: AAE 93-04
UIUL 93-0504

IGNITION AND COMBUSTION OF LUNAR PROPELLANTS

Final Report
(11 June, 1990 - 10 June, 1992)
NASA Lewis Research Center
Grant No. NAG 3-1184

Prepared by:

Rodney L. Burton and Ted A. Roberts
Department of Aeronautical and Astronautical Engineering

Herman Krier
Department of Mechanical and Industrial Engineering

University of Illinois at Urbana-Champaign
Urbana, Illinois 61801

April, 1993

IGNITION AND COMBUSTION OF LUNAR PROPELLANTS

Final Report
(11 June, 1990 - 10 June, 1992)
NASA Lewis Research Center

Prepared by:

Rodney L. Burton and Ted A. Roberts
Department of Aeronautical and Astronautical Engineering
(217)-244-6223

Herman Krier
Department of Mechanical and Industrial Engineering
(217)-333-0529

University of Illinois at Urbana-Champaign
Urbana, Illinois 61801

for

NASA Lewis Research Center

Grant No. NAG 3-1184

Michael L. Meyer
NASA Technical Officer

April, 1993

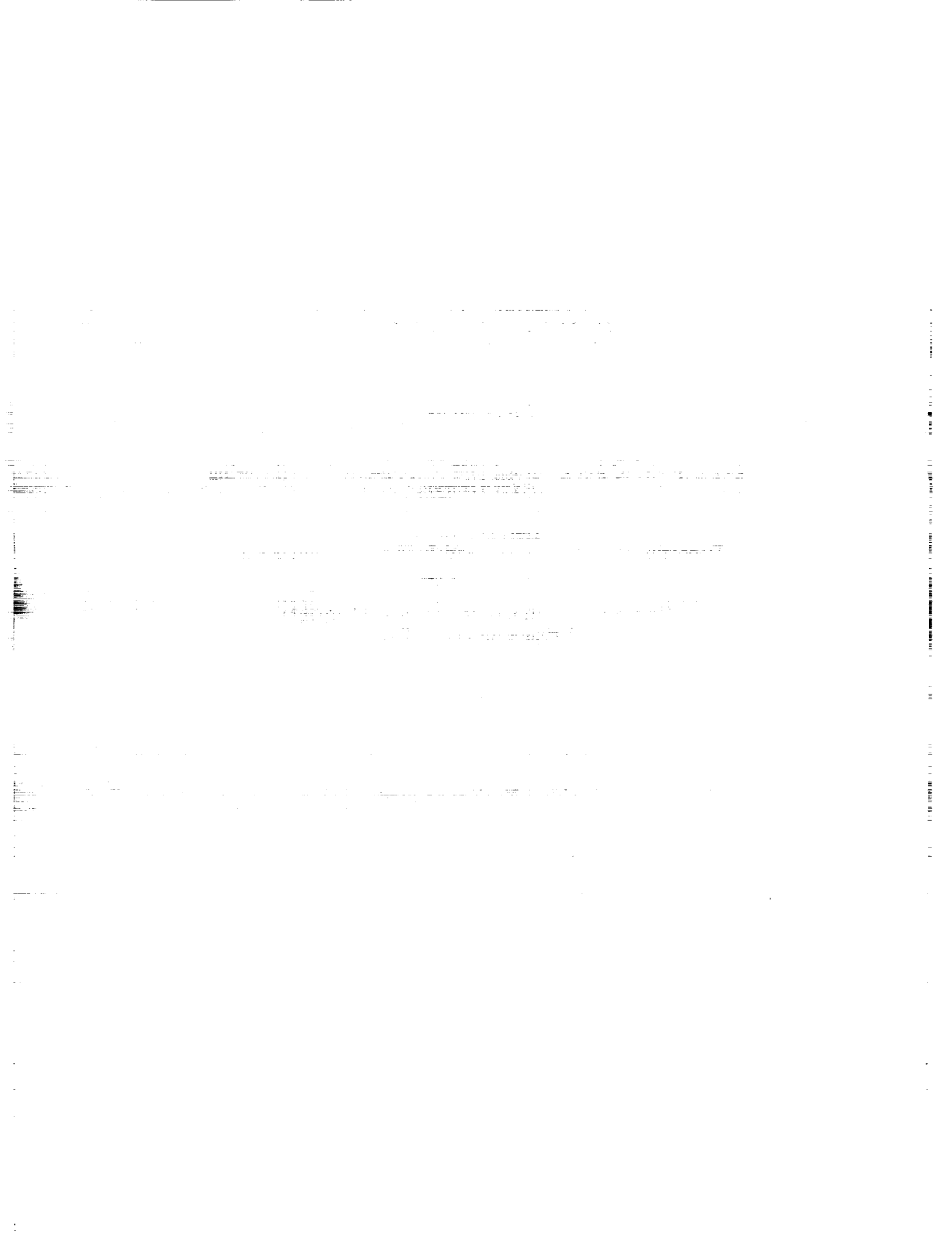

ABSTRACT

The ignition and combustion of Al, Mg, and Al/Mg alloy particles in 99% O_2 / 1% N_2 mixtures is investigated at high temperatures and pressures for rocket engine applications. The 20 μm particles contain 0, 5, 10, 20, 40, 60, 80, and 100 weight percent Mg alloyed with Al, and are ignited in oxygen using the reflected shock in a shock tube near the endwall. Using this technique, the ignition delay and combustion times of the particles are measured at temperatures up to 3250 K as a function of Mg content for oxygen pressures of 8.5, 17, and 34 atm. An ignition model is developed which employs a simple lumped capacitance energy equation and temperature and pressure dependent particle and gas properties. Good agreement is achieved between the measured and predicted trends in the ignition delay times. For the particles investigated, the contribution of heterogeneous reaction to the heating of the particle is found to be significant at lower temperatures, but may be neglected at gas temperatures above 3000 K. As little as 10% Mg reduces the ignition delay time substantially at all pressures tested. The particle ignition delay times decrease with increasing Mg content, and this reduction becomes less pronounced as oxidizer temperature and pressure are increased.

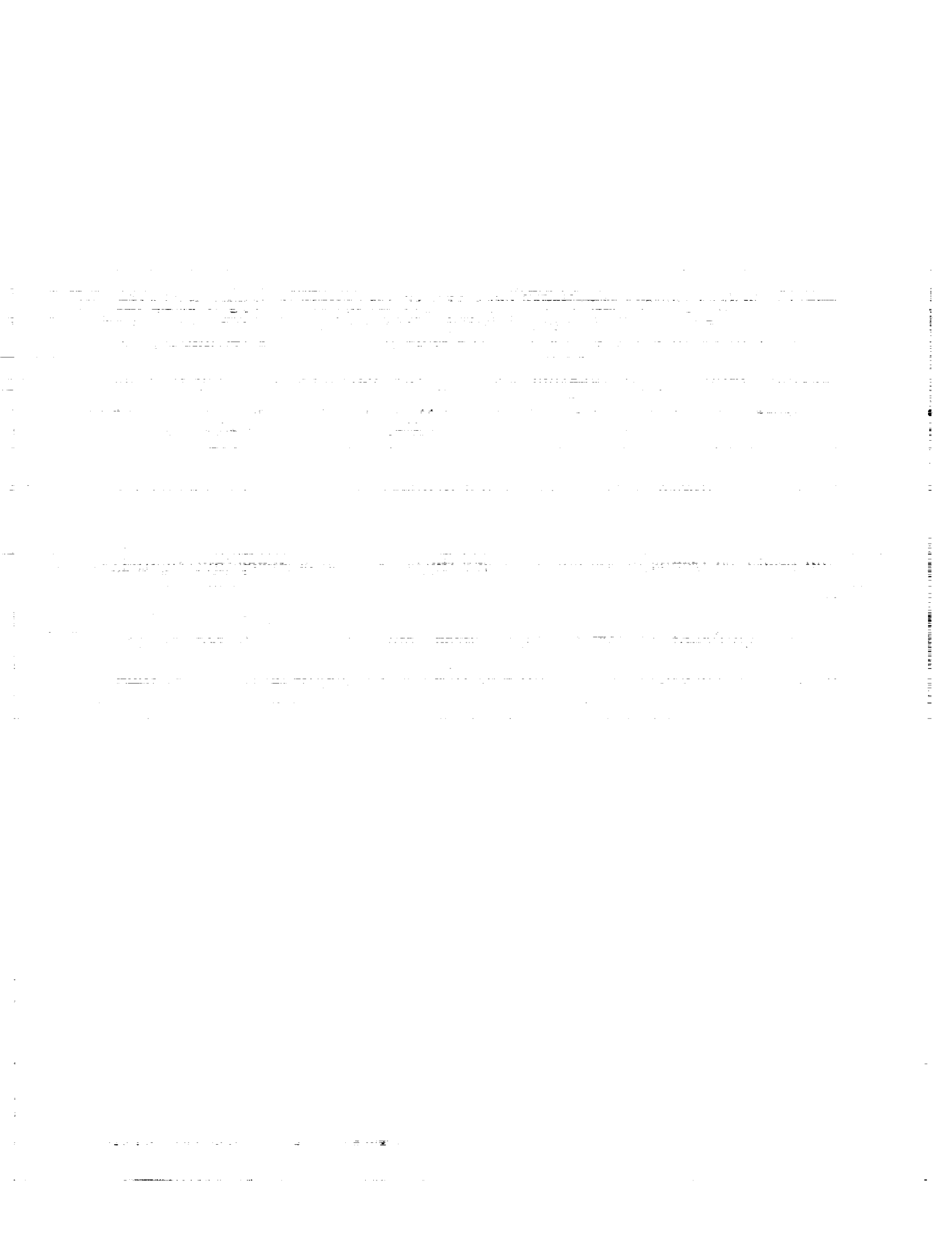

ACKNOWLEDGMENTS

This report is based on the Ph.D. Thesis of Dr. Ted A. Roberts.

The author would like to gratefully acknowledge his thesis advisor, Prof. Rodney L. Burton, for his continuing guidance and advice, and for providing him with the opportunity to pursue the research that resulted in this thesis. The author would also like to acknowledge Prof. Herman Krier for his great assistance in this research area.

The time required to gather the data for this research was significantly reduced through the dedicated efforts of Ted P. Zackro, who spent many long hours working with the author in the Lunar Metal Combustion Laboratory. The author would also like to thank Tom W. Megli, whose keen mind and drive to completely understand a problem kept the author on his toes.

Special thanks is given to Monica M. Doyle, who provided a great deal of moral support and assistance throughout the duration of this research effort. The encouragement of Michael L. Meyer is also acknowledged.

This work was made possible through funding provided by the NASA Lewis Research Center under grant NAG3-1184 and the NASA Graduate Student Researchers Program. The additional support of the UIUC Research Board is gratefully acknowledged.

The author would also like to thank: D. Robertson of Univ. of Missouri at Rolla, Harte Metals, Valimet Inc., M. Brewster, W. Solomon, B. Hilko of G.T.-Devices Inc., B. Coverdill, C. Swann, D. Tempel, P. Hetman, and A. Schroeder for their important and greatly appreciated contributions.

TABLE OF CONTENTS

LIST OF TABLES

LIST OF FIGURES

NOMENCLATURE

A_s	particle surface area (m^2)
A_1	heterogeneous reaction rate pre-exponential constant (kg/m^2-s)
a	sound speed (m/s)
Bi	Biot number: Bi = $(\bar{h}r_p)/(3k_p)$
C_D	spherical drag coefficient, defined in Eqs. (3.16) and (3.17)
C_W	knife blade wake coefficient
c	specific heat (kJ/kg-K)
c_p	constant pressure specific heat (kJ/kg-K)
C.S.	contact surface
d	diameter (m)
d_{eff}	effective spherical particle diameter (m)
E	internal energy (kJ)
E_a	heterogeneous reaction activation energy (cal/mole)
e	particle coefficient of restitution: $e = v_{pr} / v_{pi}$
e_{ht}	total energy transferred to particle convectively (kJ)
e_{ox}	total energy produced by heterogeneous reaction (kJ)
F_D	drag force (N)
F_{g_o}	gravitational force (N)
F_T	thrust (N)
g_o	acceleration due to gravity at the earth's surface (m/s^2)
H	enthalpy (kJ)
$\bar{h}$	surface averaged convective heat transfer coefficient: $\bar{h} = Nu\ k_g / 2\ r_p$ (W/m^2-K)
I_{hv}	intensity of electromagnetic radiation (W/m^2)
I_{sp}	specific impulse (sec)
$(I_{sp})_{vac}$	vacuum specific impulse (sec)

Kn	Knudsen number based on particle diameter: $Kn = \lambda_g / d_p \sim M_p / Re_p$
k	thermal conductivity (W/m-K)
k_B	Boltzmann's constant, $k_B = 1.381 \times 10^{-23}$ J/K
k_s	heterogeneous reaction rate constant (kg/m^2-s)
L_f	enthalpy of fusion (kJ/kg)
l	length (m)
M	Mach number
m	mass (kg)
$\dot{m}_p$	propellant mass flow rate (kg/s)
Nu_p	surface averaged Nusselt number, defined in Eq. (3.23)
p	absolute gas pressure (atm)
Q_v	heat of vaporization (kJ/kg)
q_r	specific heat of reaction (kJ/kg of metal)
$\dot{q}_c$	rate of convective heat transfer (W)
$\dot{q}_r$	rate at which energy is released by chemical reaction (W)
$\dot{q}_{rad}$	rate at which energy is lost radiatively (W)
R	gas constant (kJ/kg-K)
R_h	head of expansion wave
R_t	tail of expansion wave
R_u	universal gas constant (8.314 J/mole-K)
Re_p	particle Reynolds number: $Re_p = 2\rho_g \lvert v_g - v_p \rvert r_p / \mu_g$
r	radius (m)
S_i	incident shock wave
S_p	frontal area of spherical particle (m^2)
S_r	reflected shock wave
S_{tr}	transmitted shock wave
T	absolute temperature (K)

T_o	absolute background surface temperature (K)
T_p	absolute particle temperature (K)
t	time (s)
t_b	particle burn time (s)
t_{ign}	particle ignition delay time (s)
u_e	effective exhaust velocity (m/s)
V	volume (m^3) or electrical voltage (V)
$\overline{V}$	molecular volume (cm^3/mole)
v	magnitude of velocity (m/s)
v_{pi}	magnitude of particle velocity prior to reflection from endwall (m/s)
v_{pr}	magnitude of particle velocity after reflection from endwall (m/s)
W	molecular weight (g/mole)
w	absolute uncertainty
$\dot{w}_p$	weight flow of propellant (N/s)
X	mole fraction
x	spatial coordinate (m)
x_δ	distance from knife blade leading edge (m)
Y	mass fraction

Greek Symbols

α	linear coefficient of thermal expansion (K^{-1})
β	volumetric coefficient of thermal expansion (K^{-1})
γ	ratio of specific heats
δ_{kb}	knife blade boundary layer height (m)
δ_{ox}	oxide film thickness (m)
ε	emissivity
η_{ox}	fraction of particle ignition energy contributed by heterogeneous

	surface reaction, defined in Eq. (4.1)
λ_g	mean free path of gas molecules (m)
μ	viscosity (Pa-sec)
ν_i	stoichiometric coefficient of i^{th} species
ρ	density (kg/m^3)
σ	Stefan-Boltzmann constant: $\sigma = 5.670 \times 10^{-8}$ $W/m^2\text{-}K^4$ or molecular diameter (nm)

Subscripts and Symbols

Al	aluminum
alloy	aluminum/magnesium alloy
b	black body
bp	boiling point
bs	bow shock flow conditions
d	diaphragm
e	equilibrium
eff	effective
ew	endwall
f	frozen
g	gas
he	head-end
i	i^{th} species
ign	ignition
kb	knife blade
liq	liquidus
Mg	magnesium
max	maximum
mp	melting point
o	initial
ox	oxide
p	particle

s_i	incident shock wave
w	window
1	undisturbed driven gas
2	driven gas through which incident shock wave has passed
3	fully expanded driver gas
4	undisturbed driver gas
5	reflected shock conditions

CHAPTER 1: INTRODUCTION

1.1 MOTIVATION OF RESEARCH

Pure and alloyed aluminum, magnesium, boron, zirconium, and beryllium are among the metals that have been considered as rocket fuels [1]*. Generally, powders of these metals are added to the propellants of solid fuel motors to increase the propellant density and motor specific impulse. In addition, the high levels of acid (HCl) produced by current hydroxy terminated polybutadiene (HTPB) solid propellants is found to be largely neutralized by the addition of Mg powder to the binder [2]. Metal powders have also been mixed with liquid hydrocarbon fuels to form slurries that can be pumped into liquid-type combustion chambers. As early as 1958, the NACA (the predecessor of NASA) successfully flew a small Mg-JP slurry fueled ramjet [3]. More recently, the NASA Lewis Research Center has directed the development of metallized gel propellants for use in bipropellant systems [4]. The size of the metal powders used as propellant additives generally range from 10-40 μm, although particle sizes ranging from 5 - 200 μm have been used [1].

Currently, development of a metal-LOX rocket engine is being considered as part of NASA's Indigenous Propellants Program which would use propellants derived solely from lunar materials [5]. Utilization of such an engine could lower the cost of future space exploration missions by significantly lowering the mass of propellant that must be launched from the Earth's surface. Analysis of lunar soils indicate they are primarily composed of oxides [6]. These oxides can be processed chemically to yield their constituent metals and oxygen, which may then be used in combination as a rocket propellant. Due to their high heats of reaction and relatively high densities, of primary interest

* Number refers to Reference section at end of text.

are aluminum and magnesium, which compose approximately 9% and 4% of lunar soils, respectively [6].

A measure of a rocket engine's performance is given by its specific impulse, I_{sp}, which is defined as its generated thrust (T_r) divided by its weight flow of propellant ($\dot{w}_p$). If the nozzle exhaust pressure is equal to the external pressure, the specific impulse is simply given by [7]:

$$I_{sp} \equiv \frac{T_r}{\dot{w}_p} = \frac{\dot{m}_p u_{eq}}{\dot{m}_p g_o} = \frac{u_{eq}}{g_o} \tag{1.1}$$

where $\dot{m}_p$ is the propellant mass flow rate, g_o is the value of gravity at the Earth's surface, and u_{eq} is the equivalent exhaust velocity of the gases. Since the propellant comprises a large fraction of a chemical rocket's mass, it is desirable to have as high an I_{sp} as possible [8].

The ideal vacuum specific impulse (see Appendix A) of an Al/Mg-LOX rocket engine is plotted in Fig. 1.1 as a function of the oxidizer to fuel ratio (O/F) for various Al/Mg alloy compositions. The calculations are made using NASA's Gordon-McBride program [9] and assume a chamber pressure of 1000 psia, a nozzle area ratio of 77.5, and equilibrium gas composition. Pure Al yields a maximum vacuum specific impulse of approximately 284 sec. For pure Mg, the maximum ideal performance is calculated to be $I_{vac} \cong 272$ sec. The reduction in the vacuum specific impulse with increasing Mg content is due to a corresponding reduction in the Al/Mg alloy specific heat of reaction (see Fig. 3.14).

The performance of an actual Al/Mg-LOX rocket engine will be significantly less than predicted in Fig. 1.1 due to two significant losses associated with metal combustion. The first is incomplete combustion of the metal particles which results in the loss of potential chemical energy. The

second is the two-phase flow losses which result from the inability of the condensed-phase oxide (Al_2O_3, MgO, and $MgO \bullet Al_2O_3$) and unburnt metal particles to maintain thermal and kinetic equilibrium with the expanding carrier gases in the nozzle [7].

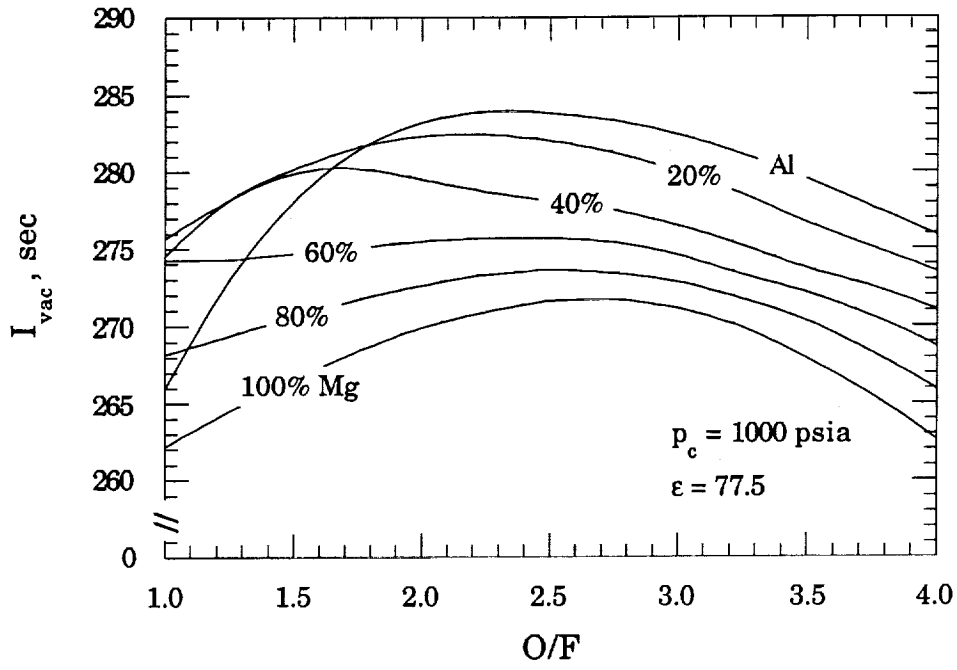

Fig. 1.1: Calculated ideal vacuum specific impulse of an Al/Mg-LOX rocket engine. Calculations are made using the NASA Gordon-McBride program [9]. O/F is the oxidizer to fuel mass ratio.

Wickman et al. [10] investigated theoretically the non-ideal performance of various metal-LOX rocket engines. The percent reduction in I_{sp} of these engines was calculated assuming a chamber pressure of 1000 psia, a throat radius of 1 to 7 inches, and a nozzle expansion ratio of 50. For the Mg-LOX combination, Wickman et al. predict a 13 percent and 6 percent reduction in I_{sp} corresponding to throat radii of 1 inch and 7 inches, respectively. For identical throat radii, Wickman et al. predict a 7 percent and 3 percent reduction in I_{sp} for

the Al-LOX propellant combination for throat radii of 1 inch and 7 inches, respectively.

In order to develop an Al/Mg-LOX rocket engine with performance approaching that of Fig. 1.1, a number of critical issues must be resolved. First, a suitable ignition technique must be developed. Second, the particle size distribution of the powdered Al/Mg alloy should be chosen to insure complete combustion within the thrust chamber, based on experimentally measured particle ignition delay and combustion times. It is likely the ignition and combustion times will depend on alloy composition, indicating an optimum composition may exist. Third, to reduce two-phase flow losses, the composition of the alloy particles should be tailored to minimize the size of the condensed-phase oxide products that result from their combustion.

To logically address these design issues, a detailed knowledge of the ignition and combustion characteristics of Al/Mg alloy particles in high temperature, high pressure oxygen is required. An understanding of the complicated mechanisms involved in the ignition and combustion of an alloy begins with an examination of the corresponding mechanisms associated with the constituent metals. Therefore, the following section will discuss the generally accepted mechanisms of Al and Mg particle ignition and combustion.

1.2 IGNITION AND COMBUSTION BEHAVIOR OF Al AND Mg PARTICLES

A large body of information exists concerning the ignition and combustion of metal particles, particularly Al, due to their importance as additives used to raise the propellant density and specific impulse of solid rocket motors. Price [1] presents a detailed review of the difficulties associated with the combustion of metallized propellants. Frolov et al. [11] survey experiments performed in the

former Soviet Union on the ignition and combustion of metals and their effect on the combustion of solid propellants.

The ignition and combustion behavior of metal particles is considerably more complex than that of the more commonly used liquid fuel droplets. During the pre-ignition heating period, a substantial oxide film can form on the particle's surface, retarding the particle's ignition. During combustion, the accumulated oxide film can inhibit transport of oxidizer and metal vapor in the reaction zone. The specific ignition and combustion processes depend on the physical characteristics of the metal and the properties of the oxidizing atmosphere in which the particle is heated to ignition and then burned.

After entering the high temperature environment of an operating combustion chamber, the ignition of a metal particle results from heating of the particle to its ignition temperature through a combination of convective heat transfer, from the hot gas to the particle, and the heat generated by the particle's own heterogeneous surface reactions [12]. As discussed by Fox et al. [13], the concept of ignition is poorly defined, and definitions that are useful in an analytical study are commonly not so in an experimental study. Based on the relatively short residence time of a particle within the combustion chamber of a rocket engine, the present investigation will define the ignition temperature as that which coincides with the onset of the rapid, luminous, detached gas-phase combustion of particular interest.

According to Price [1], some of the physical properties important to the ignition behavior of Al and Mg particles are:

1) The ratio of the oxide volume to the volume of metal from which it is formed, Φ. If $\Phi < 1$, the oxide film is said to be permeable and will allow the transport of oxidizer and metal vapor. If $\Phi > 1$, the oxide film is considered impermeable and inhibits the heterogeneous surface

reactions that may occur on the particle's surface. At room temperature, $\Phi_{Al} = 1.28$ and $\Phi_{Mg} = 0.81$ [14].

2) The ratio of the coefficients of thermal expansion of the metal to that of its oxide film, η. If $\eta > 1$, the oxide film will be stressed during the pre-ignition heating period and nascent metal will be exposed to the oxidizing atmosphere, resulting in a heterogeneous reaction. Calculations indicate that $\eta > 1$ for Al, Mg, and all of the Al/Mg alloys (see section 3.4.6).

3) The melting point of the oxide is important in the case of Al. As a result of the relatively high normal boiling point (~ 2767 K) of Al, an Al particle is believed to ignite when its temperature reaches the melting point of Al_2O_3 (~2300 K) Ignition is defined here as the transition from the "slow" heterogeneous reactions of the pre-ignition heating period to the "fast" detached gas-phase reactions marked by a substantial increase in particle luminosity.

4) The low solubility of Al_2O_3 in molten Al, low interfacial surface tension between Al_2O_3 and Al, and high Al_2O_3 surface tension causes the molten oxide to retract and form a lobe on the surface of the particle. This retraction of the oxide continuously exposes nascent metal to the gaseous oxidizer, significantly increasing the rate of particle heating due to surface reaction.

5) When the boiling point of the metal is reached and a solid oxide film persists, the internal pressure of the metal vapor destroys the film and rapid combustion commences. This is typical of Mg, which has a relatively low normal boiling point (~1367 K) while its oxide, MgO, has a rather high melting point (~3105 K).

Price notes further that these characteristics have been experimentally verified, but depend in particular upon the composition and properties of the oxidizing atmospheres in which the particle is being ignited.

The general picture of an Al or Mg particle burning in the detached gas-phase regime is shown in Fig. 1.2 [1]. The particle is assumed to be burning in a mildly convective environment. Assuming the particle Reynolds number is small, the molten metal will be spherically shaped due to the action of surface tension [15]. In the case of Al, a lobe of retracted oxide may be present on the particle's surface and is believed to be at least partially responsible for the particle spinning and fragmentation that is often associated with Al particle combustion [16-18].

Surrounding the particle is a detached flame envelope in which the metal vapor and oxidizer react to form small (submicron to 1-2 μm) condensed oxide droplets. As opposed to the homogeneous gas-phase reactions associated with the combustion of liquid hydrocarbon fuel droplets, it is believed the detached gas-phase combustion of metal droplets proceeds in a heterogeneous manner on the surface of the growing detached oxide particles [19]. These condensed oxides are then convected away from the vicinity of the burning particle to form a "tail" of particles.

The precise nature of the ignition and combustion of an Al or Mg particle is dependent upon the properties of the oxidizing atmosphere to which it is exposed. The numerous experimental studies which have deduced these phenomena will be briefly summarized in the next section. An exhaustive review of metal ignition and combustion research is beyond the scope of this work. However, several general surveys of this field have been published and are recommended for review by the reader. Among these are those of Markstein [20], Kubaschewski and Hopkins [14], Frolov, et al. [11], Pokhil et al. [21], Breiter et al. [22], and Price [1].

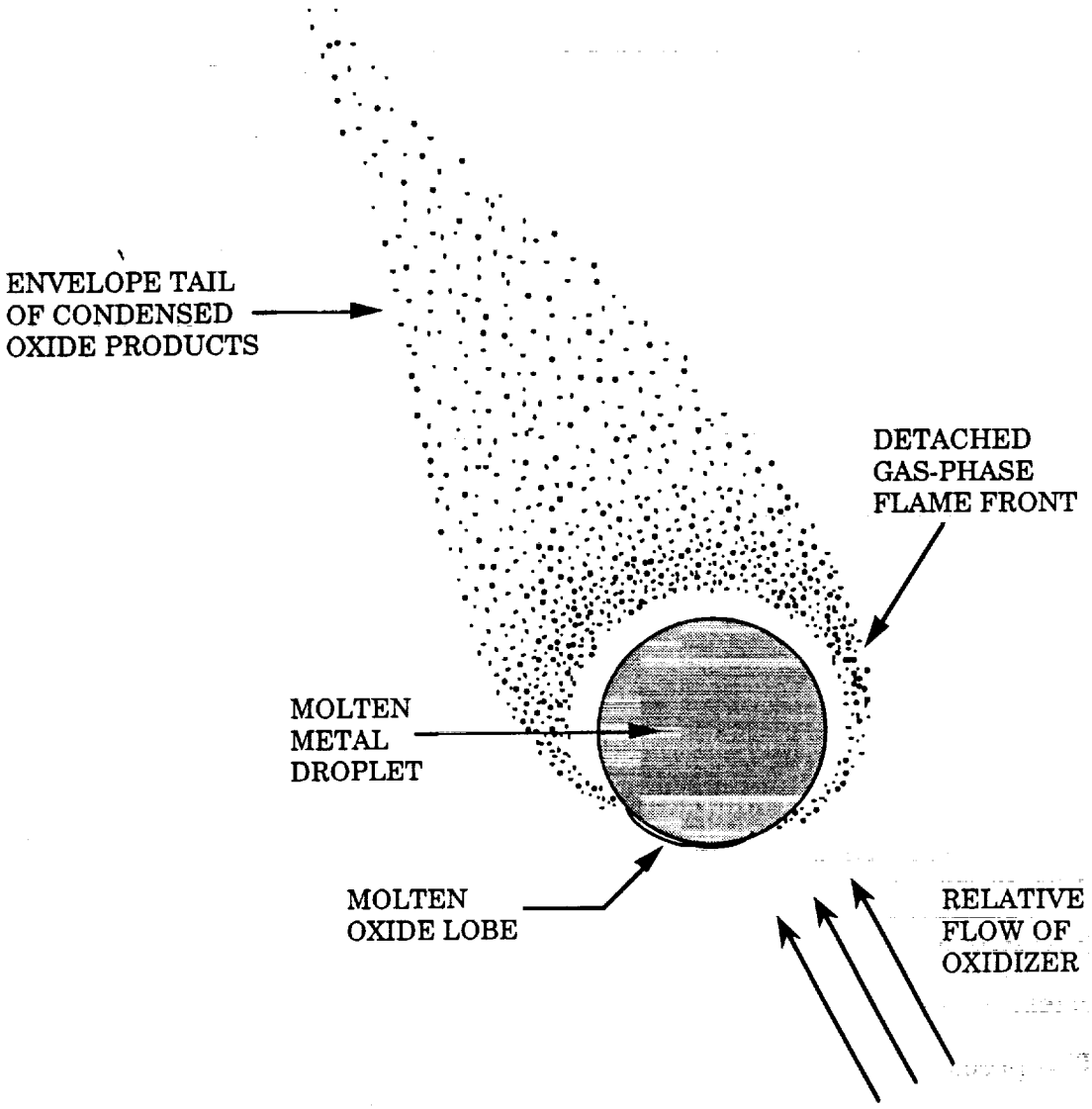

Fig. 1.2: Representative schematic of an Al or Mg particle burning in the detached gas-phase regime. The condensed oxide lobe may be present in the case of Al combustion, but is generally not present in the case of Mg combustion.

1.3 REVIEW OF PREVIOUS RESEARCH

The following is a brief survey of published research concerning the ignition and combustion of Al, Mg, and Al/Mg alloy particles. The majority of the articles focus on the combustion characteristics of Al, due to its widespread

use as a propellant additive. Magnesium has not been used extensively as a rocket fuel additive due to its lower heat of reaction. Therefore, published research concerning Mg particle combustion is less prevalent.

The favorable characteristics of Mg (e.g., low normal boiling point and permeable oxide film) have led to a number of investigations directed toward determining the benefits of alloying Mg with Al. These publications will be discussed in some detail, as they are closely related to the objective of the present research effort.

The articles discussed in the following two sections are presented in chronological order, the only exceptions being those instances in which the same author(s) have published related work several years apart.

1.3.1 Survey of Pure Al and Mg Particle Ignition and Combustion Research

Friedman and Macek [16] studied the ignition and combustion of aluminum particles (15 - 67 μm diameter) in a propane/oxygen/ nitrogen flat flame burner. The oxygen concentrations ranged from -10 (fuel-rich) to 40 mole percent and the pressure was 1 atm. The particle ignition was successfully modeled using a simple lumped capacitance energy balance that assumed a Nusselt number of 2 (low Reynolds number, continuum flow) and accounted for the initial particle acceleration period. This analysis indicates a particle ignition delay time that is proportional to the square of the particle diameter. Heating due to heterogeneous surface reaction was neglected.

Friedman and Macek found that particle ignition occurred only when the ambient gas temperature was between 2210 K and 2360 K, which brackets the Al_2O_3 melting point. This result was independent of the fraction of available free oxygen. The particle combustion process was found to be complex and

involved unsymmetrical burning and fragmentation. The authors suggest that superheating of the molten Al may contribute to the fragmentation process, although no supporting evidence was presented.

The quenched combustion of 30 to 150 μm diameter Al particles was studied using an oxygen/hydrogen burner operated at atmospheric pressure by Drew et al. [15]. High speed photography showed that the burning Al particles were surrounded by a zone of oxide "smoke." Quenched samples, examined microscopically, indicated that this "smoke" was composed of oxide particles ranging in size from 5 μm diameter down to 50 Å diameter, which was the optical limit of the instrument. Evidence of a "lense" cap, or lobe, of oxide was attributed to agglomeration of the molten oxide layer.

The vapor-phase combustion of Al and Mg was investigated extensively, both analytically and experimentally, by Brzustowski and Glassman [23,24]. The authors developed a model of the vapor-phase combustion of Al and Mg based on Spalding's classical model used to describe the combustion of hydrocarbon fuel droplets [25]. To verify their model, Al wires and Mg ribbons were ignited in mixtures of dry oxygen and argon at pressures up to 450 psia [23]. The theory and experiment agreed well for experimental conditions in which the particles clearly burned in the detached gas-phase regime.

Over the oxygen and pressure ranges of their experiments, Brzustowski and Glassman identified seven Al regions and nine Mg regions in which distinctly different combustion phenomena occurred. In the regions of particular interest to the present research, i.e. high pressure and pure oxygen, the reaction occurred so close to the droplet surface that its details could not be deduced. It was reported that the Al wires ignited when the accumulated oxide coating melted and exposed the molten metal while the Mg ribbons ignited in a vapor-phase manner.

Kuehl [26] presents modified versions of both the metal particle ignition model of Friedman and Macek [16] and the vapor-phase combustion model of Brzustowski and Glassman [23]. The ignition model was altered to include the increased rate of heat transfer due to a constant convection velocity and the change in the particle's size, density, and thermal capacity at its melting point. The vapor-phase combustion model was altered to accommodate oxidizers other than oxygen, such as water which produce noncondensible gases like hydrogen. In addition, the heat capacities and thermal conductivities of the fuel (metal vapor) and inert species are treated in a more complete fashion. Theoretical burning rates for Al particles as a function of oxygen fraction (in argon) are presented.

Prentice [17,27] studied the combustion of single particles of Al in various oxidizers using both a xenon flash heating device and a Nd-glass laser as the ignition source. The initially square Al foils form spherical droplets upon melting, resulting in droplet sizes ranging from 100 to 500 μm diameter. Prentice states that a 400 μm diameter Al particle burning in air at one atmosphere does not have an integral molten oxide film on the particle's surface at any time during its combustion [27]. Quenched specimens show a clearly delineated, complex, detached gas-phase flame structure.

Experimentally measured Al particle combustion times as a function of particle diameter are presented for 20% oxygen/argon and air atmospheres at a pressure of 0.93 atm [17]. Particles were found to burn to completion in the vapor-phase regime in the oxygen/argon atmospheres, while those burned in air generally fragmented. In the 20% oxygen/argon atmospheres, the burn time was found to be proportional to particle diameter.

Macek [28] presents experimental data on the minimum ambient gas temperature required to ignite 35 - 45 μm diameter Al particles as a function of

oxygen partial pressure. The measurements were made utilizing a flat flame burner and a closed bomb. The minimum gas temperature for ignition approaches 2300 K (the melting point of Al_2O_3) as the partial pressure of oxygen goes to zero. At an oxygen partial pressure of 1.7 atm, the minimum gas temperature dropped to approximately 2130 K. Macek attributed the ignition of the Al particles in gases, at temperatures well below the melting point of Al_2O_3, to surface oxidation, which enables the particle temperature to rise above that of the surrounding gas due to particle self-heating. Combustion studies indicated Al probably burns in a vapor-phase manner.

The ignition and combustion of Al particles (70 and 140 μm diameter) in the combustion products of a solid propellant burning in a closed bomb at pressures of 10 to 100 atm was investigated by Belyaev et al. [29]. The primary oxidizing species present were H_2O, CO_2, and CO. The particle burn times were found to be nearly independent of pressure above 20 atm, but were found to rise slightly with decreasing pressure below this value. The burn time was found to be a strong function of the oxidizer mole fraction. For a given gas composition, the Al particle burn time was found to be related to the particle diameter by $t_b \sim (d_p)^{1.5}$. Belyaev et al. found the particle ignition delay time to be independent of the gas composition and pressure, a strong inverse function of the gas temperature, and proportional to the square of the particle diameter.

The ignition limits of small (1 to 46 μm diameter) Al particles in oxygen/nitrogen/argon and water vapor atmospheres were studied by Gurevich et al. [30]. Their results indicate that, for diameters below approximately 25 μm, the Al ignition limit is a nonlinear function of particle diameter. The particle diameter corresponding to the minimum ignition temperature depends on the composition of the oxidizer and, for a given particle diameter, the ignition limit was found to decrease with increasing oxygen content.

Wilson and Williams [18] made detailed measurements of the burning characteristics of 50 μm diameter Al particles in oxygen/argon atmospheres. A single particle, initially mounted on a 10 μm diameter glass fiber, was ignited using a high intensity laser pulse. A detached flame envelope existed in accordance with Glassman's criterion [31] for vapor-phase combustion. As the oxygen fraction was increased from 0.1 to 1.0, the particle burn rate increased by an order of magnitude and the radius of the detached flame envelope nearly doubled.

Keshavan and Brzustowski [32] studied the ignition of Al particle streams carried in an oxygen stream and ignited by a propane/oxygen pilot flame. Two Al particle size distributions having average diameters of 25 and 120 μm were employed in particle/gas weight fractions ranging from 0.1 to 0.5. The particle ignition delay times were measured photographically and predicted using the simple thermal ignition model of Friedman and Macek [16], which was modified to include the effect of radiative heating from the downstream burning particle cloud and heating of each particle by a finite volume of gas.

Keshavan and Brzustowski found that the smallest particles ignited first and subsequently ignited the surrounding larger particles in a manner similar to flame spreading. The ignition delay time of these smallest particles could be predicted by assuming they were heated to the melting point of aluminum oxide by a finite volume of hot gas. The predicted ignition delay time increased with particle weight fraction, but this was not confirmed experimentally.

The combustion of laser-ignited 100 μm diameter Mg particles in various atmospheres (oxygen/argon, carbon dioxide/argon, water vapor) at atmospheric pressure was studied by Law and Williams [33]. Various modes of ignition were discerned. Regular, gas-phase combustion occurred only in atmospheres with dilute oxidizers. The combustion process generally involved a detached gas-

phase flame zone, accumulation of solid oxide on the particle's surface, jetting, spinning, and fragmentation.

Merzhanov [12] developed a detailed thermal theory of metal particle ignition, including the presence of particle self-heating due to heterogeneous surface reactions, and validated the theory experimentally using electrically heated wires. Exponential and parabolic expressions were assumed for the kinetic equations of the surface oxidation. Merzhanov stated that when a parabolic oxidation law is used along with physically realistic parameters, the initial state (e.g., thickness) of the oxide film is of no importance.

Merzhanov found that Al would ignite in carbon dioxide only by the Friedman-Macek mechanism (melting of the oxide layer), as particle self-heating was completely absent [12]. The reaction of Al and oxygen was found to proceed according to the parabolic law, but no dependence on the initial thickness of a specially grown oxide film was evident up to an initial thickness of 0.5 μm.

The shock wave ignition of Mg powder was investigated by Fox et al. [13,34]. Two sieved powders were employed, a 100 mesh powder with a bulk average diameter of 17 μm and a 325 mesh powder that had a bulk average diameter on the order of 5 μm. The particles were ignited in the high velocity flow induced by an incident shock wave in oxygen/nitrogen mixtures. A detailed convective heat transfer and kinematic model of the particle ignition process is presented.

The measured ignition delay times of Fox et al. correlated well with the predicted particle melting times. The ignition process was believed to result from the onset of surface erosion, which produced, in the wake, metal vapor which immediately reacted with the oxidizer. The ignition delay time was independent of oxygen concentration, which was varied from 2.3 to 100 percent.

Disperse particle clouds simulated isolated particle ignition, while compact clouds exhibited substantial particle to particle interaction.

The ignition and combustion of aluminum foil samples (2 cm x 2 cm) having thicknesses that ranged from .01 to .10 cm were studied in pure oxygen and in atmospheres representative of the combustion products of solid propellants by Driscoll et al. [35,36]. The Al samples were mounted on the endwall of a shock tube and a reflected shock wave was used to produce temperatures and pressures up to 5150 K and 40 atm, respectively. In order to compensate for the thermal inertia of the endwall, the Al sample was mounted on a Pyrex plate and electrically preheated to 700 K prior to the test.

In pure oxygen at a pressure of 7 atm, Driscoll et al. determined that the ignition limit of the Al sample was 2390 K, just slightly above the 2300 K value typically reported for measurements at atmospheric pressure. It was reported that small particles emitted from the sample surface were seen to ignite at oxygen temperatures as low as 2000 K. The authors suggested that these particles may have been lacking an oxide coating [35].

Brewster and Taylor [37] have investigated the radiative properties of Al particles burning in the combustion products of ammonium perchlorate. Measurements were performed in a closed bomb at pressures ranging from 44 to 75 atm. Intensity measurements indicated that the effective blackbody emission temperature of the burning Al droplets is in excess of the adiabatic flame temperature, calculated assuming complete Al combustion. The higher intensities were ascribed to continuous emissions from Al_2O_3 droplets in the flame envelope as well as the from the molten Al droplet. Brewster and Taylor concluded that emission from the flame envelope and particle must be considered in analyzing the radiative transfer in burning Al particles.

Recently, Boiko et al. [38] measured the ignition delay time of clouds of Al, Al/Fe, and Mg particles in oxygen using the reflected shock region of a shock tube. The oxygen temperature and pressure ranged from 1000 - 2000 K and 10 - 30 atm, respectively. Although the experiments were performed near the endwall of the shock tube, the interaction of the particle samples with the endwall (particularly the endwall thermal layer) were not discussed. The experimental measurements were compared to predictions based on a simple thermal ignition model similar to that of Friedman and Macek, which neglected particle self-heating due to heterogeneous surface reaction.

The measured ignition delay times for both Al and Mg were found to be strong functions of the gas temperature. Assuming a Mg ignition temperature of 1368 K, equal to the normal boiling point of Mg at 1 atm rather than the true pressure-dependent boiling point of Mg, yielded satisfactory agreement between the predicted and measured ignition delay times. However, in order to obtain similar agreement for Al, an ignition temperature of 1820 K had to be assumed, which is significantly less than the ~2300 K melting temperature of Al_2O_3. Although Boiko et al. conclude that it is necessary only to consider the convective heating of the particles when predicting their ignition delay time, this lower "apparent" Al ignition temperature appears to contradict this conclusion.

Although there now exists a large body of work concerning the combustion of metals, many uncertainties still exist, as was recently discussed by Steingberg et al. [39]. They found that the combustion phase (i.e., heterogeneous or vapor-phase) of burning metals, including Al and Mg, could not be accurately predicted using any existing criterion that is based on the thermophysical properties of the metals. In addition, Steinberg et al. pointed out that inconsistencies in published property values and definitions related to metal combustion still remain.

1.3.2 Survey of Al/Mg Alloy Particle Ignition and Combustion Research

Fassell et al. [40] investigated the combustion characteristics of several metal powders in the combustion products of an air/oxygen/natural gas torch at atmospheric pressure. Of all the Al-base alloys, they found that the Al/Mg system provided the best increase in combustion performance. The most rapidly burning Al/Mg alloy composition was found to have a Mg content of 35%, which coincides closely with the Mg-rich eutectic composition [41]. The addition of impurities (~2%) of various metals to this optimum Al/Mg alloy composition decreased the burn rate of the alloy substantially in all cases.

Breiter et al. [42] investigated the ignition and combustion of 125 μm diameter Al/Mg alloy particles as a function of alloy composition. The experiments were performed in the combustion products of a solid propellant that was burned in a closed bomb of nitrogen at pressures of 20 and 40 atm.

Breiter et al. found that the Al/Mg alloy particle ignition delay and burn times initially decreased with increasing Mg content. After reaching a minimum at approximately 70 weight percent Mg, the ignition delay and burn times began to rise slightly with further increases in Mg content. This behavior was attributed to the variation in boiling point, protective nature of the solid oxide film (in the case of the ignition process), and heat of reaction with alloy composition (see Figs. 3.15, 3.17, and 3.14, respectively) [42]. The authors believed that the particles burned in a detached gas-phase manner, based on the observation that the photographically measured tracks were 3 to 5 times greater than the initial particle size.

A possibly important phenomena observed by Breiter et al. [42] , and later by Popov et al. [43], was the "explosive" combustion of the Al/Mg alloy particles. It was observed that a large fraction of the particles shattered during

combustion, producing numerous smaller particles that continued to burn to completion. The fraction of exploding particles increased rapidly with Mg content until all particles explode at a Mg content of 55 - 65%. Increasing the Mg content further resulted in a slight reduction in the fraction of particles that were observed to explode.

Popov et al. [43] investigated the combustion of single Al/Mg alloy particles at atmospheric pressure in air and in the combustion products of burning solid propellants. The particles studied had compositions ranging from 5 to 95 percent Mg and were spherical in shape with diameters of 100 to 600 μm. The particles were placed on the tip of a sharp tungsten needle and the combustion process was studied using high-speed photography.

When burned in air, Popov et al. found that Al/Mg alloy particles burned in two stages. During the first stage Mg was preferentially burned, leaving an Al-rich droplet to be consumed during the second stage. In the combustion products of the solid propellant, the Al/Mg alloy particles burned explosively in a manner similar to that observed by Breiter et al. [42]. Popov et al. attributed this explosive combustion to the fact that Al and Mg have large differences between their normal boiling points (1366 K and 2767 K for Mg and Al, respectively). The explosive combustion was preceded by heterogeneous reactions over the entire surface of the particle, and these reactions are believed to result in violent evaporation of the Mg, resulting in disruption of the particle [43]. This explosive phenomena was most likely to occur at high gas temperatures.

A possible explanation for the explosive combustion of Al/Mg alloy particles observed by Breiter et al. [42,] and Popov et al. [43] is the disruptive combustion of emulsified and multicomponent fuel droplets investigated by Lasheras et al. [44]. They experimentally investigated the combustion of droplets of binary mixtures of n-paraffins to determine the conditions of fuel

composition and oxidizer gas flow which would promote disruptive burning. Disruptive burning is characterized by homogeneous nucleation within the droplet (formation of a bubble at the droplet's center), thus causing the droplet to fragment explosively.

Lasheras et al. showed that a requirement for disruption to occur is that a minimum difference in the normal boiling points of the components must exist (the normal boiling points of Al and Mg differ by 1400 K). In addition, a certain initial concentration of the more volatile component must exist and must be within a limited range defined by the relation of the homogeneous superheat limit of the mixture to the normal boiling point of the less volatile component. The variation in the percentage of exploding Al/Mg particles observed in the research efforts discussed above may be the result of this composition dependence.

Breiter et al. [22] provide a detailed review of the theories and supporting experimental evidence of metal ignition. Particular emphasis is placed on describing the variation of ignition characteristics with composition for various alloys, including the Al/Mg system. The ignition limits of alloy powders (< 50 μm diameter) were measured using the differential thermal analysis method [22] in heated dry air at atmospheric pressure. It is important to note that the heat-removal ignition technique that was employed by Breiter et al. determines the onset of self-sustained heterogeneous reaction, as opposed to the transition to the detached gas-phase combustion regime of interest for rocket engine applications.

Breiter et al. found that the ignition limit was closely correlated with the Al/Mg alloy melting points (see Fig. 3.11). They explained this behavior by the fact that the metal expands considerably as it melts, weakening the oxide film and facilitating the particle ignition. In addition, the authors stated that the

non-protective nature of the oxide film is believed to remain non-protective (like that of Mg) to Al contents in excess of 85 percent, above which the oxide film becomes so protective that ignition is prevented even at the maximum experiment temperature of 1273 K.

The combustion of Al/Mg alloy particles (66 to 185 μm diameter) in water vapor has been studied by Ozerov and Yurinov [45]. The high temperature water vapor (~1800 K) was produced by a diffusional hydrogen-oxygen burner and the experiment pressure ranged from 1 to 6 atm. It was found, depending on the gas temperature, that particles with Mg contents of less than ~10% burned in either a detached gas-phase or heterogeneous manner. Particles having Mg contents in excess of 10% always burned in the detached gas-phase manner similar to pure Mg. The particle burn times decreased linearly with increasing Mg content and increased with an increase in gas pressure.

Most recently, Megli [46] has extended the results of the present study to the ignition of 20 μm diameter Al/Mg alloy particles in water vapor/argon mixtures. The measurements were performed at a gas pressure of 8.5 atm and gas temperatures as high as 3300 K. Megli's results indicated that the contribution of heterogeneous surface reactions to the particle heating is less significant in water vapor/argon mixtures than in pure oxygen. The particle ignition delay time was found to decrease in a nearly linear manner with increasing Mg content.

1.4 RESEARCH OBJECTIVE

It is evident from the preceding literature review that the physics of Al, Mg, and Al/Mg alloy particle ignition and combustion is extraordinarily complex. The specific physical processes involved (e.g., heterogeneous versus

gas-phase reaction, etc.) are a complicated function of the particle composition as well as the oxidizer composition, temperature, and pressure. The difficulty involved in generalizing these results to the specific case of the ignition and combustion of Al/Mg alloy particles in hot, high pressure oxygen is substantial.

The primary objective of this research effort is to measure experimentally the ignition delay and combustion times of ~20 μm diameter Al, Mg, and Al/Mg alloy particles in hot, high pressure oxygen, similar to conditions that would exist inside the thrust chamber of an operating Al/Mg-LOX rocket engine. These measurements are made in the high temperature and pressure, quiescent oxygen atmosphere produced behind the reflected shock wave in a shock tube. The reflected shock technique developed here is similar to that used by Boiko et al. [38] and by Seeker et al. in the study of coal particle ignition [47].

Another goal of this research effort is the development of a model of the particle heating, which incorporates the physics of the reflected shock technique, that can be used to analyze the experimentally measured ignition delay times. As part of this modeling effort, a detailed review of the published thermophysical properties of Al, Mg, and Al/Mg alloy is performed. Where there exist gaps in the known thermophysical properties of the alloys, approximations are made, based on the properties of the pure metals.

This work represents a direct contribution to the field of metal combustion. A new experimental technique is developed which allows the study of the ignition and combustion of small particles in a high temperature and pressure gas. To the author's knowledge, the results of this work represent the first published measurements of the ignition delay and combustion times of Al/Mg alloy particles in oxygen ranging in temperatures from 1750 K to 3250 K and pressures from 8.5 atm to 34 atm.

CHAPTER 2: EXPERIMENTAL TECHNIQUE

2.1 REFLECTED SHOCK COMBUSTION TECHNIQUE

In the present investigation, the ignition and combustion of approximately 20 μm diameter Al, Mg, and Al/Mg alloy particles is studied in the high temperature and pressure region of gas produced by reflection of a shock wave from the endwall of a shock tube. This region of gas is particularly suited for particle combustion studies since the flow velocity there is nearly zero. The experimental gas temperatures which can be attained using the reflected shock technique can be more than twice as high as those attained using the incident shock alone [48]. However, the usefulness of the reflected shock technique is limited by the short duration of the constant reflected shock conditions.

Figure 2.1 shows a typical wave diagram which illustrates the physics of a shock tube which has a reduction in cross-sectional area at the diaphragm. A detailed explanation of the wave diagram and the physics of the shock tube can be found in Appendix B. At time t = 0, the large diameter driver section (region 4) is filled with high pressure helium and the smaller diameter driven section (region 1) is filled with low pressure oxygen. After the diaphragm ruptures, the helium expands into the low pressure oxygen and produces the incident shock wave, S_i, which races toward the shock tube end wall. When the incident shock wave reaches the endwall, its reflection produces the reflected shock wave, S_r, which then travels back up the tube. The experimental test time, t_{test}, is then limited by the arrival of pressure disturbances, produced by the interaction of the reflected shock wave and the contact surface (C.S.), at the shock tube endwall.

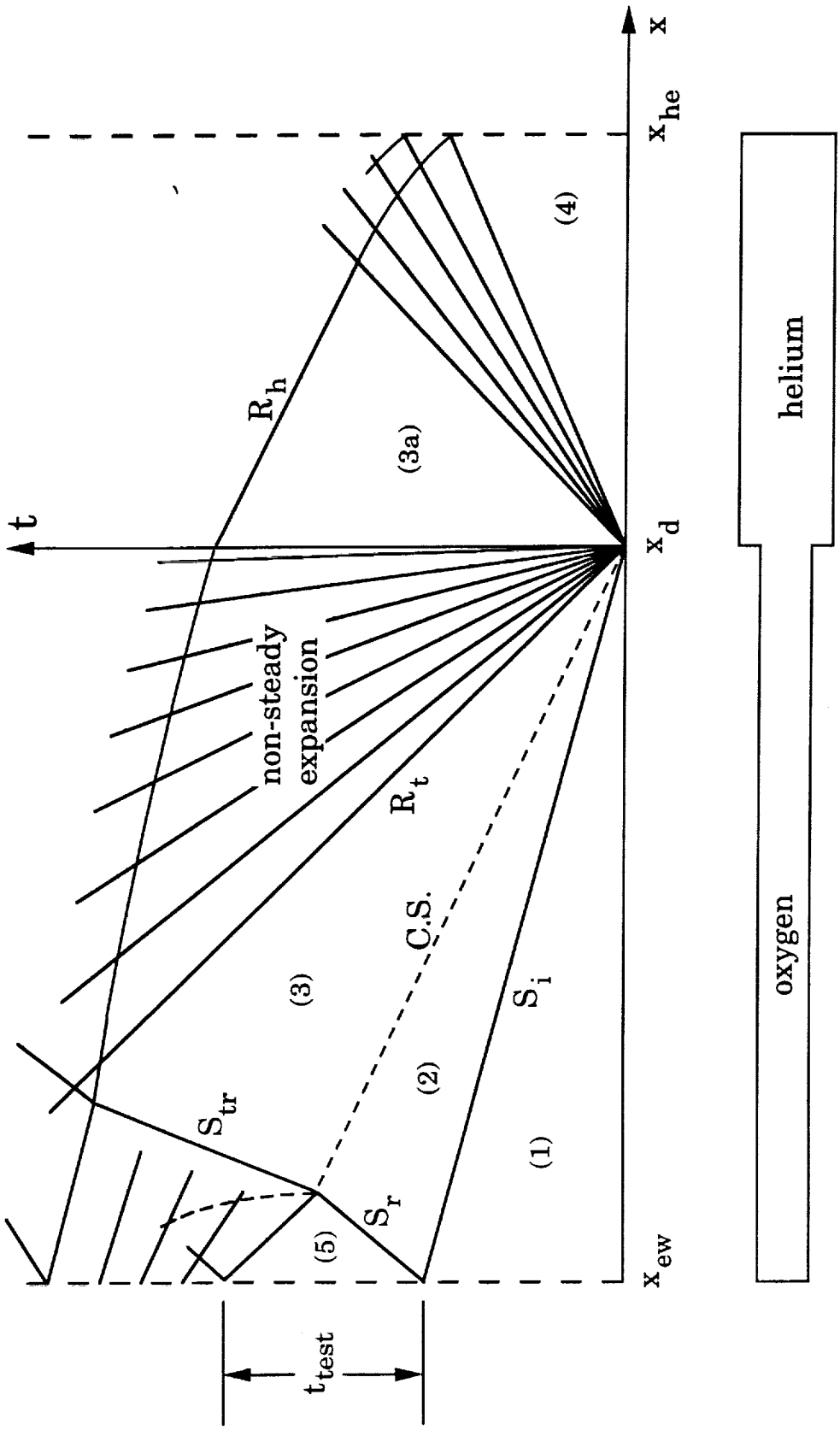

Fig. 2.1: Wave diagram for a shock tube with a reduction in cross-sectional area at the diaphragm.

In order to study the ignition and combustion of small metal particles in the reflected shock region, a new experimental technique has been developed and is shown schematically in Fig. 2.2. Figures 2.2a through 2.2d show the cross-section of the shock tube endwall region. The endwall has a 1.5 inch diameter observation window, for optical access, and a hobby knife blade mounted on a stainless steel post. Figure 2.2a shows the situation which exists just prior to the incident shock wave's arrival at the endwall. The particles are mounted on the knife blade tip in the quiescent oxygen driven gas. The incident shock wave is moving toward the endwall and is followed by a supersonic flow which is moving in the same direction.

In Fig. 2.2b, the incident shock wave lies between the knife blade and the observation window. The supersonic oxygen following the shock wave is entraining the metal particles and is accelerating them toward the observation window. Figure 2.2c shows the situation which exists after the incident shock wave has reflected from the endwall and moved past the location of the knife blade. The metal particles are dispersed and continue to move toward the window through the stagnant, hot, high pressure oxygen created by the reflected shock wave. The particles finally reflect from the observation window, are further dispersed, and are heated to the point of ignition and then burned as shown in Fig. 2.2d. The metal particle ignition and combustion times are then measured by recording the radiative emission of the particles through the endwall observation window.

A representative photodiode signal is shown in Fig. 2.3 along with the corresponding endwall pressure record. The scaled signal voltage is plotted as a function of time. The beginning of the test, t=0, is taken to coincide with the time of shock reflection. Ignition delay time, t_{ign}, is measured from the time of shock reflection to the point when half the peak amplitude of the photodiode signal is

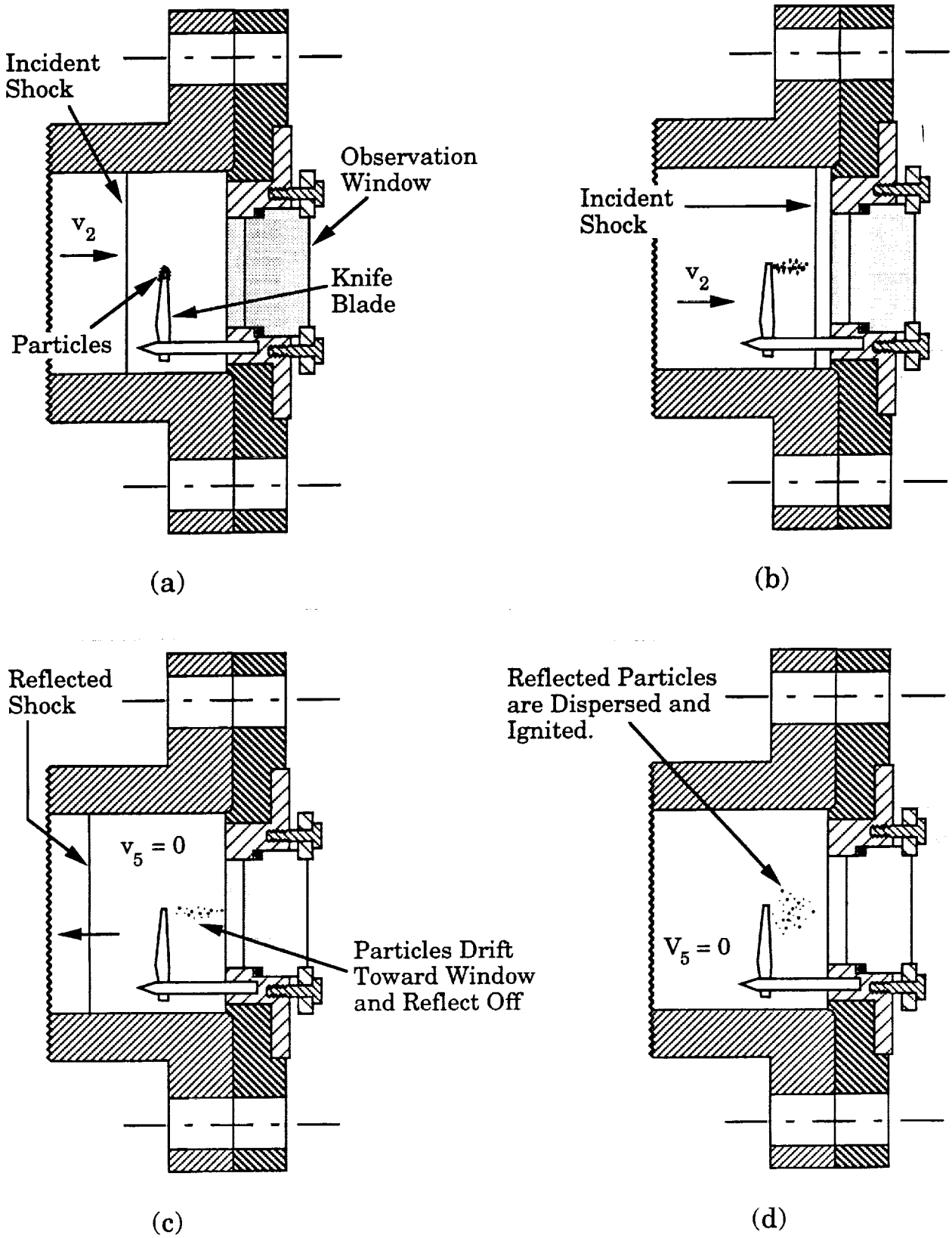

Fig. 2.2: Schematic of the developed knife blade particle mounting technique.

reached, as shown in Fig. 2.3. Combustion time, t_b, is determined when the light signal falls to half of its peak value. Oscillations in the photodiode signal can introduce a ~ 30 μs uncertainty in these times. The length of the quasi-steady test time, t_{test}, is limited by the arrival of unsteady compression waves at the endwall (see Fig. 2.24 and related discussion). The test time is generally greater than the overall particle ignition and combustion time.

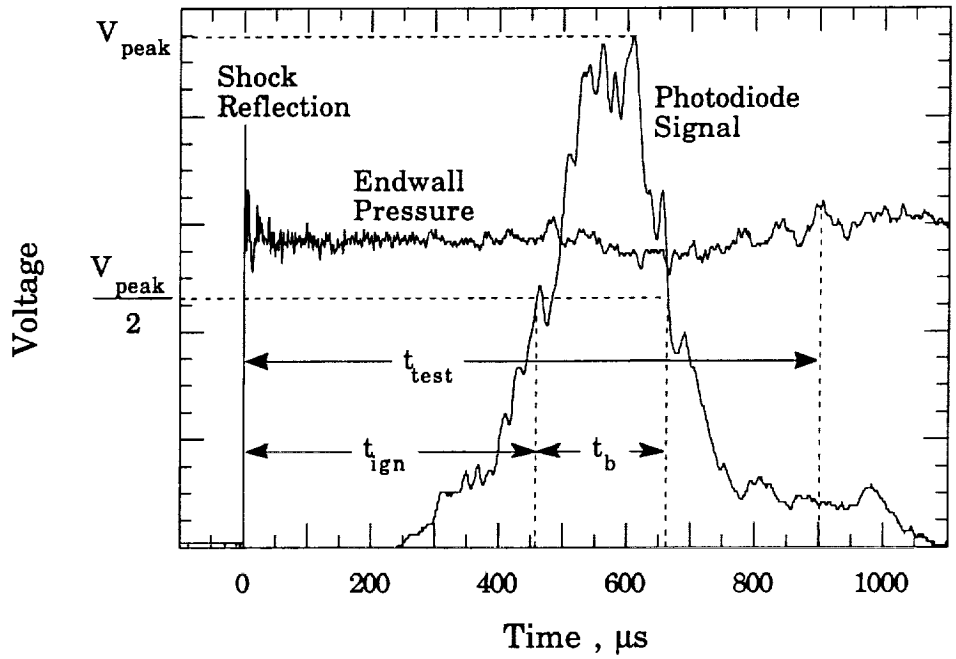

Fig. 2.3: Typical photodiode and endwall pressure records. The signals correspond to 10% Mg particles, d_{eff} = 20.7 μm, T_5 = 2230 K, p_5 = 34.1 atm.

The relatively short experimental test time requires use of powders composed of small diameter particles. The following section will describe the composition and size distribution of the Al/Mg alloy powders used in this investigation. The shock tube facility constructed as part of this investigation will be discussed in detail.

2.2 DESCRIPTION OF METAL POWDERS

The powders used in this experiment are spherically atomized Al, Mg, and Al/Mg alloys containing 0, 5, 10, 20, 40, 60, 80, and 100 weight percent Mg. The characteristics of each alloy powder is given in Table 2.1, along with the name of the manufacturer. All of the powders were donated by the manufacturer unless noted. The raw powders were composed of particles ranging in size from submicron to approximately 100 μm diameter. To obtain experimental measurements that can be meaningfully analyzed, it is necessary to sieve the powders to obtain narrow size distributions with a known mean diameter. In addition, to insure ignition of the particles prior to the end of the quasi-steady reflected gas conditions, their mean diameters must be less than 25 μm.

The raw powders are dry sieved using a Gilson vibratory 3" sieve shaker, Model SS-5. The sieve mesh sizes used are #635, 500, 450, 400, and 325, which correspond to mesh openings of 20, 25, 30, 38, and 45 μm, respectively. The tolerance on all of the mesh openings is ± 3 μm. The sieving is performed by stacking the sieves in increasing mesh size. The raw powder is then placed in the top sieve and the stack is placed in the shaker. The sieves are periodically inspected to assess the degree of particle separation. The inspection is performed in two ways: 1) visually with a 20X loupe and 2) by monitoring the number of small particles which continue to fall through the sieves onto plastic film placed between the sieves. Each powder was sieved for at least 20 hours. The majority of the experiments performed in this investigation used the powders separated by the 20 - 25 μm sieve combination.

The metal powders, both raw and sieved, are stored in individual vessels which are then placed in a covered plastic container along with anhydrous

calcium sulfate, which acts as a desiccant. The sieved powders are placed in individual, short, capped test tubes as shown in Fig. 2.4. The shallow depth of the test tubes provides convenient access to the powder for mounting on the tip of the knife blade. As is evident, the amount of powder which remains after sieving is quite small. However, since an individual experiment burns only 5,000 to 10,000 particles, the small quantity of powder produced is more than adequate for the purposes of this experiment.

Table 2.1: Characteristics of the 20-25 μm Sieved Al, Mg, and Al/Mg Alloy Powders.

Mg	$(Mg)_{actual}$	Shape	d_{eff} (μm)			Manufacturer
(%)	(%)		Mean	Median	Std. Dev.	
0	0.0	spheroidal	21.6	21.7	2.4	Valimet Inc.
5	5.4	spheroidal	20.5	20.8	2.7	Valimet Inc.
10	9.8	spheroidal	20.7	21.0	2.1	Valimet Inc.
20	20±2	spherical	21.2	21.4	2.2	D. Robertson[a]
40	40±2	spherical	21.5	21.5	2.5	D. Robertson
60	60±2	spherical	21.6	21.9	2.6	D. Robertson[b]
80	80±2	spherical	21.8	21.9	1.8	D. Robertson[b]
100	99.9+	spherical	21.5	21.4	2.0	Hart Metals

[a]Dr. David Robertson of the Center for Pyrometallurgy at the University of Missouri-Rolla.

[b]Powder donated by Sean O'Connor of Hercules Incorporated.

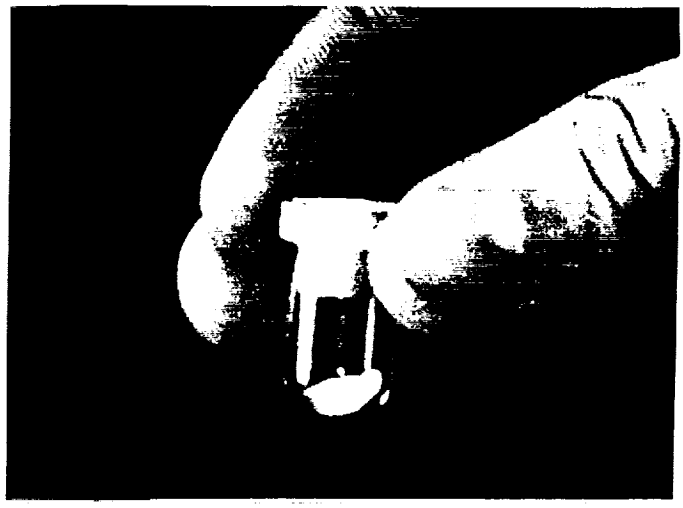

Fig. 2.4: Photograph of sieved powder stored in a short, capped test tube.

Figures 2.5 - 2.12 show photomicrographs and measured effective particle diameter histograms for all of the 20 - 25 μm sieved powders. The photomicrographs were taken with an ISI-DS130 scanning electron microscope (SEM) at a magnification of 300X. Each histogram is based on the dimensions of 200 individual particles measured with a Bausch and Lomb SteroZoom®7 optical microscope from 200X SEM photomicrographs. The optical microscope is set to a magnification of 7X and used a measuring reticle with a precision of .01 mm/div. The uncertainty of each measurement is estimated to be ± 1 div, which corresponds to a ± .2 μm dimensional error.

The particles will be in a liquid state for a majority of the time it takes to heat them to the point of ignition. Therefore, it is assumed that the initially non-spherical particles become spherical upon melting. The effective particle diameter is defined to be equal to the equivalent spherical diameter which conserves the particle mass (or volume). The non-spherical particles are treated

as either prolate spheriods or cylinders. A particle is defined to be a prolate spheroid if its major and minor axes differ by more than 1 μm. The effective particle diameter of a prolate spheroid is given by:

$$d_{eff}^{p\text{-}s} = \left[l_1 (l_2)^2 \right]^{\frac{1}{3}} \tag{2.1}$$

where l_1 and l_2 are the lengths of the major and minor axes, respectively. Particles which are clearly cylindrical have effective diameters which are given by:

$$d_{eff}^{cyl} = \left[\frac{3}{2} l\, d^2 \right]^{\frac{1}{3}} \tag{2.2}$$

where l and d are the length and diameter of the cylinder, respectively. Table 2.1 above presents the measured mean and median effective particle diameters, as well as the standard deviation, of each 20-25 μm sieved alloy. It is found that the powder samples have mean effective diameters which range from 20.5 μm to 21.8 μm with relatively small standard deviations of 1.8 μm to 2.7 μm.

Examination of the photomicrographs in Figs. 2.5-2.12 shows that the powders containing 0, 5, and 10 weight percent Mg can be characterized as composed of spheroidal particles, while the remaining powders can be characterized as being composed of spherical particles. Nearly all of the powder compositions are found to have a number of smaller "satellite" particles clinging to them. Figures 2.13-2.16 show SEM photomicrographs of typical particles taken at a magnification of 3000X. The pure Al (0% Mg) particle shown in Fig. 2.13a is found to have a "wrinkled" surface and the 5% Mg particle in Fig. 2.13b has a rough, irregular surface. As the Mg content of the alloy is increased further, the surface roughness is found to decrease until the surface

of the 60% Mg particle, shown in Fig. 2.15b, is nearly flawless. The surface roughness is then found to increase slightly as the Mg content rises to 100%, as can be seen in Fig. 2.16.

Figure 2.17 presents SEM photomicrographs (200X magnification) of pure Mg particles, which are sieved with the 30-38 μm and 38-45 μm sieve combinations. Each of these powders are mixed with the 20-25 μm Mg particles to produce powders with bimodal size distributions. These bimodal powders are then used to validate the individual nature of the particle ignition and combustion, which results from the knife blade particle mounting technique.

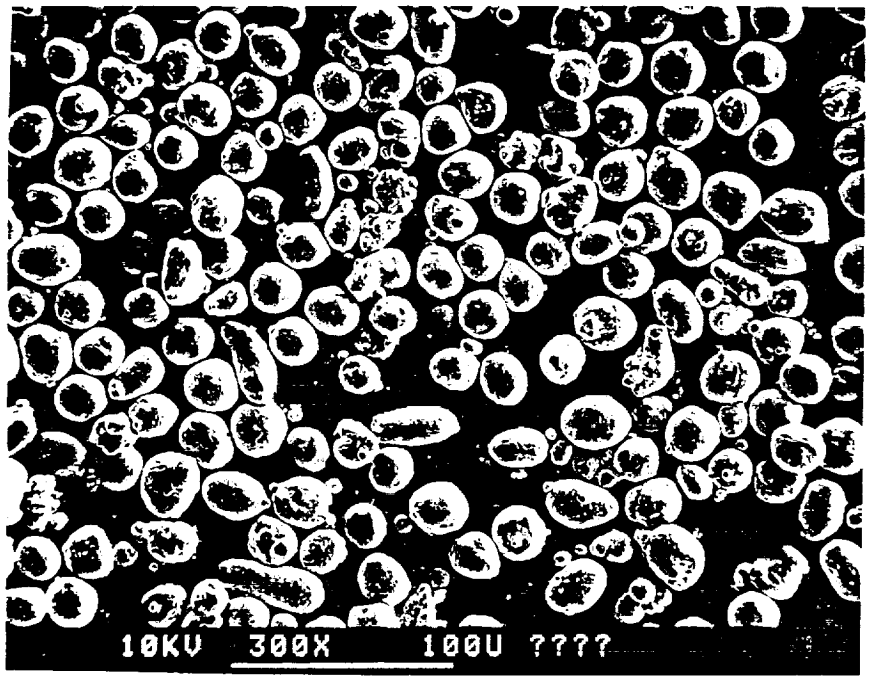

(a)

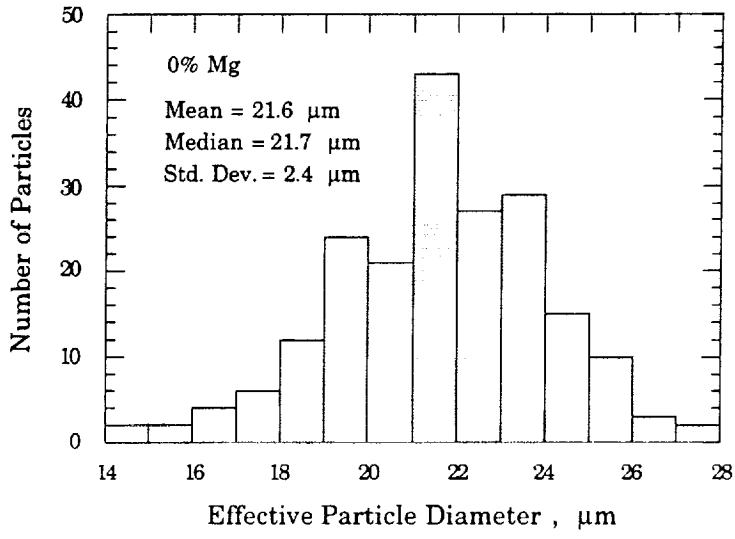

(b)

Fig. 2.5: Photomicrograph and particle size distribution of 0% Mg (pure Al) powder. a) SEM photomicrograph at 300X magnification. b) Histogram based on 200 individual particle measurements.

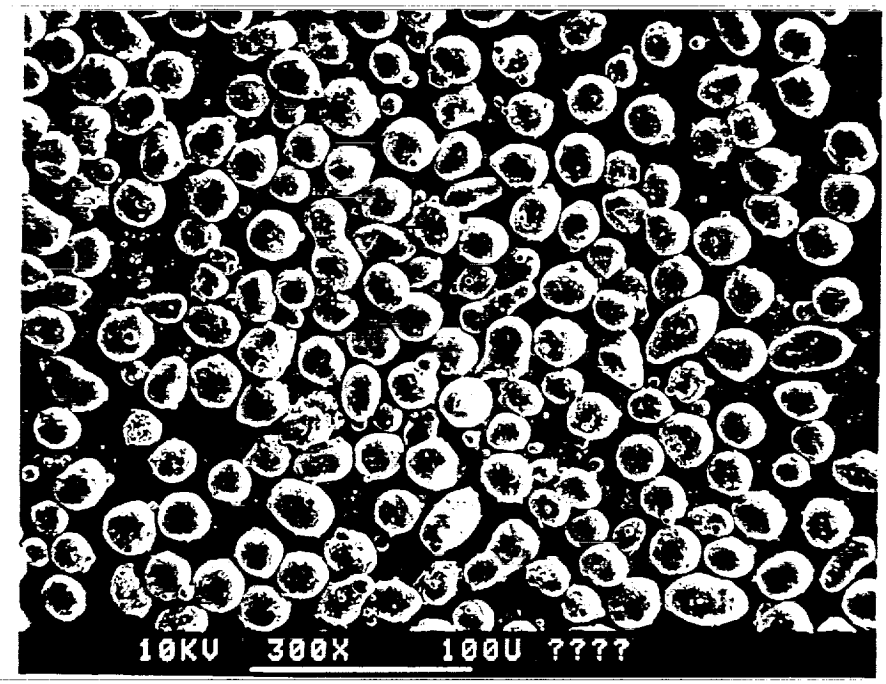

(a)

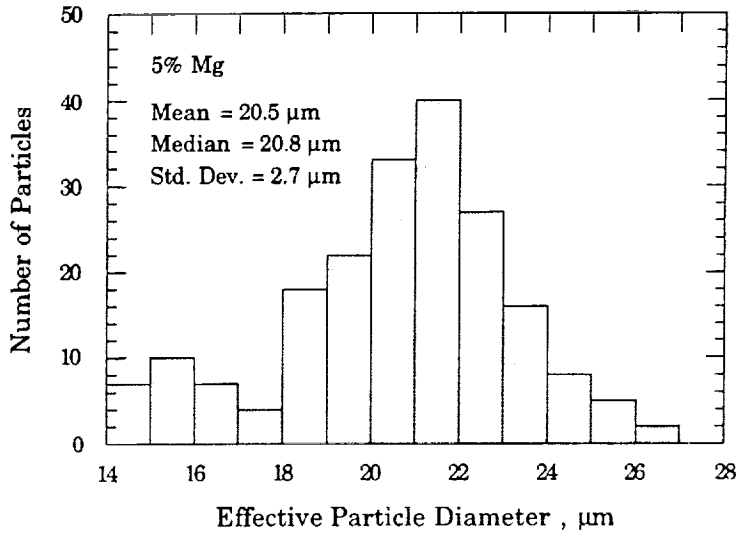

(b)

Fig. 2.6: Photomicrograph and particle size distribution of 5% Mg powder. a) SEM photomicrograph at 300X magnification. b) Histogram based on 200 individual particle measurements.

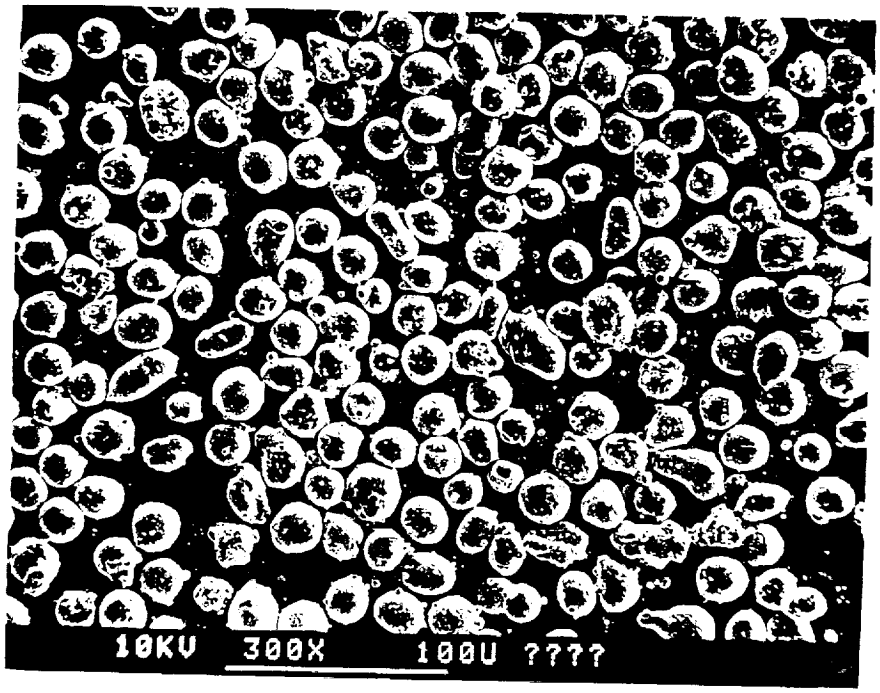

(a)

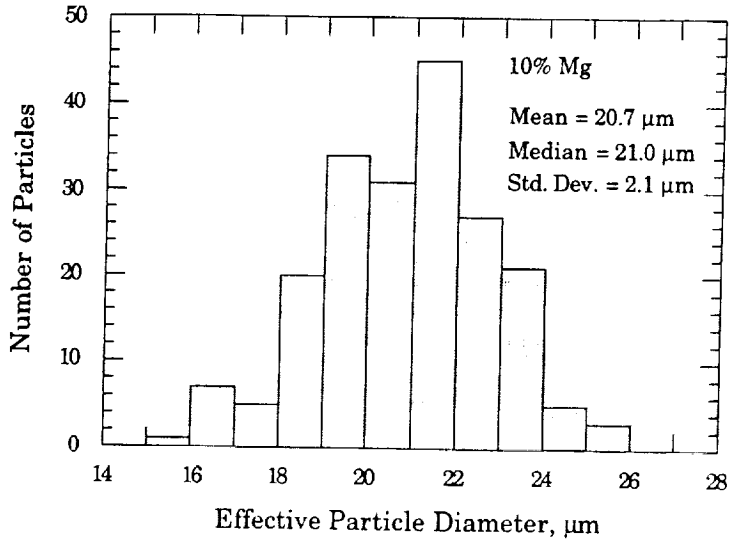

(b)

Fig. 2.7: Photomicrograph and particle size distribution of 10% Mg powder. a) SEM photomicrograph at 300X magnification. b) Histogram based on 200 individual particle measurements.

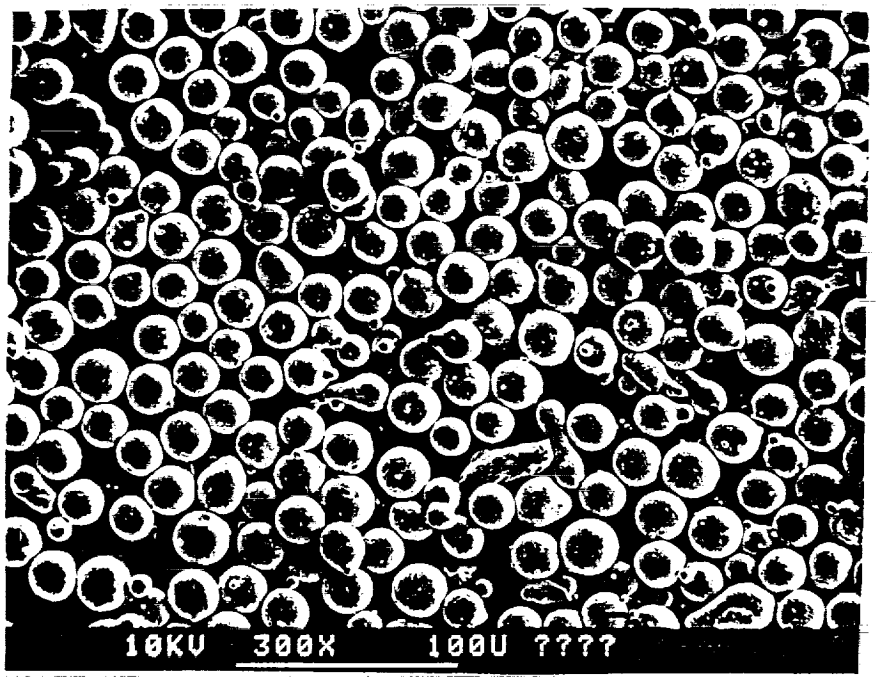

(a)

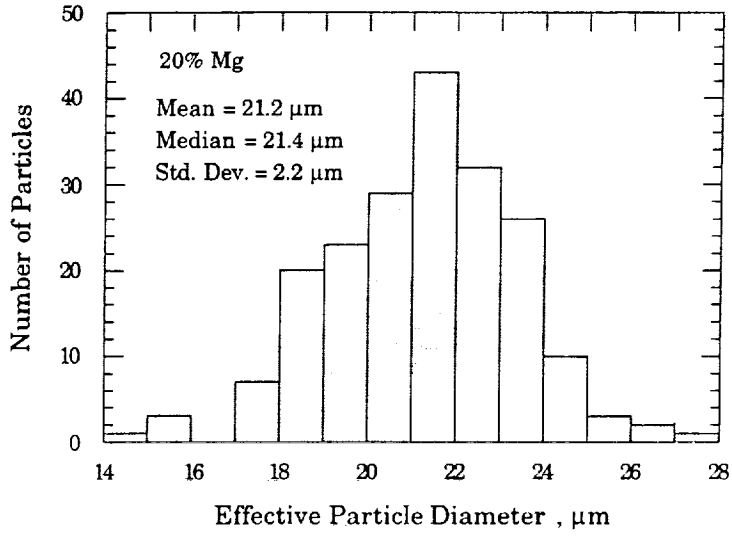

(b)

Fig. 2.8: Photomicrograph and particle size distribution of 20% Mg powder. a) SEM photomicrograph at 300X magnification. b) Histogram based on 200 individual particle measurements.

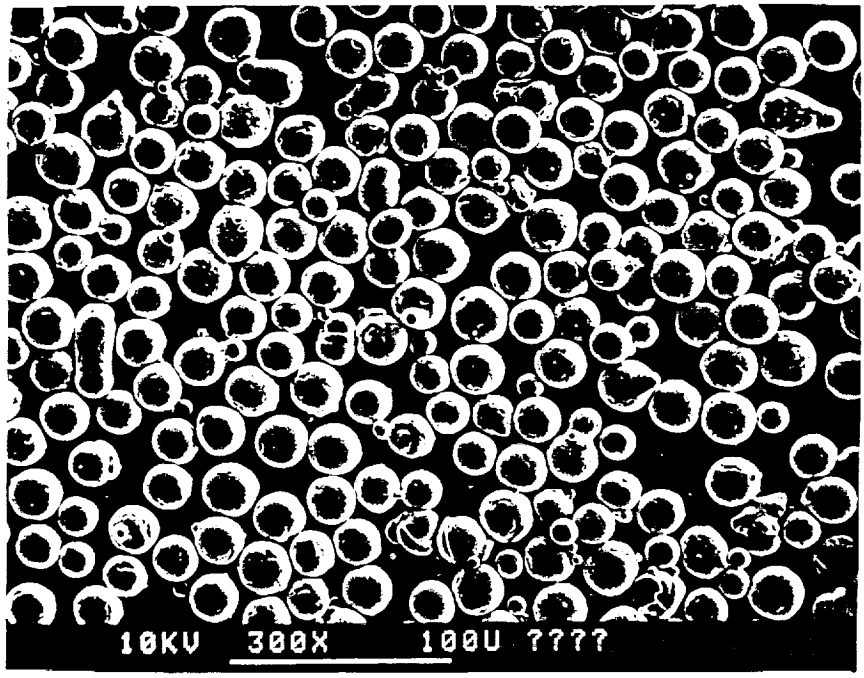

(a)

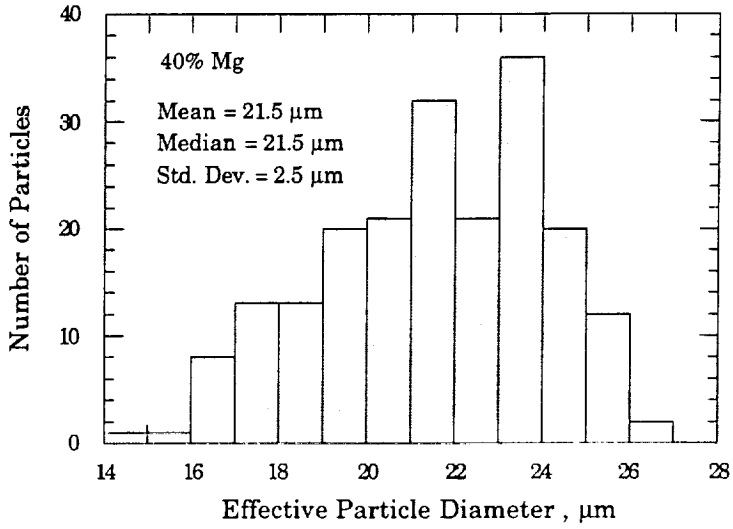

(b)

Fig. 2.9: Photomicrograph and particle size distribution of 40% Mg powder. a) SEM photomicrograph at 300X magnification. b) Histogram based on 200 individual particle measurements.

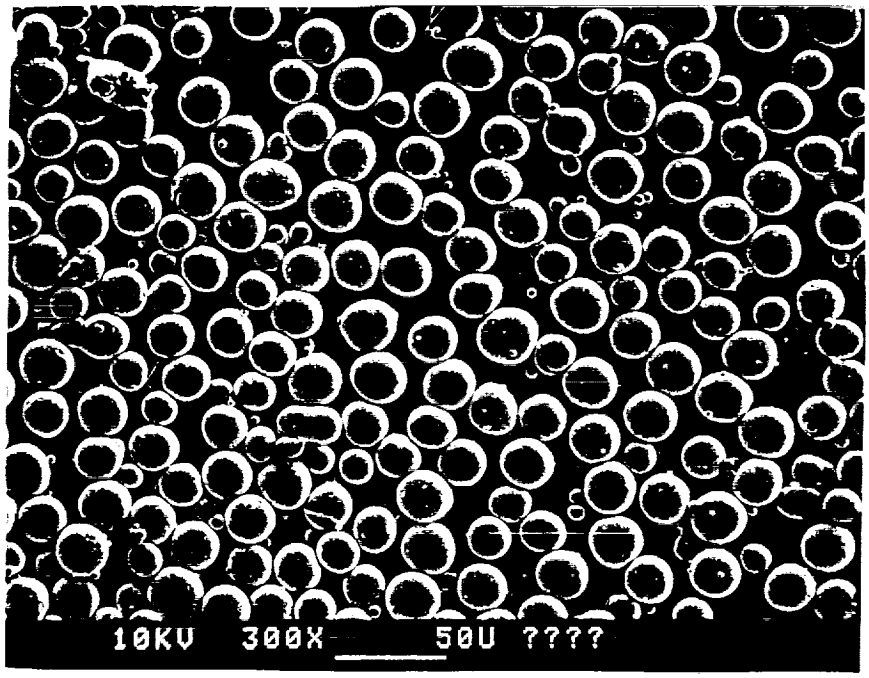

(a)

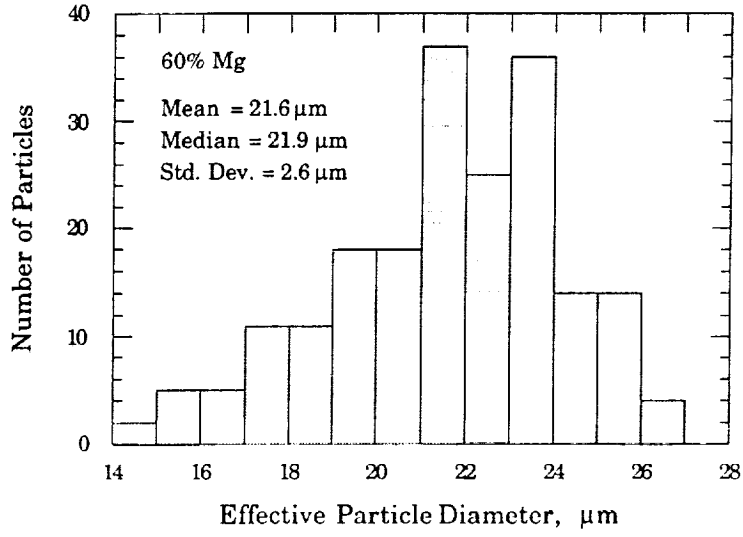

(b)

Fig. 2.10: Photomicrograph and particle size distribution of 60% Mg powder. a) SEM photomicrograph at 300X magnification. b) Histogram based on 200 individual particle measurements.

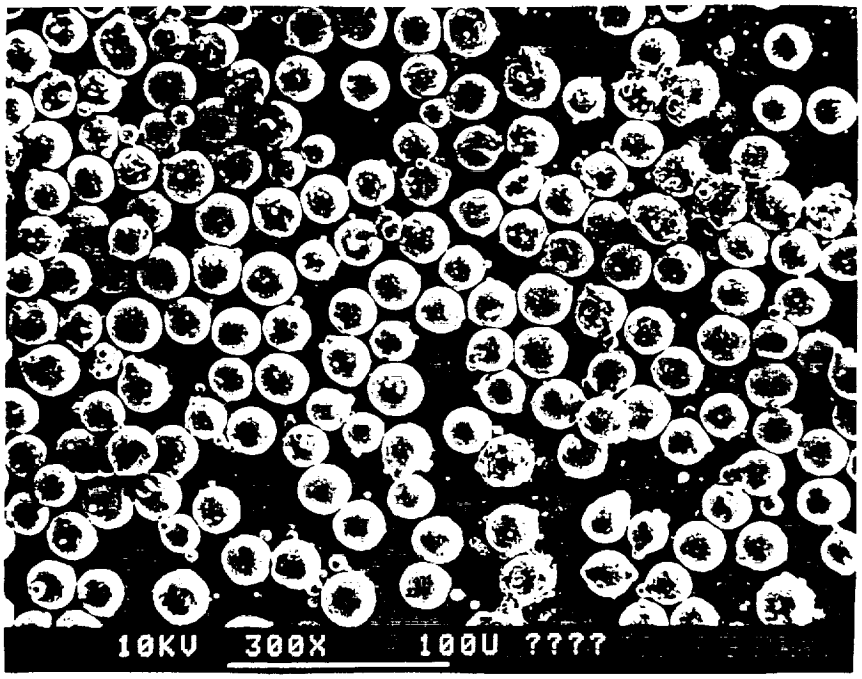

(a)

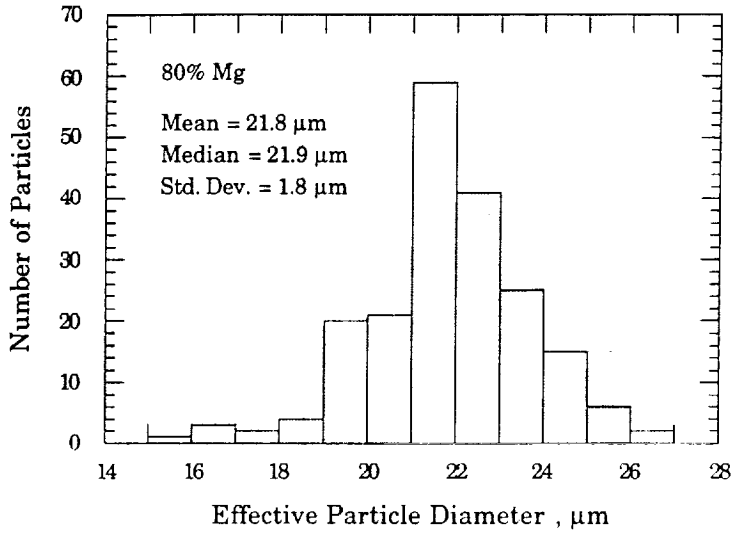

(b)

Fig. 2.11: Photomicrograph and particle size distribution of 80% Mg powder. a) SEM photomicrograph at 300X magnification. b) Histogram based on 200 individual particle measurements.

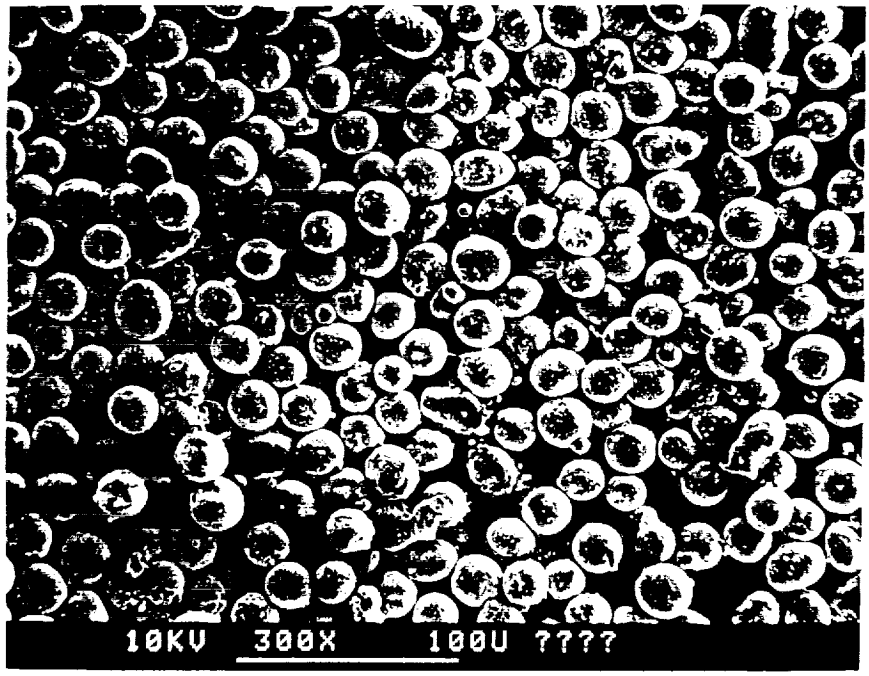

(a)

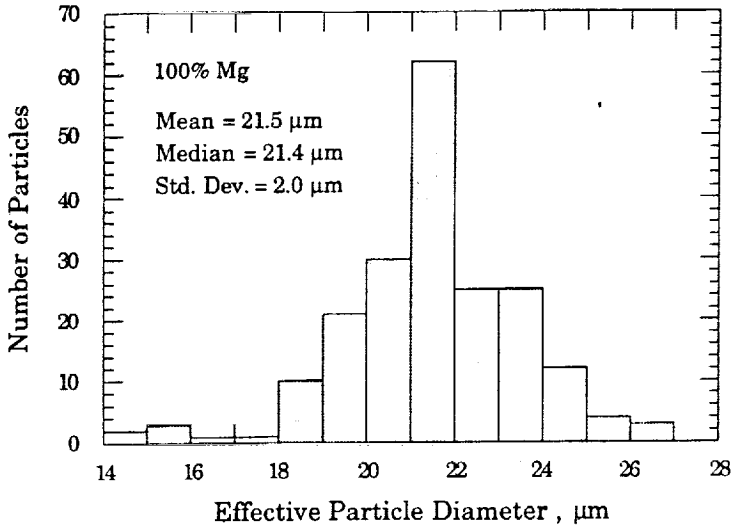

(b)

Fig. 2.12: Photomicrograph and particle size distribution of 100% Mg (pure Mg) powder. a) SEM photomicrograph at 300X magnification. b) Histogram based on 200 individual particle measurements.

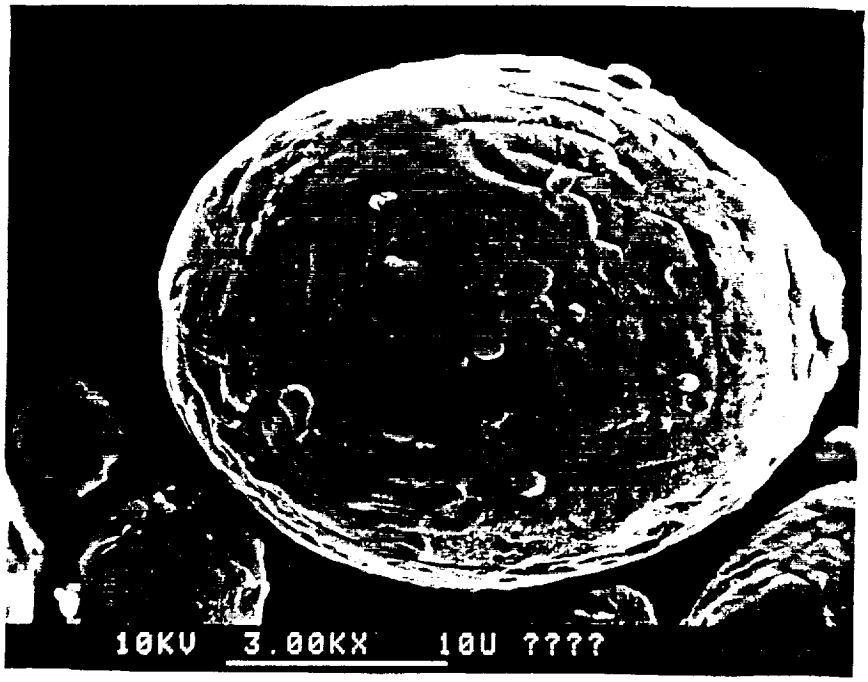

(a)

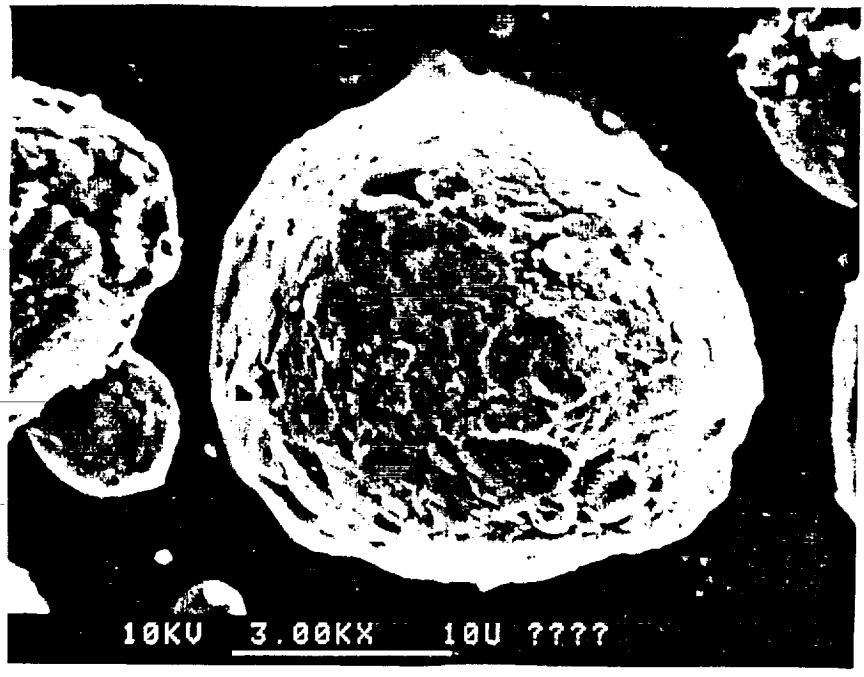

(b)

Fig. 2.13: Photomicrographs of individual 0% and 5% Mg particles at a magnification of 3000X. a) 0% Mg. b) 5% Mg.

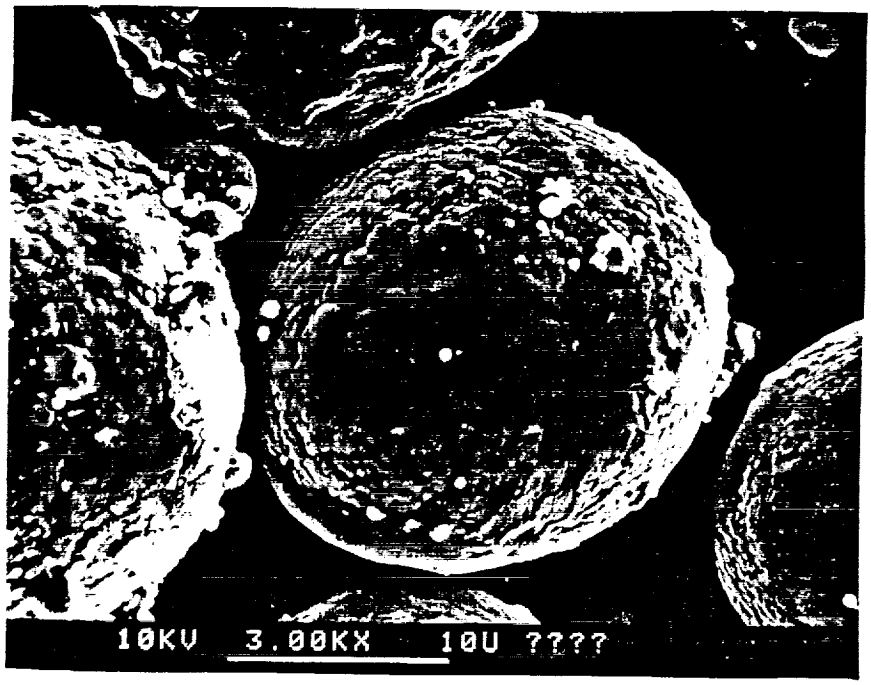

(a)

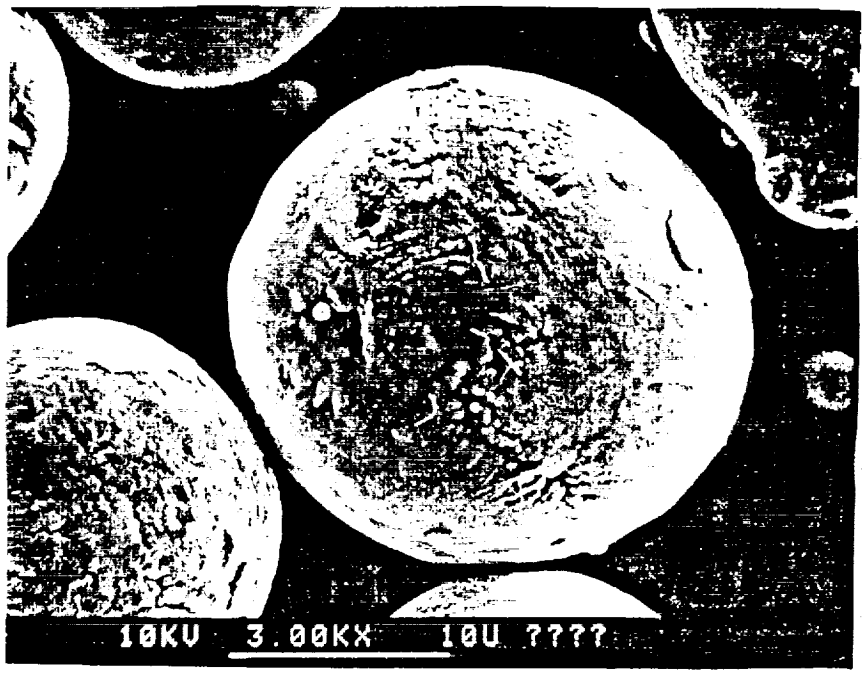

(b)

Fig. 2.14: Photomicrographs of individual 10% and 20% Mg particles at a magnification of 3000X. a) 10% Mg. b) 20% Mg.

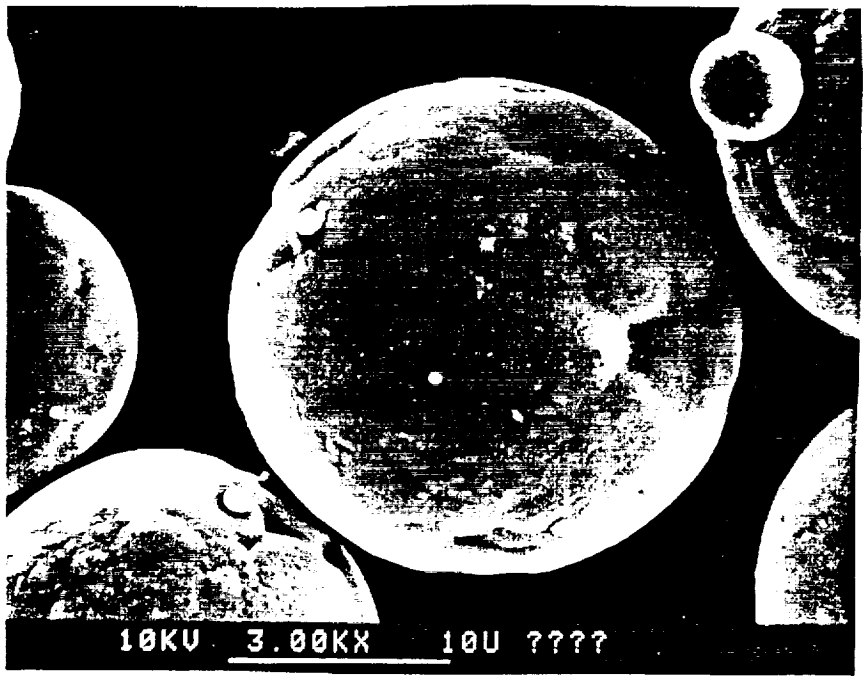

(a)

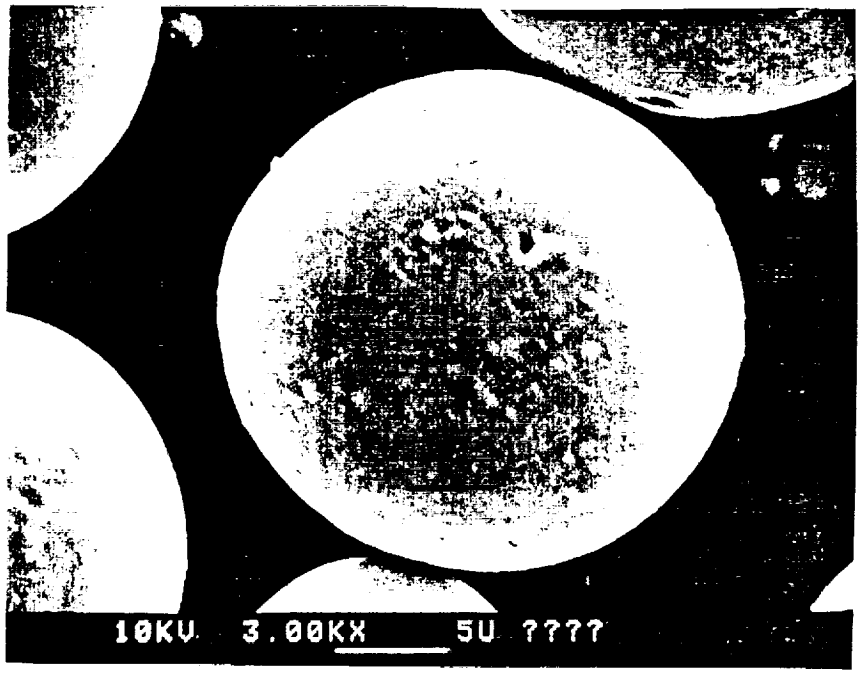

(b)

Fig. 2.15: Photomicrographs of individual 40% and 60% Mg particles at a magnification of 3000X. a) 40% Mg. b) 60% Mg.

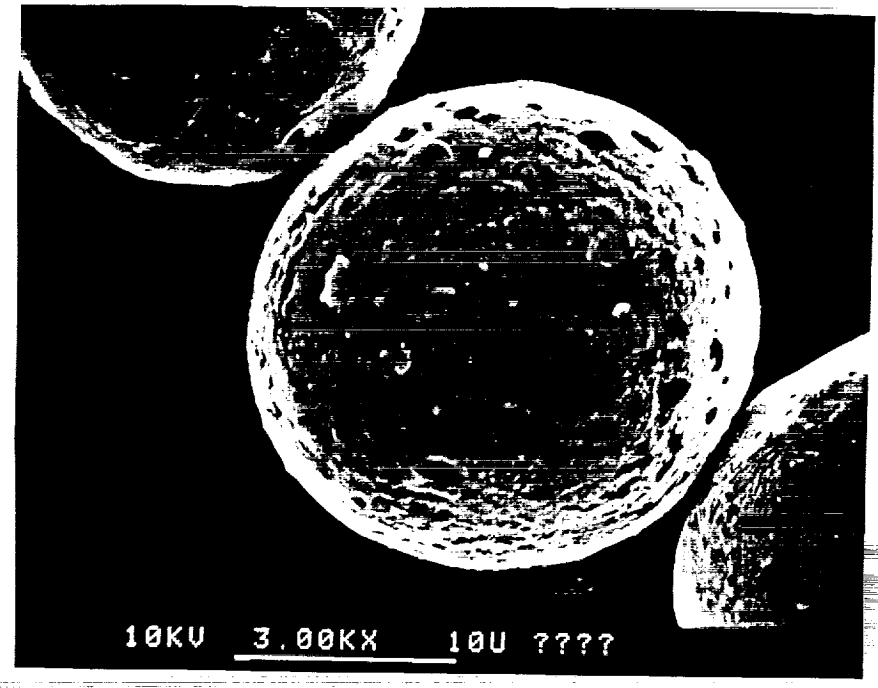

(a)

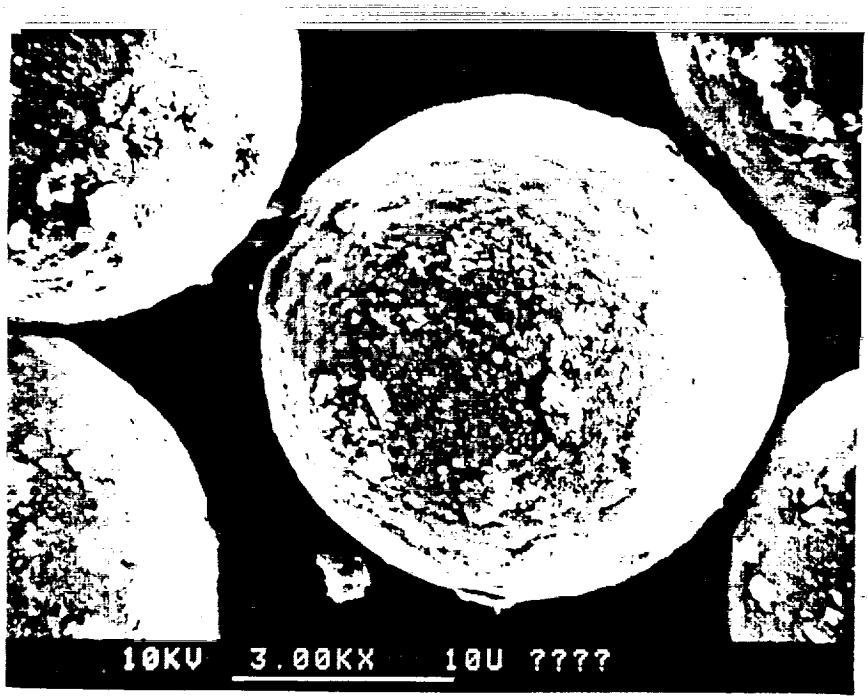

(b)

Fig. 2.16: Photomicrographs of individual 80% and 100% Mg particles at a magnification of 3000X. a) 80% Mg. b) 100% Mg.

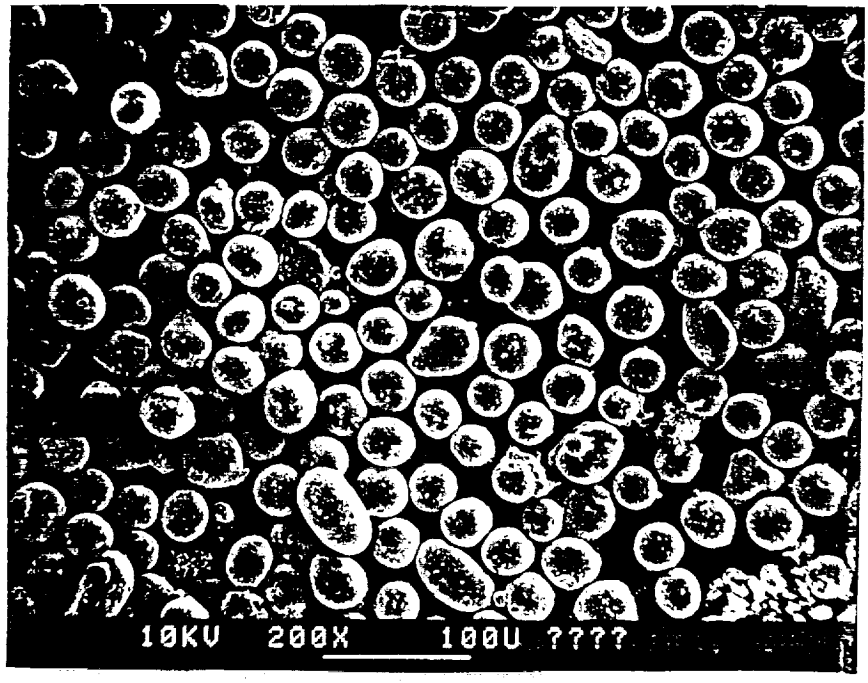

(a)

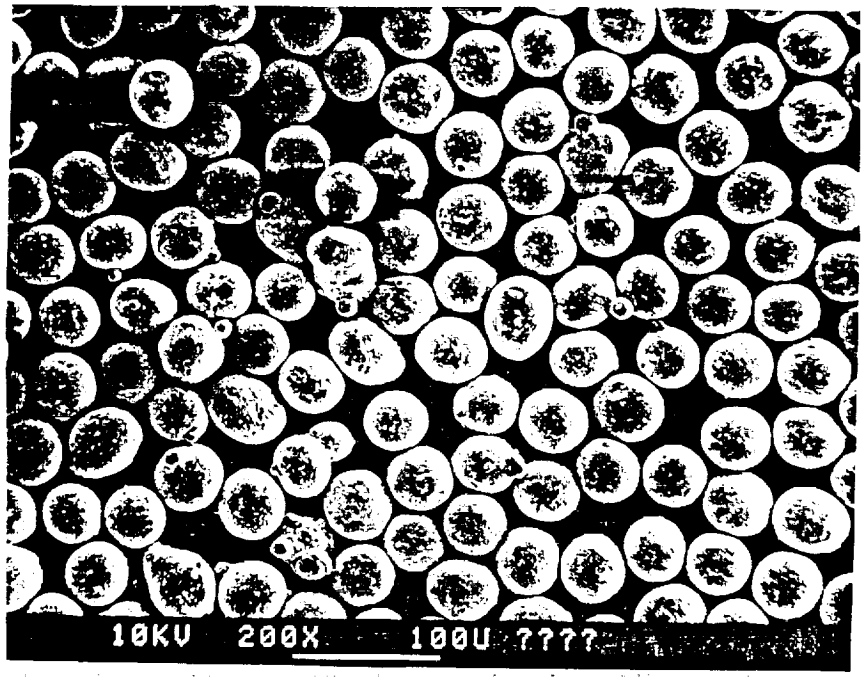

(b)

Fig. 2.17: Photomicrographs of the 100% Mg particles used to produce powders with bimodal size distributions. 200X magnification. a) 30-38 μm mesh combination b) 38-45 μm mesh combination.

2.3 DESCRIPTION OF SHOCK TUBE FACILITY

2.3.1 Shock Tube Construction

The high temperature and pressure oxygen required to study the metal particle ignition and combustion is produced using a stainless steel, helium driven shock tube, which has a reduction in cross-sectional area at the diaphragm. Shown in Fig. 2.18 is a photograph of the entire shock tube as seen from the driven end. Visible in the foreground is the optical bench and photo-diode optical assembly used to measure the radiation emitted by the burning particles. The shock tube control room is visible in the left-foreground of the photograph.

The overall dimension of the shock tube is shown in Fig. 2.19a. The shock tube sections are aligned using a precise male/female flange system and are sealed using standard o-rings. The driver section (high pressure He) is composed of two 5 foot long sections of stainless steel pipe, each with an inner diameter of 6.377" and a wall thickness of 0.562". The assembled driver sections were hydrostatically tested to 3000 psia, and the working pressure is limited to half of that value, p_{max} = 1500 psia. The cross-sectional area of the shock tube is contracted just prior to the diaphragm section, as is shown in Figs. 2.19a and 2.19b. The diameter of the driven section is 3.500", which corresponds to a contraction area ratio of 3.32.

The double diaphragm arrangement is shown in detail in Fig. 2.19b. Diaphragms (typically multilayered Mylar) are placed on either side of the diaphragm section. This diaphragm technique allows the driver and driven gases to be precisely set prior to firing, resulting in a 1% reproducibility of the incident shock Mach number. The driver section is mounted on rollers to

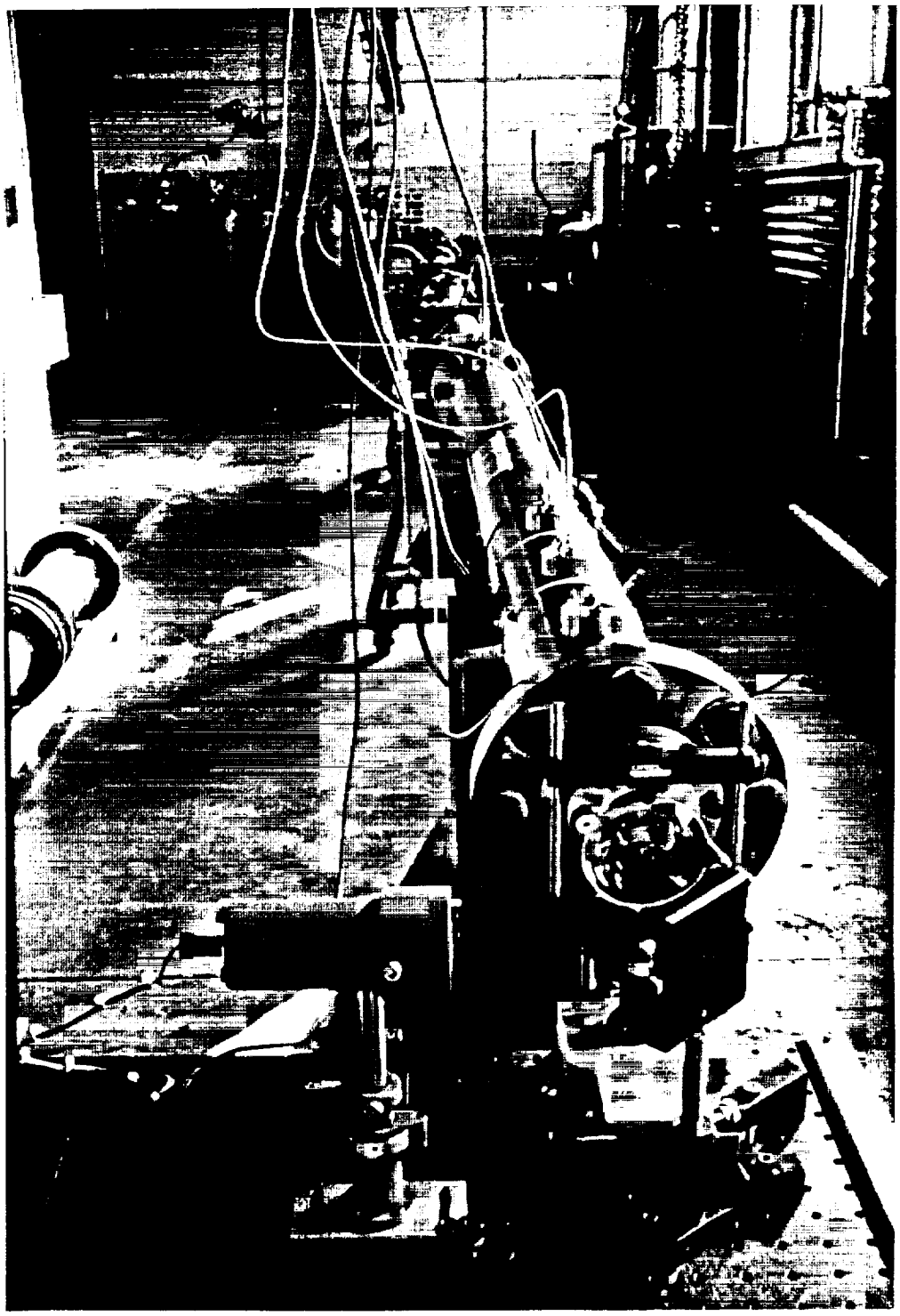

Fig. 2.18: Photograph of the stainless steel shock tube. The driven-end/test section is in the foreground along with the photodiode system.

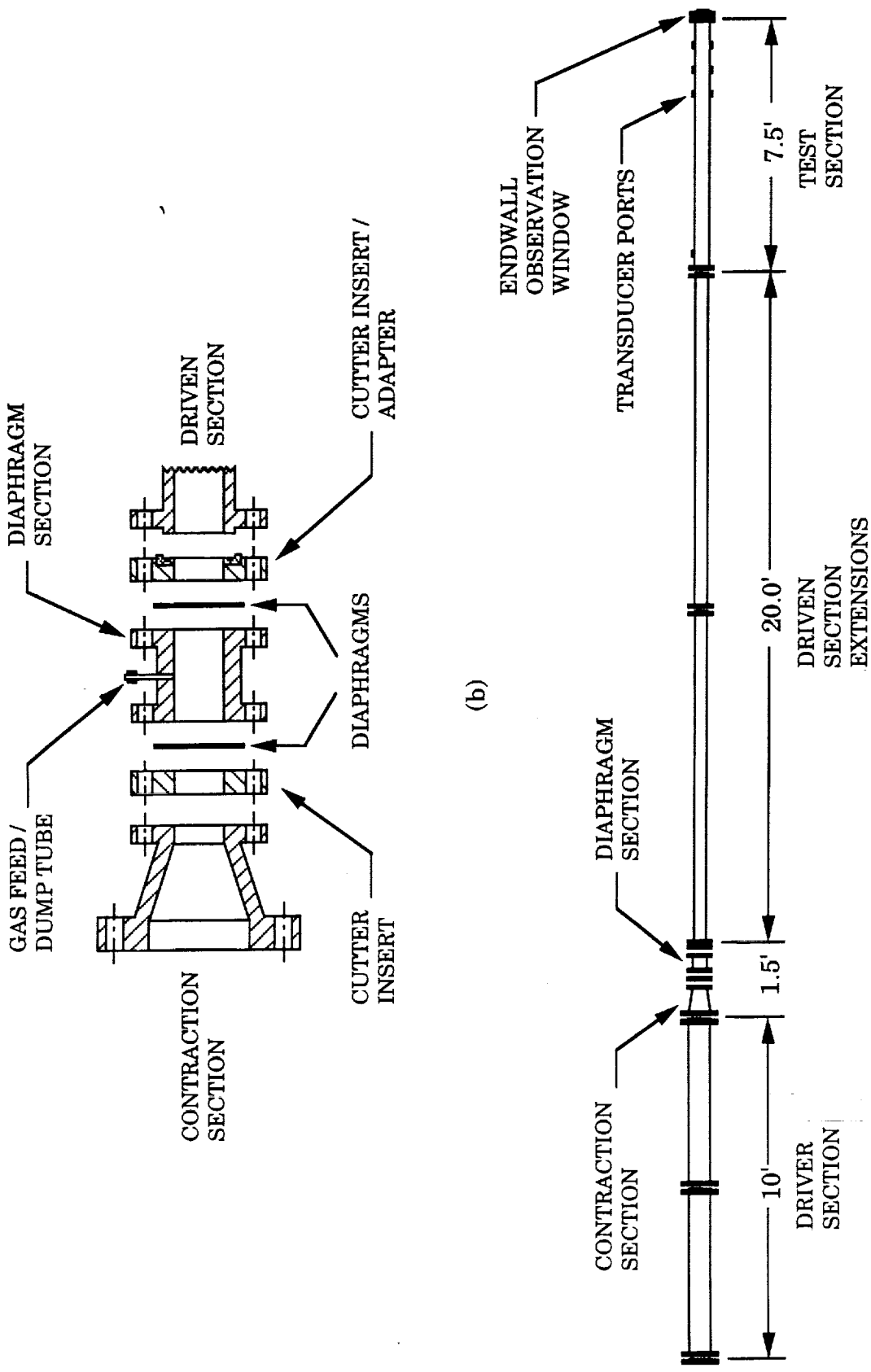

Figure 2.19: Overall dimensions of the helium driven shock tube and detail of the double diaphragm assembly.

provide access to the diaphragms. The diaphragms are replaced one at a time while the diaphragm section remains firmly bolted to either the driver or driven section, insuring that the shock tube maintains its alignment.

Downstream of the diaphragm section is the driven section (low pressure O_2) of the shock tube. The driven section consists of two 10 foot long extensions and the 7.5 foot long test section. The driven section extensions have an inside diameter of 3.500" and a wall thickness of 0.375". The extensions are constructed from seamless stainless steel pipe and 150#, 3.5" stainless steel slip-on flanges. The stainless steel test section has an inside diameter of 3.5" and a wall thickness of 0.750". The test section has six sidewall instrument ports located within 24" of the endwall. These ports are used to mount the sidewall pressure transducers and the digital recorder's external trigger. One additional port, used to evacuate and pressurize the entire driven section, is located 7 feet from the endwall.

The observation window assembly is mounted directly on the endwall of the driven section. The assembly contains the knife blade mounting post, the polycarbonate/quartz window, and a single endwall pressure transducer used to record the arrival of the incident shock and the temporal history of the quasi-steady reflected shock pressure.

2.3.2 Shock Tube Performance

The test conditions which will exist behind the reflected shock are functions of the oxygen's initial pressure and temperature, as well as the Mach number of the incident shock wave, M_{s_i}. The initial temperature of the oxygen is fixed at the temperature of the room. The initial oxygen pressure is set to a pre-determined value prior to firing the shock tube. The Mach number of the

incident shock is a function of the shock tube geometry (contraction ratio), the pressure ratio across the diaphragm, and the properties of the driver and driven gases (see Appendix B).

Figure 2.20 shows the required incident shock Mach number versus the reflected gas temperature (T_5) as a function of the reflected gas pressure (p_5). The calculations are made using the NASA Gordon-McBride code [9] assuming the driven gas is pure oxygen. As the reflected oxygen temperature is increased, substantially higher incident shock Mach numbers are required. The slight divergence of the curves of constant p_5 is due to dissociation of the diatomic oxygen, which necessitates an increase in the incident shock Mach number needed to attain a given T_5.

Shown in Fig. 2.21 is the initial driven section pressure plotted versus the incident shock Mach number for various reflected shock pressures. The Gordon-McBride code is again used to calculate these results assuming the driven gas is pure oxygen initially at room temperature. The results show that, for a given p_5, the required initial driven section (O_2) pressure decreases with increasing incident shock Mach number. It is also found that the reflected shock pressure ratio, p_1/p_5, is a function of M_{s_i} only. Thus, the three curves presented are simply multiples of each other and could be represented as a single curve if normalized by p_5.

The experimentally measured performance of the shock tube is shown in Fig. 2.22a for a reflected gas pressure of $p_5 \cong 17$ atm. The log of the shock tube driver/driven pressure ratio, p_4/p_1, is plotted versus M_{s_i}. The solid curve is a best fit of the experimental data. The results show that p_4/p_1 increases substantially as the incident shock Mach number is increased.

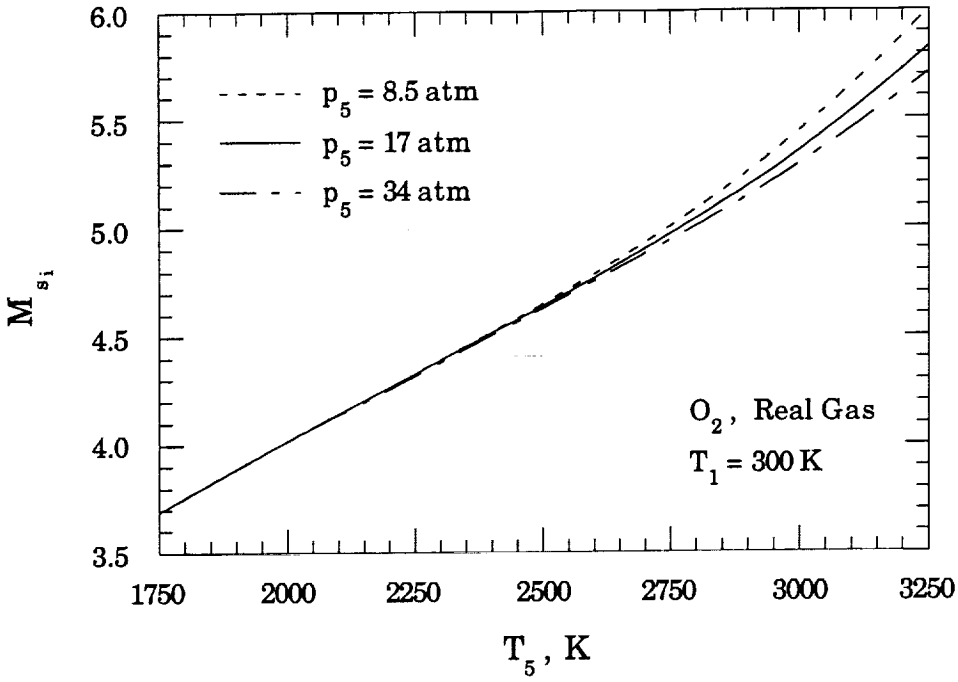

Fig. 2.20: Calculated incident shock Mach number versus the reflected gas temperature and pressure. Calculated with the NASA Gordon-McBride code, pure O_2, T_1 = 300 K.

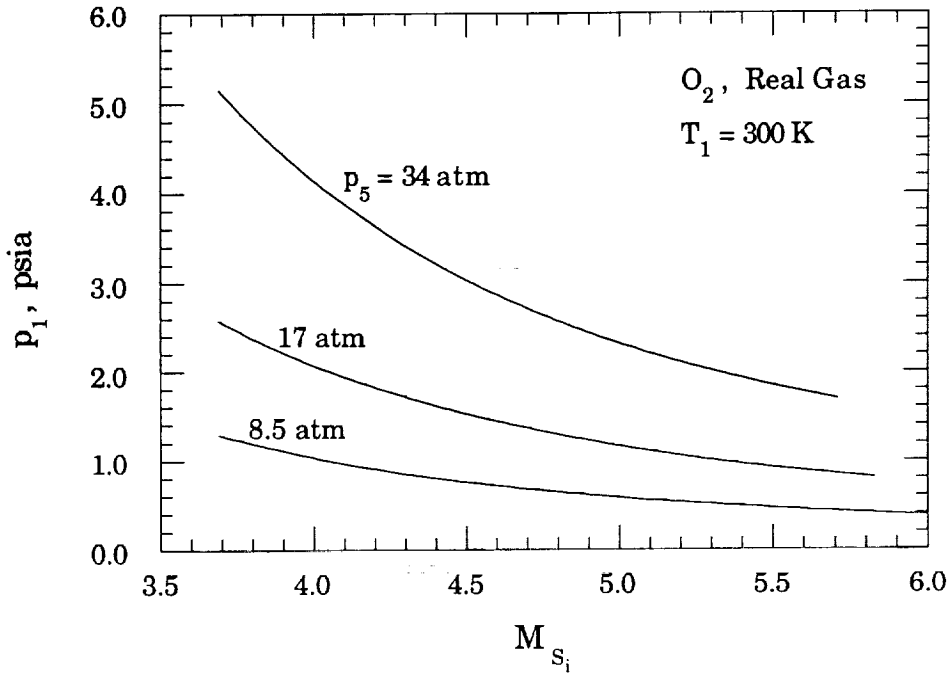

Fig. 2.21: Required initial driven section pressure versus the incident shock Mach number and reflected pressure. Calculated with the NASA Gordon-McBride code, pure O_2, T_1 = 300 K.

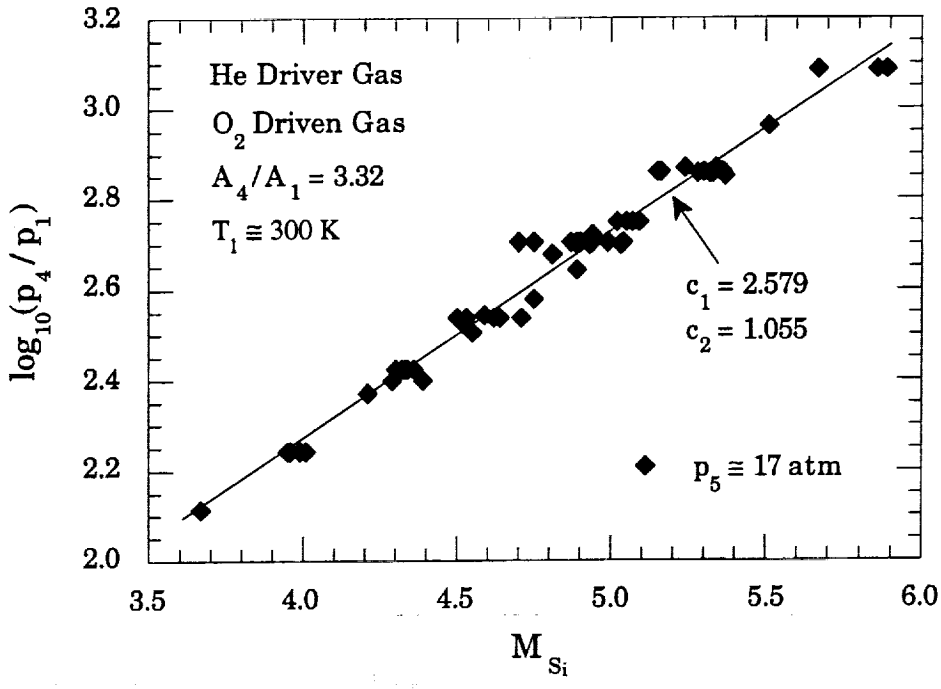

(a)

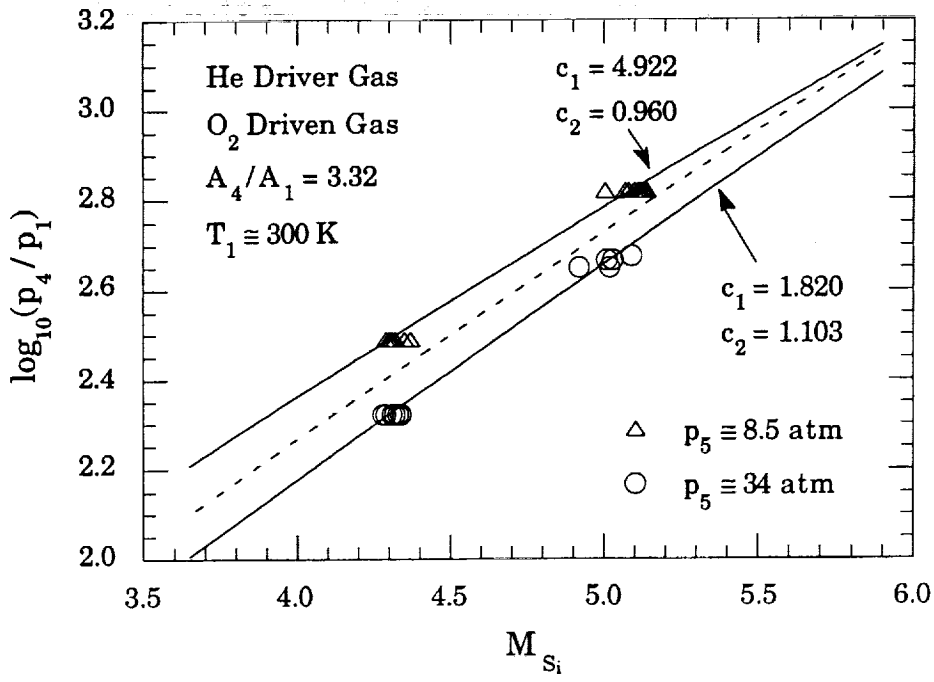

(b)

Fig. 2.22: Measured shock tube performance as a function of the reflected pressure. a) $p_5 \equiv 17$ atm. b) $p_5 \equiv 8.5$ atm and 34 atm. c_1 and c_2 refer to curve fits of the form: $p_4/p_1 = c_1 \exp(c_2 M_{S_i})$.

Shown in Fig. 2.22b is the experimentally measured shock tube performance at reflected shock pressures of $p_5 \cong 8.5$ atm and 34 atm. The majority of the experiments at these pressures use reflected gas temperatures of $T_5 \cong 2225$ K and 2775 K, which correspond to incident shock Mach numbers of approximately 4.33 and 5.1, respectively. The solid curves are best fits of theexperimental data and the dashed curve is the best fit of the data presented in Fig. 2.22a. For a given incident shock Mach number (or reflected gas temperature), the required shock tube pressure ratio is found to increase as p_5 is increased.

Using the calculated initial driver pressures presented in Fig. 2.21 and the experimentally measured shock tube performance presented in Fig. 2.22, the initial pressure of the He in the driver section can be calculated. Figure 2.23 shows the results of these calculations. The driver pressure is plotted, versus the incident shock Mach number, as a function of the reflected shock pressure. The driver pressure rises rapidly with increasing M_{s_i} (or T_5). The maximum allowable driver pressure is 1500 psia, so that for p_5 = 34 atm, M_{s_i} and T_5 are limited to 5.56 and 3150 K.

Using the information provided in Figs. 2.20 - 2.23, the initial driver and driven pressures are specified in the following manner:

1) The desired reflected shock temperature and pressure are chosen.
2) The magnitude of the incident shock Mach number, M_{s_i}, is read from Fig. 2.20.
3) The initial driven section pressure, p_1, is read from Fig. 2.21.
4) The initial driver pressure, p_4, is read directly from Fig. 2.23.

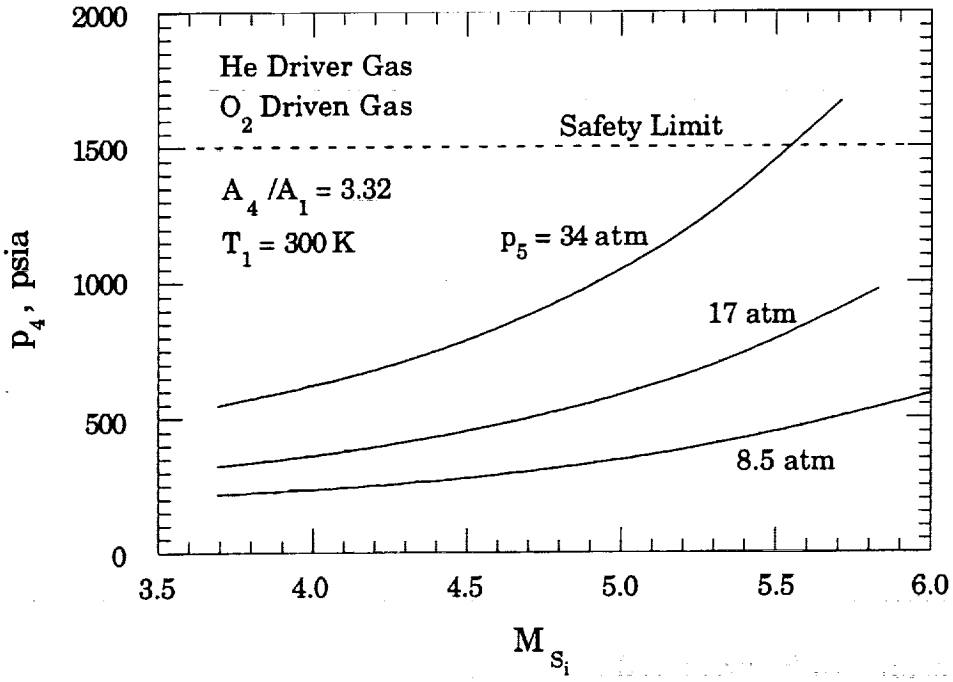

Fig. 2.23: Required driver pressure as a function of M_{S_i} and p_5. The curves are calculated from the real gas calculations of Fig. 2.21 and the experimental measurements of Fig. 2.22.

The maximum allowable mean diameter of the metal powder is limited by the duration of the quasi-steady reflected shock conditions. As was discussed in Section 2.1, the reflected shock test time is limited by the arrival of disturbances, created by the interaction of the reflected shock and the contact surface, at the endwall. For the conditions of this experiment, the reflected disturbances are always weak shocks /compression waves (see Appendix B).

Figure 2.24 presents representative endwall pressure histories as a function of test pressure and incident shock Mach number. The signal voltages have been normalized, and then offset, in order to clearly display the individual signals. The approximate test time of each signal is also marked. It is clear that the end of the quasi-steady gas conditions is not well defined. Therefore, the test conditions are taken to end when the endwall pressure begins its final

monotonic rise and reaches a voltage that is approximately 10 percent greater than the voltage of the reflected plateau region.

Figure 2.24a shows the effect of the reflected shock pressure on the endwall pressure history for $M_{s_i} = 4.33$ ($T_5 = 2225$ K). As p_5 is increased, the voltage of the plateau region levels out and the test time is found to increase slightly. The effect of M_{s_i} on the endwall pressure history is shown in Fig. 2.24b for $p_5 \cong 17$ atm. It is found that the severity of the disturbances caused by non-ideal shock reflection (see Appendix B) and those reflected from the contact surface increase with increasing M_{s_i}. In addition, the rate of increase of the endwall pressure after the quasi-steady gas conditions cease to exist increases substantially with M_{si}. The quasi-steady test time is inversely related to the magnitude of the incident shock Mach number or the reflected gas temperature.

Figure 2.25 shows a collection of measured test times plotted as a function of the incident shock Mach number. Figure 2.25a presents a large number of measurements taken at $p_5 \cong 17$ atm. The solid curve is a third order polynomial fit of the data. For the data shown, the reflected gas temperature varies from 1750 K to 3280 K. The test time decreases in a nearly linear fashion from 1300 μs at $M_{s_i} = 3.55$ to 300 μs at $M_{s_i} = 5.9$. The effect of p_5 on the measured test time is shown in Fig. 2.25b. The solid curve corresponds to the curve fit of Fig. 2.25a. The results indicate that the measured test time is inversely related to p_5. The variation of t_{test} with p_5 is less pronounced at higher incident shock Mach numbers.

The endwall pressure histories are not used to directly measure the reflected shock pressure, since the calibration constant of the endwall pressure transducer was found to vary with use. However, the fast rise time (~0.2 μs) of the endwall transducer did not deteriorate with use, allowing accurate

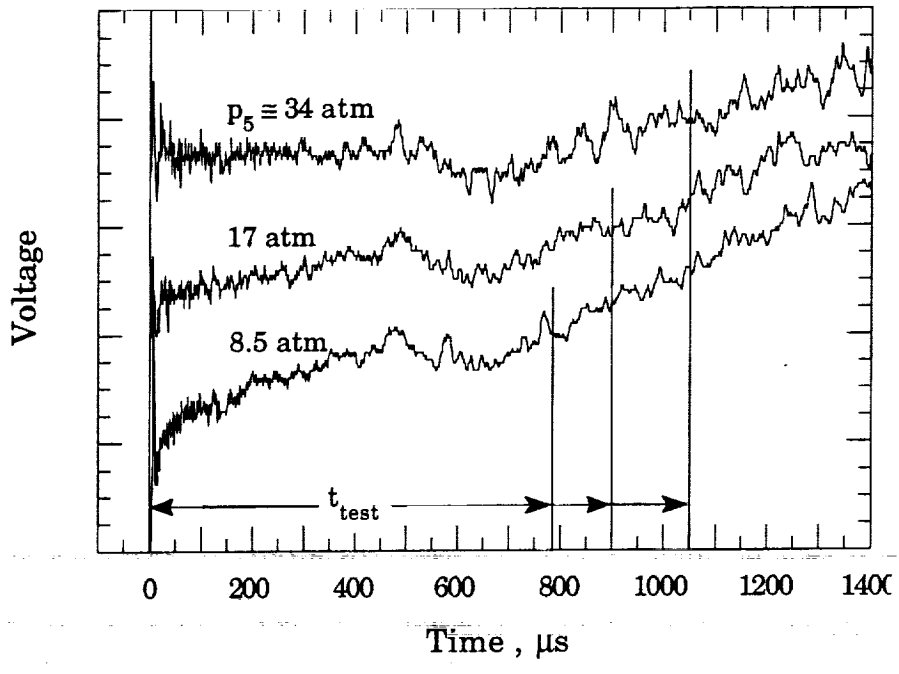

(a)

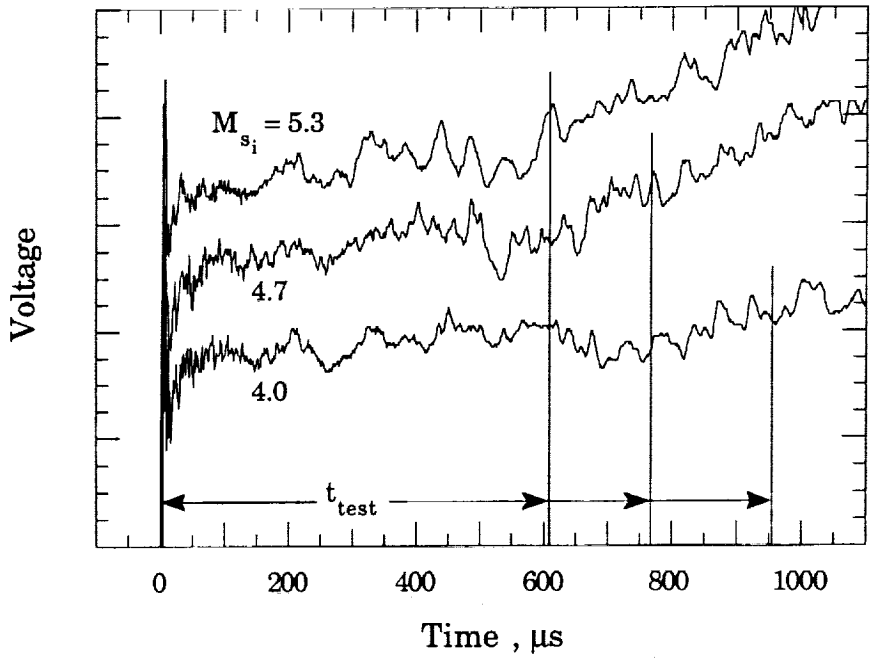

(b)

Fig. 2.24: Effect of reflected shock pressure and incident shock Mach number on the measured temporal history of the endwall pressure. a) Effect of p_5 when $M_{s_i} \cong 4.33$ ($T_5 \cong 2230$ K) b) Effect of M_{s_i} when $p_5 \cong 17$ atm.

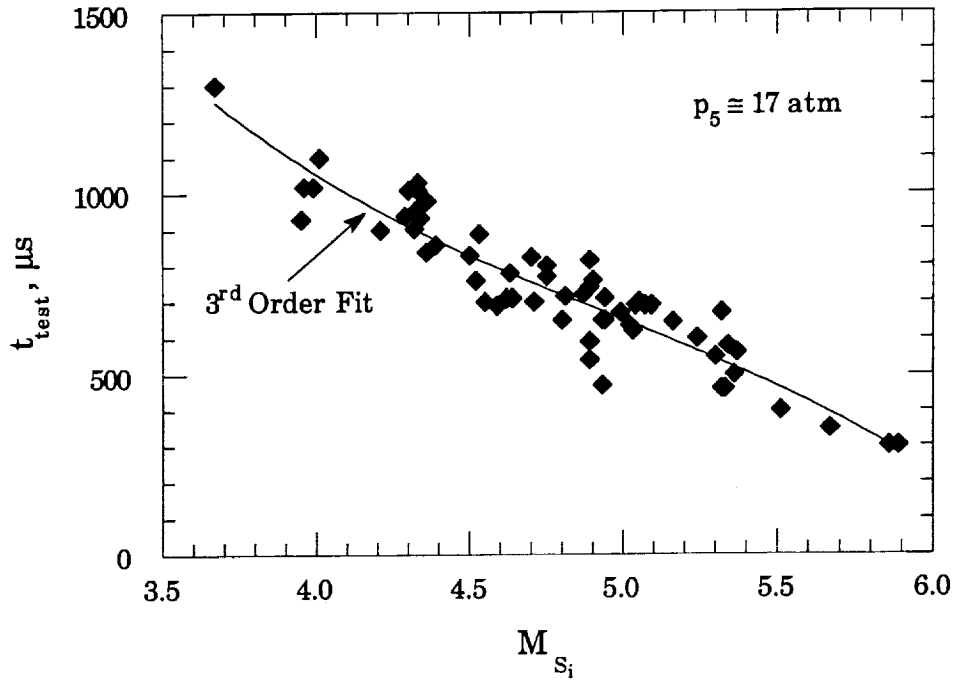

(a)

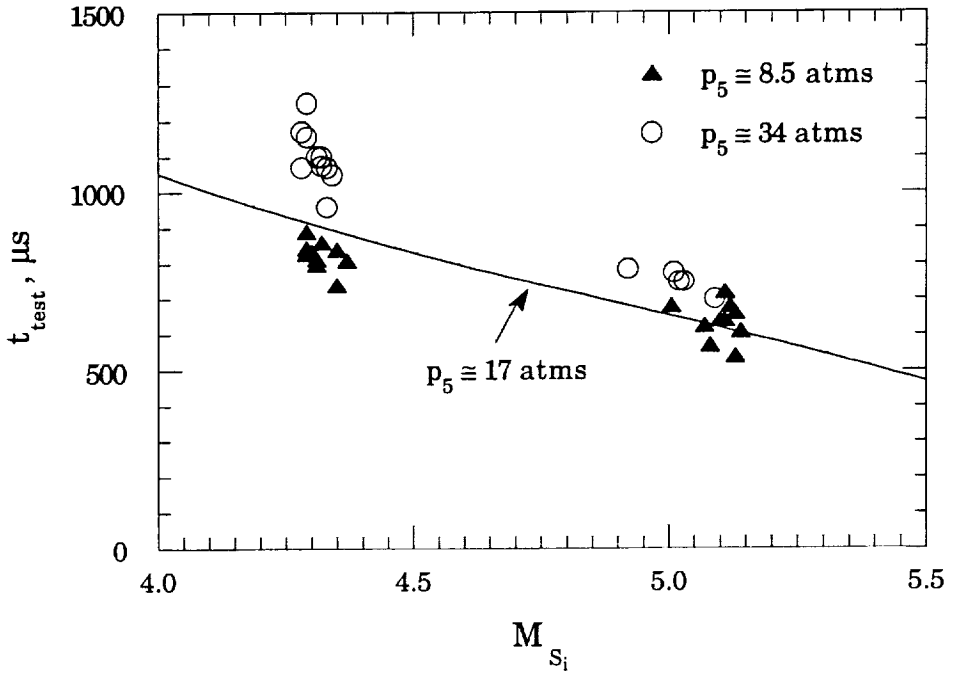

(b)

Fig. 2.25: Measured experimental test time versus incident shock Mach number as a function of reflected pressure. a) $p_5 \cong 17$ atm. b) $p_5 \cong 8.5$ and 34 atm, curve is the fit of Fig. 2.25a.

measurement of the incident shock velocity used to calculate precisely the reflected shock pressure using the NASA Gordon-McBride program [9], which calculates complex chemical equilibrium gas compositions.

2.3.3 Design of Endwall Observation Window and Knife Blade Particle Mount

Experimentation in the high temperature and pressure gases created by the reflected shock near the shock tube endwall is complicated by two factors. The first is the difficulty in constructing an endwall section that allows convenient optical access for instrumentation. The second is the presence of an endwall thermal layer resulting from the unsteady transfer of heat from the hot oxygen to the cool endwall material. Care must be taken to insure that the combustion process being studied does not occur within the cooler gas of this thermal layer.

Shock tube driven sections of rectangular cross section[35,38] are often constructed solely to facilitate the mounting of observation windows flush with the sidewalls. The shock tube used in this research was partially constructed from existing shock tube sections of circular cross section. Therefore, it was necessary to develop an endwall mounted observation window.

An assembly drawing of the endwall observation window is shown in Fig. 2.26 and a sectional drawing is shown in Fig. 2.27. The removable stainless steel endwall port contains the observation window, the endwall pressure transducer, and the knife blade particle mount. The entire window/transducer/knife blade assembly is designed to be easily removed as a unit from the shock tube's endwall flange to facilitate particle mounting and endwall cleaning. The window assembly is attached to the endwall flange with eight 3/8-16 hex socket head cap screws and is sealed with an o-ring.

The observation window consists of a 1.5 inch diameter x 0.25 inch thick optical grade quartz disk (supplied by Behm Quartz Industries, Inc.), a 2.0 inch diameter x 1.0 inch thick optical grade polycarbonate disk, an o-ring, and a stainless steel restraining ring. The window is assembled by inserting the o-ring and polycarbonate disk into the endwall port and then securing it with the restraining ring using six 5/16-18 hex socket head shoulder screws. Each shoulder screw has a 3/4 inch Belleville spring and a precisely machined washer which apply a force of between 2200 lb and 3000 lb. The lower load limit of 2200 lb insures that the impact of the shock wave will not move the window. The upper load limit of 3000 lb insures that the window is not deformed (crushed) by the restraining ring, which would cause the quartz disk to protrude into the shock tube.

After securing the polycarbonate disk in the endwall port, the edges of the quartz disk are coated with a high temperature, low volatility RTV sealant (Bowman RTV red, No. 21441), and slipped into place. The RTV sealant holds the quartz disk in place and acts as a cushion between the steel port and the brittle quartz. This window design takes advantage of the excellent impact characteristics of the polycarbonate by using it to carry the entire load. The quartz protects the polycarbonate from the hot oxygen and its hardness allows the window to be cleaned without scratching. This design has been extremely successful, as the first window assembly constructed lasted for more than 100 shock tube firings and the replacement is still being used after more than 250 firings.

The endwall pressure transducer (described in section 2.4.2) is inserted through the restraining ring and screwed into the endwall port using 1/2-20 threads. The transducer is sealed by wrapping the entire threaded length with Teflon tape.

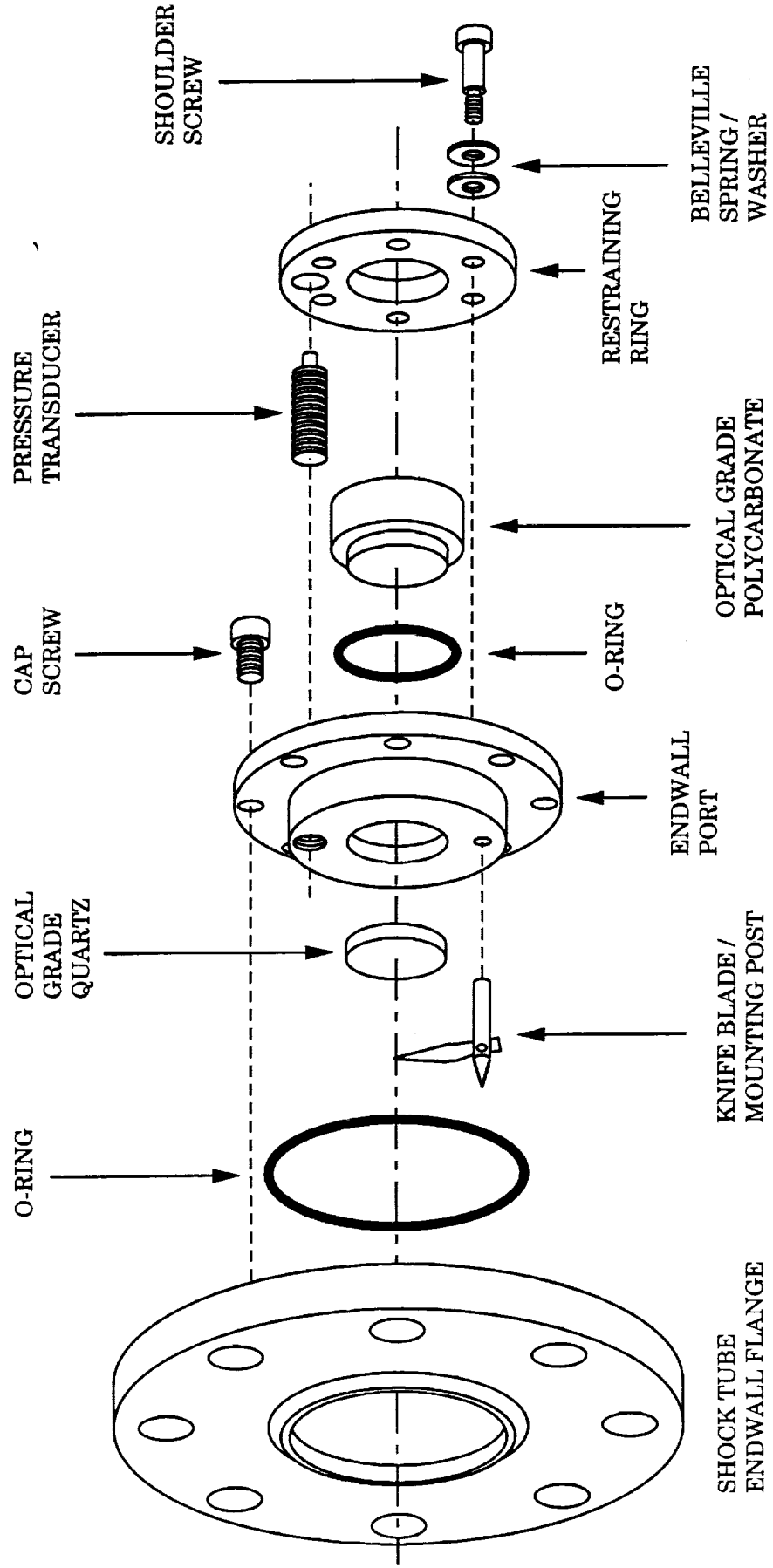

Fig. 2.26: Endwall observation window, knife blade mount, and pressure transducer assembly.

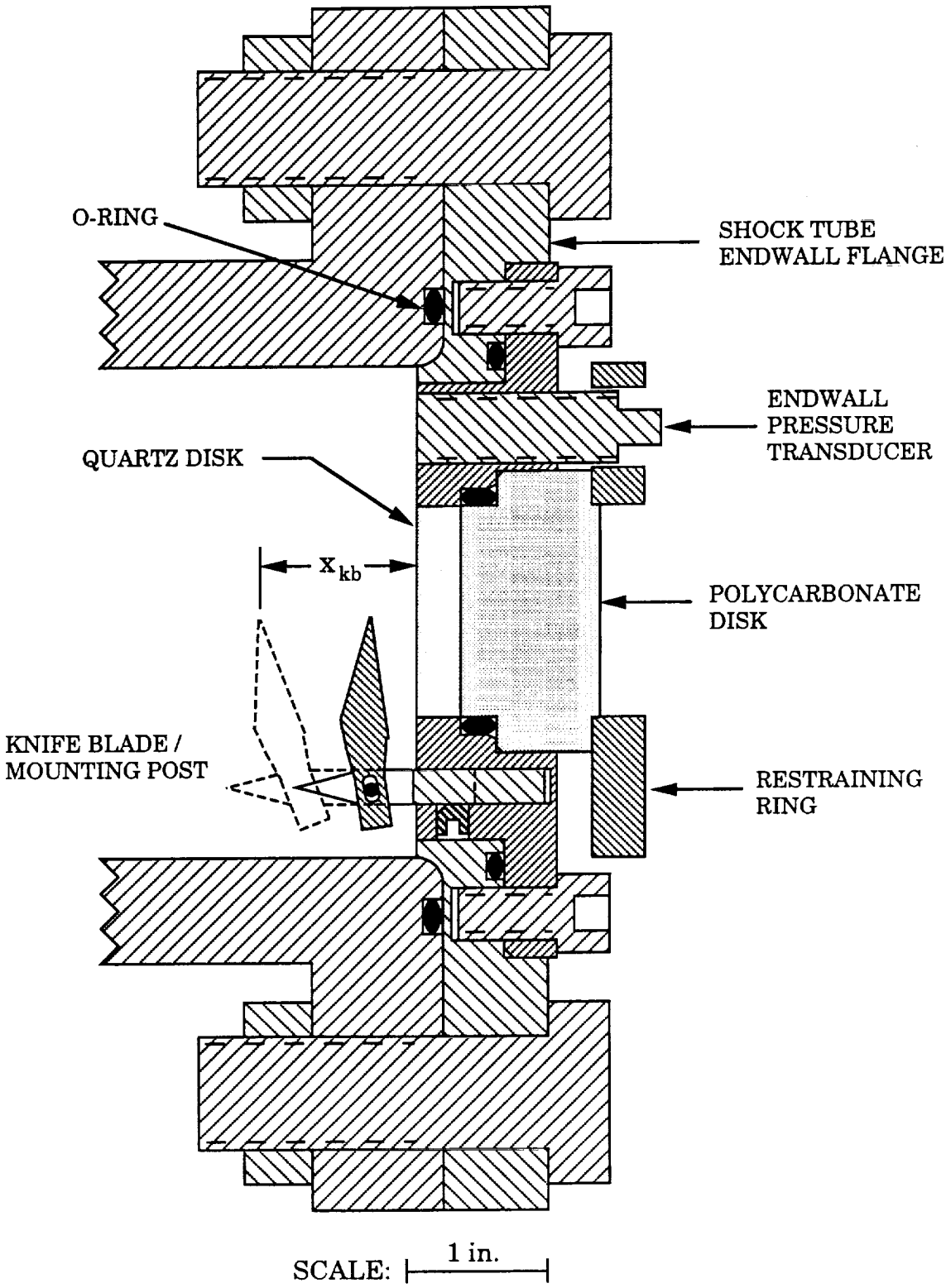

Fig. 2.27: Sectional drawing of the endwall observation window assembly.

The particle mounting technique developed here uses a hobby knife blade (X-Acto #11) mounted on a conically-tipped 0.25 inch diameter stainless steel post which projects from the face of the endwall port, as shown in Fig. 2.27. The knife blade is placed in a slit in the post and clamped with a small screw. The post is placed in a hole tapped into the face of the port, and is pinned with a set screw.

The knife blade mounting distance, x_{kb}, is equal to the distance from the endwall to the nearest edge of the knife blade tip. The maximum mounting distance is approximately 1.2 inch (30 mm) and is represented in Fig. 2.27 by the dashed outline of the knife blade and mounting post. Normally, x_{kb} is varied between 0.12 inch (3 mm) , 0.16 inch (4 mm), and 0.32 inch (8 mm), all of which are near the mounting distance shown in Fig. 2.27. The optimum knife blade mounting distance is a function of the magnitude of the particle acceleration, which increases with reflected shock pressure, and the melting time of the particles. If the mounting distance is too large, the particles will melt before reaching the endwall, will shatter upon impact, and the resulting fragments will ignite and burn (see section 4.1).

As described in section 2.1, a small amount of metal powder is placed on the knife blade tip. Particle adhesion is provided by touching the blade to a fingertip before dipping the blade in the sieved particles. Fig. 2.28 shows a photomicrograph of pure Mg particles mounted on the tip of the knife blade taken at a magnification of 35X. The measured mean diameter of the particles is 21.5 μm. The tip of the blade has been ground down to remove the point, which is found to melt and retract into a spherical droplet for the gas conditions of interest. The particles cover the blade tip in a nearly uniform single layer. Using this photomicrograph, it is estimated that between 5,000 and 10,000 particles are mounted for each experiment.

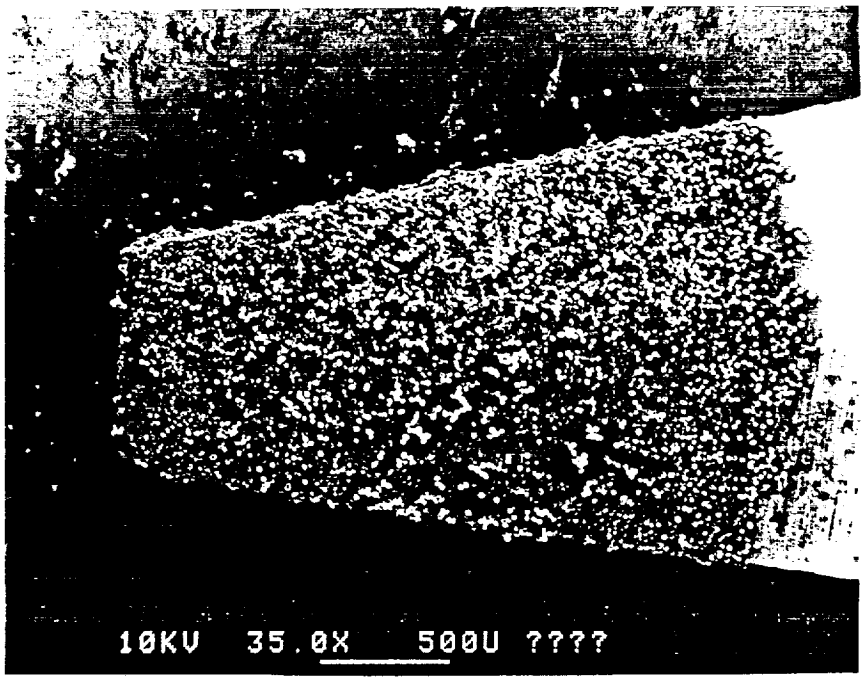

Fig. 2.28: Photomicrograph of pure Mg particles mounted on the knife blade tip. Mean particle diameter is 21.5 mm. Magnification is 35 X.

A photograph of the assembled endwall observation window and knife blade particle mount is shown in Fig. 2.29 prior to insertion in the shock tube endwall. The endwall pressure transducer is mounted and covered with a protective layer of thin brass (see section 2.4.3). A nominal quantity of mounted particles are visible on the tip of the knife blade.

The effect of the knife blade and mounting post on the reflection of the shock wave is assessed by recording the endwall pressure with and without the knife blade assembly mounted. When the post is removed from the endwall port, the mounting hole is filled with a flush mounted plug. Argon is chosen as the driven gas for these tests, since the interaction of the reflected shock and the shock tube boundary layer is less severe for monatomic gases than it is for diatomic gases [48,49]. The reduction in random disturbances in the endwall

pressure record will make it possible to discern any disturbances that are a direct result of the knife blade's presence.

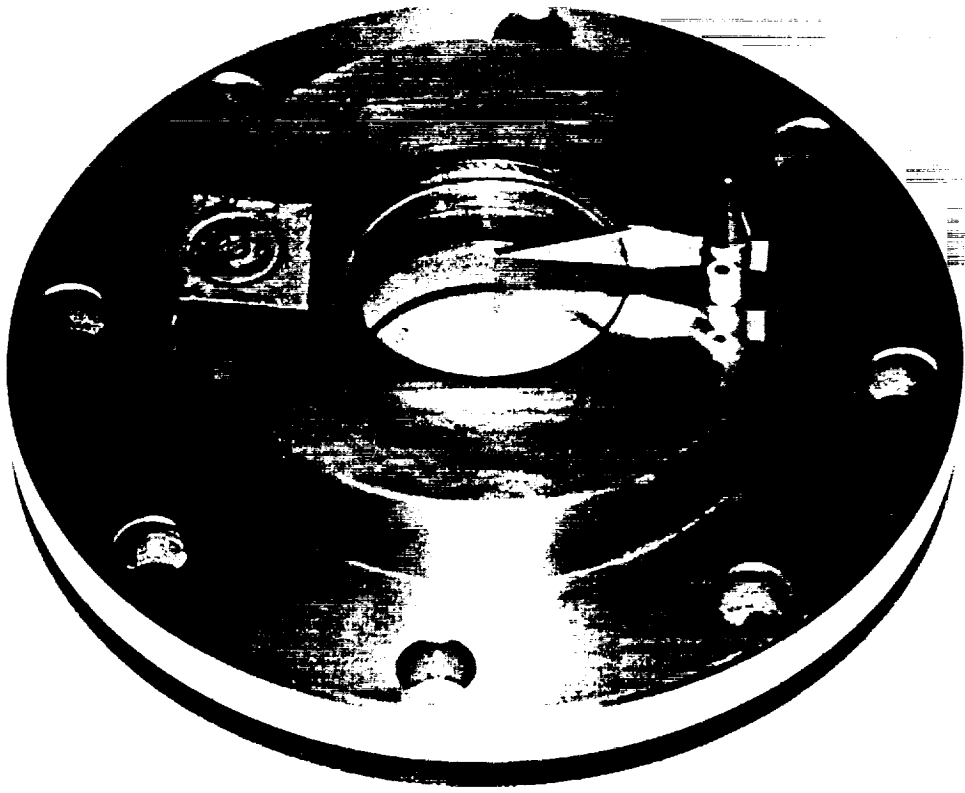

Fig. 2.29: Photograph of the endwall observation window prior to insertion in the shock tube endwall. Protective brass transducer covering is opposite the knife blade. Mg particles are mounted on the knife blade tip.

Figure 2.31 shows the recorded endwall pressure with and without the knife blade assembly mounted. The experiment conditions for the case in which the knife blade assembly is not mounted are: $M_{s_i} = 2.88$, $T_5 = 2005$ K, and $p_5 = 17.1$ atm. The experiment conditions for the case in which the knife blade is

mounted are: $M_{s_i} = 2.86$, $T_5 = 1980$ K, $p_5 = 16.8$ atm, and $x_{kb} = 6$ mm. To clearly show both pressure records, the one recorded without the knife blade mounted has been shifted by -25 percent of its mean reflected plateau voltage. The character of the records are found to be nearly indistinguishable from each other.

Figure 2.31 also shows the absolute value of the difference between the two pressure records. The magnitudes of the two signals are essentially identical for a time of 450 μs. The discrepancy between the two records for times greater than 450 μs cannot be attributed to the presence of the knife blade, since disturbances from the knife blade would reach the pressure transducer within 200 μs of shock reflection. These variations are most likely due to the inherent differences which are found to occur between experiments, with or without the knife blade mounted.

For comparison, Fig. 2.31 compares two endwall pressure records for identical experiment conditions with the knife blade assembly mounted in each case. The full scale signal is the same as that plotted in Fig. 2.30. The experiment conditions are $M_{s_i} = 2.86$, $T_5 = 1980$ K, $p_5 = 16.8$ atm, and $x_{kb} = 6$ mm for both records. Again, the signals are nearly identical and the absolute value of the voltage difference is quite small.

These measurements indicate that the magnitude of any disturbances created by the knife blade and mounting post are indistinguishable from the normally occurring pressure disturbances associated with the non-ideal reflection of the shock wave (see section 2.4.2 and Appendix B).

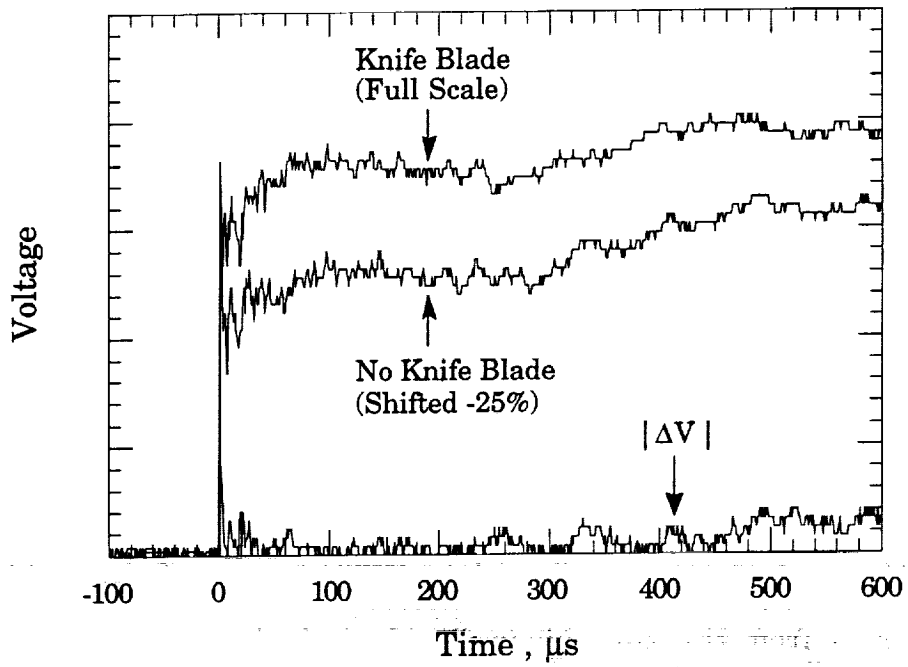

Fig. 2.30: Comparison of endwall pressure signals recorded with and without the knife blade and mounting post.

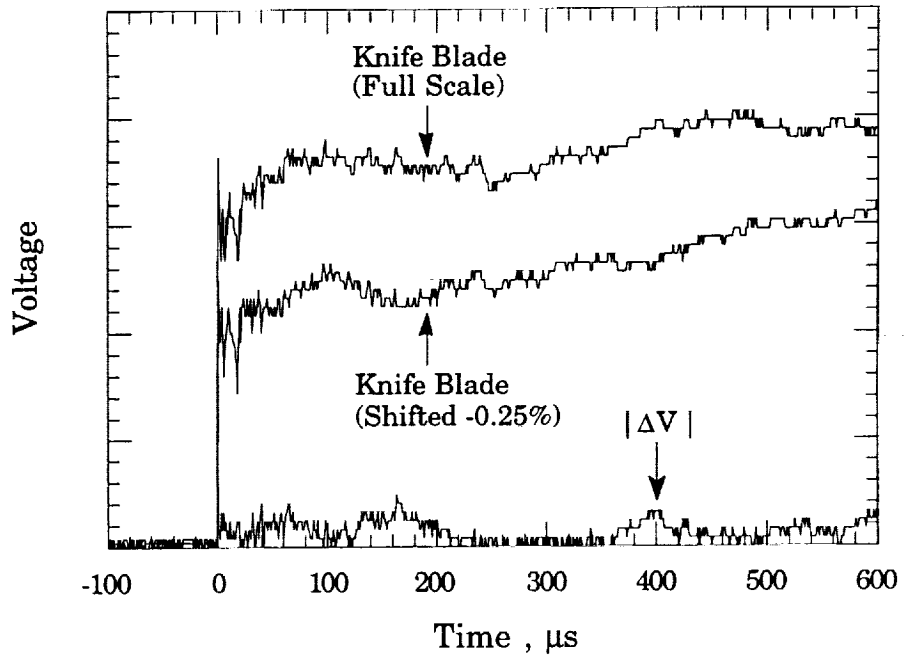

Fig. 2.31: Comparison of two endwall pressure signals recorded for identical experimental conditions. $M_{s_i} = 2.86$, $T_5 = 1980$ K, $p_5 = 16.8$ atm, and $x_{kb} = 6$ mm for both records.

2.3.4 Double Diaphragm Technique and Diaphragm Construction

In order to produce accurately an incident shock wave of specified Mach number, it is necessary to adjust precisely the conditions of the driver and driven section gases prior to diaphragm rupture. Several techniques have been developed [48] in which a single diaphragm, separating the high and low pressure gases, is mechanically or electrically ruptured at the desired moment. The double diaphragm technique employed here, as shown in Fig. 2.19b, avoids the use of mechanical or electrical devices to fire the shock tube.

The double diaphragm technique involves choosing diaphragms which have burst pressures that are equal to approximately 70 percent of the desired driver pressure. The pressure in the diaphragm section, located between the two diaphragms, is then set equal to 50 percent of the driver pressure. The resulting pressure difference across each diaphragm remains below their burst pressure. After adjusting the driver and driven gas pressures, the shock tube is fired by relieving the pressure in the diaphragm section. This allows the pressure difference across the driver side diaphragm to rise above the burst pressure, resulting in diaphragm rupture. The high pressure He then ruptures the driven side diaphragm, expands into the low pressure oxygen, and produces the incident shock wave.

The diaphragms are constructed from multiple layers of 0.005" and 0.01" thick Mylar. The diaphragms are cut with scissors in the shape of 6" wide octagons from readily available 24" x 40" sheets of Mylar. The measured burst pressure of these diaphragms is plotted in Fig. 2.32 as a function of the number of Mylar layers used, N_d. The burst pressure of the diaphragms constructed using 0.010" thick Mylar are directly proportional to N_d, and are accurately described by:

$$p_{burst} = 146\, N_d\ ,\ \text{psia} \tag{2.3}$$

The measured burst strength of a single layer of 0.005" thick Mylar is approximately 90 psia. Thus, by combining the 0.005" and 0.001" thick Mylar sheets, it is possible to construct diaphragms which burst at pressures ranging from 90 psia to 750 psia. At pressure differences above 750 psia, the diaphragms are found to slip between the flanges and become wrinkled, resulting in gas leakage.

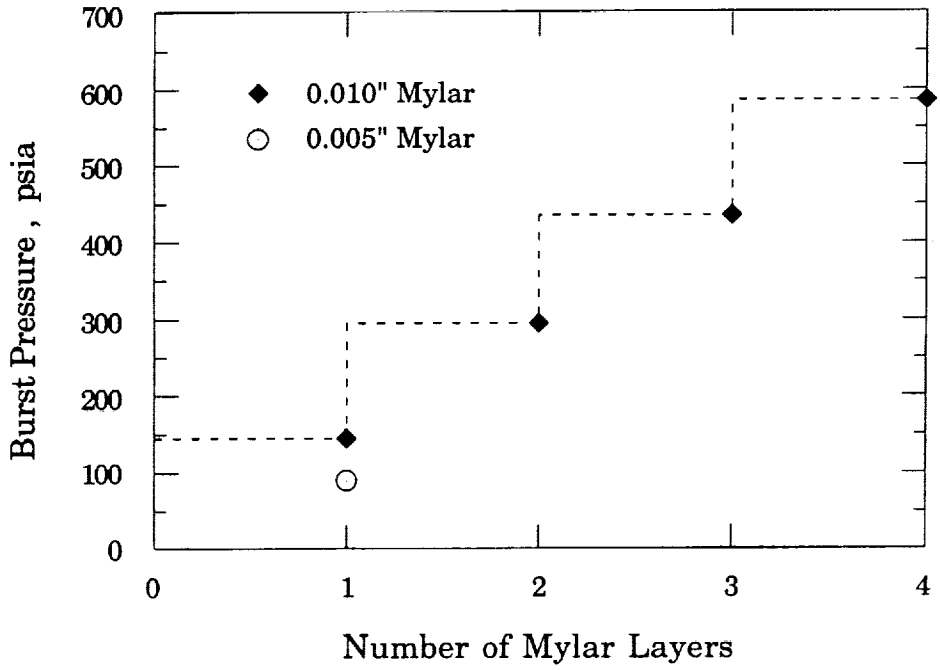

Fig. 2.32: Measured Mylar diaphragm burst pressure as a function of the number of layers used to construct it.

Figure 2.33 shows a photograph of the contraction and diaphragm sections of the shock tube. The driver-side diaphragm flange is unbolted and opened. A burst diaphragm is visible, wedged in the flange of the driven section.

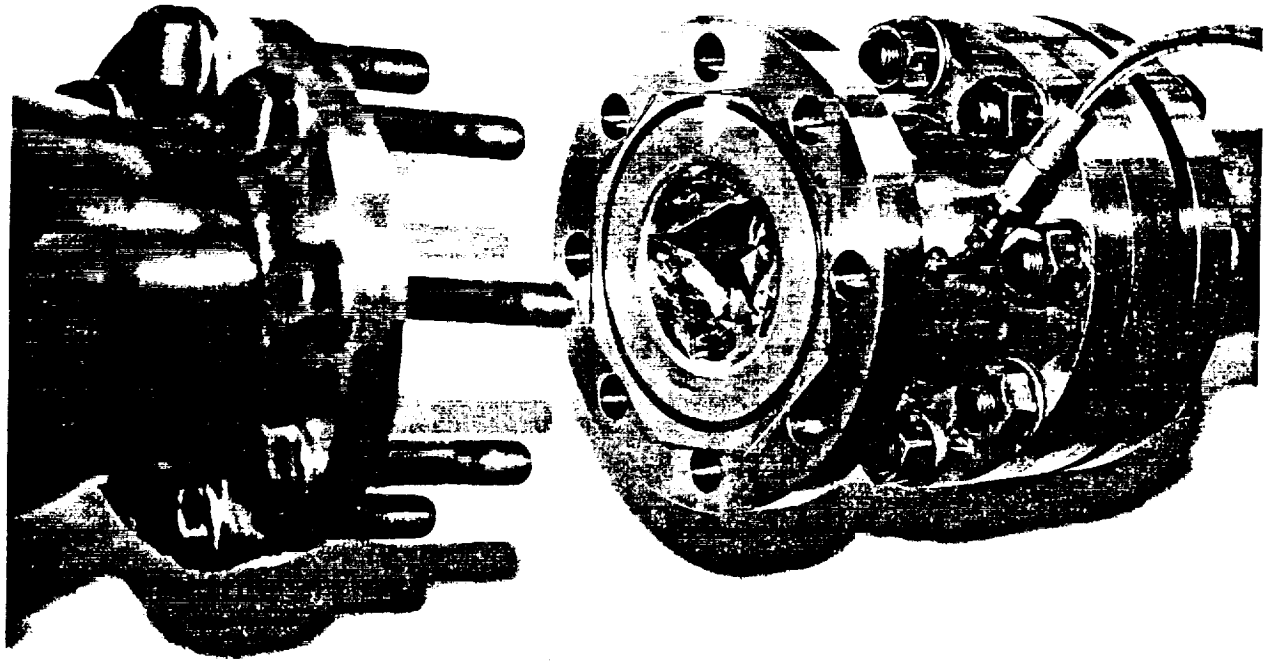

Fig. 2.33: Photograph of shock tube diaphragm section. A burst diaphragm is visible in the open driver-side diaphragm flange.

The ruptured Mylar diaphragms produce a large number of small fragments which are entrained by the expanding He and carried down the driven section toward the test section. These fragments range in size from several centimeters to micrometers. Particles which reach the high temperature oxygen near the shock tube endwall are melted or burned. Figure 2.34 shows a photograph of the endwall observation window taken after an experiment. The surface of the window and endwall are covered with charred and melted diaphragm material.

This type of burned diaphragm remnants are found on the inside of the shock tube up to a distance of approximately 8 inches from the endwall. Beyond

this distance, the fragments remain in the cool helium which exists on the other side of the contact surface, and can simply be wiped away with a damp sponge. The burned material must be carefully removed using a single-edged razor blade and abrasive pads.

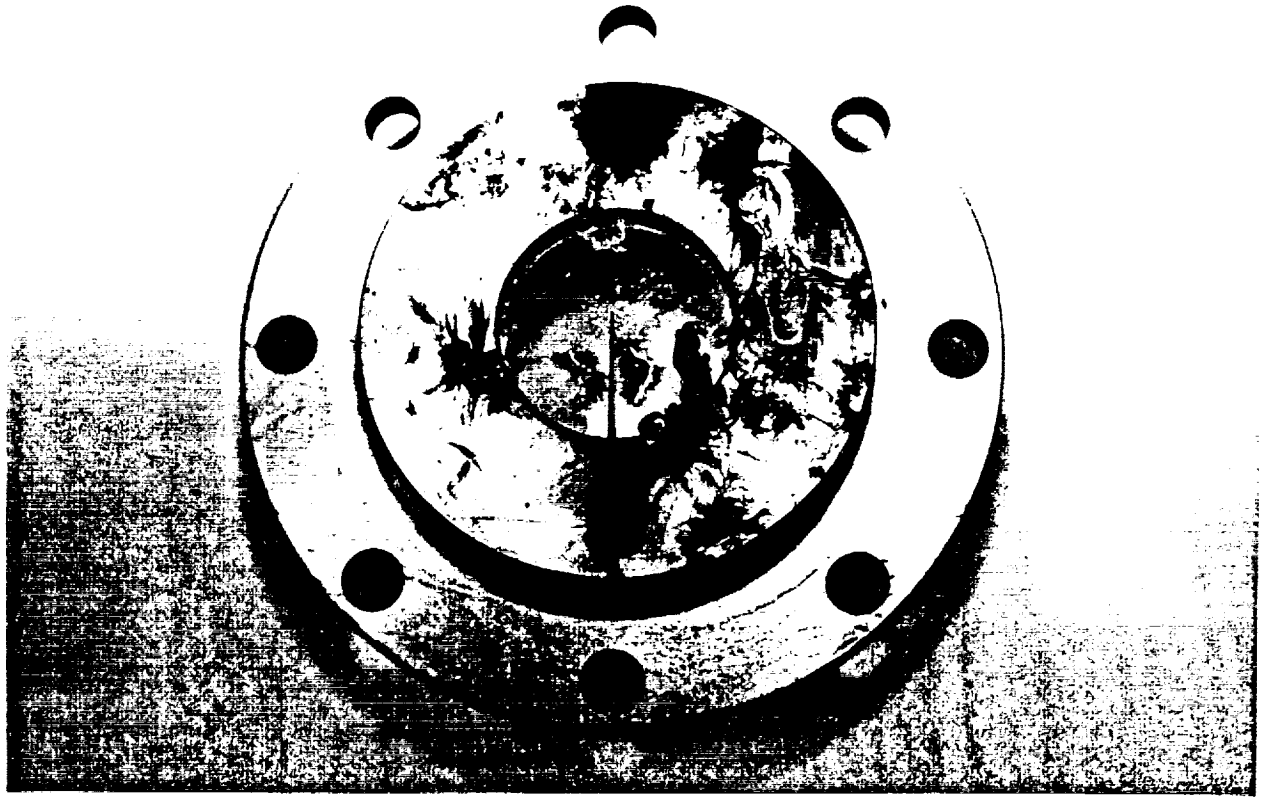

Fig. 2.34: Photograph of shock tube observation window after an experiment. Diaphragm fragments are melted and charred.

After each experiment, the entire shock tube must be carefully cleaned to insure that the diaphragm fragments do not ignite and interfere with the metal particle combustion measurements. The shock tube is cleaned by pulling an

abrasive synthetic cleaning pad, formed into a cylinder which fits tightly inside the driven section, from the endwall to the diaphragm section. This is done several times to loosen small fragments and remove the larger ones. Then a similarly shaped damp sponge is pulled through the driven section several times to remove the finer Mylar fragments. The scrubbers are pulled through the shock tube using 40 lb. monofilament fishing line, one end of which is initially pulled through the shock tube using a small, battery powered, four-wheel-drive, Stomper® toy truck. After cleaning, air is drawn through the driven section until thoroughly dried.

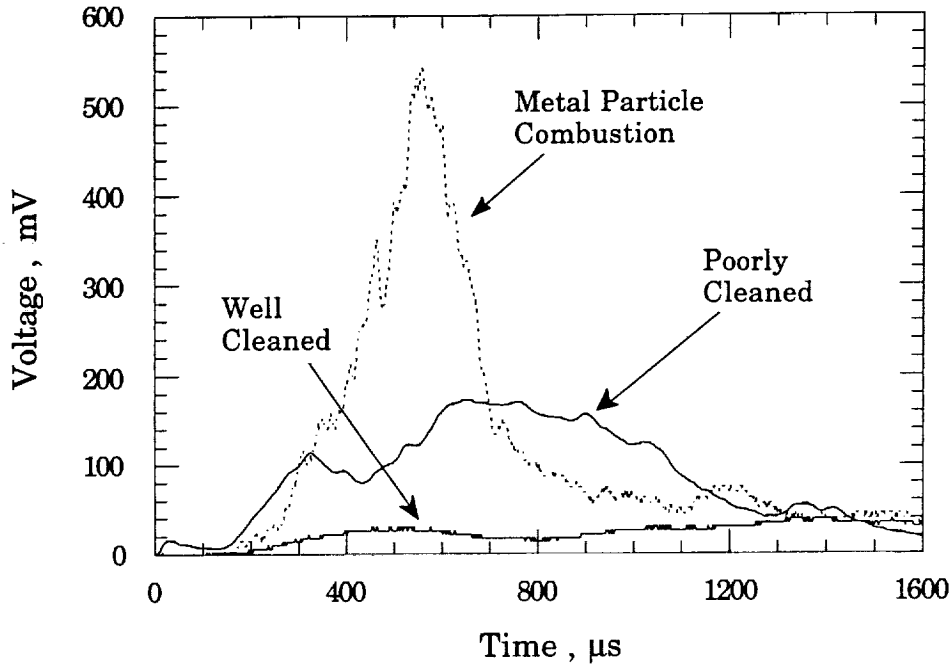

Fig. 2.35: Comparison of background radiation emitted from a "well" cleaned and a "poorly" cleaned shock tube. $T_5 \cong 2750$ K.

Careful cleaning of the shock tube is critical, as is illustrated in Fig. 2.35. The two solid curves correspond to photodiode records used to assess the background radiation caused by the combustion of extraneous particles. Both

signals were recorded for oxygen temperatures of ~2750 K. The signals labeled as "poorly cleaned" and "well cleaned" were measured at oxygen pressures of ~8.5 atm and ~17 atm, respectively. For comparison, the dashed curve shows a representative photodiode measurement of metal particles burning in ~2750 K, 17 atm oxygen. If the tube is not well cleaned, the magnitude of the background radiation can approach that of the burning particles. However, careful cleaning of the shock tube can reduce the background radiation by an order of magnitude.

2.3.5 Shock Tube Operation

After thoroughly cleaning the shock tube, replacing the diaphragms, and mounting the particles on the knife blade tip, the observation window assembly is mounted in the endwall flange. At this point, the driven and driver section gases are set to the desired initial conditions. The gas handling system used to evacuate and then pressurize the shock tube is shown schematically in Fig. 2.36. All of the shock tube pressure lines, electrical wires, and coaxial data acquisition cables are carried in a cable tray which hangs above the shock tube and dropped to the tube at the desired location.

The helium supply lines are 0.25 inch stainless steel tubing and the oxygen supply line is 0.25 inch copper tubing. The driver section vent line is constructed of 0.375 inch stainless steel tubing to reduce the time required to drain the shock tube in an emergency. The supply lines are coupled to the shock tube through flexible 0.25 inch braided stainless steel hose to allow free movement of the entire shock tube, which is mounted on rollers.

The driver and diaphragm section pressurization and shock tube firing are carried out from the safety of a control room. The shock tube's control panel wiring diagram is shown in Fig. 2.38 and a photograph of the panel is displayed

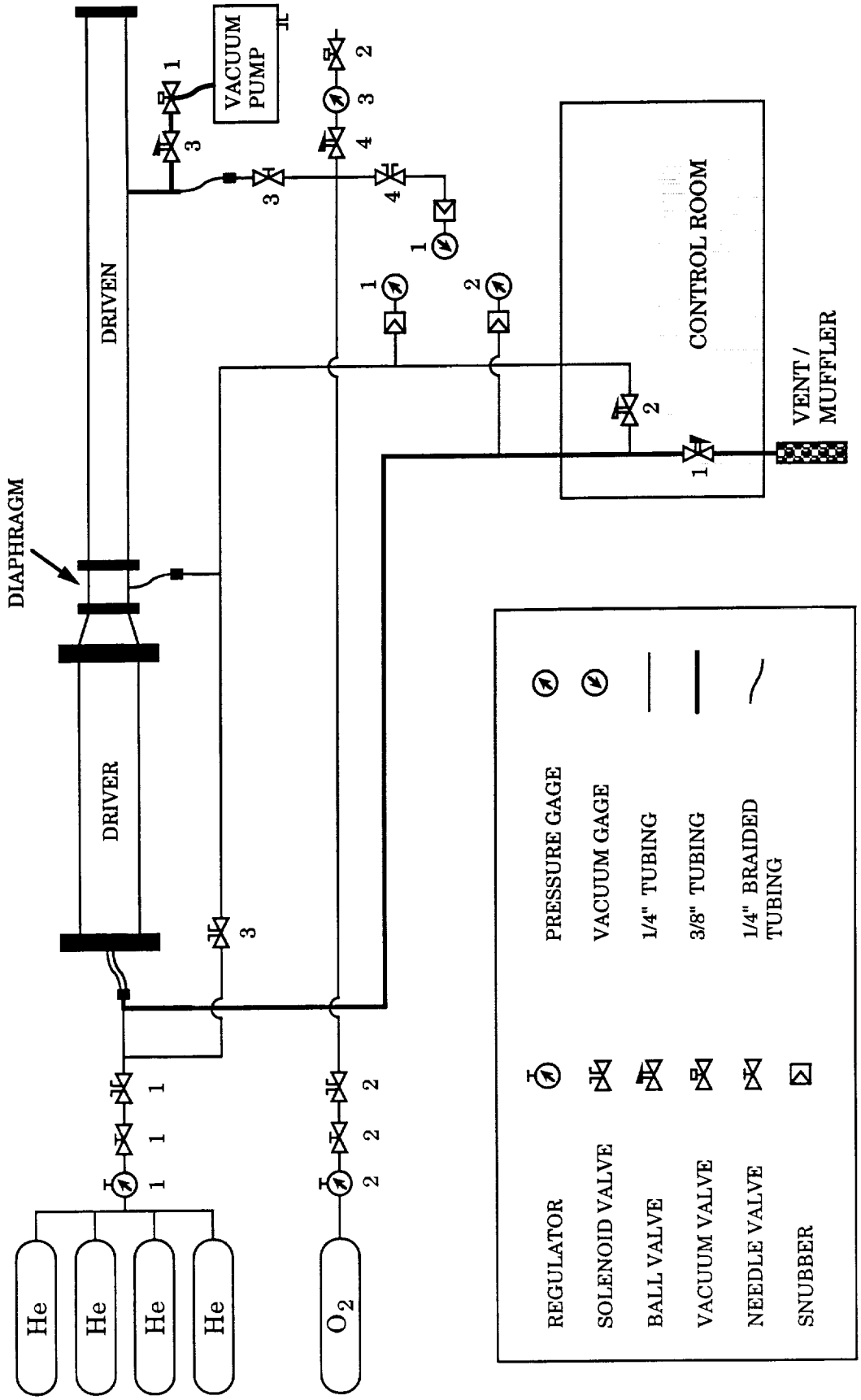

Fig. 2.36: Schematic of shock tube gas handling system.

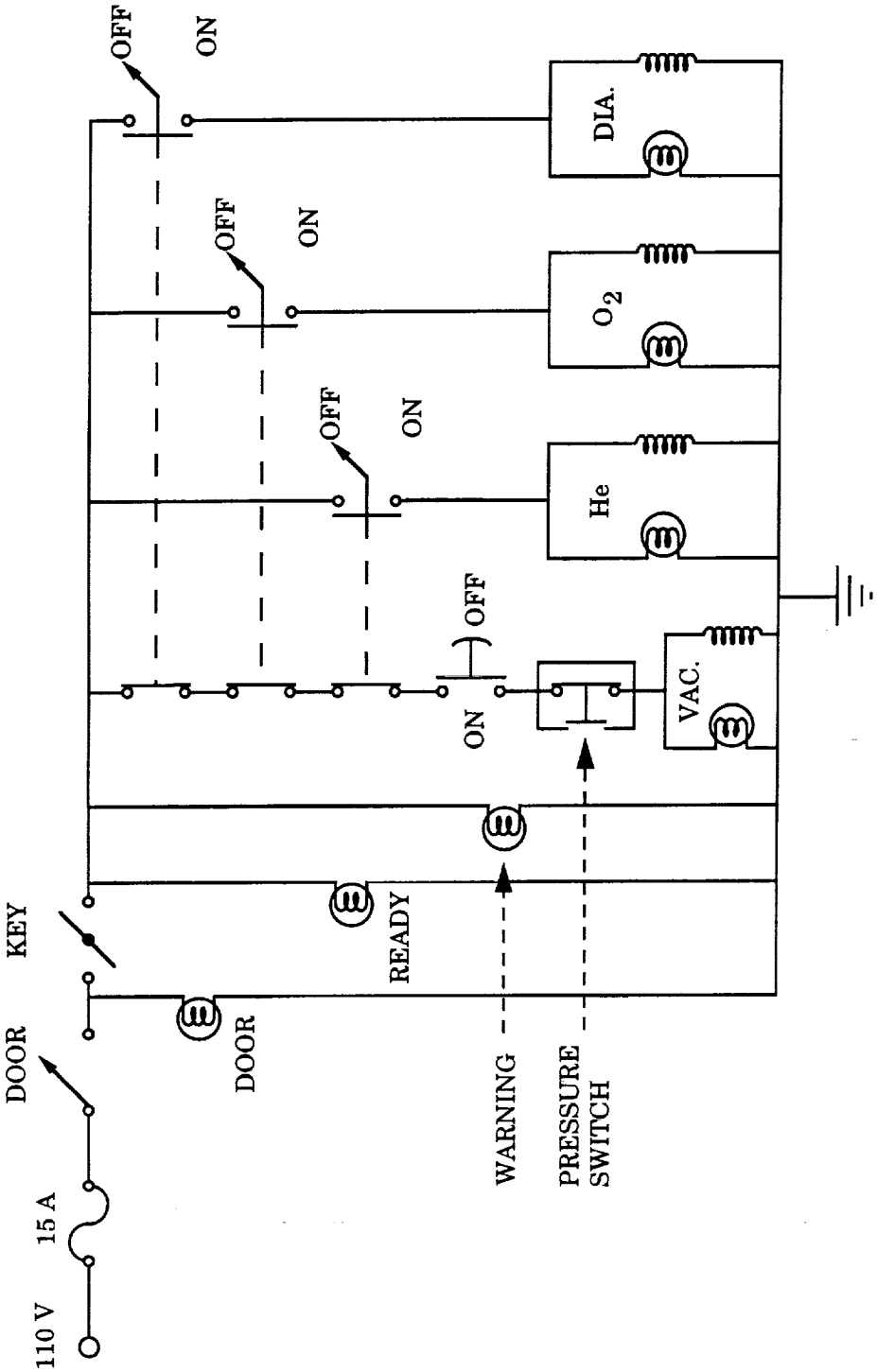

Fig. 2.37: Shock tube control panel wiring diagram.

C-2

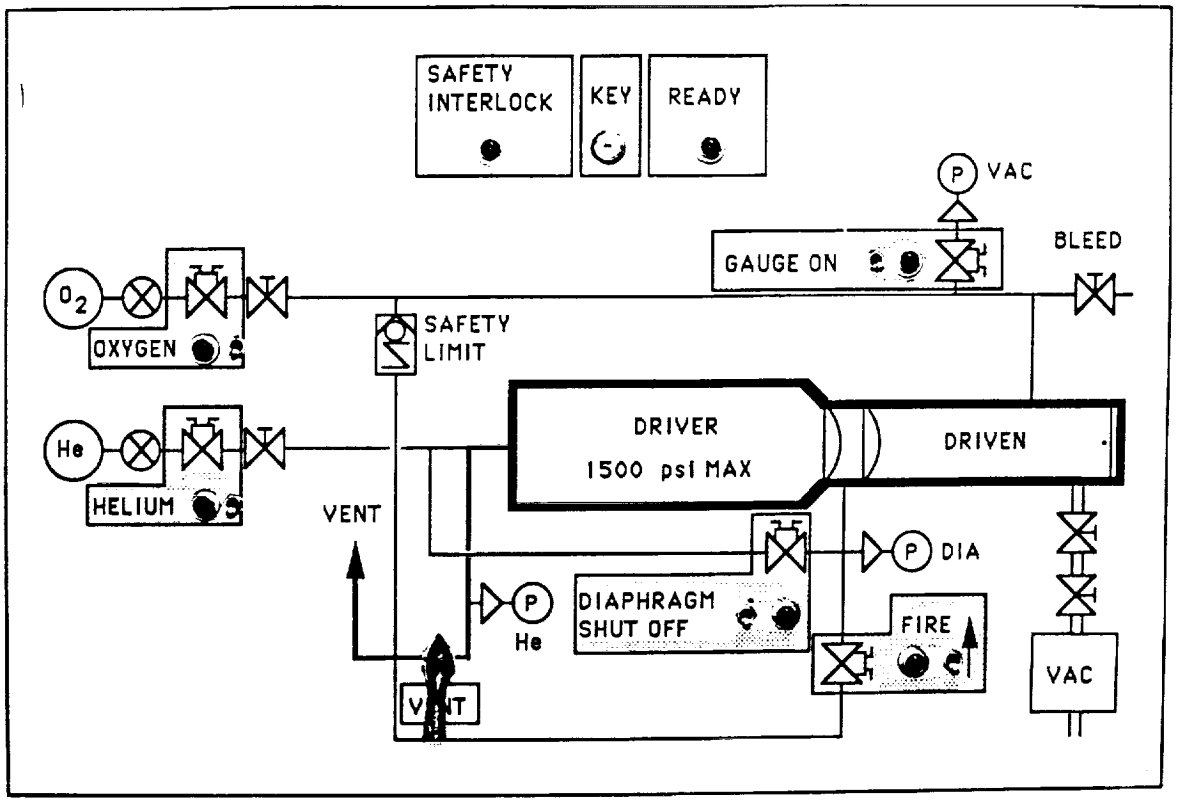

Fig. 2.38: Photograph of the shock tube control panel. The toggle switch labeled "FIRE", and the corresponding solenoid valve, were replaced with a manual ball valve after this photograph was taken.

in Fig. 2.38. After the photograph was taken, the toggle switch labeled "FIRE", and the associated solenoid valve, were replaced by a manual ball valve. This change was made after the orifice of the solenoid valve was repeatedly fouled with diaphragm fragments. The ball valve completely solved this problem.

The pressure in the driver, diaphragm, and driven sections are monitored from the control room, using the analog gages shown in the photograph presented in Fig. 2.39. The gages are mounted in a control room window adjacent to the control panel. The pressure gages read 0 to 3000 psig,

the vacuum gage reads 0 to 100 kpa vacuum, and all the gages have an accuracy of 0.25 percent. Extreme care is taken to protect the vacuum gage from accidental exposure to high pressure gas. As shown in Fig. 2.37, the vacuum gage is electrically isolated using a solenoid valve whenever any other solenoid valve is operated, or when a pressure sensitive safety switch detects a driven section pressure in excess of 1 psig. In addition, a momentary switch is used to operate the vacuum gage solenoid so that it cannot remain energized inadvertently.

Helium is supplied to the shock tube from a manifold of four standard T-bottles (300 SCF), each having an initial pressure of 2500 psia, permitting as many as twelve firings from the set of four bottles. The quoted purity of the helium is 99.995 percent. A single T-bottle of oxygen (328 SCF) is used to pressurize the driven section. The oxygen has a quoted minimum purity of 99.5 percent, with nitrogen being the major impurity, and a maximum moisture content of 50 ppm.

After mounting the endwall observation window in the shock tube, the driven section is pumped down to 0.73 psia using a small vacuum pump. The driven section is then pressurized with oxygen to 65 psia. For driven section pressures above 1 atm, the pressure is measured by opening ball valve #4 (refer to Fig. 2.36) and reading pressure gage #3. The oxygen is then vented from the driven section through vacuum valve #2. The driven oxygen pressure is then pumped down to the desired value.

Following this pressurization sequence, the composition of the driven section gas can be determined by calculating the mole fractions of the constituent gases using Dalton's law of partial pressures [25]:

$$X_i = \frac{p_i}{p} \tag{2.4}$$

where X is the mole fraction, p the gas pressure, and i refers to the i^{th} gas species. The residual air remaining after the initial pump down is composed of 0.57 psia nitrogen and 0.15 psia oxygen. After pressurizing with the bottled oxygen to 65 psia, the nitrogen partial pressure is raised to $p_{N_2} = 0.57 + 65 \times 0.005 = 0.89$ psia and the oxygen partial pressure is raised to $p_{O_2} = 0.15 + 65 \times 0.995 = 64.83$ psia. The resulting driven gas used in each experiment is composed of 98.6 percent oxygen and 1.4 percent nitrogen.

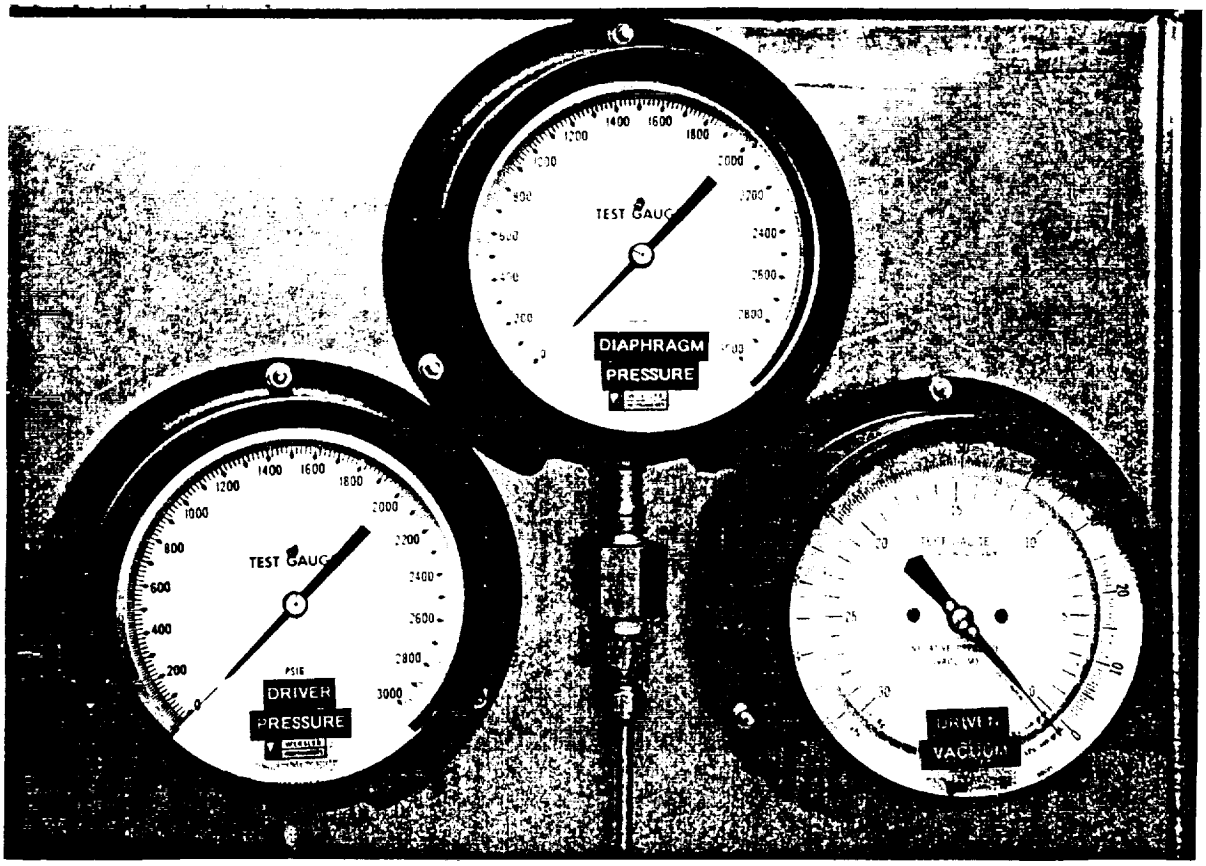

Fig. 2.39: Photograph of the gages used to measure the driver, diaphragm, and driven section pressure. Each gage has an accuracy of 0.25 percent.

The small fraction of nitrogen remaining in the driven section will be neglected when calculating the reflected shock gas properties used to tabulate and model the experimental measurements. The effect of neglecting nitrogen on the calculated reflected shock temperature is shown in Fig. 2.40. The figure shows the difference between the T_5 calculated for the 98.6% O_2 / 1.4% N_2 mixture, $(T_5)_{O_2/N_2}$, and the T_5 calculated for pure O_2, $(T_5)_{O_2}$, plotted as a function of the measured incident shock Mach number, M_{s_i}. The relative error, $\{(T_5)_{O_2/N_2} - (T_5)_{O_2}\} / (T_5)_{O_2} \times 100\%$, is also plotted in Fig. 2.40. The assumed initial driven gas temperature is 300 K and the driven pressure is varied to produce a reflected shock pressure of 17 atm.

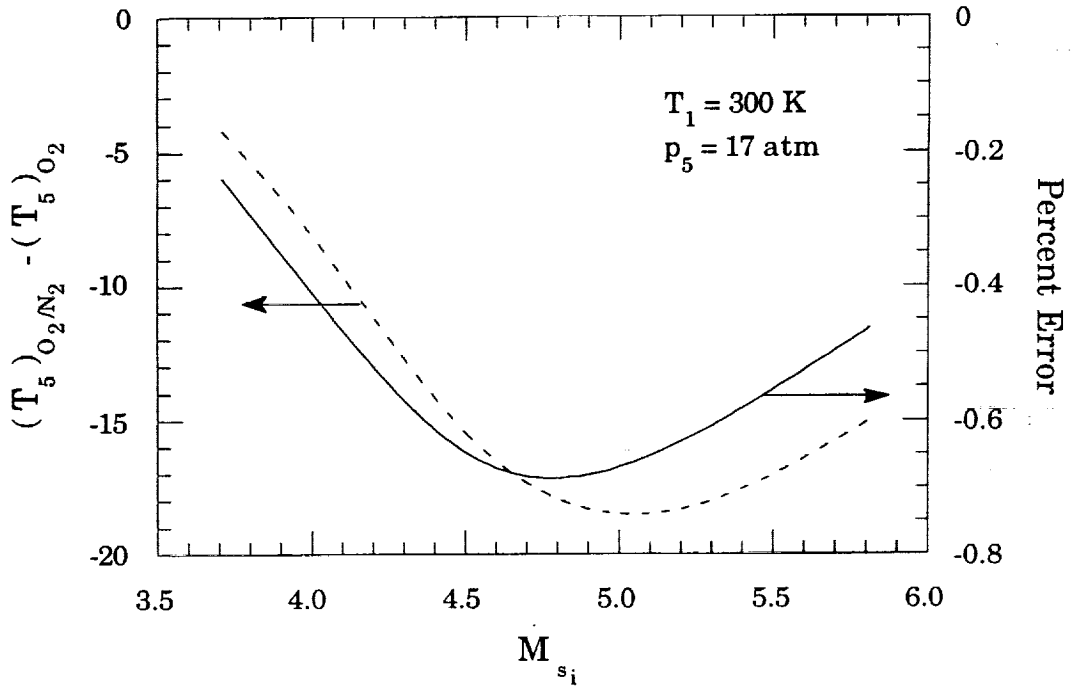

Fig. 2.40: Comparison of the reflected shock temperature calculated assuming the driven gas is pure O_2 and a mixture of 98.6% O_2 / 1.4% N_2. The calculations are performed with the Gordon-McBride code [9].

The results shown in Fig. 2.40 indicate that neglecting the nitrogen produces an error in T_5 which is small compared to the experimental uncertainty associated with the non-ideal reflection of the shock wave from the shock tube endwall (see section 2.4). Neglecting the presence of N_2 in the calculation of T_5 results in a maximum underprediction of ~17 K and a maximum relative error of ~0.73 percent.

The shock tube driver section can now be pressurized with helium. The diaphragm and driver sections are pressurized simultaneously by opening the diaphragm solenoid valve (#3) prior opening the driver solenoid valve (#1). When the diaphragm and driver section pressures reach half of the required driver pressure, the diaphragm valve is closed. The driver section pressure continues to rise until the desired value is reached, at which time the driver valve is closed.

After arming the data acquisition system's external trigger, the shock tube "FIRE" valve (ball valve #2) is opened, which vents the diaphragm gas and ruptures the diaphragms. The high pressure gases which remain in the tube after the experiment are immediately vented by opening the "VENT" valve (ball valve #1), and are released through a muffler mounted several feet above the control room for safety.

2.4 DATA ACQUISITION AND DIAGNOSTIC SYSTEMS

2.4.1 Digital Recorder and Pressure Transducer System

A block diagram of the shock tube's data acquisition system is shown in Fig. 2.41. At the center of the system is a Soltec ADA-1000 8 bit, 10 Mhz digital waveform recorder. The recorder has a memory length of 64,000 samples per channel in which to store the measurements obtained from three shock tube

pressure transducers and the photodiode detector. The recorder is externally triggered using a pressure-sensitive mechanical closing switch to detect the arrival of the incident shock wave at the test section. The recorded data is then downloaded to an IBM-AT computer through an IEEE-488 parallel port for storage and analysis. The computer is also used to control the digital recorder.

The three pressure transducers are used to measure the velocity of the incident shock wave. The endwall transducer is also used to monitor the endwall pressure to determine the duration of the quasi-steady reflected shock conditions. Figure 2.42 shows the test section mounting arrangement of the three pressure transducers and the external trigger. The first sidewall transducer is located 60.8 cm (23.94 in.) from the endwall and is the first to record the pressure jump associated with the passing incident shock wave. Located directly opposite is the recorder's external trigger. The second sidewall transducer is mounted 40.8 cm (16.06 in.) from the endwall and the endwall transducer is mounted directly on the endwall.

The high speed pressure transducers are purchased from PCB Piezotronics, Incorporated. The transducers use a tourmaline sensing element to produce extremely fast rise times, which are quoted to be on the order of 0.2 μs. The sidewall and endwall transducers are shown unmounted in Fig. 2.43. The sidewall transducers (top of photograph) have a 0.1 inch (2.54 mm) diameter sensing diaphragm surface, a range of 10,000 psi, a sensitivity of 1.0 mV/psi, and a resolution of 1.0 psi. The endwall transducer (bottom of photograph) has a sensing diaphragm surface diameter of 0.125 inch (3.18 mm), 2000 psi range, 1.0 mV/psi sensitivity, and a resolution of 1.0 psi.

Each transducer uses an in-line source follower amplifier (also shown in Fig. 2.43) to drive long input cables. The source follower is attached to the transducer with a 3 inch length of low noise coaxial cable. Each

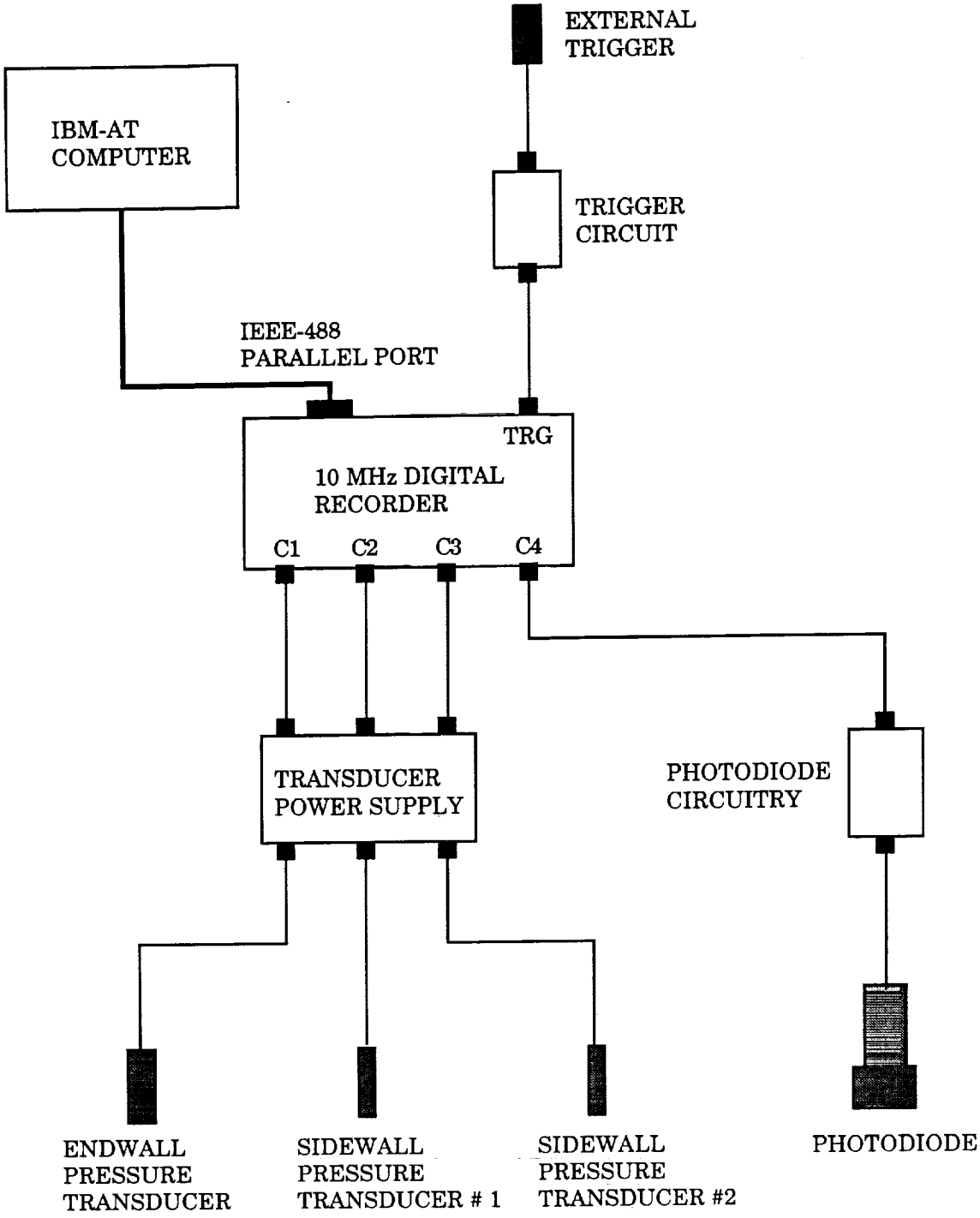

Fig. 2.41: Block diagram of the shock tube data acquisition system. The system is used to record the strength of the incident shock wave, the endwall pressure, and the radiation emitted by the burning particles..

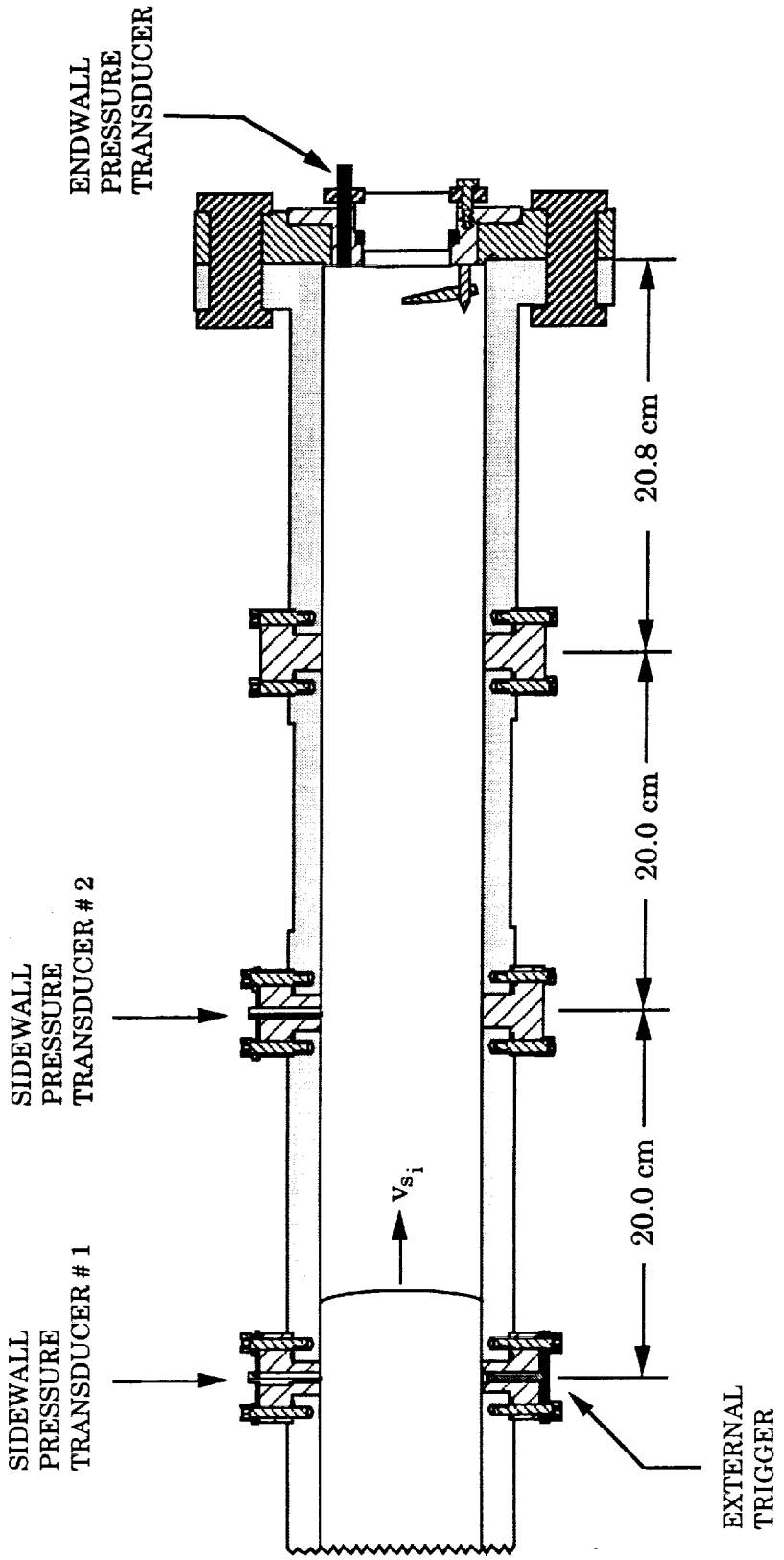

Fig. 2.42: Arrangement of the shock tube pressure transducers and recorder trigger. The system is used to detect the incident shock wave, measure its velocity to determine its strength, and monitor the endwall pressure.

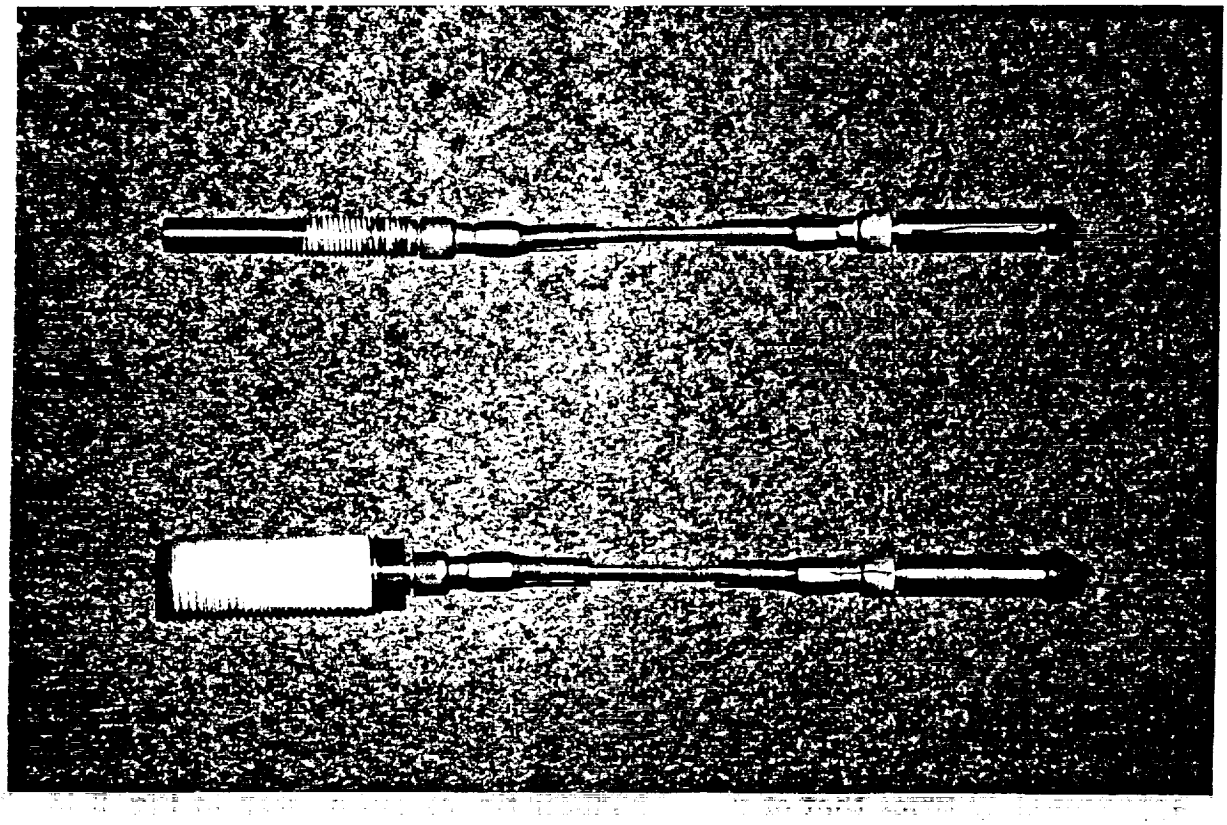

Fig. 2.43: Photograph of the sidewall (top) and endwall (bottom) piezoelectric pressure transducers and source follower amplifiers. The mounting threads are covered with Teflon tape.

transducer/source follower combination is connected to the power supply, located inside the control room, with 50 feet of standard coaxial cable.

Careful mounting of the pressure transducers in the shock tube wall is critical. The sensing diaphragm surface of the sidewall transducers must be mounted flush with the inner wall of the shock tube in order to avoid disturbing the high-speed flow behind the incident shock wave. To accomplish this, the sidewall transducers are mounted in instrument ports machined from half-hard naval brass.

The detail of the instrument port is shown in Fig. 2.44 and a photograph is shown in Fig. 2.45. The port hole has a diameter of 0.75 inches (19.05 mm) and the instrument port is machined to conform exactly to the inner radius of the shock tube, as shown in Fig. 2.44b. The sidewall transducer is threaded into a 1/4-20 tapped hole until its tip is flush with the inner wall. The transducer threads are sealed with Teflon tape and a small o-ring, which is forced into the exposed threads using an aluminum pressure plate. The pressure plate is held by the two-hex head cap screws which are used to attach the instrument port to the tube wall. The entire assembly is seated in shallow flats machined into the tube wall at the location of the port hole. The o-ring used to seal the assembly is clearly visible in Fig. 2.45.

The pressure transducer's sensing diaphragm surface is covered with a piece of 0.0025 inch (0.064 mm) thick tape which has a diameter that is approximately twice that of the transducer tip, as can be seen in Fig. 2.45. The tape acts as a thermal barrier between the sensing diaphragm surface and the high temperature, high velocity flow following the incident shock wave. If the tape is not present, the piezoelectric crystal expands as it is heated by the hot gas, producing a negative signal voltage. The tape also provides limited protection against scorching the ceramic coating which is meant to protect the sensing diaphragm. To avoid damage, the sidewall transducers are never mounted in the instrument port located closest (~21 cm) to the shock tube endwall. This insures that they will never be exposed to the extremely high temperature and high pressure oxygen produced by the reflected shock wave (see Appendix B).

The endwall transducer is similarly mounted in the endwall port, as was discussed in section 2.3.3 and shown in Figs. 2.26, 2.27, and 2.29. The transducer is sealed with Teflon tape. Since the endwall transducer must

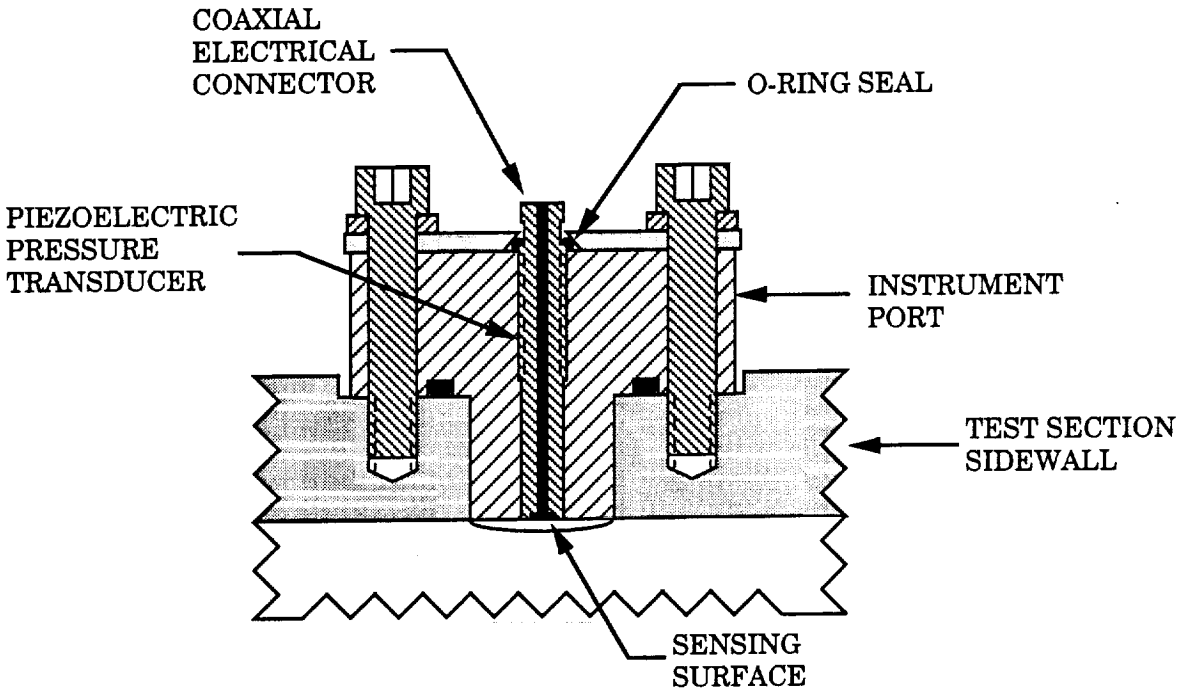

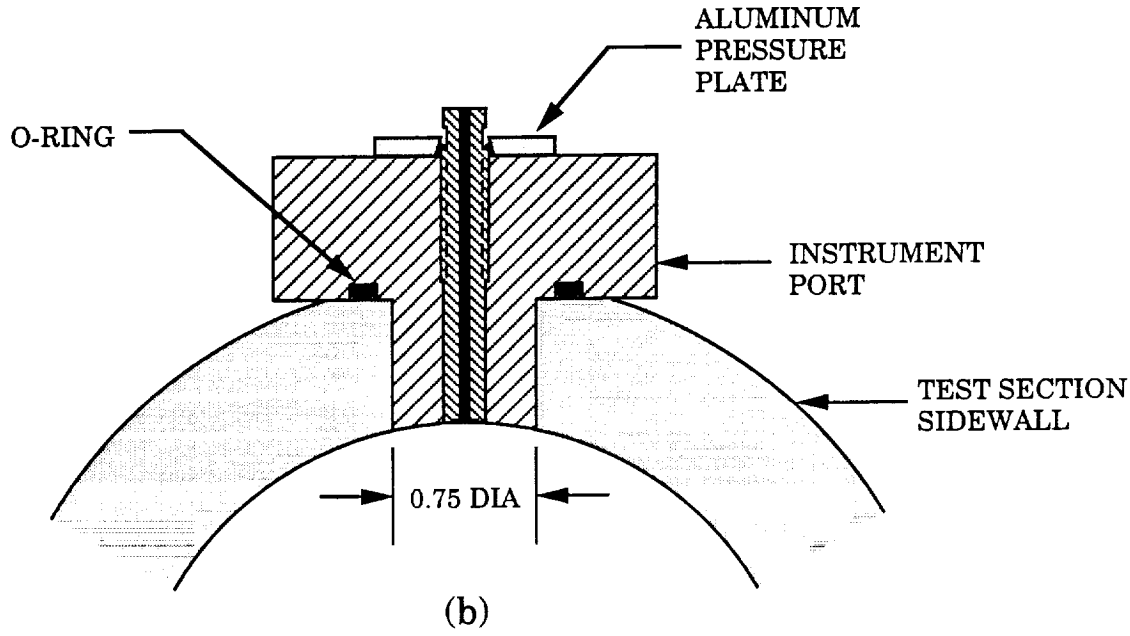

Fig. 2.44: Installation of a piezoelectric pressure transducer in a sidewall instrument port. a) Section taken along the shock tube axis. b) Section taken perpendicular to shock tube axis.

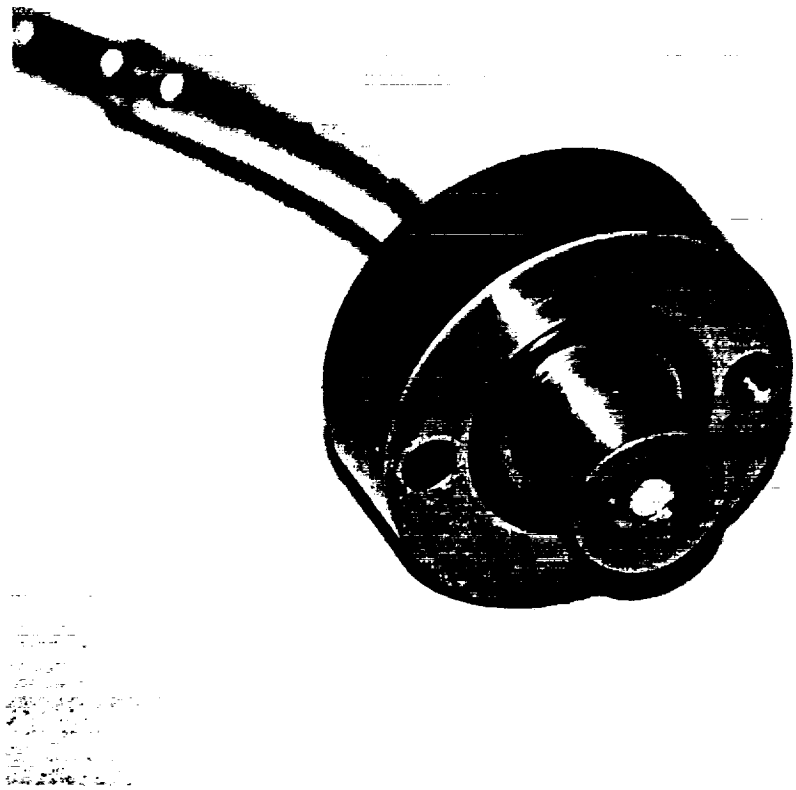

Fig. 2.45: Photograph of a piezoelectric pressure transducer mounted in a brass sidewall instrument port. Note the protective layer of 0.0025 inch thick tape, and concave radiused tip to conform to shock tube ID.

necessarily be exposed to the hot oxygen behind the reflected shock wave, a technique for protecting the transducer is developed that does not substantially effect its transient response.

The endwall transducer is manufactured with a ceramic protective coating applied to the sensing diaphragm surface. This coating can withstand high temperature, non-oxidizing gaseous environments of short duration (msec time scales). However, it was found that the ceramic coating can be badly burned in one shot under the conditions of interest here, i.e., oxygen to 3250 K and 34 atm.

The manufacturers recommendation in this type of situation is to apply a protective layer of 0.0085 inch (0.21 mm) thick black vinyl tape to the diaphragm surface. This tape is sufficiently thin that it does not materially affect the response time of the transducer. However, it was found that in the presence of the hot high pressure oxygen, the tape is severely burned. The additional heat of the combustion, coupled with the high temperature oxygen, destroys the ceramic surface and makes the transducer inoperative. It is also desirable to eliminate the possibility of light emitted from the combustion of the tape interfering with the photodiode measurements.

The solution developed here is to protect the transducer with a 0.001 - 0.002 inch (0.025 or a 0.050 mm) thick brass foil held in place with double-sided tape of 0.0025 inch (0.0625 mm) thickness [50]. The thinner foil is used at pressures below 17 atm and the thicker foil at pressures above 17 atm. The dimensions of the foil and double sided tape are made twice that of the transducer, so the center of the foil protects the transducer and the outer edge is sealed to the inside wall by the tape. This technique prevents oxygen from reaching the transducer tip during the experimental duration of a few milliseconds. After applying the foil and tape, a dull-pointed plastic tool is used to force the brass foil to conform tightly to the transducer tip. The technique is shown schematically in Fig. 2.46 and the protective brass covering is visible in the photograph of Fig. 2.29. Note that the foil is indented around the diameter of the transducer so the foil can flex as pressure is applied.

The response of the endwall transducer protected with black vinyl tape and 0.001 inch thick brass foil and tape is shown in Fig. 2.47, for a reflected shock pressure and temperature of approximately 16.5 atm and 2250 K ($M_{s_i} \cong 4.30$). With the black vinyl tape (Fig. 247a) the pressure rise time is observed to be <1 μs. The signals shown in Fig. 2.47b are with brass foil and

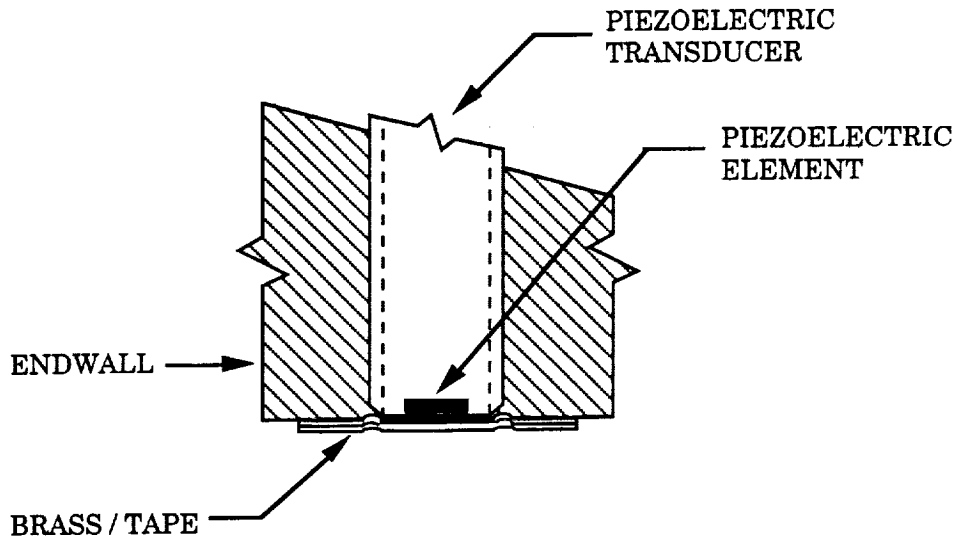

Fig. 2.46: Application of protective layer of brass foil and tape to the endwall mounted piezoelectric pressure transducer.

tape, recorded on separate shots with identical initial conditions. The two signals presented show the response variation that is possible when the brass foil and tape are used. The vertical scale of Fig. 2.47b has been increased to clearly show the signal overpressure spikes.

The dashed curve of Fig. 2.47b shows a pressure signal that rises promptly at shock impact to ~120 mV (~10 atms) in 1 μs, followed by a slower rise to the full 200 mV (16.5 atms) over a period of 5 μs. An overpressure spike of 2 μs width is also observed here, but following this spike the expected quasi-steady pressure is recorded by the transducer. The overpressure spike is not always present, and can be eliminated altogether when the brass foil and tape are applied with extreme care, as shown by the solid curve in Fig. 2.47b. This signal has a rise time that is as fast as that recorded with the black vinyl tape, alone.

Although the transducer's rise time is unaffected with proper application of the brass foil and tape, the sensitivity of the transducer is usually lowered

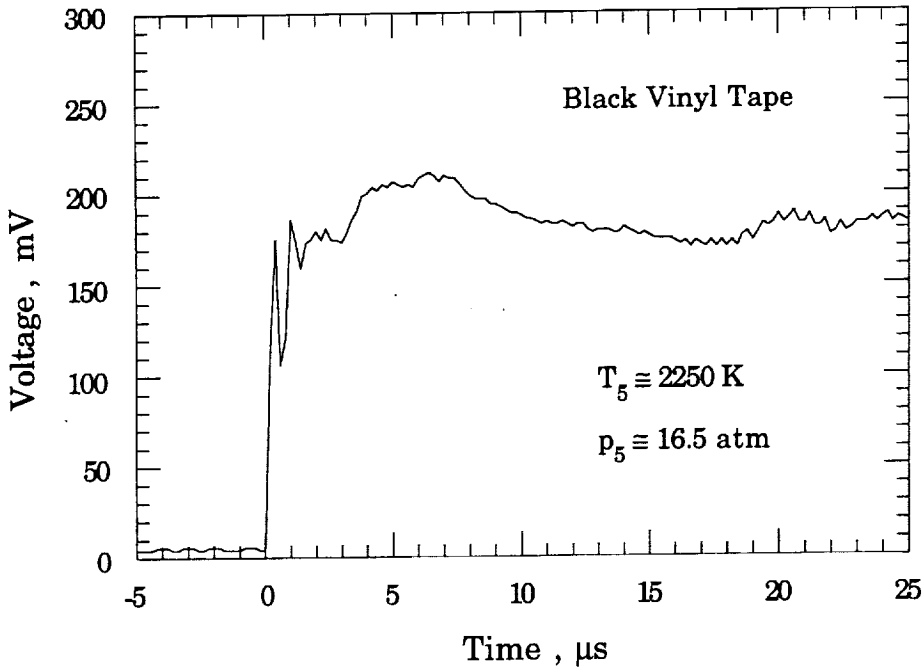

(a)

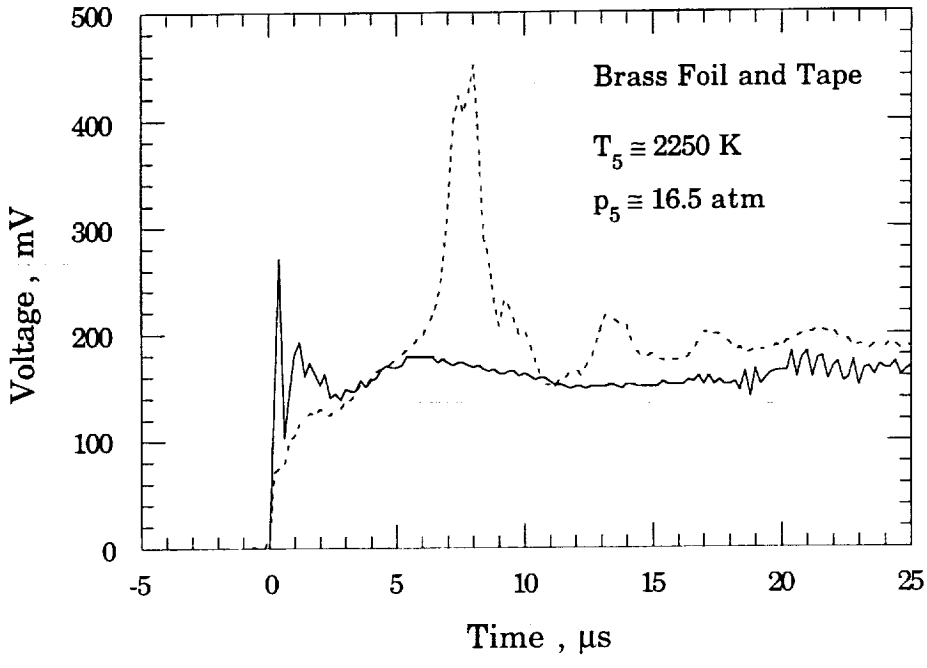

(b)

Fig. 2.47: Response of the endwall pressure transducer when protected with black vinyl tape or brass foil and tape. a) Black vinyl tape. b) 0.001 inch thick brass foil and double-sided tape.

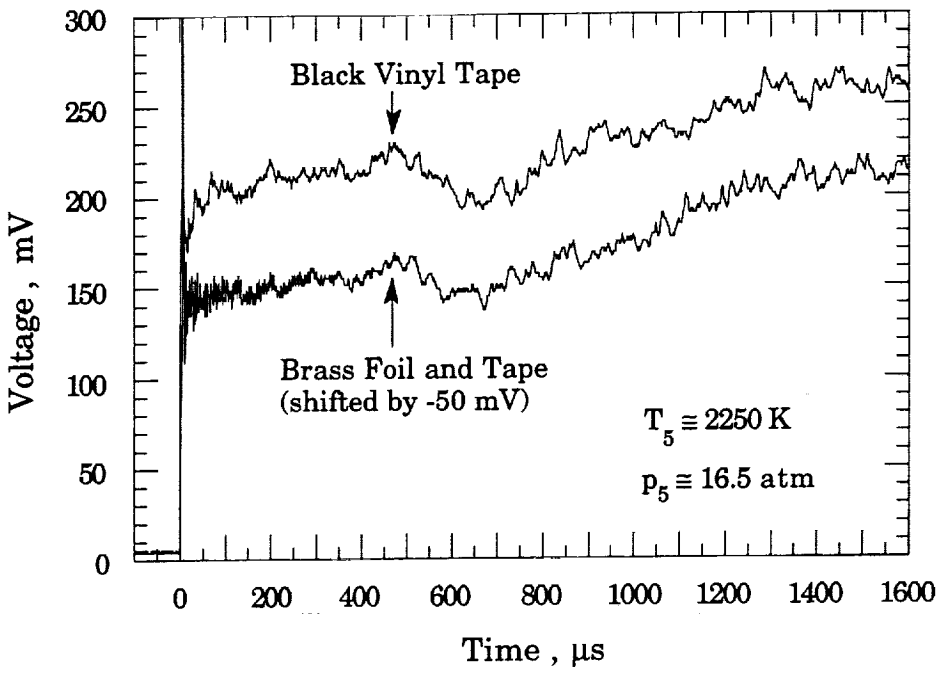

Fig. 2.48: Long term response of the endwall pressure transducer when protected with black vinyl tape or brass foil and tape.

slightly. Calibration of the system after applying the protective layer may be possible in some applications, but this is not done here since the endwall transducer's primary purpose is to measure the time of shock reflection and the duration of the experiment conditions. The reflected shock pressure and temperature are then calculated from the measured incident shock velocity using the NASA Gordon-McBride code.

The effect of the brass foil and tape on the character of the long term endwall pressure signal is shown in Fig. 2.48. The black vinyl tape signal is the same as that shown in Fig. 2.47a and brass foil and tape signal is the same as the dashed curve of Fig. 2.47b. The signal recorded for the brass and tape is shifted by -50 mV so that both signals can be clearly shown. The long term character of the pressure signals are nearly identical, indicating that the brass and tape protective layer will not affect the measurement of the test duration.

The brass foil and tape technique can be reused several times, depending on the reflected oxygen conditions. For oxygen at 2250 K and 8 atm, a single brass foil can be left in place and used up to 20 times. For oxygen at 2250 K and 34 atm, a single foil can be used only once or twice. Figure 2.49 shows photographs of a brass foil after the foil had been used to protect the endwall transducer several times. The three tabs at the bottom of the brass patch are tucked between the endwall port and the endwall flange to facilitate sealing.

(a) (b)

Fig. 2.49: Brass foil repeatedly used to protect the endwall piezoelectric pressure transducer from hot oxygen. a) Surface exposed to the hot oxygen. b) Surface that faced the transducer.

Figure 2.49a shows the side of the brass exposed to the hot oxygen and Fig. 2.49b shows the protected side. The larger circular pattern is the outline of the transducer tip and the inner circular pattern is the imprint of the sensing

diaphragm. The brass is damaged around the edges and the entire exposed side is highly oxidized. The transducer side of the brass, particularly in the area of the sensing diaphragm, remains in good condition. When black vinyl tape is used to protect the transducer, it is usually charred severely after the shot, as was shown in Fig. 2.34.

2.4.2 External Trigger for the Digital Recorder

The velocity of the incident shock wave ranges from 1200 m/s to 1900 m/s in order to produce the reflected oxygen temperatures of interest. The large shock velocities, and short particle ignition and combustion times, result in a measurement window of less than 2 msec from the time the shock wave passes sidewall transducer #1 to the end of particle combustion. To synchronize the digital recorder with this short measurement window, an external trigger is constructed to detect the incident shock wave's arrival at the test section.

Once the digital recorder has been armed, it will begin recording when it detects a change in the voltage of the trigger. The simple circuit shown in Fig. 2.50 forms the basis of the external trigger developed here. The ON-OFF switch is used to arm the trigger. As the shock wave passes the trigger, the detection switch is closed, and the recorder senses a voltage drop of 9 volts and begins recording. The recorder is capable of 0-100% pre-trigger, which allows the recording of "negative" time, i.e. time prior to the change in the external trigger voltage. The recorder's pre-trigger feature means that a slow trigger response time, on the order of a msec, is tolerable.

The construction of the external trigger is similar to that of the sidewall transducer, as shown in Fig. 2.51. A sidewall instrument port is used to house the trigger. As shown in Figs. 2.51a and 2.51b, No. 14 AWG wire is pushed

through the tapped whole of the instrument port and the remaining volume is filled with high temperature RTV sealant. The No. 14 AWG wire leads are pinned beneath a notched steel plate to withstand high pressure. The steel plate is anchored with the socket-head cap screws used to mount the instrument port. The no. 14 AWG wires are spliced to no. 22 AWG wires before entering the trigger's circuit box.

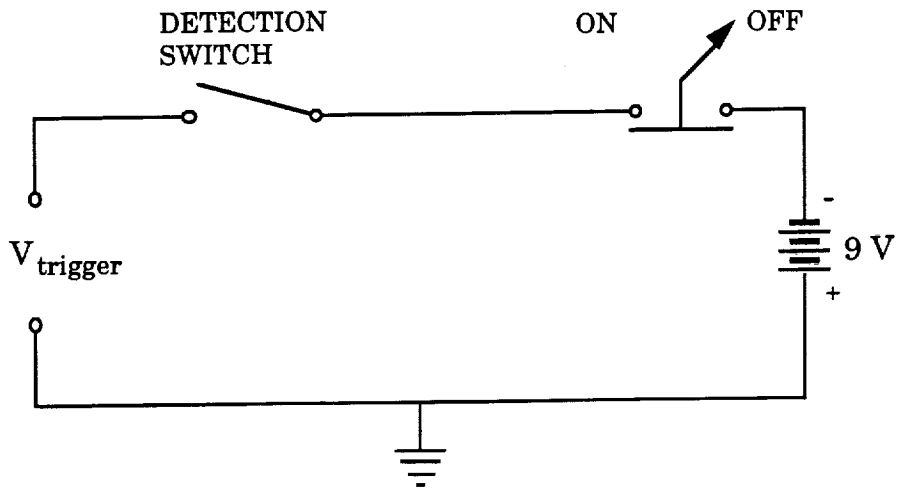

Fig. 2.50: Electrical circuit on which the construction of the external trigger is based. The detection switch senses the passage of the incident or reflected shock wave.

The detailed construction of the external trigger shock wave sensor is shown in Fig. 2.51c. The end of the copper wire leads are exposed approximately 0.1 inch (2.5 mm) from the inner wall of the shock tube. Solder is then neatly formed on the exposed tip of each wire. The solder is carefully shaped with a small file and modeling knife to form the diaphragm mount and contact. The contact and diaphragm mount are recessed into the instrument port approximately 0.004 inches (0.1 mm) and 0.002 inches (0.05 mm), respectively.

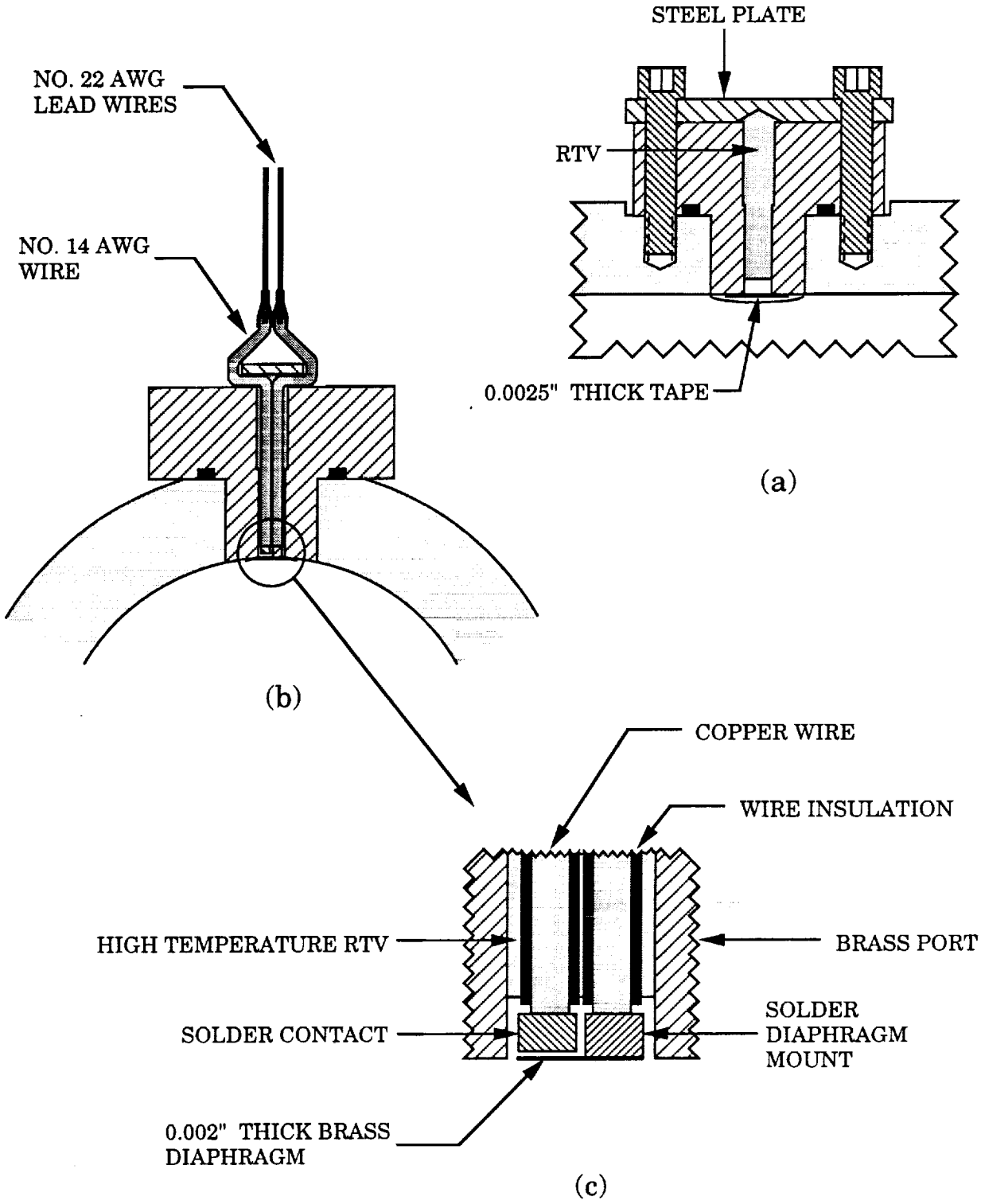

Fig. 2.51: Construction of the external trigger used to detect the incident shock wave. a) Section taken along shock tube axis. b) Section taken perpendicular to shock tube axis. c) Detail of sensor.

The 0.002 inch thick brass diaphragm is attached to the mount with additional solder.

The construction is completed by covering the sensing area with 0.0025" thick tape to protect the fragile diaphragm from the high velocity flow behind the incident shock wave. A pinhole is punctured in the tape to allow the gas pressure on either side of the diaphragm to equilibrate prior to firing the shock tube. As the incident shock wave passes the trigger location, the instantaneous pressure rise deflects the diaphragm, touches the contact solder, and completes the circuit.

Proper construction of the external trigger results in a nominal response time of approximately 40 μs. In some instances, the pressure rise behind the incident shock wave is not large enough to deflect the diaphragm completely. However, when the reflected shock wave reaches the trigger location, the large pressure rise associated with it will always deflect the diaphragm and complete the circuit. The trigger response in this latter case is on the order of 1 msec, well within the digital recorder's nominal pre-trigger setting. Out of 280 shock tube firings, the trigger failed to close (i.e., produce the triggering voltage) only twice, yielding a reliability of better than 99 percent.

2.4.3 Measurement of M_{s_i} and Calulation of T_5 and p_5

The system of pressure transducers, the external trigger, and the data acquisition system described in the previous sections are used to measure accurately the velocity of the incident shock wave, v_{s_i}. The Mach number of the incident shock wave, M_{s_i}, is easily calculated using the known speed of sound in the undisturbed oxygen. The measured value of M_{s_i} and the initial oxygen temperature and pressure, T_1 and p_1, are used to calculate the reflected shock

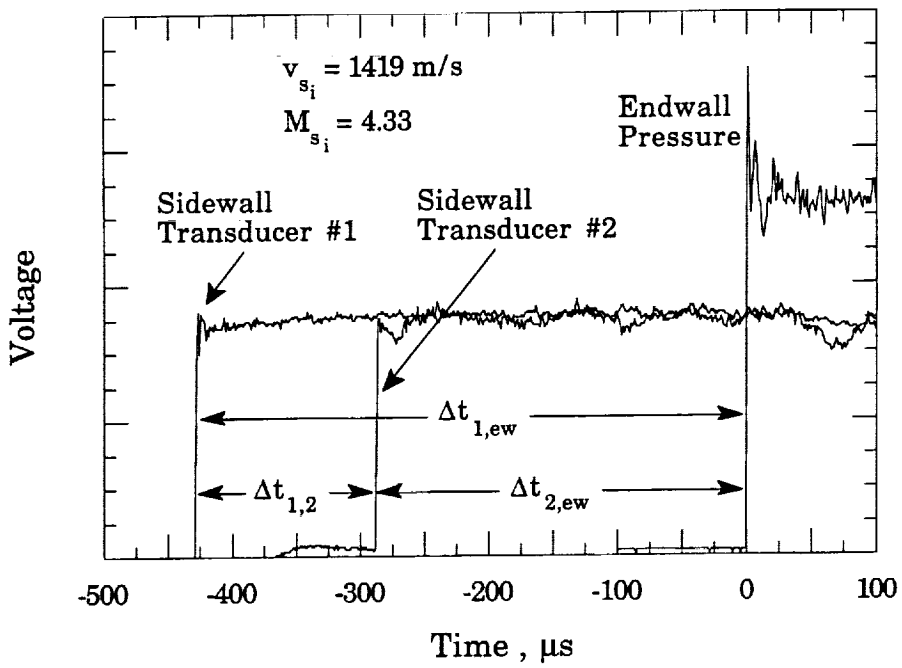

(a)

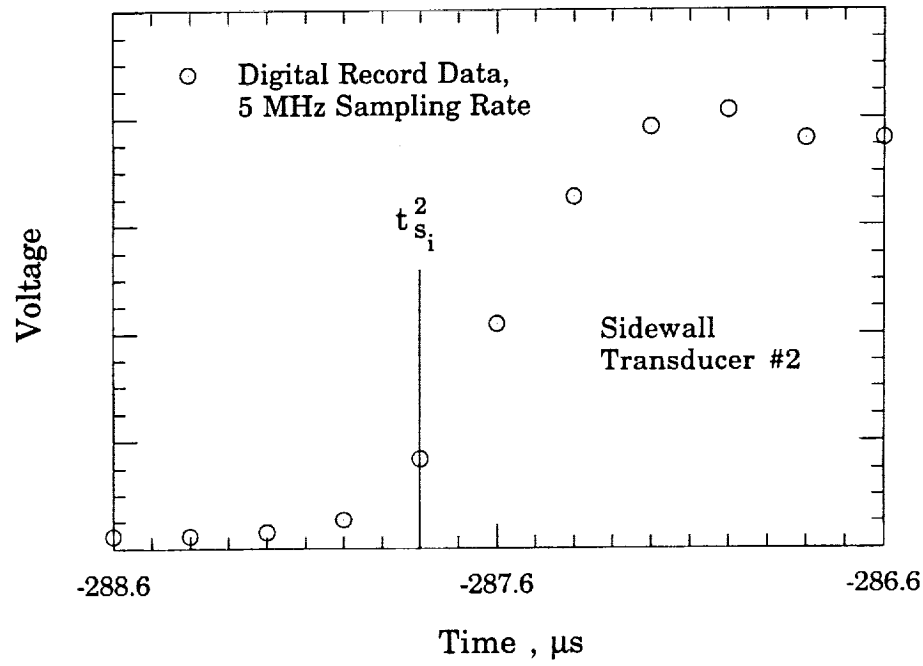

(b)

Fig. 2.52: Pressure transducer signals used to measure the velocity of the incident shock wave. a) Typical signals used to measure shock wave time intervals. b) Typical measurement of arrival time.

properties of the oxygen using the NASA Gordon-McBride code [9]. The code solves the classical one-dimensional shock relations (see Appendix B), using an iterative approach that includes the variable composition and properties of the oxygen. The reflected temperature and pressure is calculated assuming chemical equilibrium exists in each region of the gas.

The sidewall and endwall pressure signals shown in Fig. 2.52 are typical of those from which the velocity of the incident shock wave is calculated. The voltage is arbitrary and the sidewall signals have been scaled (enlarged) for presentation. The arrival of the shock wave at each transducer location is determined as shown in Fig. 2.52b, where the second sidewall transducer's signal is plotted on an expanded time scale. The data points shown in figure 2.52b are recorded at a sampling rate of 5 MHz. The shock wave's arrival time is determined by selecting the first point at which the transducer voltage clearly rises above the signal noise. As shown in Fig. 2.52b, the arrival time of the shock wave at the location of the second sidewall transducer is $t^2_{s_i}$ = -287.8 μs. Using a similar analysis, the arrival times at the remaining transducer locations are determined for each experiment.

To increase the accuracy of the shock velocity measurement, an average velocity is calculated from the measured shock wave arrival times and the known transducer distance intervals using the relation:

$$v_{s_i} = \frac{1}{3}\left(\frac{\Delta x_{1,2}}{\Delta t_{1,2}} + \frac{\Delta x_{2,ew}}{\Delta t_{2,ew}} + \frac{\Delta x_{1,ew}}{\Delta t_{1,ew}}\right) \tag{2.5}$$

where

$$\left.\begin{aligned} \Delta t_{1,2} &= t^2_{s_i} - t^1_{s_i} \\ \Delta t_{2,ew} &= t^{ew}_{s_i} - t^2_{s_i} \\ \Delta t_{1,ew} &= t^{ew}_{s_i} - t^1_{s_i} \end{aligned}\right\} \tag{2.6}$$

The fixed distance intervals between the transducer locations are (see Fig. 2.42):

$$\left.\begin{aligned} \Delta x_{1,2} &= 20.0 \text{ cm } (7.87 \text{ in}) \\ \Delta x_{2,ew} &= 40.8 \text{ cm } (16.0 \text{ in}) \\ \Delta x_{1,ew} &= 60.8 \text{ cm } (23.94 \text{ in}) \end{aligned}\right\} \tag{2.7}$$

The incident shock Mach number is calculated from:

$$a_1 = \sqrt{\gamma_1 R_1 T_1} \tag{2.8}$$

$$M_{s_i} = \frac{v_{s_i}}{a_1} \tag{2.9}$$

where a_1, γ_1, R_1, and T_1 are the sound speed, ratio of specific heats, gas constant, and temperature of the undisturbed oxygen. T_1 is read, just prior to firing the shock tube, from a thermometer attached directly to the driven section.

2.4.4 Uncertainty Analysis

The uncertainty of the calculated experimental temperature and pressure is a function of the uncertainty in the measurement of the incident shock Mach number and the initial temperature and pressure of the driven oxygen. The uncertainties in these quantities are estimated following the analysis presented by Holman [51].

The uncertainty in the calculated result R of an experiment depends on the uncertainty of each measurement on which it is based. R is a known

function of the independent variables, x_1, x_2, x_3, ..., x_n. The result can be written in the form:

$$R = R(x_1, x_2, x_3, \ldots, x_n) \tag{2.10}$$

If the uncertainty in the result is w_R, and the uncertainties in the independent variables are w_1, w_2, w_3, ..., w_n, then the uncertainty in the calculated result is given by:

$$w_R = \left[\left(\frac{\partial R}{\partial w_1}\right)^2 w_1 + \left(\frac{\partial R}{\partial w_2}\right)^2 w_2 + \ldots + \left(\frac{\partial R}{\partial w_n}\right)^2 w_n\right]^{\frac{1}{2}} \tag{2.11}$$

Thus, the analysis of the experimental uncertainties depends on the ability to explicitly calculate or approximate the derivatives of the experimental result, R.

Combining Eqs. (2.5) and (2.9) yields the following explicit relationship for the incident shock Mach number:

$$M_{s_i} = \frac{v_{s_i}}{a_1} = \frac{1}{3\sqrt{\gamma_1 R_1 T_1}}\left[\frac{\Delta x_{1,2}}{\Delta t_{1,2}} + \frac{\Delta x_{2,ew}}{\Delta t_{2,ew}} + \frac{\Delta x_{1,ew}}{\Delta t_{1,ew}}\right] \tag{2.12}$$

The uncertainty in γ_1 and R_1 are assumed to be zero. Differentiating Eq. (2.12) with respect to the seven independent variables, substituting into Eq. (2.11), and using the fact that $v_{s_i} \equiv \Delta x_{i,j} / \Delta t_{i,j}$ results in the following expression for the uncertainty in M_{s_i}:

$$w_{M_s} = \frac{1}{3a_1}\left\{K\left[(v_{s_i})^4 (w_{\Delta t})^2 + (v_{s_i})^2 (w_{\Delta x})^2\right] + \frac{3}{4}\left(\frac{v_{s_i}}{T_1}\right)^2 (w_{\Delta x})^2\right\}^{\frac{1}{2}} \tag{2.13}$$

where $$K = \frac{1}{(\Delta x_{1,2})^2} + \frac{1}{(\Delta x_{2,ew})^2} + \frac{1}{(\Delta x_{1,ew})^2} = 33.71\ m^{-2} \qquad (2.14)$$

The constant K is a function of the transducer spacing only, and therefore is known for a given transducer arrangement.

The temperature of the driven oxygen is measured with a liquid-in-glass (alcohol) thermometer that is in direct thermal contact with the outer surface of the test section. The oxygen and test section temperatures are assumed to be equal. The uncertainty of the temperature measurement is taken to be $w_{T_1} = \pm 0.25$ K.

The uncertainty in the measurement of each time interval, $w_{\Delta t}$, depends on the sampling rate of the digital recorder. A small number of the experiments use a sampling rate of 1 MHz while the rest use a sampling rate of 5 MHz. The uncertainties in the measured time intervals are assumed to be $w_{\Delta t} = \pm 1$ μs and $\pm$ 0.4 μs for sampling rates of 1 MHz and 5 MHz, respectively. These uncertainties are conservative, and should account for the transducer rise time variations that may occur when protective coverings are applied.

The diameter of the sidewall transducer's sensing diaphragm surface is 0.1 inch (2.54 mm). Therefore, the uncertainty in the transducer spacing is taken to be half of this dimension, $w_{\Delta x} = \pm 0.05$ inch (1.3 mm).

Using these uncertainties and assuming T_1 = 300 K, w_{M_s} is calculated and the result is plotted as a function of the incident shock Mach number in Fig. 2.53. The uncertainty is calculated for both of the sampling rates used. The uncertainty increases linearly with M_{s_i}, and is reduced by less than a factor of two when the sampling rate is increased from 1 MHz to 5 MHz. The largest uncertainty of w_{M_s} = 0.026 is less than 0.5 percent of the Mach number being measured.

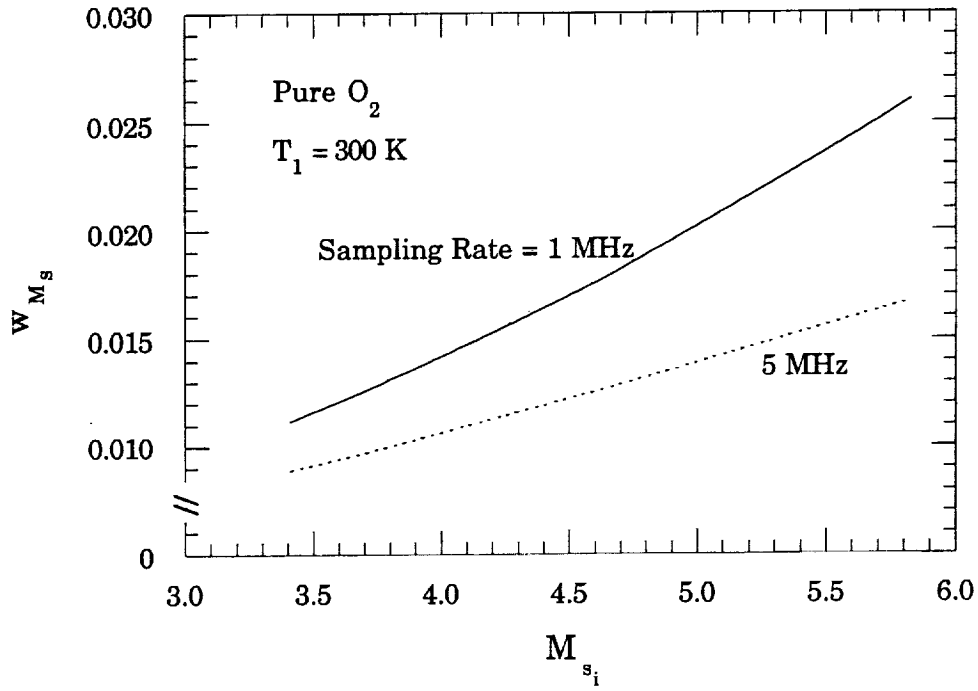

Fig. 2.53: Absolute uncertainty w_{M_s} in the measurement of the incident shock Mach number. Calculations assume: pure O_2, T_1 = 300 K, $w_{T_1} = \pm 0.25$ K, $w_{\Delta x} = \pm 1.3$ mm, and $w_{\Delta t} = \pm 1$ μs and ±0.4 μs at sampling rates of 1 MHz and 5 MHz, respectively.

The uncertainties in the calculated experiment conditions, T_5 and p_5, can be estimated in a similar manner. Explicit relations for the reflected shock temperature and pressure in terms of γ_1, T_1, p_1, and M_{s_i} can be derived if the oxygen is assumed to be calorically and thermally perfect, and the flow is assumed to be one dimensional.

The ideal relation for the reflected shock temperature is (see Appendix B):

$$T_5 = T_1 \frac{\left[2(\gamma_1 - 1) M_{s_i}^2 + (3 - \gamma_1)\right]\left[(3\gamma_1 - 1) M_{s_i}^2 - 2(\gamma_1 - 1)\right]}{(\gamma_1 + 1)^2 M_{s_i}^2} \tag{2.15}$$

The uncertainty in the calculated T_5 can then be written as:

$$w_{T_5} = \left[\left(\frac{\partial T_5}{\partial T_1} w_{T_1} \right)^2 + \left(\frac{\partial T_5}{\partial M_{s_i}} w_{M_s} \right)^2 \right]^{\frac{1}{2}} \tag{2.16}$$

where

$$\frac{\partial T_5}{\partial M_{s_i}} = \frac{4\, T_1 (\gamma_1 - 1)}{(\gamma_1 + 1)^2 M_{s_i}^3} \left[M_{s_i}^4 (3\gamma_1 - 1) + (3 - \gamma_1) \right] \tag{2.17}$$

and $\partial T_5 / \partial T_1$ is trivial.

Equations (2.15) - (2.17) are used to estimate the uncertainty in T_5 by treating the oxygen as both an ideal and a real (variable property) gas. The uncertainty in the driven oxygen temperature is assumed to be $w_{T_1} = \pm 0.25$ K and the uncertainty in the incident shock Mach number, w_{M_s}, is treated as a variable function of M_{s_i} and is read directly from Fig. 2.53. When the oxygen is treated as an ideal gas the differentials in Eq. (2.16) are calculated explicitly. When treating the oxygen as a real gas, the differentials are numerically calculated based on the results obtained from the NASA Gordon-McBride code.

Figure 2.54 shows the estimated uncertainty in the calculated reflected shock temperature of pure oxygen plotted for sampling rates of 1 MHz (dashed curves) and 5 MHz (solid curves). The reflected shock pressure is assumed to be 17 atm in all cases. The ideal calculations assume $\gamma_1 = 1.393$ and indicate that the uncertainty is a linear function of T_5. However, the uncertainty of the calculated reflected shock temperature, based on variable gas properties, is found to be a nonlinear function of T_5. For a sampling rate of 5 MHz, the uncertainty rises from a minimum of ~7 K at $T_5 = 1750$ K to a maximum of ~10 K at $T_5 = 2550$ K, and then decreases to ~8.5 K at $T_5 = 3250$ K. This nonlinear variation is the result of the dissociation of the oxygen, which reduces the magnitude of the $\partial T_5 / \partial M_{s_i}$ with increasing Mach number (or increasing T5). The magnitude of the reflected shock pressure has a negligible effect on w_{T_5}.

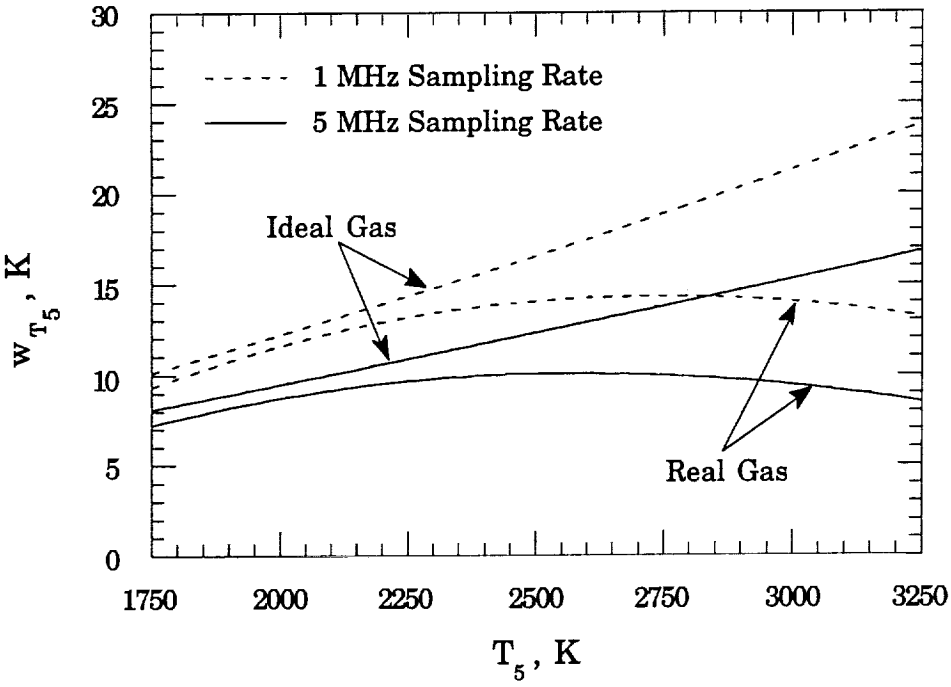

Fig. 2.54: Absolute uncertainty in the calculation of the reflected shock temperature. Calculations assume: pure O_2, T_1 = 300 K, $w_{T_1} = \pm 0.25$ K, variable w_{Ms} (Fig. 2.53), and $w_{\Delta t} = \pm 1$ μs and ± 0.4 μs at sampling rates of 1 MHz and 5 MHz, respectively.

The ideal relation for the reflected shock pressure is given by (see Appendix B):

$$p_5 = p_1 \left[\frac{2\gamma_1 M_{s_i}^2 - (\gamma_1 - 1)}{(\gamma_1 + 1)} \right] \left[\frac{(3\gamma_1 - 1) M_{s_i}^2 - 2(\gamma_1 - 1)}{(\gamma_1 - 1) M_{s_i}^2 + 2} \right] \tag{2.18}$$

The uncertainty in p_5 can thus be calculated from:

$$w_{p_5} = \left[\left(\frac{\partial p_5}{\partial p_1} w_{p_1} \right)^2 + \left(\frac{\partial p_5}{\partial M_{s_i}} w_{M_s} \right)^2 \right]^{\frac{1}{2}} \tag{2.19}$$

where

$$\frac{\partial p_5}{\partial M_{s_i}} = \frac{4\gamma_1 p_1 (3\gamma_1 - 1)(\gamma_1 - 1)}{(\gamma_1 + 1)\left[(\gamma_1 - 1) M_{s_i}^2 + 2\right]^2} \left[M_{s_i}^5 + \frac{4}{(\gamma_1 - 1)} M_{s_i}^3 - \frac{(\gamma_1 + 5)}{(3\gamma_1 - 1)} M_{s_i} \right] \tag{2.20}$$

and $\partial p_5 / \partial p_1$ is trivial from Eq. (2.18).

The vacuum gage is calibrated to zero pressure prior to each experiment. This procedure results in a driven pressure uncertainty of $w_{p1} = \pm 0.02$ psia ($\pm$ 0.13 kPa). Using this uncertainty and the variable w_{M_s} (Fig. 2.53), the uncertainty in p_5 is calculated as a function of the reflected shock temperature assuming a reflected pressure of 17 atm, as shown in Fig. 2.55. Results are presented for constant ($\gamma_1 = 1.393$) and variable oxygen properties as well as sampling rates of 1 MHz (dashed curve) and 5 MHz (solid curve).

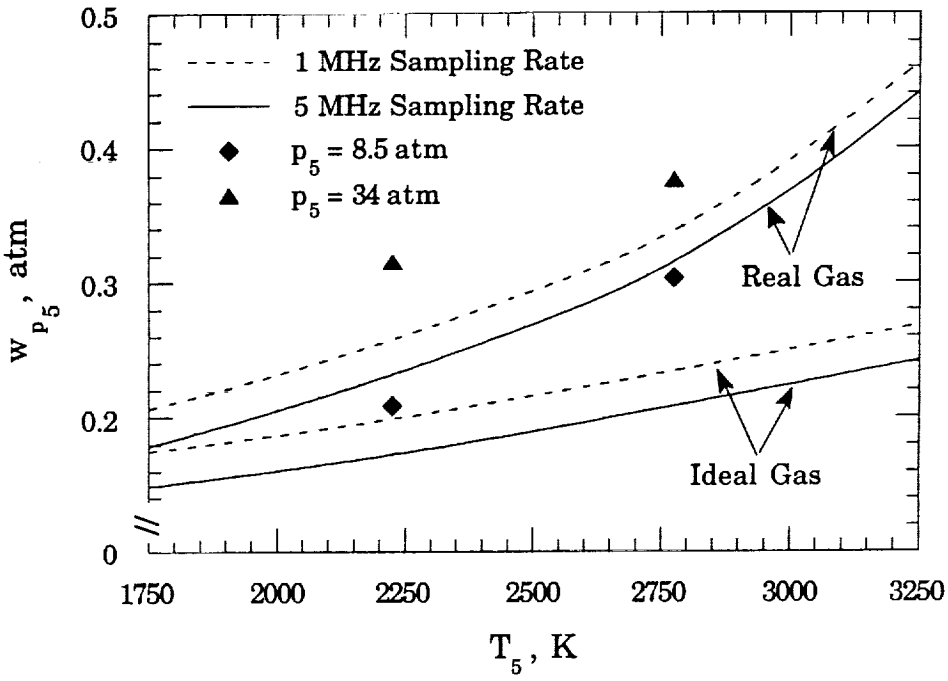

Fig. 2.55: Absolute uncertainty in the calculation of the reflected shock pressure. Calculations assume: pure O_2, $T_1 = 300$ K, $w_{p1} = \pm 0.02$ psia, variable w_{Ms} (Fig. 2.53), and $w_{\Delta t} = \pm 1$ µs and ± 0.4 µs at sampling rates (SR) of 1 MHz and 5 MHz, respectively. Curves correspond to $p_5 = 17$ atm, diamonds to 8.5 atm, and the triangles to 34 atm.

The uncertainty in p_5, calculated assuming an ideal gas, increases linearly with increasing T_5. However, the uncertainty of the real gas

calculations is found to increase in a nonlinear manner with increasing T_5. The majority of experiments are performed at $p_5 \cong 17$ atm and use a sampling rate of 5 MHz. Therefore, the uncertainty in the calculated reflected shock pressure is normally less than 3.0 percent. The single data points plotted in Fig. 2.55 correspond to reflected shock pressures of 8.5 atm and 34 atm. They are calculated assuming variable property oxygen, 5 MHz sampling rate, and reflected shock temperatures of 2225 K and 2775 K. The maximum uncertainties in the calculated reflected pressure at p_5 = 8.5 atm and 34 atm are 3.5 percent and 1.1 percent, respectively.

2.4.5 Error Associated With Non-Ideal Shock Reflection

The largest uncertainty associated with the calculation of T_5 and p_5 is undoubtedly due to the non-ideal behavior of the reflected shock wave [48,52]. The ideal calculations assume that the reflection of the incident shock wave is one-dimensional and produces a single normal reflected shock wave. In practice, however, the reflected shock wave interacts with the shock tube sidewall boundary layer, formed by the incident shock wave, and its strength is reduced [49,53,54].

Strehlow and Cohen [49] studied the reflected shock technique in various gases, including O_2. They found that the measured reflected shock velocities were lower than those predicted from theory. Strehlow and Cohen concluded that, for argon in the temperature range 1500 K to 3000 K, the actual reflected gas temperature could be 300 K to 500 K below that predicted by theory.

Further work by Skinner [53] and Brabbs et al. [54] established that, although the reflected shock wave is weaker than predicted, the reflected temperature deficit in argon is more likely on the order of 30 K to 60 K for

incident shock Mach numbers ranging from 2.5 (~1530 K) to 3.5 (~2870 K), respectively. They hypothesized that, since the flow velocity must be zero at the endwall, the flow must be brought completely to rest by weak, adiabatic compression waves. These compression waves continue to heat the gas adiabatically to just slightly below that predicted by ideal shock theory.

It was later stated by Strehlow and Cohen [55] that the best estimate at that time (1962) was that the reflected gas temperature is approximately 30 K to 50 K above theoretical in the range 1500 K < T_5 < 3000 K. This conclusion was based on the experimental evidence of Strehlow and Case [56] and Rudinger [57], and the theoretical work of Mirels and Braun [58].

In 1965, Palmer et al. [59] reviewed the literature available related to the error associated with calculating the reflected shock gas conditions from the measurement of the incident shock Mach number. Based on numerous studies, including several in which the reflected temperature was measured directly using spectroscopic techniques, Palmer et al. concluded that, for argon shocks in typical tubes at initial pressures in excess of 50 torr, the reflected shock temperatures at the endplate are only slightly below the ideal values. They state that the error is not more than 10 K, 25 K and 50 K for reflected shock temperatures of 1000 K, 1750 K, and 2500 K, respectively.

It is clear that the existing experimental evidence is often contradictory. In addition, it is difficult to generalize shock tube results obtained in different laboratories [56]. To the author's knowledge, deviations from ideality have yet to be correlated in terms of deviations in incident shock velocity, as Strehlow had hoped [56], allowing investigators to calculate the true reflected shock temperature from their data. A review of recent literature indicates that the non-ideal reflection of the shock wave is generally ignored, and the reflected gas

temperature is stated to be equal to that calculated assuming ideal reflection [35,38,47,60].

In the discussion of the experimental results presented in Chapter 4, the stated reflected shock temperature and pressure will be equal to that calculated using the NASA Gordon-McBride code, which considers the variable properties of the gas, but assumes ideal shock reflection. The reader should be aware of the previously discussed uncertainties when considering the experimental data.

2.4.6 Photodiode and Photographic Optical Systems

The optical system shown in Fig. 2.56 is used to measure the radiation emitted by the burning Al/Mg alloy particles near the endwall of the shock tube. The drawing is to scale and the shock tube is rotated about its axis through an angle of 90 degrees so that the knife blade particle mount lies within the plane of the optical system. The dimensions shown are typical for each experiment.

An 80 mm diameter aspheric collecting lense, with a focal length of f.l. = 66 mm, is used to maximize the amount of light collected. The collecting lens is mounted approximately 78 mm from the inside surface of the observation window. The path of the collected light is turned 90 degrees with a flat mirror that is mounted 140 mm from the collecting lense. The light then enters the photodiode housing through a 30 mm diameter, f.l. = 50 mm focussing lense which concentrates the light rays on the small, 6 mm diameter photodiode detector. The photodiode housing is mounted 15 cm off of the shock tube axis to protect it from damage in the event the endwall observation window fails catastrophically.

After reflection of the shock wave, the 5,000 to 10,000 metal particles initially mounted on the knife blade are dispersed into a cloud which then

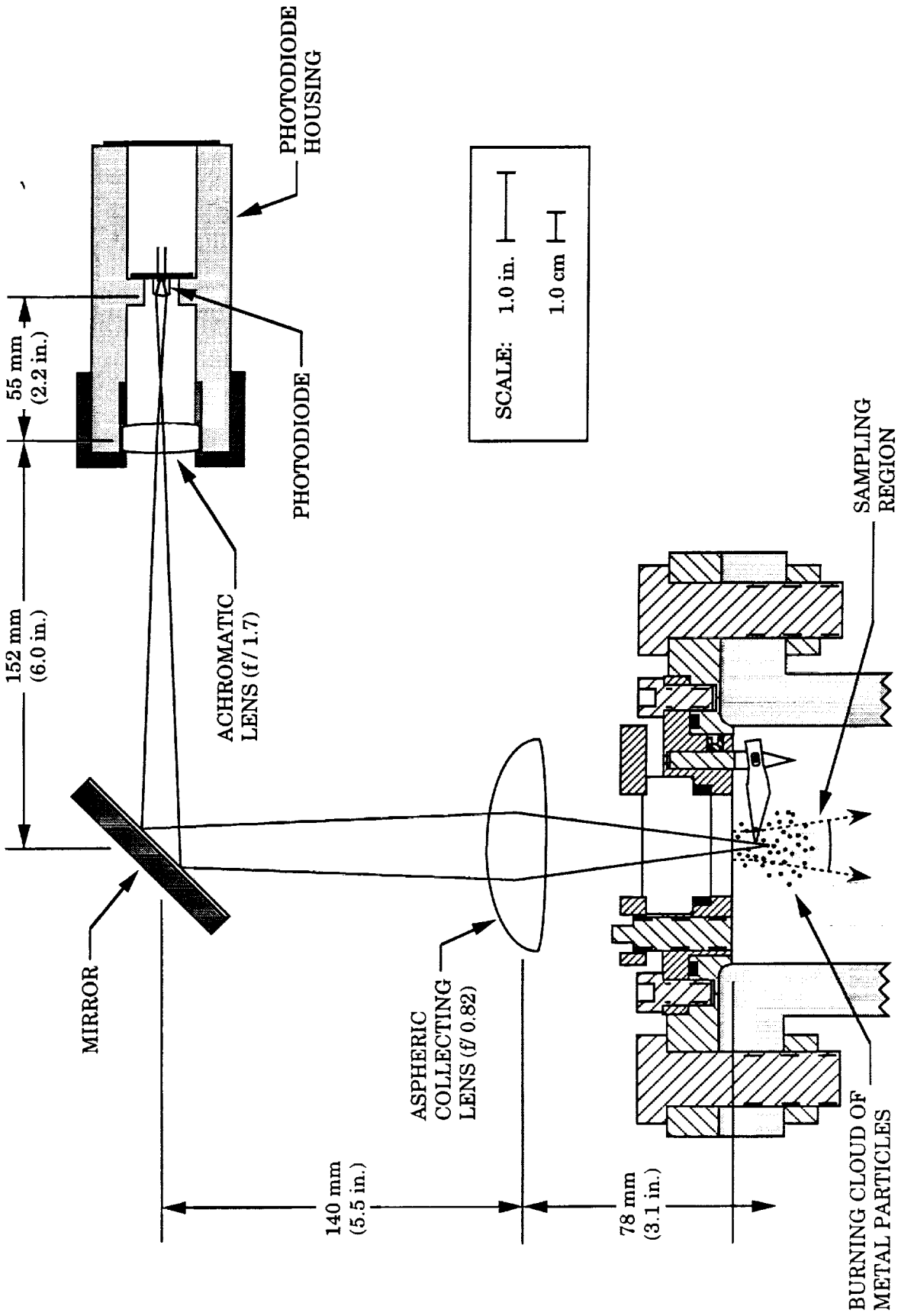

Fig. 2.56: Photodiode optical measurement system. Drawing is to the scale shown.

ignites. Theoretical calculations (refer to Chapter 3) indicate that the cloud will extend up to distances on the order of 25 mm from the endwall. The experimentally measured sampling region of the photodiode optical system is represented by the shaded area in Fig. 2.56. The sampling region is defined as the volume of space in which a particle can reside and still have a fraction of its emitted light detected by the photodiode system.

The boundary of the sampling volume is determined by placing a diffuse light source (made from a 60 watt light bulb placed behind a sheet of wax paper) on the optical axis and measuring the initial strength of the photodiode signal, V_0. The aperture of an iris diaphragm, located coincident with the diffuse source, is closed until the photodiode voltage drops to $0.95V_0$. This aperture diameter is then taken as the boundary of the sampling region. The measured boundary values of the sampling region are plotted in Fig. 2.57 as a function of axial distance from the shock tube endwall. Figure 2.57 also shows the corresponding measured photodiode voltage, V_0, normalized by the maximum value recorded.

At the surface of the endwall observation window, which is represented by the hatched area in Fig. 2.57, the sampling region has a radius of $r_s \cong 6$ mm (0.24 mm). Beyond x = 8 mm (0.32 in.), the radius of the sampling region slowly increases with increasing distance from the endwall. The photodiode voltage is maximum when the diffuse light source is located near the focal point of the collecting lense, $x_{f.l.} \cong -12$ mm (0.47 in.), which is outside of the endwall test section due to physical constraints. The measured photodiode voltage within the sampling region decreases linearly with distance from the surface of the window. As the light source is moved from the window surface to x = 25 mm (1 in.), the photodiode voltage decreases by approximately 25 percent.

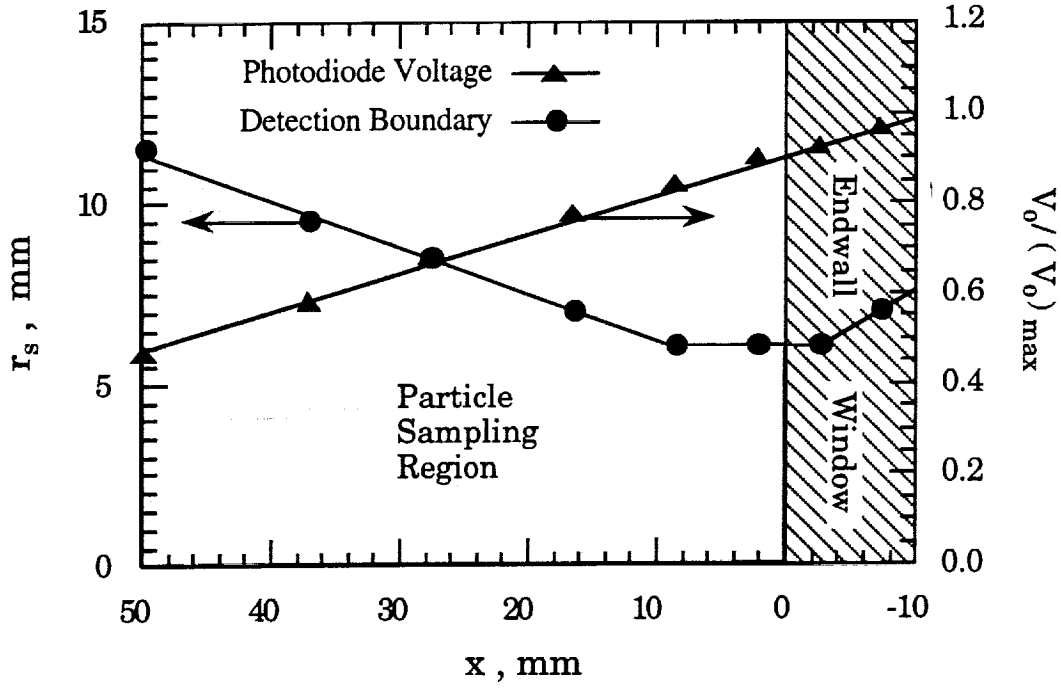

Fig. 2.57: Measured dimension and sensitivity of the optical sampling region of the photodiode detector. The hatched area represents space occupied by the endwall observation window.

The photodiode system consists of a Motorola MRD500 semiconductor photo detector and its associated circuitry. The light sensing surface of the MRD500 photo detector has an active area of 5 mm^2 and is encased in a convex glass lens. The photo detector has a quoted minimum sensitivity of 1.2 $\mu A/mW/cm^2$ and is sensitive throughout the visible and near infrared spectral range, as shown in Fig. 2.58. The peak response of the detector occurs at a wavelength of 0.8 μm.

The photodiode electrical circuit used to convert the photo detector's current into a suitable signal voltage is shown in Fig. 2.59. The reverse-bias photodiode is at +9 V. The photodiode produces a current that is proportional to the intensity of the light, $I_{h\nu}$, that strikes its surface. The recorded voltage, V_{rec}, is then produced by passing the photodiode current through the shunt resistor, R_s. The RC time constant, τ_{RC}, of the system is determined by the shunt

resistance and the capacitance of the electrical connections between the photodiode circuit and the digital recorder. The shunt resistance is R_s = 1 or 5 kΩ and the signal is carried to the digital recorder using 40 feet of standard 50 Ω coaxial cable that has a capacitance of 30 pf/ft. The resulting time constant is τ_{RC} = 1.2 μs and 6.0 μs for R_s = 1 and 5 kΩ, respectively. The majority of the measurements are made using R_s = 1 kΩ.

Prior to each experiment, the photodiode optical system is adjusted to maximize the signal obtained from a 0.5 in. (12.5 mm) diameter diffuse light source placed inside the shock tube near the endwall window. The aspheric collecting lens is mounted on a positioning stage which allows approximately one inch of axial travel relative to the shock tube endwall. After adjusting the optics, the collecting lens is retracted so that the endwall window port can be removed and the particles mounted. After replacing the window, the lens is returned to its previously adjusted position. The photodiode optical system is visible in the foreground of the photograph shown in Fig. 2.1. The box lying near the photodiode mount contains the electrical circuit for the photodiode detector.

Figures 2.60 through 2.63 show typical photodiode signals recorded for each of the 20-25 μm sieved alloy powders. The signals were recorded for oxygen conditions of $T_5 \cong 2220$ K and $p_5 \cong 34$ atm. The shock wave reflects from the endwall at time t = 0 in each case. The small oscillations and spikes in the light signals, which are typical of signals recorded for oxygen temperatures below 2500 K, can introduce uncertainties of ~30 μs in the ignition delay and combustion times. As the oxygen temperature is increased, the magnitude of these oscillations decrease substantially.

At lower oxygen temperatures, T < 2500 K, measurements are generally repeated two or three times to minimize the uncertainty. At higher oxygen temperatures, T > 2500 K, a single measurement is generally sufficient for alloy

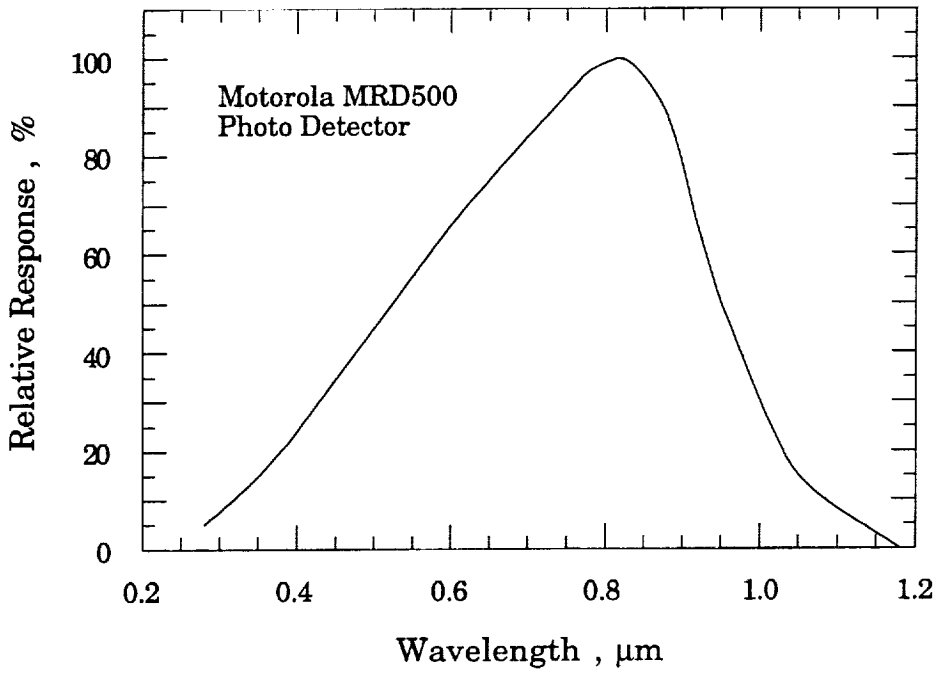

Fig. 2.58: Relative spectral response of the photodiode detector. Data provided by Motorola, Inc. for the MRD500 photo detector.

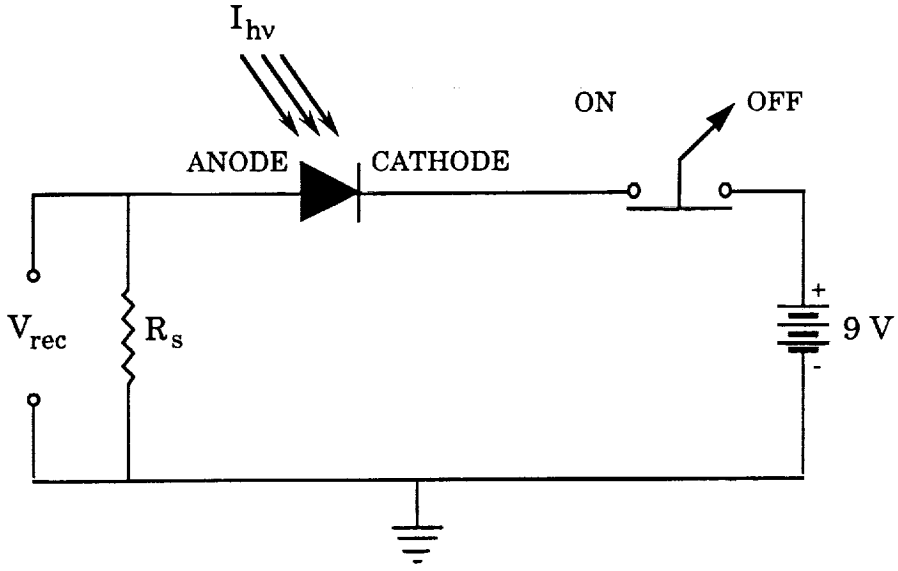

Fig. 2.59: Reverse-bias photodiode circuit. The circuit produces a suitable signal voltage from the current emitted by the photodiode detector.

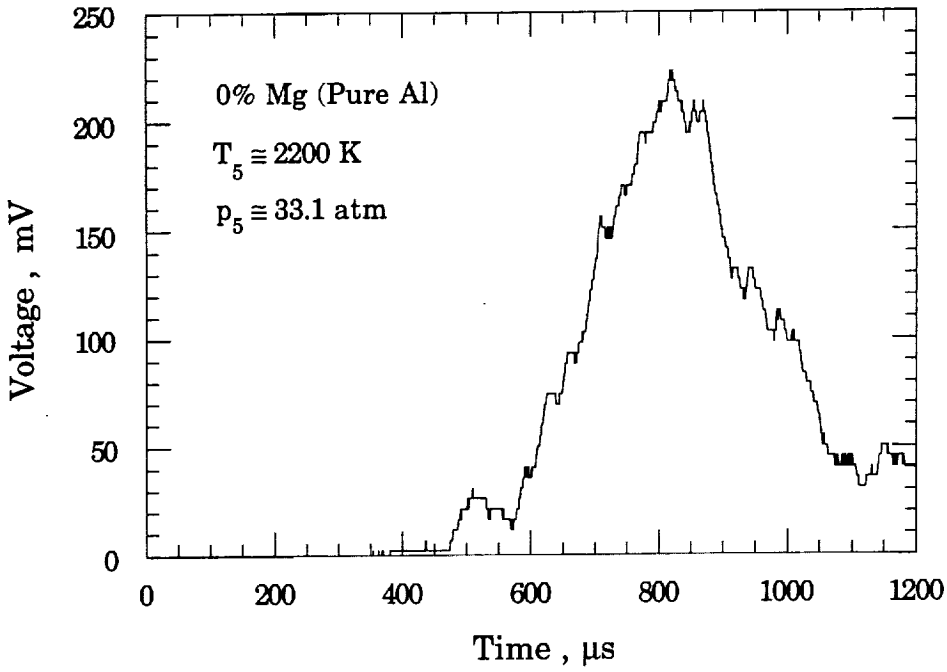

(a)

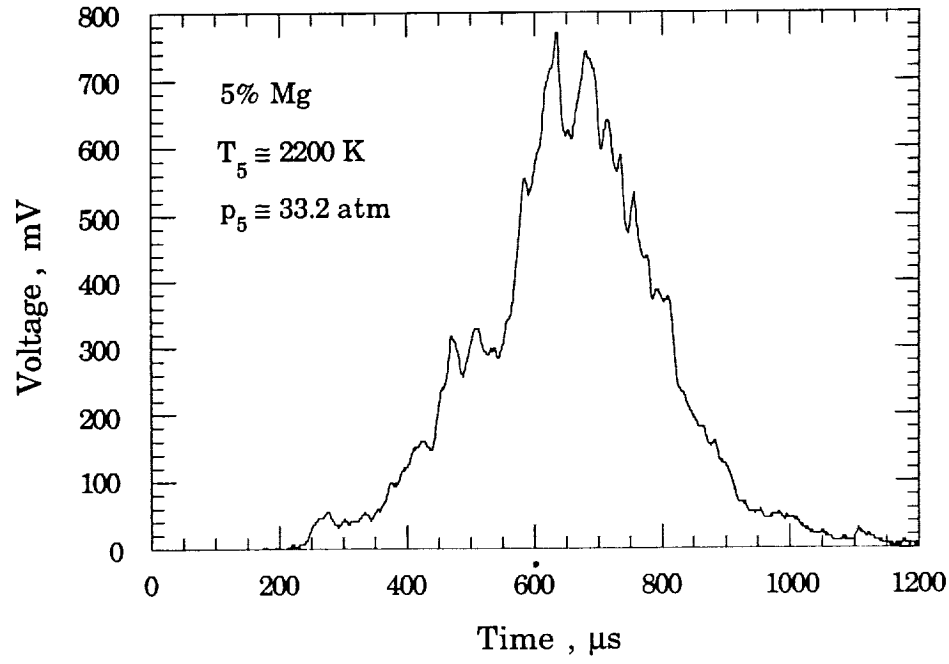

(b)

Fig. 2.60: Typical recorded light signals for 20-25 μm diameter 0% Mg (pure Al) and 5% Mg alloy particles. a) Pure Al. b) 5% Mg.

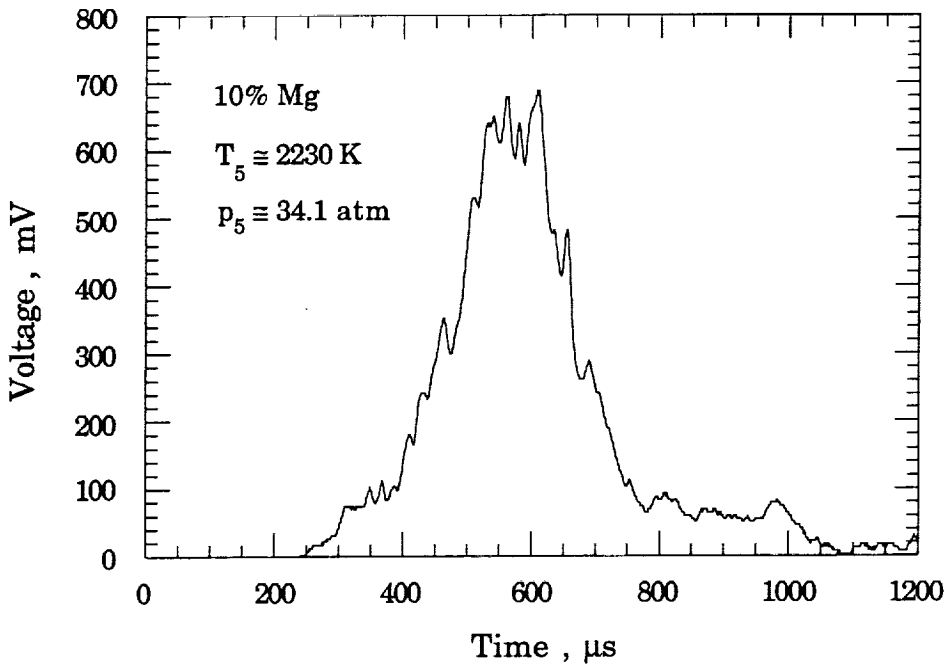

(a)

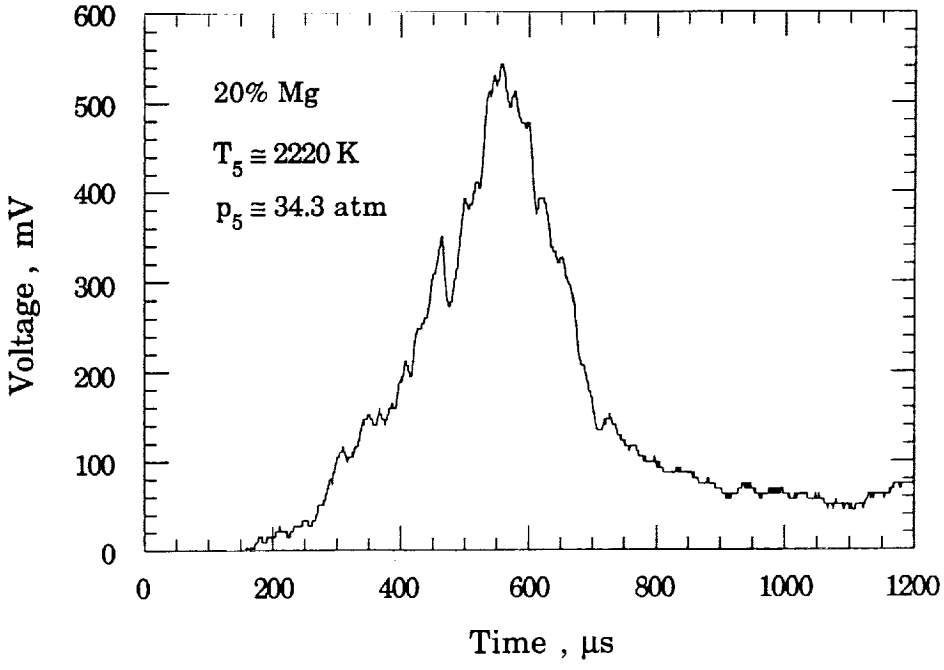

(b)

Fig. 2.61: Typical recorded light signals for 20-25 μm diameter 10% Mg and 20% Mg alloy particles. a) 10% Mg. b) 20% Mg.

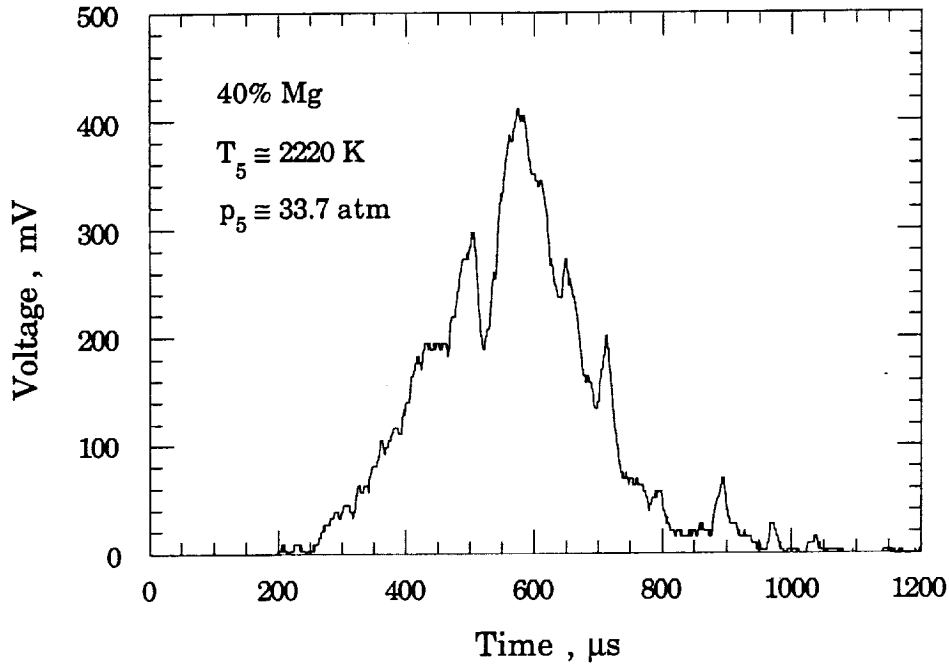

(a)

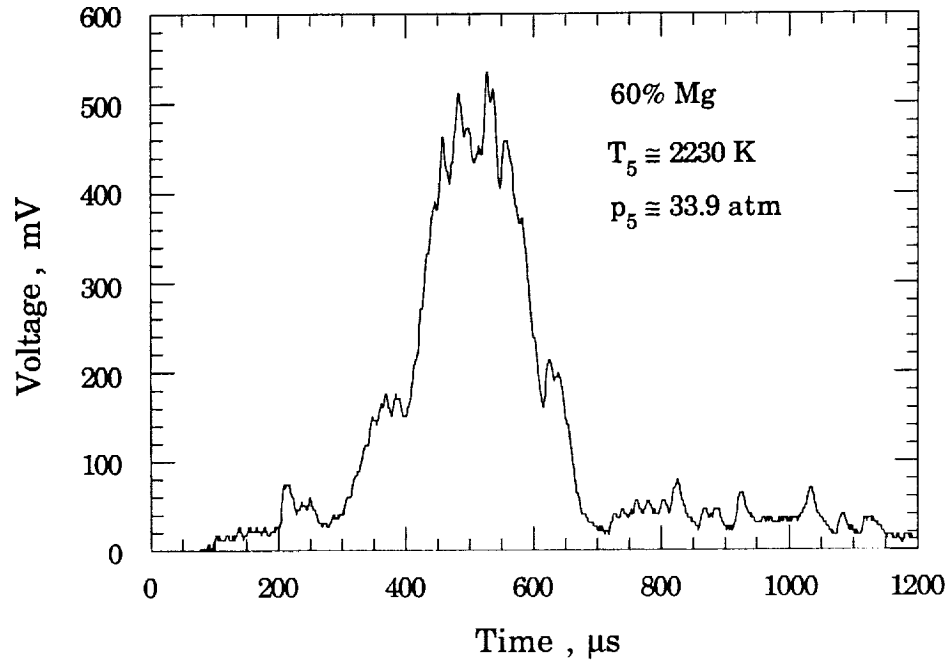

(b)

Fig. 2.62: Typical recorded light signals for 20-25 μm diameter 40% Mg and 60% Mg alloy particles. a) 40% Mg. b) 60% Mg.

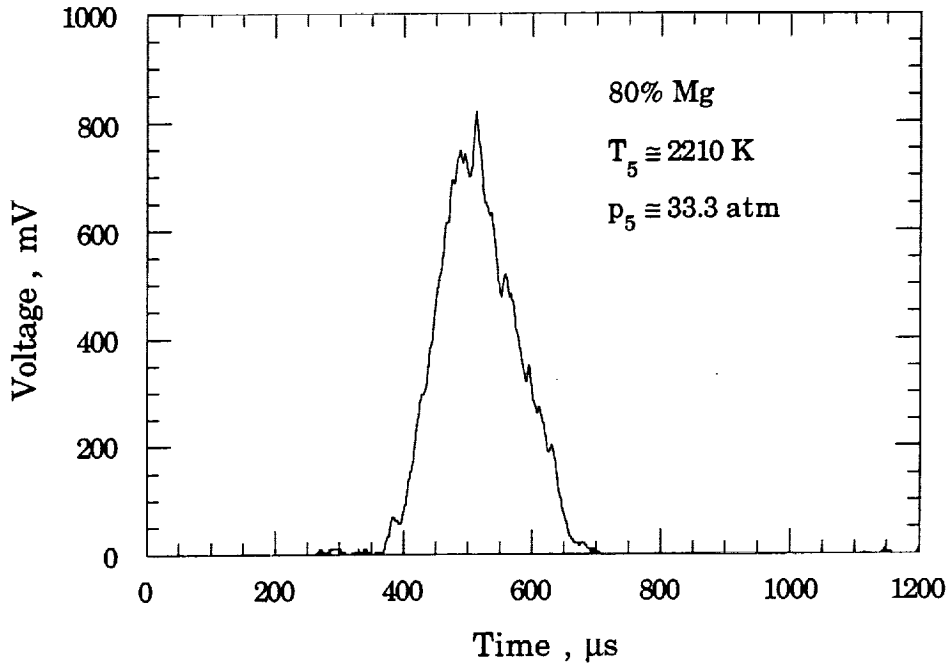

(a)

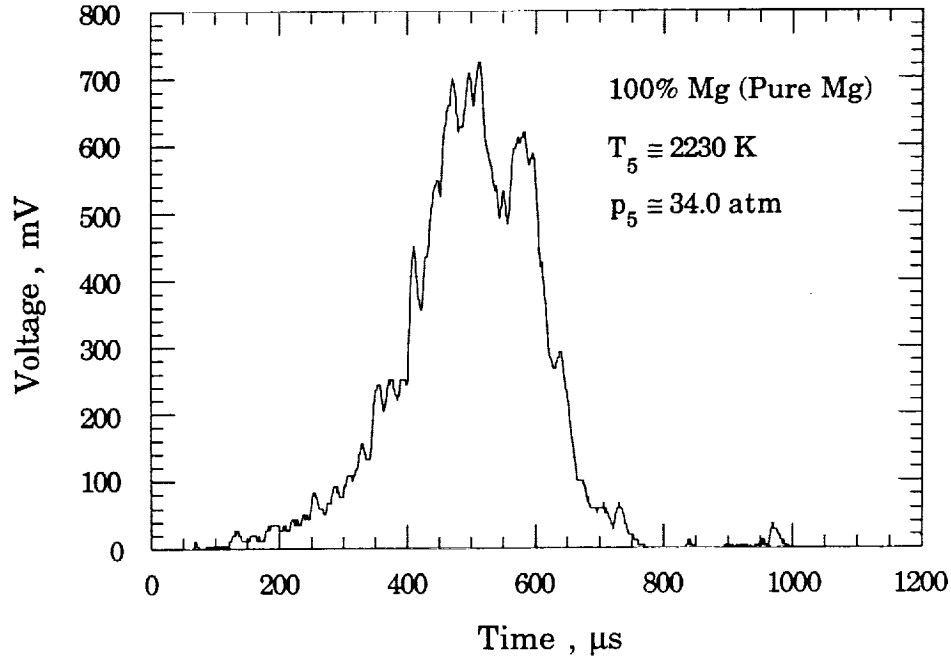

(b)

Fig. 2.63: Typical recorded light signals for 20-25 μm diameter 80% Mg and 100% Mg alloy particles. a) 80% Mg. b) 100% (pure) Mg.

compositions other than pure Al. Examination of the light signals clearly show that the particle ignition delay time decreases with increasing Mg content, as discussed extensively in Chapter 4. The peak voltage of the measured light signals are found to vary as a function of alloy content. For the series of measurements presented in Fig. 2.59 to 2.63, the peak voltage varies from a minimum of ~225 mV for pure Al particles to a maximum of ~ 850 mV for 80% Mg particles.

To corroborate the photodiode measurements and verify the knife blade mounting technique, a Cordin 350 high-speed drum camera is used to photograph the burning clouds of particles near the shock tube endwall in a limited number of experiments. Figure 2.64 shows the optical arrangement used to photograph the particle cloud. The light emitted by the burning particles is collected by the aspheric lens and turned 90 degrees by the mirror. The light then intersects a beam splitter that transmits 75% of the light to the photographic optics and reflects the rest to the photodiode system for measurement.

The Cordin 350 drum camera operates at speeds as high as 35,000 frames/sec. The camera places 224 frames, 7.4 x 10.7 mm (0.29 x 0.42 in.), on a 86.1 cm (33.88 in.) length of standard 35 mm film. The photographic optical system consisted of an achromatic 30 mm (1.18 in.) diameter lens and an 18 - 180 mm zoom lens mounted on a 43 mm (1.7 in.) extension tube. The photographic optics are set by placing a luminous image at the desired focal plane in the shock tube, then the lens positions are adjusted until a focussed image appears in the camera's viewfinder. The known image size is then used to calculate the dimension of the camera's field of view.

The high speed photographs are taken in the following manner. The shock tube is prepared for firing, the camera is loaded with film, then the entire

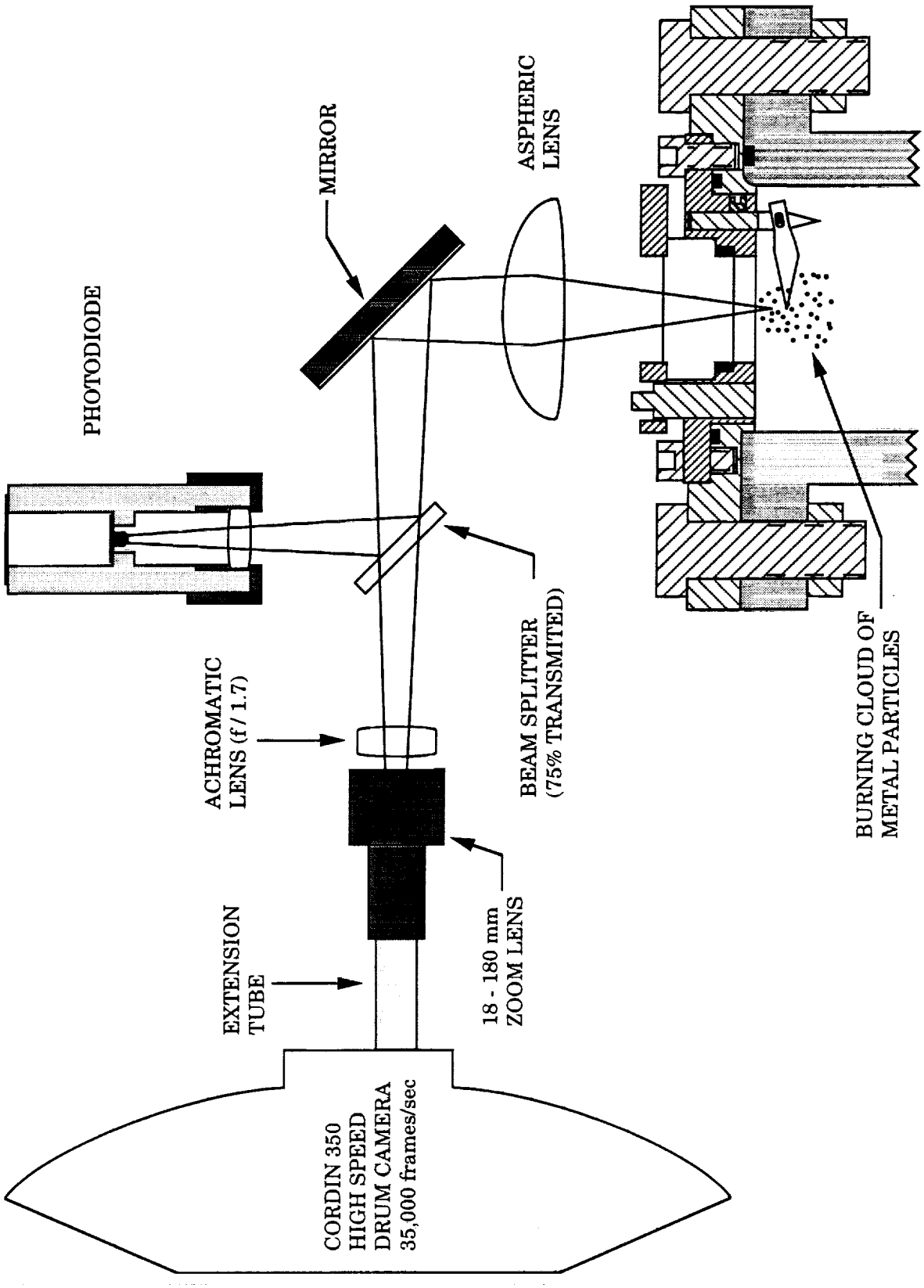

Fig. 2.64: Optical system used to photograph the burning cloud of metal particles.

camera and shock tube endwall are enclosed in a light-proof canopy. The camera is brought up to the desired speed, typically 20,000 frames/sec, and the shutter is opened. The self-luminosity of the burning particle clouds produce an image on the exposed film. Since the camera continues to run throughout the experiment, accidental multiple exposures can occur if burning diaphragm fragments enter the image plane of the photographic system.

Five photographs taken of burning alloy powder are presented in Fig. 2.65 along with the corresponding recorded light signal. The experiment conditions for these results are: 20% Mg, d_{eff} = 21.2 μm, T_5 = 2860 K, p_5 = 17.6 atm, x_{kb} = 8 mm. The camera speed is 20,000 frames/sec, so that the time between photographs is 50 μs. The focal plane of the photographic system is located approximately 4 mm (0.16 in.) from the endwall and the field of the view is approximately 13 x 9 mm (0.51 x 0.35 in.). The relatively weak photodiode signal is due to the presence of the beam splitter.

The exact time at which the photographs are taken is not known, since there is no attempt to synchronize the photography with the reflection of the shock wave. For purposes of comparison, the temporal location of the photographic record is chosen so that its peak intensity is coincident with that of the recorded light signal.

The burning particle cloud appears in the photographs as a collection of nebulous images which grow in number and brightness to the maximum shown in the center photograph. After reaching a peak, the number and brightness of these images clearly decrease in the subsequent frames. The rise and fall in the image brightness correlates well with the rise and fall of the photodiode signal. The diameter of the particle cloud is on the order of the width of the field of view, which is 13 mm. If it is assumed that the particle cloud is spherical, the photographs indicate that the knife blade mounting technique

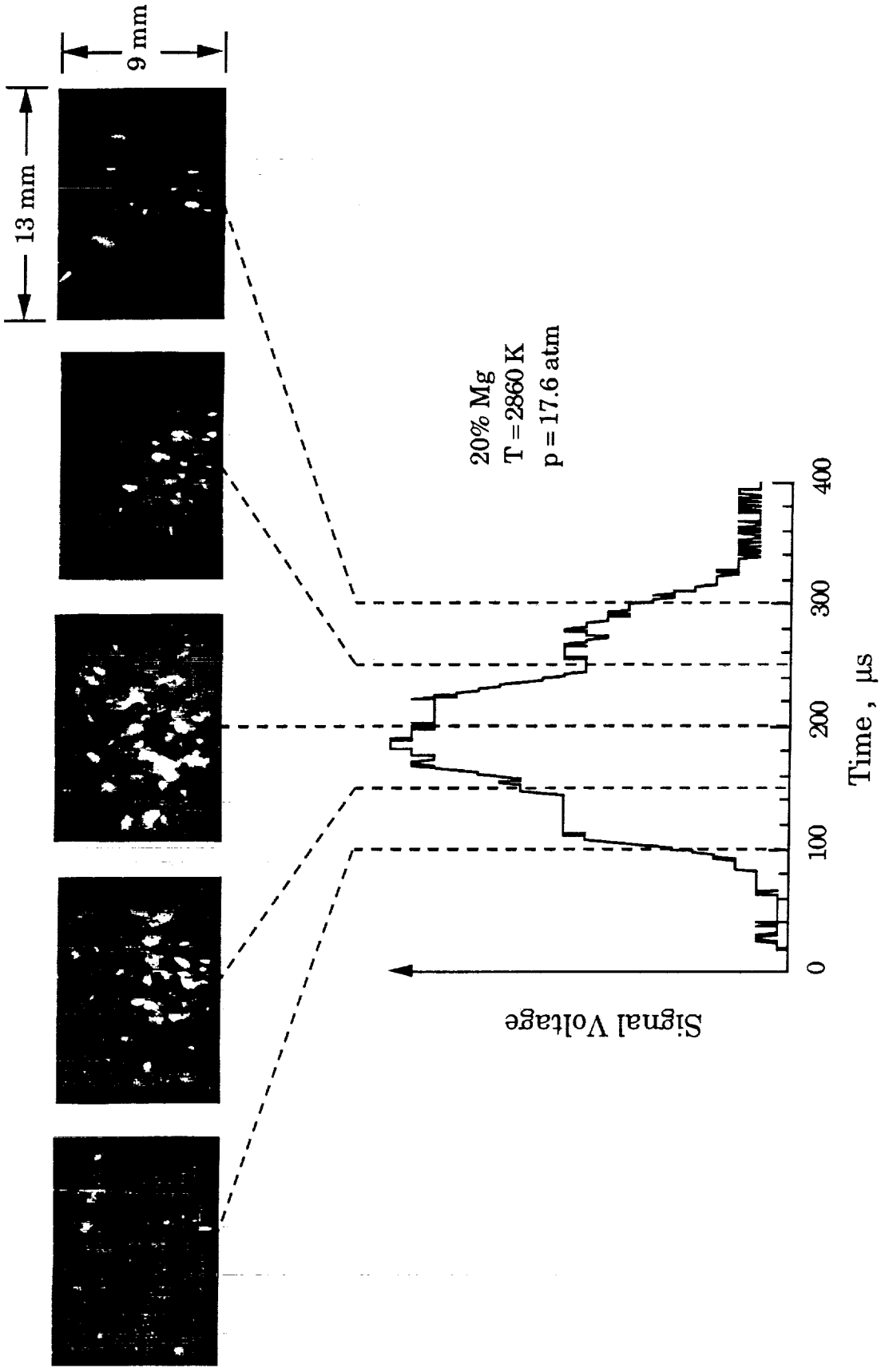

Fig. 2.65: Comparison of metal powder combustion recorded photographically and electronically.

disperses the particles over an approximately 1200 mm^3 volume of space. Assuming the cloud is composed of 10,000 particles, the calculated particle separation distance is on the order of 0.5 mm. Therefore, significant particle-particle interactions are unlikely.

CHAPTER 3: PARTICLE IGNITION MODEL

The ignition of Al/Mg alloy particles suddenly introduced into a high temperature oxidizer is a complicated process involving several modes of energy transfer and production, and the physical characteristics of the metal particles and their protective oxide films [12,22,42]. The accuracy of an ignition model depends upon the correct specification of the time-dependent rate of heat transfer from the oxidizing atmosphere to the particle's surface. The dominant mode of heat transfer in the experimental technique employed here is due to convection, thus the particle's kinematics must be accurately modeled. Particle self heating, due to the presence of heterogeneous surface reactions, must also be modeled in an appropriate manner [61].

In the sections that follow, a convective heat transfer analysis is developed that parallels the analytic approach of Fox et al. [34]. The particle energy balance and one-dimensional kinematic equations are developed. The variable material properties of the alloy particles are approximated using the published data for pure Al and Mg, and the variable nature of their protective oxide films is investigated analytically.

3.1 PARTICLE ENERGY BALANCE

The general heating problem of an initially cold (room temperature) Al/Mg alloy particle moving through high temperature oxygen is shown schematically in Fig. 3.1. The particle temperature increases with time due to the combined effects of convective heat transfer, $\dot{q}_c$, and heat produced on the surface of the particle by heterogeneous reactions, $\dot{q}_r$. As the particle temperature rises, energy is lost through radiative transfer, $\dot{q}_{rad}$, as well as

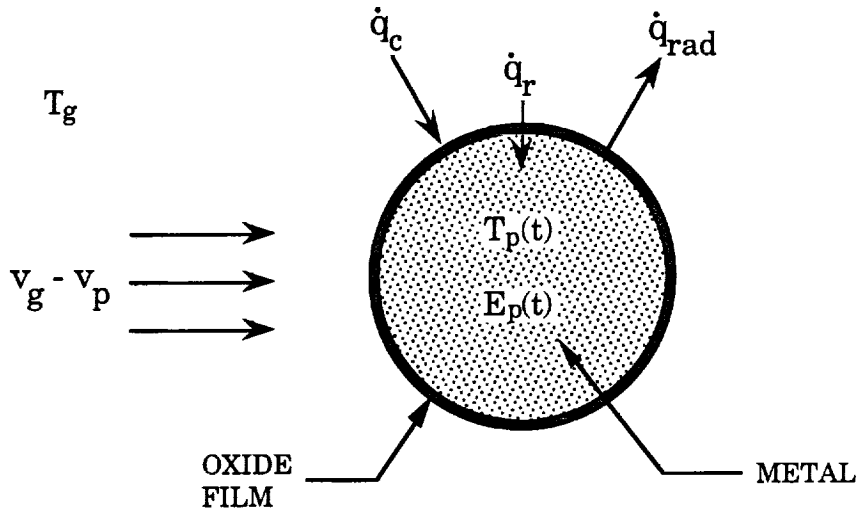

Fig. 3.1: Energy transport processes associated with the ignition of a spherical metal particle.

convective heat transfer if the particle's temperature rises above that of the oxygen due to heterogeneous reactions.

The transient particle heating problem can be substantially simplified by using a so-called "lumped capacitance solution" method [62]. The lumped capacitance method assumes that the temperature in a solid particle immersed in a liquid or gaseous medium is spatially uniform throughout the transient process. Since this assumption implies that there are no temperature gradients within the solid, the transient heating problem is formulated by considering an overall particle energy balance [62].

Before proceeding with the formulation of the particle energy equation, the validity of the lumped capacitance method for the case of Al/Mg alloy particles introduced into high temperature oxygen is assessed. The error associated with the lumped capacitance method is small if the following condition is satisfied [62]:

$$Bi \equiv \frac{\bar{h} L_c}{k_p} \leq 0.1 \tag{3.1}$$

where Bi is the Biot number, $\bar{h}$ the surface-averaged convective heat transfer coefficient, L_c the characteristic length, and k_p the particle thermal conductivity. The Biot number provides a measure of the temperature drop in the solid particle relative to the difference between the particle surface temperature and the oxygen temperature.

For spherical particles, the characteristic length is simply [62]:

$$L_c \equiv \frac{V_p}{A_s} = \frac{r_p}{3} \tag{3.2}$$

where V_p is the particle volume and A_s is the surface area. Expressing $\bar{h}$ in terms of the surface-averaged Nusselt number, $Nu_p \equiv 2\, r_p \bar{h} / k_g$, and substituting Eq. (3.2) into Eq. (3.1) yields the following relation for the Biot number:

$$Bi = \frac{1}{k_p}\left(\frac{Nu_p\, k_g}{2\, r_p}\right)\left(\frac{r_p}{3}\right) = \frac{Nu_p}{6}\left(\frac{k_g}{k_p}\right) \tag{3.3}$$

Equation (3.3) provides a simple relation for the Biot number in terms of the known particle and gas thermal conductivities and the surface-averaged Nusselt number.

For the experimental conditions investigated, the highest oxygen thermal conductivity is approximately 0.38 W/m-K (refer to Fig. 4.7) and the lowest particle thermal conductivity is approximately 80 W/m-K corresponding to liquid Mg at 923 K [63]. Therefore, the upper bound on the Biot number can be expressed as:

$$(Bi)_{max} \approx 8 \times 10^{-4}\, Nu_p \tag{3.4}$$

Noting that, for the experimental conditions of interest, the magnitude of the calculated surface-averaged Nusselt number is always less than 10

(see Fig. 3.21), Eq. (3.4) indicates that $(Bi)_{max} < 8 \times 10^{-3}$. This clearly satisfies the condition of Eq. (3.1) and indicates that the lumped capacitance method should be quite accurate under the experimental conditions of interest.

Using the lumped capacitance assumption, the particle energy equation is:

$$\frac{dE_p}{dt} = \dot{q}_c + \dot{q}_r - \dot{q}_{rad} \tag{3.5}$$

where E_p is the particle internal energy. The left-hand side of Eq. (3.5) is simply the rate of change of internal energy of the particle and is equated to the rate of energy transferred to the particle by convective heat transfer, the energy produced by particle surface reactions, and the amount of energy radiated to the surroundings. All of these energy transfer mechanisms must be accurately modeled if the particle ignition delay time is to be predicted.

A more detailed form of Eq. (3.5) is:

$$\rho_p V_p c \frac{dT_p}{dt} = -\bar{h} A_s \left(T_p - T_g\right) + A_s q_r k_s - A_s \varepsilon_p \sigma \left(T_p^4 - T_b^4\right) \tag{3.6}$$

where V_p is the particle volume, c the particle specific heat, A_s the particle surface area, q_r the alloy heat of reaction, k_s the heterogeneous reaction rate, ε_p the particle emissivity, σ the Stefan-Boltzmann constant, and T_b is the blackbody temperature of the surroundings. Equation (3.6) implicitly assumes the particle has constant density, volume, and surface area.

Assuming a spherical particle geometry and noting that $\bar{h} = Nu_p k_g / 2 r_p$, Eq. (3.6) can be rewritten as:

$$\frac{dT_p}{dt} = -\frac{3}{2} \frac{k_g}{\rho_p c r_p^2} (Nu_p)(T_p - T_g) + \frac{3}{\rho_p c r_p} \left[q_r k_s - \varepsilon_p \sigma \left(T_p^4 - T_b^4\right)\right] \tag{3.7}$$

Equation (3.7) is a first order, nonlinear, ordinary differential equation governing the time variation of the particle temperature. In order to solve Eq. (3.7), it is first necessary to specify the Nusselt number, Nu_p, the heterogeneous reaction rate, k_s, and the particle surface emissivity, ε_p. In addition, the temperature-dependent particle specific heat, c, and the remaining particle and gas properties must also be specified. Due to the nonlinear nature of Eq. (3.7), it is not possible to obtain an analytical solution without imposing restrictive conditions.

An analytical solution for the ignition delay time of a spherical particle can be obtained from Eq. (3.7) if the following assumptions are made:

1) Particle properties are constant.
2) Gas properties are constant.
3) Relative gas velocity is negligible, yielding $Nu_p = 2 = \text{constant}$.
4) Heterogeneous reactions are negligible.
5) Radiative losses are negligible.
6) Particle ignites at a definite ignition temperature, T_{ign}.

Under these assumptions, Eq. (3.7) reduces to:

$$\frac{dT_p}{dt} = -\frac{12\,k_g}{\rho_p\,c\,d_p^2}\left(T_p - T_g\right) \tag{3.8}$$

where the fact that $d_p = 2r_p$ has been used. Equation (3.8) can be rearranged and easily integrated to yield the following expression for the time required to heat a particle from an initial temperature, T_o, to the ignition temperature, T_{ign}:

$$t_{heat} = \frac{\rho_p\,c\,d_p^2}{12\,k_g}\,\ln\left[\frac{T_g - T_o}{T_g - T_{ign}}\right] \tag{3.9}$$

The time required for a solid particle to melt, t_{melt}, can be calculated by dividing the energy required to melt the particle by the rate at which energy is transferred convectively to the particle at the particle melting temperature, T_{mp}:

$$t_{melt} = \frac{m_p L_f}{\dot{q}_c} = \frac{\rho_p d_p^2}{12 k_g} \frac{L_f}{(T_g - T_{mp})} \tag{3.10}$$

where m_p and L_f are the particle mass and enthalpy of fusion, respectively. Summing Eqs. (3.9) and (3.10) yields the classical solution for the ignition delay time of a particle suddenly introduced into a quiescent, high-temperature gas [16]:

$$t_{ign} = \frac{\rho_p d_p^2}{12 k_g} \left[c \ln\left(\frac{T_g - T_o}{T_g - T_{ign}}\right) + \frac{L_f}{T_g - T_{mp}} \right] \tag{3.11}$$

Friedman and Macek have verified the general validity of Eq. (3.11) for predicting the ignition delay time of aluminum particles introduced into the combustion products of a propane/oxygen flame, if the initial convective heat transfer is handled properly [16]. Examination of Eq. (3.11) shows that the particle ignition delay time is proportional to the square of the particle diameter. Since Eq. (3.11) neglects the contribution of heterogeneous reactions to particle heating, the analysis of experimentally measured ignition delay times generally result in an apparent Al ignition temperature below 2300 K, the melting point of Al_2O_3 [16,28].

The measured particle ignition delay times of this investigation indicate that substantial particle self-heating occurs, particularly at lower gas temperatures. In addition, the knife blade particle mounting technique results in a considerable relative velocity between the gas and the particles, which leads

to substantial convective heat transfer. Based on these facts, a more complete numerical solution of Eq. (3.7) is developed and incorporates the following:

1) A one-dimensional model of the particle motion is used to predict the time-dependent particle velocity. The particle drag coefficient is calculated from an empirical relation developed specifically for small diameter particles [64].

2) To account for rarefaction of the oxygen, the surface-averaged Nusselt number is calculated from an empirical relation that is valid for continuum, slip, and a portion of the transition flow regime [34].

3) The particle's heterogeneous surface reactions are modeled using an Arrhenius type relation.

4) Radiation losses are modeled by treating the particle as a diffuse emitter with a constant emissivity, $\varepsilon_p < 1$.

5) The oxygen is treated as a variable property gas, the values of which are calulated using the NASA Gordon-McBride code [9].

6) Detailed temperature and pressure-dependent particle properties are employed.

The particle energy equation is solved simultaneously with the particle equation of motion, which provides the information needed to calculate the time-dependent convective heat transfer. The ignition delay time is defined as the time required to raise the particle temperature to the point at which the slow heterogeneous surface reactions transition to the fast detached gas-phase combustion regime.

The remaining sections of this chapter discuss in detail the development and implementation of the full kinematic ignition model. The known variable

thermophysical properties of pure Al and Mg are presented and are used to calculate, or approximate, those of the Al/Mg alloys.

3.2 MODEL OF PARTICLE KINEMATICS

A one-dimensional kinematic analysis is used to determine the motion of the spherical particles. The developed model must properly treat the initial acceleration of the particles in the supersonic gas flow induced by the incident shock wave, the continual deceleration of the particles in the quiescent gas created by the reflected shock wave, and the reflection of the particles from the endwall observation window (see Fig. 2.3). This kinematic model closely parallels that developed by Fox et al. [34] in their study of the ignition of Mg particles in the flow induced by an incident shock wave.

The motion of each particle is treated individually by writing the one-dimensional form of Newton's 2nd law of motion for a single particle mass:

$$\frac{d}{dt}(m_p v_p) = \Sigma F \tag{3.12}$$

The only external forces acting on the particle are those due to flow drag and gravity. The ratio of the drag force to the gravity force acting on the particle is given by $F_D / Fg_o \sim \rho_g |v_p - v_g|^2 / (g_o \rho_p d_p)$, where g_o is the accelertion due to gravity. For the conditions of this experiment, $F_D / Fg_o >> 1$, indicating that gravity effects can be neglected. Therefore, Eq. (3.12) can be written as:

$$m_p \frac{dv_p}{dt} = \frac{1}{2} \rho_g S_p C_D |v_g - v_p| (v_g - v_p) \tag{3.13}$$

where the mass of the particle is assumed constant and ρ_g is the gas density, S_p the frontal area of the particle, and C_D is the particle drag coefficient. Noting that for spherical particles $S_p = \pi r_p^2$ and $m_p = \rho_p (4\pi r_p^3 / 3)$, the working form of particle equation of motion is:

$$\frac{dv_p}{dt} = \frac{3}{8}\frac{\rho_g}{\rho_p}\frac{C_D}{r_p}|v_g - v_p|(v_g - v_p) \tag{3.14}$$

The corresponding equation governing the position of the particle is simply given by:

$$\frac{dx_p}{dt} = v_p \tag{3.15}$$

where x is the spatial coordinate.

The accuracy with which Eqs. (3.14) and (3.15) predict the motion of the particle is a strong function of the drag coefficient, C_D. Since Eq. (3.14) is to be solved numerically (see Appendix C), it is a simple matter to include a variable C_D that is a function of both the particle Reynolds and Mach numbers. The published empirical relations of Walsh [64], developed to accurately predict the velocity lag of small spherical particles used in LDV measurements, are employed here. The sphere drag coefficient is represented by the following set of relations [64]:

$$C_D = C_{D,C} + (C_{D,FM} - C_{D,C})\, e^{-A\, Re_p^N} \qquad Mp \geq 0.1 \tag{3.16}$$

$$C_D = \left(\frac{24}{Re_p}\right)\left(1 + 0.15\, Re_p^{.687}\right) \qquad Mp < 0.1 \tag{3.17}$$

where $Re_p = 2\rho_g |v_g - v_p| r_p/\mu_g$ is the particle Reynolds number, $M_p = |v_g - v_p| a_g$ is the particle Mach number, and $C_{D,C}$, $C_{D,FM}$, A, and N are constants which are tabulated [64] as a function of M_p for $0.1 < M_p \leq 2.0$.

Equation (3.16) defines the compressible drag coefficient and was empirically determined by Walsh [64] from the experimental data of Bailey and Hiat [65] and Zarin [66], for particle Reynolds numbers ranging from $Re_p = 20$ to 200. While the particle is exposed to the high-speed flow induced by the incident

shock wave, the calculated particle Reynolds numbers of this experiment are near Re_p = 350 (see Fig. 3.21b). Although this Reynolds number is beyond the range of data to which Eq. (3.16) was fit, the drag coefficients predicted by Eq. (3.16) for Re_p's as high as 400 are found to agree well with the data of Bailey and Hiat [65]. Equation (3.17) defines the incompressible drag coefficient and the relation is valid for $Re_p \leq 200$, which is always satisfied when $M_p < 0.1$ for the small diameter particles of interest.

The empirical drag coefficients represented by Eqs. (3.16) and (3.17) are shown graphically in Fig. (3.2). C_D is plotted versus particle Reynolds number for various values of particle Mach number. For $0.5 \leq M_p \leq 2.0$ and $20 \leq Re_p \leq 400$, the particle drag coefficient is only mildly dependent upon Re_p and M_p.

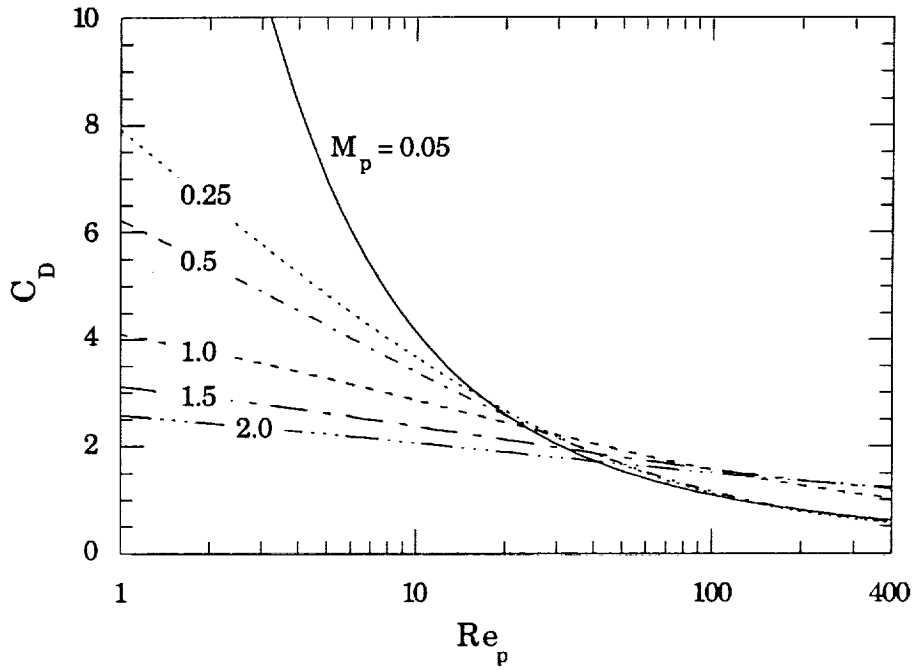

Fig. 3.2: Spherical drag coefficient as a function of Re_p and M_p. The curves are calcualted using the empirical relations published by Walsh [64].

The particle kinematic equations, Eqs. (3.14) and (3.15), assume that the gas flow is steady and there are no particle-particle interactions. In general, these assumptions are satisfied. However, during the initial acceleration of the particles in the supersonic flow induced by the incident shock wave, the particles are expected to experience multi-dimensional, time-dependent flow effects associated with the knife blade on which they are initially mounted. These non-ideal flow conditions are shown schematically in Fig. 3.3 and will slightly reduce the final velocity to which the particles are accelerated.

As indicated in Fig. 3.3, the flow Mach number in region 2 ranges between 1.6 and 2.0 for the experiment conditions of interest. As a result, weak oblique shock waves are attached to the leading edge of the knife blade. As the flow passes through the oblique shock wave, its properties are altered to those denoted as region 2', i.e. T, p, and ρ increase, while u and M decrease. As the flow passes the knife blade shoulder, a Prandtl-Meyer expansion fan alters the flow properies to those designated as region 2". Using simple shock-expansion theory [67], it can easily be shown that, for the knife blade half angle of 9.5°, the flow properties in region 2" are essentially identical to those of the undisturbed flow in region 2. In addition, it can be shown that the dynamic pressure, $(1/2)\rho_g v_g^2$, does not significantly vary through regions 2, 2', and 2", indicating that the drag exerted on a stationary particle in each region will remain nearly constant.

The wake region following the knife blade is a result of the knife blade's backward-step trailing edge. The wake is a complicated structure resulting from trailing edge oblique shock waves, the knife blade boundary layer, and the slip layer caused by the low velocity flow of the recirculation zone. The momentum decrement associated with the wake region is not easily calculated. In practice, only a small fraction of the particles, those initially mounted near

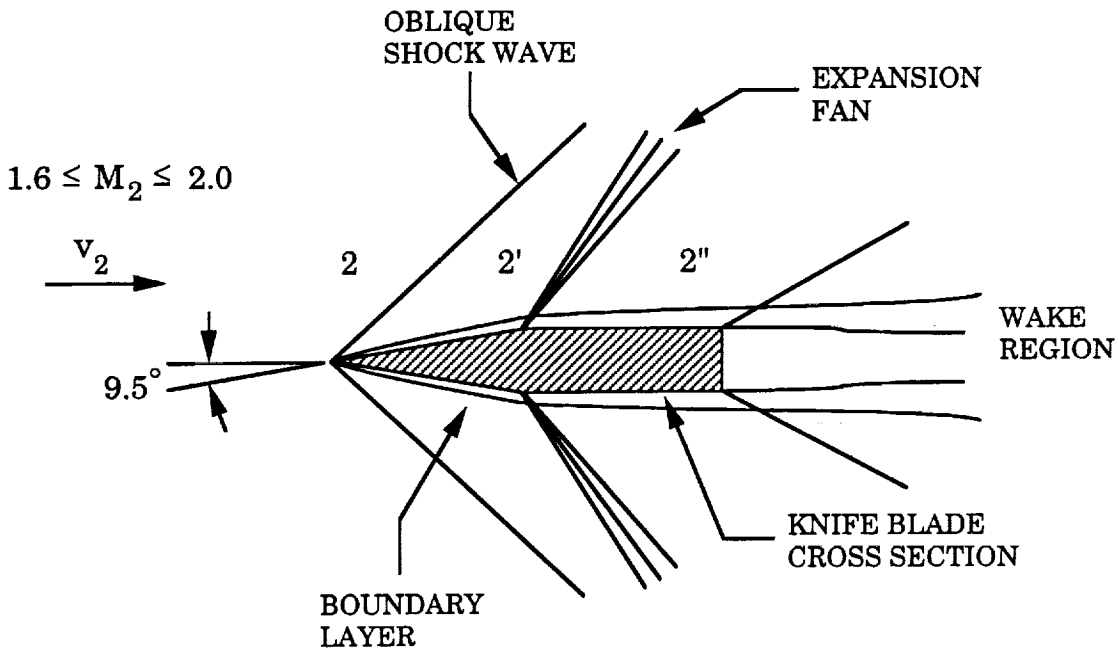

Fig. 3.3: Schematic of multi-dimensional flow effects associated with the knife blade when exposed to the supersonic flow induced by the indicent shock wave.

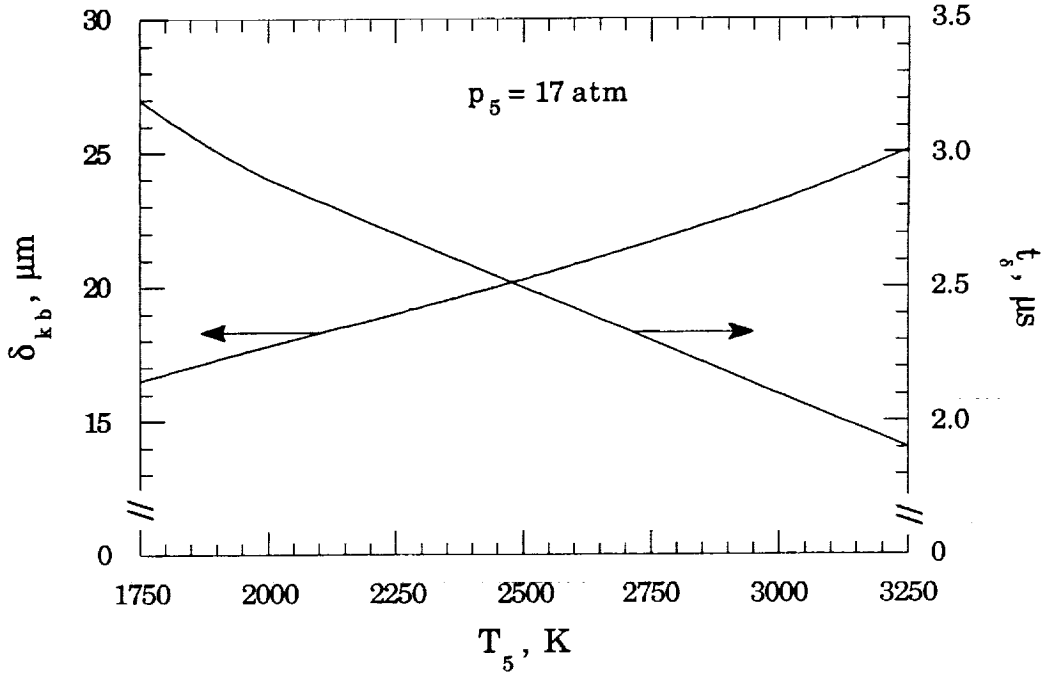

Fig. 3.4: Calculated maximum knife blade boundary layer displacement thickness and formation time versus reflected gas temperature.

the knife blade's trailing edge, will ever enter the wake region. This is because the knife blade flowfield will exist for only several μs during the time between the passage of the incident and reflected shock waves. Although the flow will impart a large velocity to the particles, they are initially stationary and are calculated to translate approximately 1 mm during the acceleration period (see Fig. 3.18), which is approximately equal to the width of the knife blade near its tip.

The final flow phenomenon associated with the knife blade is its boundary layer. As shown in Fig. 3.3, the boundary layer thickness grows from zero at the leading edge to a maximum at the trailing edge. If the boundary layer thickness is substantially larger than the diameter of the metal alloy particles, the particles may not be accelerated by the gas flow. The importance of the boundary layer can be assessed by estimating the associated displacement thickness. It is shown in Schlichting [68] that the steady state displacement thickness along a flat plate is given by:

$$\delta \cong 1.72 \sqrt{\frac{\mu x_\delta}{\rho U_\infty}} \tag{3.18}$$

and the time for it to form is given by:

$$t_\delta \cong 1.56 \frac{x_\delta}{U_\infty} \tag{3.19}$$

where x_δ is the distance from the leading edge of the plate, and ρ, μ, and U_∞ are the gas density, viscosity, and free stream velocity, respectively.

Shown in Fig. 3.4 are the maximum knife blade displacement thickness and formation time plotted as a function of the reflected shock temperature, T_5. The results are calculated using Eqs. (3.18) and (3.19) and assume that x_δ = 2 mm (knife blade trailing edge) and ρ, μ, and U_∞ are equal to their free stream values in region 2. The calculations show that the maximum

displacement thickness grows from 16 μm at 1750 K to 25 μm at 3250 K, which is comparable to the typical particle diameter of ~20 μm. The boundary layer at the trailing edge (x_δ = 2 mm) is estimated to reach steady state in a time of 3.2 μs and 1.9 μs for T_5 = 1750 K and 3250 K, respectively. The time required for the steady state boundary layer to form is significantly less than the corresponding shock transit times of approximately 20 μs and 16 μs, respectively.

The multi-dimensional flow effects discussed above are quite complex and it would be extremely difficult to model independently the loss of particle acceleration due to each. Therefore, Eq. (3.13) is modified to treat the non-ideal flow effects in a gross manner. The resulting equation of motion is simply:

$$\frac{dv_p}{dt} = \frac{3}{8}\frac{\rho_g}{r_p \rho_p} C_W C_D |v_g - v_p| (v_g - v_p) \tag{3.20}$$

where C_W is a constant coefficient which accounts for the acceleration deficit caused by the non-ideal knife blade flowfield and particle-particle collisions that may occur. The model assumes C_W = 0.8 while the particle resides in the flow induced by the incident shock and C_W = 1.0 in the quiescent gas produced by the reflected shock. The calculated particle ignition delay time is found to be a weak function of the value of C_W assumed. A 25 percent variation in C_W about the assumed value of 0.8 ($0.6 \le C_W \le 1.0$) changes the predicted ignition delay time by less than 5 percent (see Fig. 4.10).

Another difficulty encountered in calculating the motion of the particle is that of the particle's reflection from the endwall observation window. In terms of the one-dimensional analysis being used, particle reflection is treated by calculating a reflected particle velocity, v_{pr}, which is based on an assumed particle coefficient of restitution, e, and the calculated incident particle velocity, v_{pi}. The reflected and incident particle velocities are then simply related by [69]:

$$v_{p_r} = ev_{p_i} \tag{3.21}$$

Determining a suitable value for e is an extremely difficult problem. The value of e ranges from 0 to 1 for purely inelastic and elastic collisions, respectively. In general, the coefficient of restitution depends on the particle shape, material, and collision velocity [69]. Therefore, e must be determined experimentally or estimated analytically. Since the particle temperature is expected to be elevated to near the alloy melting points at the time of particle impact (see Fig. 3.22), both analytical and experimental determination of e is impractical. Analytical solutions require accurate values of the particle's material properties, such as the modulus of elasticity, which are not readily available for Al/Mg alloys at elevated temperatues.

A relatively low coefficient of restitution of e = 0.4 is used in the model based on the following considerations:

1) At the time of reflection, the alloy particles are predicted to be at a relatively high temperature (~600 K) for the experiment conditions investigated (refer to Fig. 3.22). Since the hardness of Al, Mg, and their alloys is known to decrease substantially with increasing temperature [70], the likelihood of plastic deformation is increased.

2) For a given material, the coefficient of restitution decreases with increasing impact velocity [69]. The kinematic model developed here predicts impact velocities on the order of 200 m/s, which is relatively large.

3) The non-spherical shape of the alloy particles will result in the loss of translational kinetic energy to rotational kinetic energy upon impact.

The calculated ignition delay time is found to be only mildly dependent upon the choice of e. Varying e between 0.2 and 0.6 produces a variation of approximately ±10 percent about the particle ignition delay time predicted assuming e = 0.4 (see Fig. 4.9).

3.3 SPECIFICATION OF ENERGY TRANSFER AND PRODUCTION TERMS

Before the particle energy equation (Eq. (3.7)) can be solved for the rate of change of particle temperature, the energy transfer and production terms must be specified. The specification of the rate of convective heat transfer is described in detail in the following section. The form of the heterogeneous surface reaction rate, k_s, is specified in section 3.3.2.

The remaining unknown in Eq. (3.7) is the particle surface emissivity, ε_p. In general, ε_p is a complicated function of the composition of the particle's oxide film and particle temperature. It is assumed that $\varepsilon_p = 0.9$, a constant that is independent of alloy composition and temperature. The choice of this relatively high particle emissivity is based on the work of Brewster and Taylor [37] in which the spectral intensity of burning Al particles was measured and then modeled to estimate the radiative properties of the particle surface and flame envelope. The emissivity of the oxide droplets in the flame envelope was estimated to range between 0.45 and 1.0 [37]. The choice of ε_p is not critical since, as will be shown, the radiative heat transfer is insignificant for the particle temperatures of importance, i.e. $T_p \leq 2300$ K.

3.3.1 Convective Heat Transfer

Based on the particle's time-dependent motion, determined from the numerical solution of the kinematic model outlined in the previous section (see

Appendix C), it is possible to specify the time dependent rate of convective heat transfer from the gas to the particle. The approach used here follows that of Fox et al. [34], in which an empirical formulation for the surface-averaged Nusselt number, $Nu_p = Nu_p(Re_p, M_p, Pr)$, is implemented in the solution of the particle energy equation (Eq. (3.7)). The variable oxygen properties required to complete the specification of the convective heating term in Eq. (3.7) are calculated using the NASA Gordon-McBride program [9].

The calculation of the rate of particle convective heating is complicated by the rarefaction of the oxygen. The transition from continuum flow to slip flow is taken to occur at a Knudsen number of $Kn \approx 0.01$ [13], where $Kn = \lambda_g/d_p \sim M_p/Re_p$ and λ_g is the mean free path of the gas molecules. The mean free path of a gas can be calculated from [71]:

$$\lambda_g = \left[\sqrt{2}\,\frac{p_g}{k_B T_g}\,\pi\,\sigma^2\right]^{-1} \tag{3.22}$$

where k_B is the Boltzmann constant and σ is the molecular diameter of the gas.

Figure 3.5 shows the calculated particle Knudsen number plotted as a function of gas temperature and pressure over the range of conditions investigated experimentally. The curves of Fig. 3.5 are calculated assuming $\sigma_{O_2} = 0.18$ nm [72], variable oxygen properties, and $d_p = 21.5$ μm. Continuum flow is considered to exist for $Kn < 0.01$ and slip flow for $Kn > 0.01$ [13]. The symbols shown in Fig. 3.5 indicate the temperatures at which the majority of measurements are taken at pressures of 8.5 and 34 atm. For the particle diameters of interest, the calculated Knudsen number ranges from Kn = .003 at $T_5 = 2225$ K, $p_5 = 34$ atm to Kn = .016 at $T_5 = 2775$ K, $p_5 = 8.5$ atm. Clearly, the rarefaction of the oxygen at $p_5 = 8.5$ atm must be considered in the analysis of the particle heat transfer.

Fox et al. have proposed the following empirical expression for Nu_p which agrees with experimental data for $M_p / Re_p < 0.5$, corresponding to continuum, slip, and a portion of the transition flow regimes [34]:

$$Nu_p = 2\left\{\frac{e^{-M_p}}{1 + 17\,M_p / Re_p}\right\} + 0.459\,Pr^{0.33}\,Re_p^{0.55}\left\{\frac{2}{3}\left(1 + \frac{1}{2}\,e^{-17\,M_p / Re_p}\right)\right\} \quad (3.23)$$

where $Pr = (c_p)_g\,\mu_g / k_g$ is the Prandtl number. Equation (3.23) is valid for spherical particles. Figure 3.6 presents a graphical representation of Eq. (3.23). The figure shows Nu_p plotted versus Re_p for several values of M_p. The magnitude of Nu_p drops below the continuum flow minimum value of $Nu_p = 2$ as it should for the slip and transition flow regimes [73].

The various parameters required to evaluate Eq. (3.23) and specify the rate of heat transfer, i.e. Re_p, M_p, Pr, μ_g, k_g, etc., are calculated using the NASA Gordon-McBride program [9]. During the majority of the particle heating time, the particle moves subsonically through the quiescent oxygen produced by the reflected shock wave in region 5. In this region, the oxygen properties are simply T_5, ρ_5, μ_5, k_5, etc., and evaluation of the required parameters is straightforward. However, while the particle is accelerated in the supersonic flow induced by the incident shock wave, the situation is considerably more complex due to the presence of the particle bow shock, as shown in Fig. 3.7 [34].

Figure 3.7 shows the particle flowfield that will exist as seen from the frame of reference of the particle. The knife blade oblique shock waves and expansion fans are neglected, and the properties of the approaching gas are taken to be those of the undisturbed flow in region 2. As seen by the moving particle, the flow is approaching at a relative velocity of $v_{2,p} = v_2 - v_p$ and has a relative Mach number of $M_{2,p} = (v_2 - v_p) / a_2$. The supersonic relative flow results

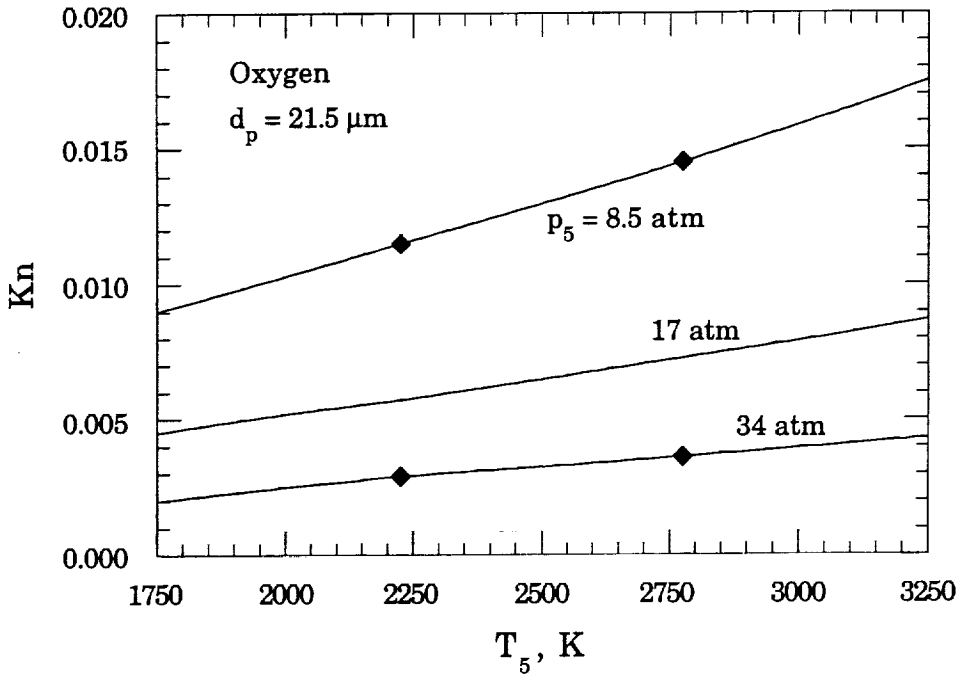

Fig. 3.5: Variation of the particle Knudsen number as a function of reflected shock gas temperature and pressure.

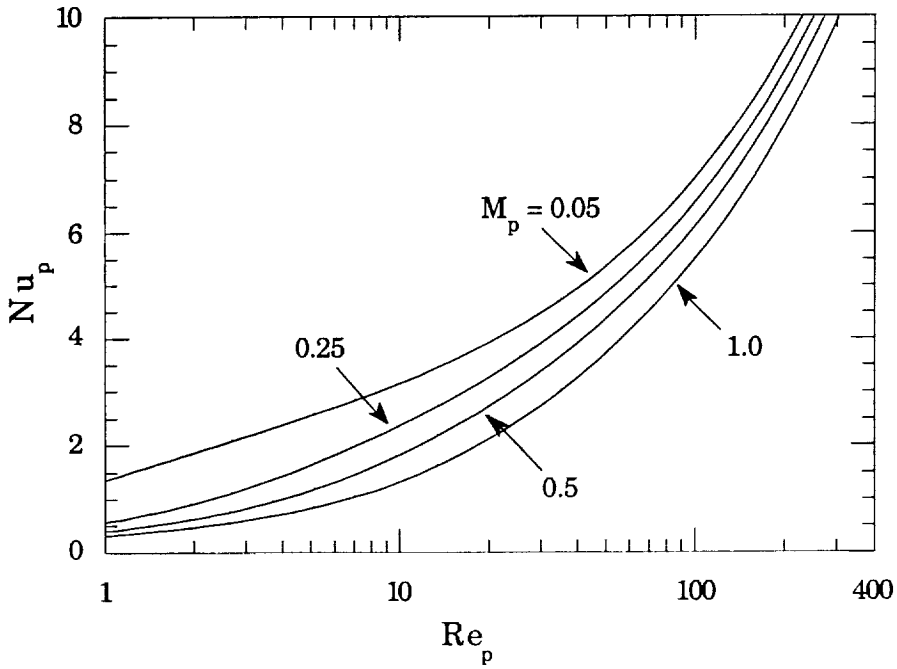

Fig. 3.6: Calculated surface-averaged Nusselt number as a function of the particle Reynolds and Mach numbers. Calculations are based on the expression formulated by Fox et al. for spherical bodies [34].

in a detached bow shock located a short distance from the particle. As the flow passes through the bow shock, it is heated, compressed, and slowed. Therefore, the state of the gas seen by the particle differs significantly from that in region 2.

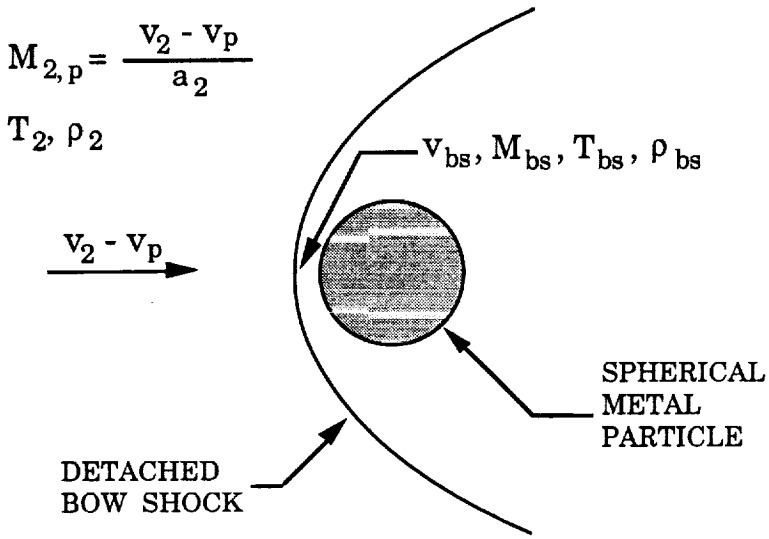

Fig. 3.7: Description of the supersonic particle flowfield that exists while the particle is accelerated in the flow induced by the incident shock wave.

When calculating the heat transfer to the particle in this supersonic region, the gas properties used are those that exist behind the particle bow shock along the stagnation streamline, as indicated in Fig. 3.7. The flow conditions in region 2 are functions of M_{s_i}, T_1, and p_1, and therefore can be expressed as a function of the experiment temperature and pressure. Figures 3.8a and 3.8b show the calculated flow properties in region 2 plotted versus T_5, calculated assuming equilibrium oxygen. M_2, v_2, and T_2 all increase with T_5 and are only slightly dependent upon p_5. The density, ρ_2, is found to decrease with increasing T_5 and is directly proportional to p_5.

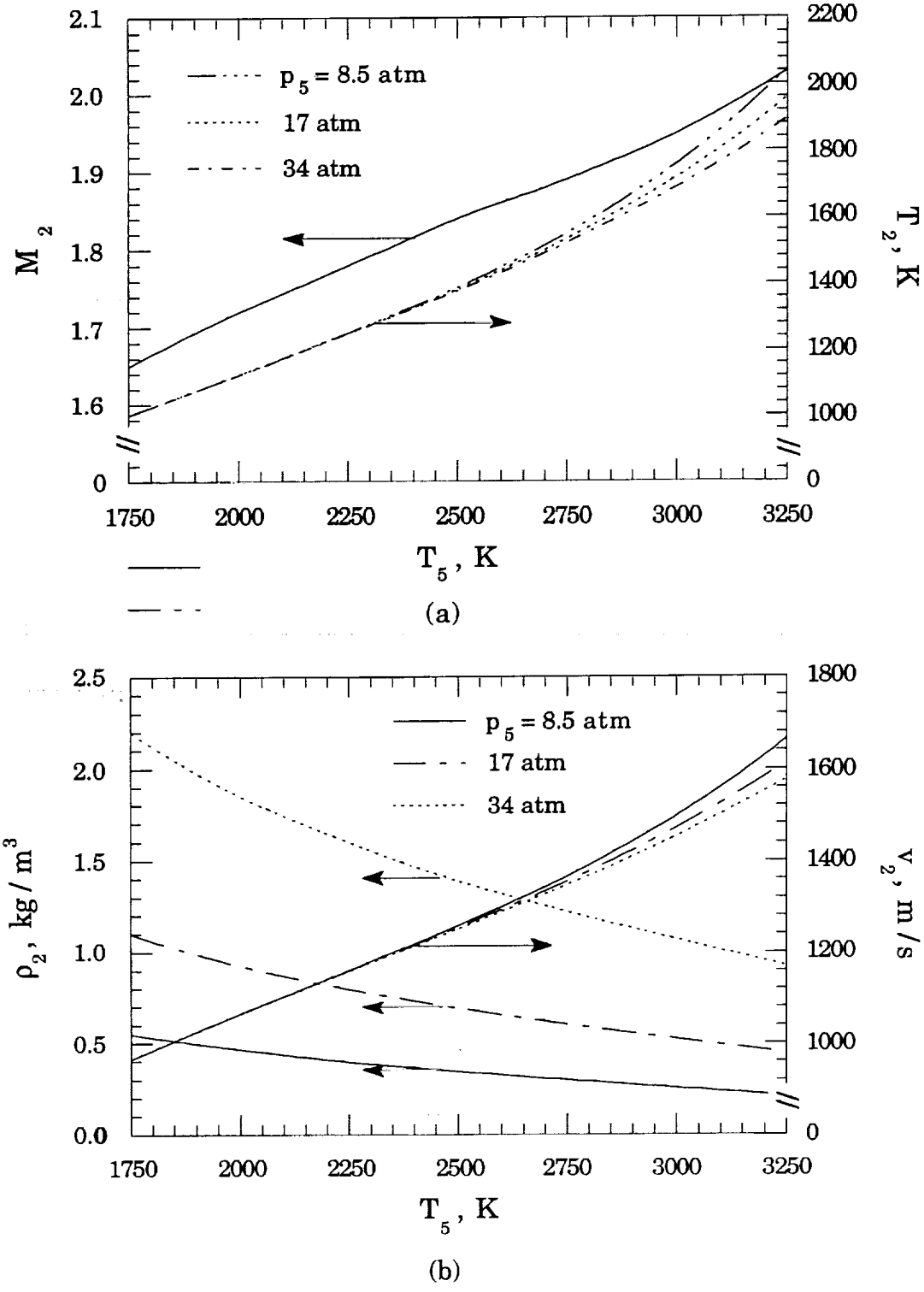

Fig. 3.8: Calculated conditions of the gas flow induced by the incident shock wave (region 2) as a function of T_5. a) Gas flow Mach number and Temperature. b) Gas flow density and velocity.

After determining the gas conditions in region 2, the corresponding conditions along the stagnation streamline behind the bow shock are easily calculated by treating the bow shock as a normal shock wave. The residence time of a fliud element in the vicinity of the particle is on the order of 10^{-8} s, which is less than the oxygen's vibrational relaxation time [34]. Therefore, the normal shock calculations assume the flow is chemically frozen. Due to the acceleration of the particle, the relative particle flow Mach number ($M_{2,p}$) is a decreasing function of time. The corresponding gas conditions behind the bow shock (denoted by a subscript bs) are calculated as a function of the absolute velocity of the particle, v_p, for each unique set of reflected shock conditions, T_5 and p_5.

The calculated Mach number, M_{bs}, and velocity , v_{bs}, of the flow behind the particle bow shock are plotted in Figs. 3.9a and 3.9b, respectively, for three values of T_5. The results are effectively independent of p_5. Both M_{bs} and v_{bs} increase with increasing particle velocity. When v_p increases to the point at which $M_{2,p}$ reaches Mach one (represented by the solid symbols in both figures), the bow shock vanishes and the relative flow Mach number and velocity are simply $M_{2,p}$ and $v_{2,p}$, respectively. If the particle velocity continues to increase beyond this point, both $M_{2,p}$ and $v_{2,p}$ will decrease linearly until they approach zero as $t \rightarrow \infty$.

Figures 3.10a and 3.10b show the calculated bow shock gas temperature, T_{bs}, and density, ρ_{bs}, plotted as a function of the particle velocity. T_{bs} is only mildly dependent upon the reflected shock pressure while ρ_{bs} is directly proportional to p_5. Both T_{bs} and ρ_{bs} decrease linearly from maximums at $v_p = 0$. When the relative particle flow Mach number drops below one, the bow shock vanishes and $T_{bs} = T_2$ and $\rho_{bs} = \rho_2$, independent of v_p. This phenomena is clearly shown by the horizontal portions of the curves. It is noted, however, that

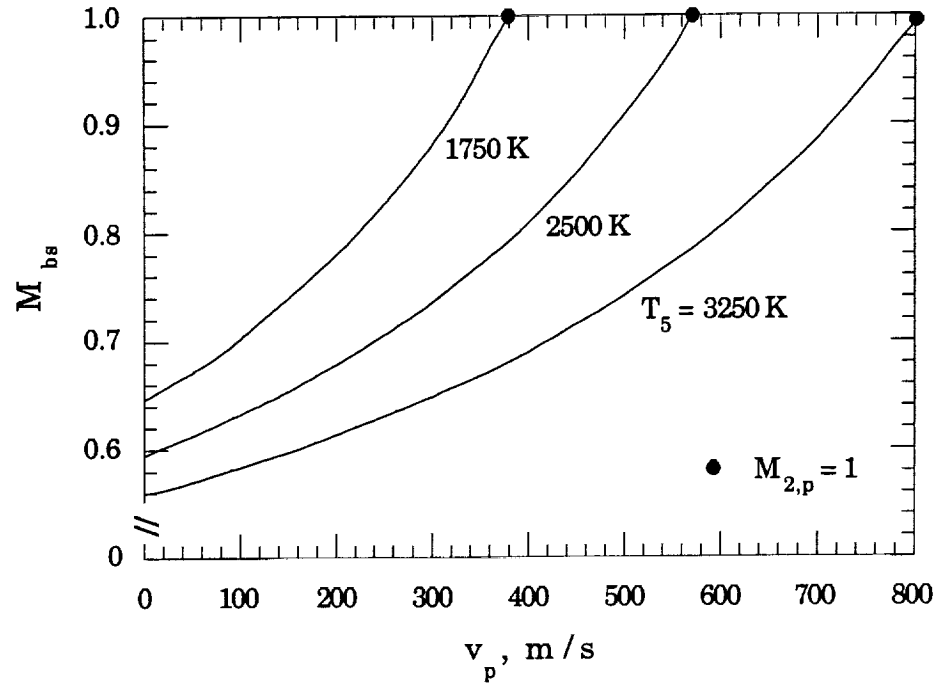

(a)

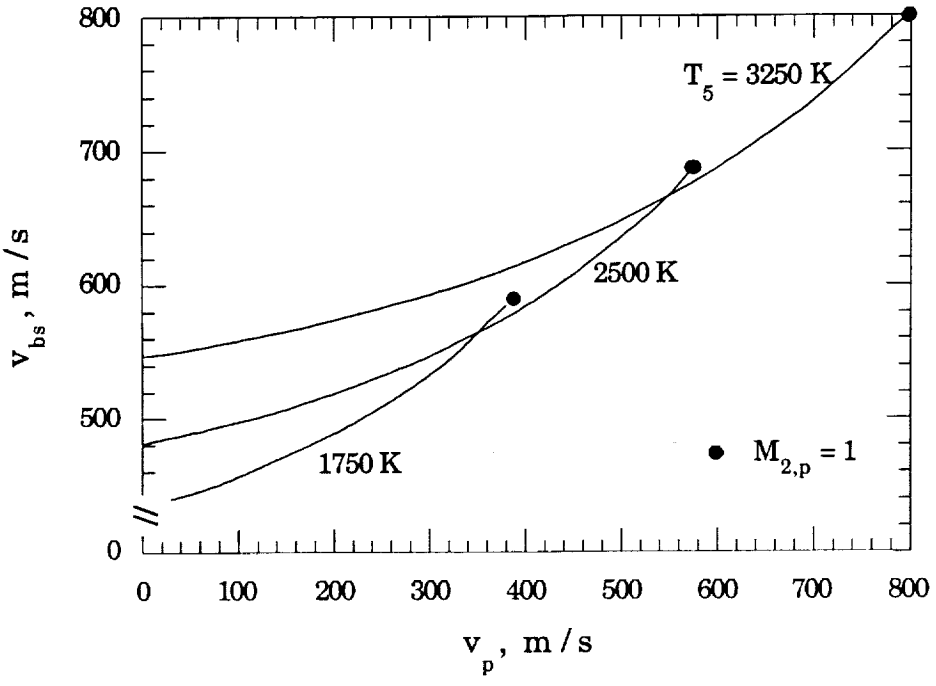

(b)

Fig. 3.9: Calculated relative flow Mach number and velocity behind the particle bow shock as a function of particle velocity. a) Bow shock Mach number. b) Bow shock velocity.

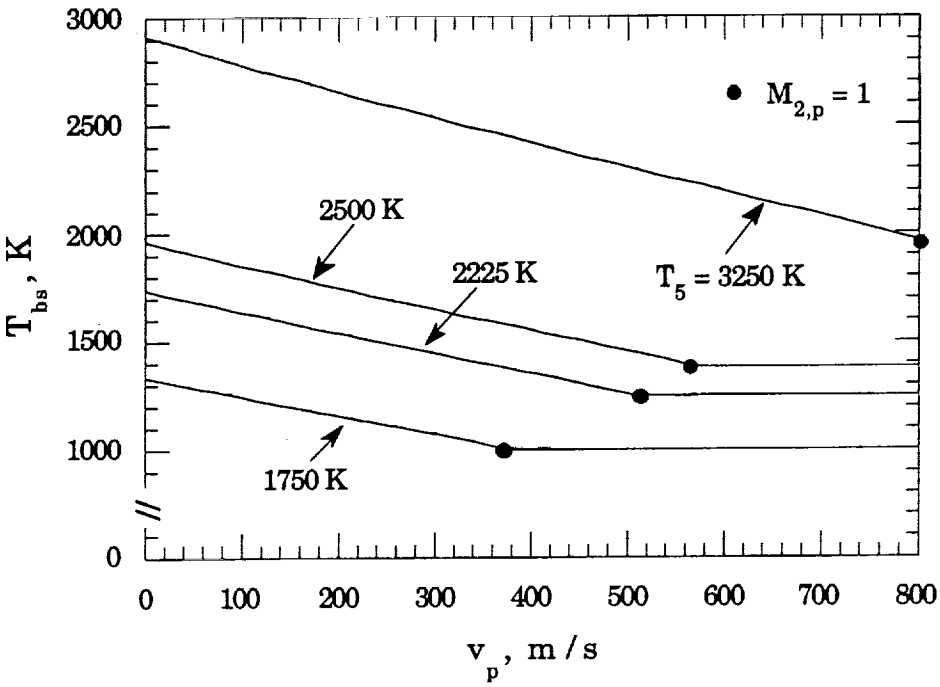

(a)

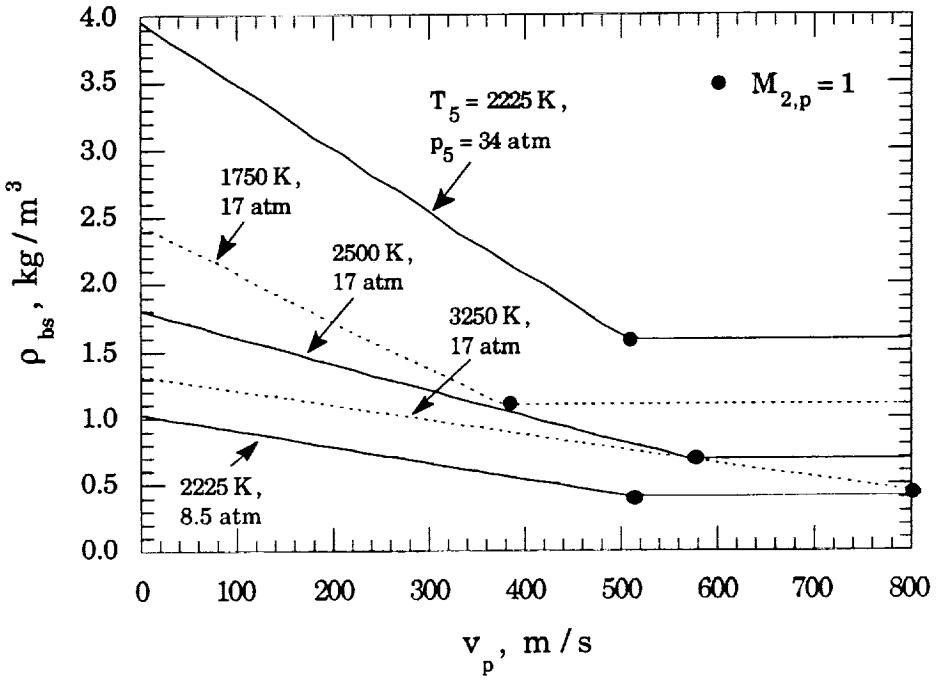

(b)

Fig. 3.10: Calculated gas temperature and density behind the particle bow shock as a function of particle velocity. a) Bow shock gas temperature. b) Bow shock gas density.

$M_{2,p} < 1$ is not expected to occur here due to the extremely short particle acceleration periods.

The properties of the gas behind the bow shock are calculated for each set of reflected shock conditions, T_5 and p_5, of interest. The results are tabulated as a function of v_p and are used as part of the numerical solution of the particle ignition delay time described in detail in Appendix C. During the particle acceleration period, the calculated particle velocity is used to determine the corresponding bow shock gas properties. These gas properties, in turn, are used to calculate the instantaneous rate of heat transfer to the particle's surface for use in the solution of the particle energy equation, Eq. (3.7).

3.3.2 Heterogeneous Reaction Rate

The heterogeneous reactions that occur on the surface of the Al/Mg alloy particles are quite complex (refer to the detailed discussion in Chapter 1). The contribution of these reactions to the particle energy balance (Eq. (3.7)) is specified by the term:

$$\dot{q}_r = A_s q_r k_s \tag{3.24}$$

where it is assumed that all of the energy produced by the surface reaction is absorbed by the particle and contributes to the temperature rise. A_s and q_r (see section 3.4) are known for a given particle diameter and alloy composition. The heterogeneous surface reaction rate k_s, however, remains to be formulated.

In the present analysis, the several mechanisms contributing to the overall surface reaction (see chapter 1 and section 3.4) will be treated in an integrated manner by assuming that the reaction rate can be described by a simple Arrhenius type of relation. The general expression for the surface reaction rate of a linearly oxidizing metal is given by [14]:

$$k_s^l = A_l \exp\left(-\frac{E_a}{R_u T_p}\right) \tag{3.25}$$

where A_l is the linear pre-exponential constant, E_a the reaction activation energy, R_u is the universal gas constant, and the surface temperature is taken to be equal to that of the particle since Bi << 1. If the metal oxidizes parabolically (i.e., oxidation rate decreases parabolically with time, due to the increasing thickness of the oxide layer), as may be the case for Al, Reynolds [74] gives the following relation for the surface reaction rate:

$$k_s^p = \frac{B_p}{2\delta_{ox}\rho_{ox}\alpha} \exp\left(-\frac{E_a}{R_u T_p}\right) \tag{3.26}$$

where B_p is the parabolic pre-exponential constant, δ_{ox} the thickness of the oxide film, ρ_{ox} the density of the oxide, and α the ratio of the mass of oxide to the mass of oxygen forming it. Noting that ρ_{ox} and α are constants, Eq. (3.26) can be simplified to:

$$k_s^p = \frac{A_p}{\delta_{ox}} \exp\left(-\frac{E_a}{R_u T_p}\right) \tag{3.27}$$

where $A_p = B_p/(\rho_{ox}\,\alpha)$. Equation (3.27) shows that the reaction rate of a parabolically oxidizing metal is inversely proportional to the thickness of the oxide layer that has formed on the particle's surface.

Two values of the Mg activation energy are reported in the literature, $(E_a)_{Mg}$ = 23,700 and 50,500 cal/mole [14]. Reynolds gives an Al activation energy of $(E_a)_{Al}$ = 22,800 cal/mole[74]. The true nature of the metal reaction rates cannot in general be described as purely linear or parabolic. Kubaschewski and Hopkins [14] state that the Mg oxidation rate is parabolic at room temperature (300 K) and becomes linear at temperatures above 500 K, and Al oxidation is parabolic at room temperature and then becomes asymptotically linear at temperatures above 500 K.

For simplicity, the experimental measurements will be modeled assuming the linear form of k_s (Eq. (3.25)) and assuming that the activation energy of Mg and all of the Al/Mg alloys have activation energies equal to that of Al, i.e. $(E_a)_{Mg} = (E_a)_{alloy} = (E_a)_{Al} = 22{,}800$ cal/mole. Under these assumptions, the only remaining unknown in Eq. (3.25) is the pre-exponential constant, A_1, which will be determined empirically from the measured particle ignition delay times. The sensitivity of the ignition delay calculations to the assumed form of k_s, in the case of Al, and the choice of the reaction activation energy, in the case of Mg, will also be investigated.

3.4 VARIABLE Al/Mg ALLOY THERMOPHYSICAL PROPERTIES

Before the physics of the metal particle ignition delay time can be accurately modeled and understood, knowledge of the thermophysical properties of the metal is required. Equation (3.7) shows that the rate at which the particle is heated is inversely proportional to the particle density. The rate of particle heating due to the heterogenous surface reactions cannot be specified without information concerning the alloy-dependent specific heat of reaction, q_r. Finally, the transition from the slow heterogenous surface reaction regime to the fast detached gas phase combustion regime is believed to occur near the alloy boiling points.

The following sections will detail the known Al, Mg, and Al/Mg alloy thermophysical properties. As shown in Table 3.1, the commonly quoted physical properties of Al and Mg vary substantially between the two pure metals, indicating that significant variations in the alloy properties will exist. Where gaps exist in the known alloy dependent properties, approximations are made based on the generally well-characterized properties of the pure metals.

Also included in Table 3.1 are various properties of the dominant oxides formed from the reaction of Al/Mg alloys and O_2.

Table 3.1: Standard constant properties of Al, Mg, Al_2O_3, MgO, and $MgO \bullet Al_2O_3$.

Physical Property	Al	Mg	Al_2O_3	MgO	$MgO \bullet Al_2O_3$
ρ @ 300 K, g/cm^3	2.700 [b]	1.740 [b]	3.984 [f]	3.582 [f]	3.584 [f]
T_{mp} @ 1 atm, K	933 [a]	923 [a]	2327 [a]	3105 [a]	2408 [a]
T_{bp} @ 1 atm, K	2767 [d]	1366 [a]	-	-	-
L_f, kJ/kg	396.7 [a]	348.9 [a]	1090 [a]	1930 [a]	1350 [a]
Q_v, kJ/kg	10,770 [d]	5,600 [c]	-	-	-
k @ 300 K, W/m-K	238 [b]	156 [b]	15-29 [g]	6.3-38 [g]	-
W, g/mole	26.98 [a]	24.31 [a]	101.96 [a]	40.30 [a]	142.27 [a]
β_{solid}, T_o = 300 K, 10^{-5} K^{-1}	~7.6 [b]	~5.5 [b]	2.7 [g]	4.5 [g]	3.6 [h]

[a] Reference [75]

[b] Reference [76]

[c] Reference [77]

[d] Reference [78]

[e] Reference [62]

[f] Reference [14]

[g] Calculated from data presented in Reference [79]

[h] Calculated assuming $\beta_{MgO \bullet Al_2O_3} = (\beta_{Al_2O_3} + \beta_{MgO}) / 2$

3.4.1 Al/Mg Equilibrium Phase Diagram

An understanding of the variable physical properties of Al/Mg alloys begins with an examination of the simplified equilibrium phase diagram shown in Fig. 3.11 [41]. The most obvious characteristic of the phase diagram is the variation in the liquidus temperature, T_{liq}, as a function of Mg content. The liquidus temperature is a maximum for pure Al (933 K) and decreases at a nearly linear rate to the Al-rich eutectic (723 K) at 36.5 wt.% Mg. The liquidus temperature then remains nearly constant until the overall minimum (710 K) is reached at the Mg-rich eutectic, 67.7 wt.% Mg. T_{liq} then increases at a nearly linear rate to that of pure Mg (923 K).

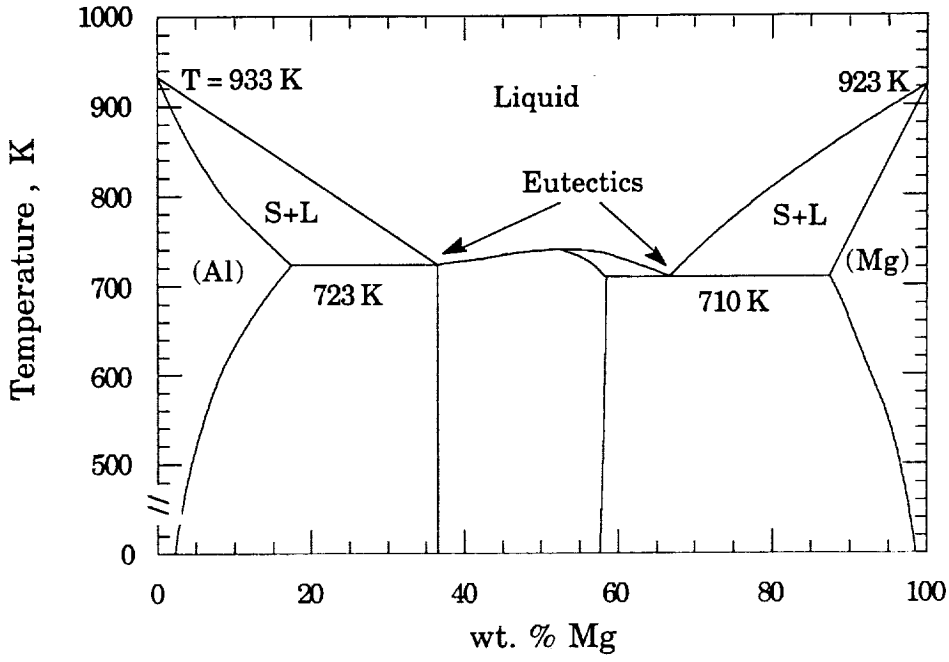

Fig. 3.11: Al/Mg equilibrium phase diagram. Regions marked as S+L contain a mixture of solid and liquid. Diagram constructed using data published by Murray [41].

For alloy compositions in the central plateau region, $36.5 \leq$ wt.% Mg ≤ 67.7, the liquidus and melting temperature, T_{mp}, coincide. As these alloys melt, their temperatures will remain constant at $T_{mp} = T_{liq}$ while an amount of energy equivalent to the enthalpy of fusion, L_f, is absorbed. However, for alloy compositions in the ranges $0 <$ wt. % Mg < 36.5 and $67.7 <$ wt. % Mg < 100, T_{mp} is substantially less than T_{liq}. These alloys absorb either a fraction or all of their enthalpy of fusion over a temperature range, and both solid and liquid alloy will exist simultaneously as indicated by the notation S + L in Fig. 3.11.

3.4.2 Al/Mg Alloy Density

Examination of Eq. (3.7) shows that the rate of particle heating is inversely proportional to density, or particle mass for a given particle diameter. Figure 3.12a shows the variation in Al/Mg alloy density as a function of composition for several temperatures. The curves are calulated using the following relation for the theoretical bulk density of a mixture [80]:

$$\rho_{alloy} = \left[\frac{Y_{Al}}{\rho_{Al}} + \frac{Y_{Mg}}{\rho_{Mg}} \right]^{-1} \tag{3.28}$$

where Y_{Al} and Y_{Mg} are the mass fractions of Al and Mg, respectively. The symbols that appear in Fig. 3.12a represent the measured solid alloy density at T = 300 K [70] and are in excellent agreement with the corresponding calculations. The particle mass, which remains constant throughout the pre-ignition heating period, is calculated using the calculated solid alloy densities.

Figure 3.12a also shows the effect of temperature on the liquid alloy density. The calculations are based on the published density variation of pure Al

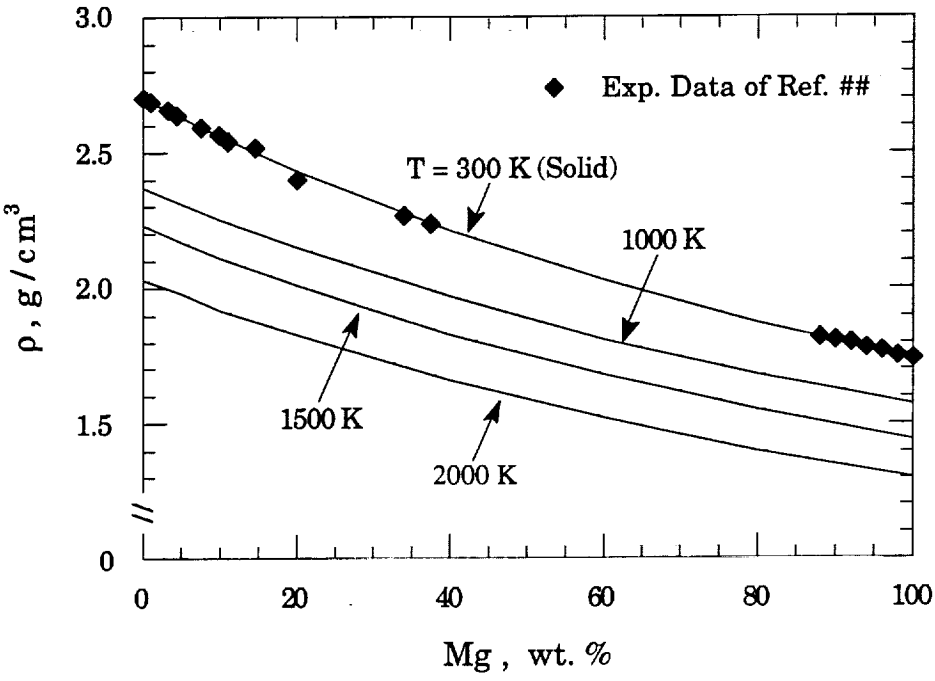

(a)

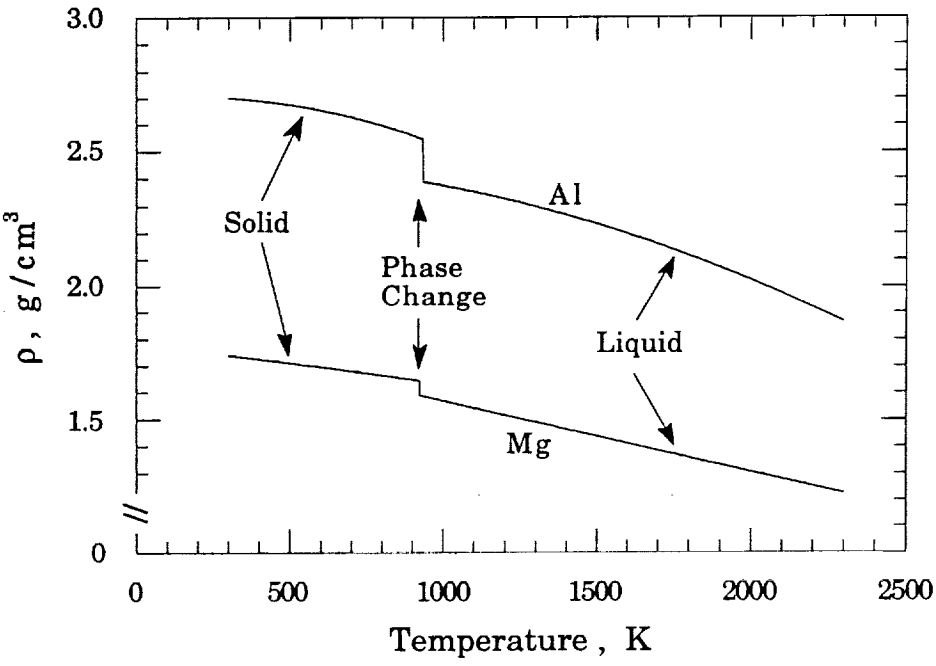

(b)

Fig. 3.12: Variation of Al/Mg alloy, Al, and Mg density as a function of composition and temperature. a) Alloy density versus composition. b) Temperature dependence of Al and Mg density.

and Mg, which is plotted in Fig. 3.12b. Based on the graphical data of Murray [41], the variation in Al density with temperature is given by:

$$(\rho_{Al})_{sol} = 2.697 + 9.16\times10^{-5}T - 2.70\times10^{-7}T^2 \quad g/cm^3 \qquad 300\ K < T < 933\ K \qquad (3.29a)$$

$$(\rho_{Al})_{liq} = 2.453 + 5.94\times10^{-5}T - 1.37\times10^{-7}T^2 \quad g/cm^3 \qquad 933\ K < T \qquad (3.29b)$$

Similarly, the Mg density is given by [76]:

$$(\rho_{Mg})_{sol} = 1.778 - 1.23\times10^{-4}T \quad g/cm^3 \qquad 300\ K < T < 923\ K \qquad (3.30a)$$

$$(\rho_{Mg})_{sol} = 1.835 - 2.65\times10^{-4}T \quad g/cm^3 \qquad 923\ K < T \qquad (3.30b)$$

The density of the alloys decrease with increasing temperature and drop substantially upon changing phase, as shown for the pure metals in Fig. 3.12b.

3.4.3 Al/Mg Alloy Specific Heat

Examination of the particle energy balance (Eq. (3.7)) shows that the rate of particle heating is inversely proportional to the particle specific heat, c. The temperature-dependent specific heat of pure Al and Mg [75] is plotted in Fig. 3.13a as the solid curves. The solid phase specific heat of both Al and Mg rises in a nearly linear manner with temperature until the melting point is reached. At that point, the Mg specific heat rises abruptly to its liquid value and the Al specific heat drops slightly to its liquid value. The liquid specific heats are constant until the boiling point is reached for both pure metals.

The dashed curves in Fig. 3.13a correspond to the calculated specific heats for the alloys. The calculations assume a mass-averaged specific heat for both

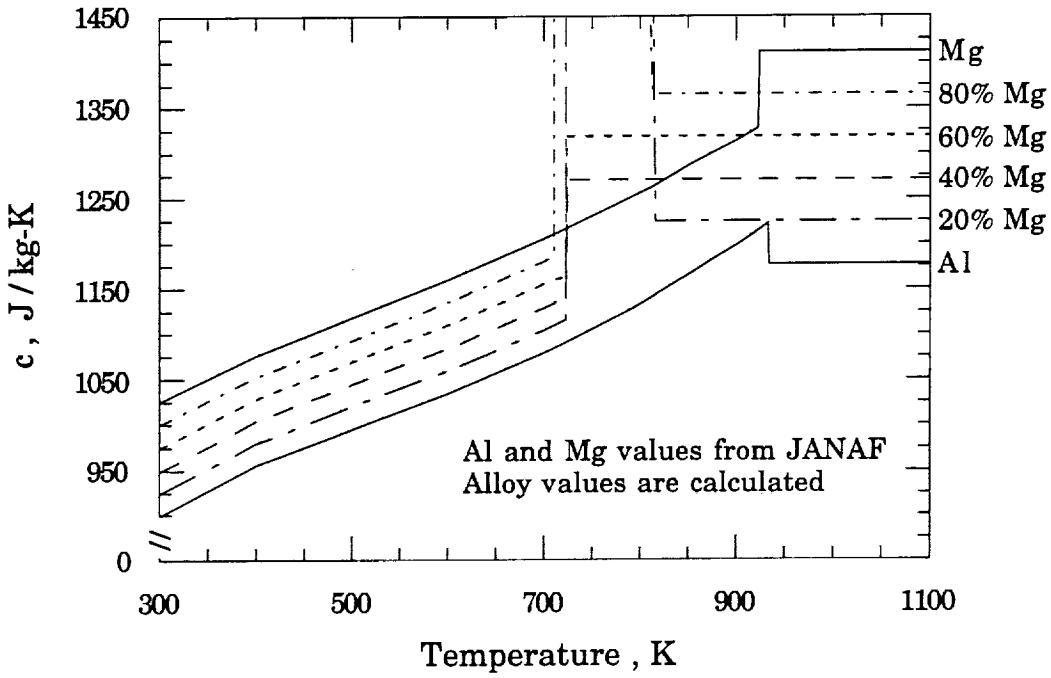

(a)

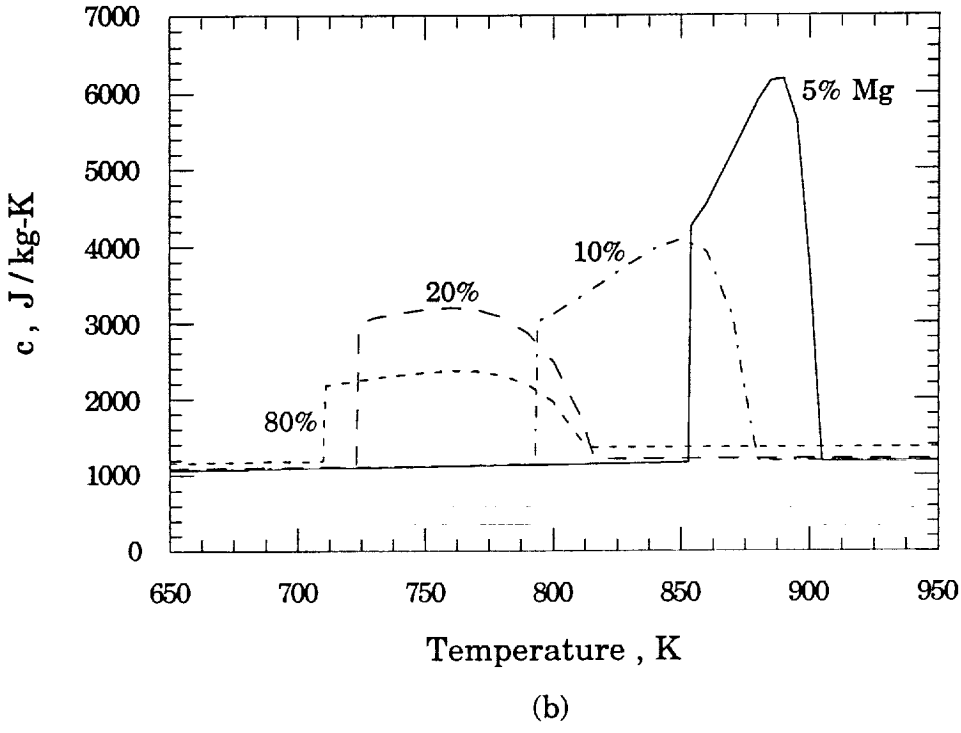

(b)

Fig. 3.13: Temperature dependent specific heat of Al/Mg alloy as a function of temperature. a) Overall variation of c. b) Expanded view of the calculated specific heat in the alloy melt regions.

the solid and liquid phases of the form:

$$c_{Y_{Mg}} = Y_{Mg}\, c_{Mg} + \left(1 - Y_{Mg}\right) c_{Al} \tag{3.31}$$

where Y_{Mg} is the mass fraction of Mg in the alloy. The mass-averaged specific heat should be accurate for the liquid phase, since the alloy is found to essentially behave as an ideal solution at 1000 K [41]. Assuming a mass-averaged specific heat for the solid phase may be less accurate, but the error introduced should be small since the majority of the particle heating time is spent in the liquid phase.

Figure 3.13b shows an expanded view of the alloy specific heat over the melting range (see Fig. 3.11). The enthalpy of fusion, L_f, can be expressed as an effective specific heat [46], allowing the heating model to correctly calculate the rise in particle temperature through the alloy melt regions. The enthalpy of fusion of alloys with compositions from pure Al to the Al-rich eutectic is taken as that of pure Al, $(L_f)_{Al}$ = 397 kJ/kg [75]. The enthalpy of fusion of alloys with compositions from the Mg-rich eutectic to pure Mg is taken as that of pure Mg, $(L_f)_{Mg}$ = 349 kJ/kg [75]. Alloys with compositions that fall between the two eutectics are assumed to have enthalpies of fusion equal to that measured for the Al-rich eutectic, $(L_f)_{36.5\ wt.\%Mg}$= 304 kJ/kg [41].

3.4.4 Al/Mg Alloy Specific Heat of Reaction

The specific heat of reaction, q_r, is a function of the alloy composition and the temperature at which the reaction proceeds. The equation describing the stoichiometric reaction of an arbitrary Al/Mg alloy with oxygen is given by:

$$[a]\mathbf{Al} + [1 - a]\,\mathbf{Mg} + \left[\frac{1}{2}\left(1 + \frac{a}{2}\right)\right]\mathbf{O_2} \rightarrow \left[\frac{a}{2}\right]\mathbf{Al_2O_3} + [1 - a]\,\mathbf{MgO} \tag{3.32}$$

where the bold symbols represent the reactant and product species, a is the mole fraction of Al in alloy, and the bracketed terms are the stoichiometric coefficients. Although the reaction described by the right-hand-side of Eq. (3.32) also produces the double oxide $MgO \bullet Al_2O_3$ (see Fig. 3.16), it can easily be shown that the sum of its enthalpy difference and standard heat of formation is simply equal to the sum of the enthalpy differences and standard heats of formation of one mole of Al and one mole of Mg. Therefore, the above simplified chemical reaction is suitable for the calculation of q_r.

In general, the heat of reaction is given by [25]:

$$\Delta H_r = \sum_i (\nu_i H_i)_{products} - \sum_i (\nu_i H_i)_{reactants} \tag{3.33}$$

where ν_i is the stoichiometric coefficient of the i^{th} species and H_i is defined as:

$$H_i \equiv \left\{(H_T^o - H_{298}^o) + \Delta_f H^o\right\}_i \tag{3.34}$$

The enthalpy difference, $(H_T^o - H_{298}^o)$, and the standard heat of formation , $\Delta_f H^o$, are tabulated as a function of temperature for each chemical species [75]. Based on Eqs. (3.32) - (3.34), the heat of reaction per mole of Al/Mg alloy consumed can be written as:

$$\Delta H_{alloy} = \frac{a}{2} H_{Al_2O_3} + (1 - a) H_{MgO} - a H_{Al} - (1 - a) H_{Mg} - \frac{1}{2}\left(1 + \frac{a}{2}\right) H_{O_2} \tag{3.35}$$

The specific heat of reaction is then simply given by $q_r = \Delta H_{alloy} / W_{alloy}$, where W_{alloy} is the alloy molecular weight.

Equation (3.35) is used to calculate q_r as a function of alloy composition and temperature, the result being shown in Fig. 3.14. The calculations are based on published enthalpy differences and heats of formation [75]. The step increases in the specific heat of reaction are associated with the phase change of

each alloy at their respective melting points. Other than the step change, the alloy heat of reaction is essentially independent of temperature and is simply a linear function of alloy composition.

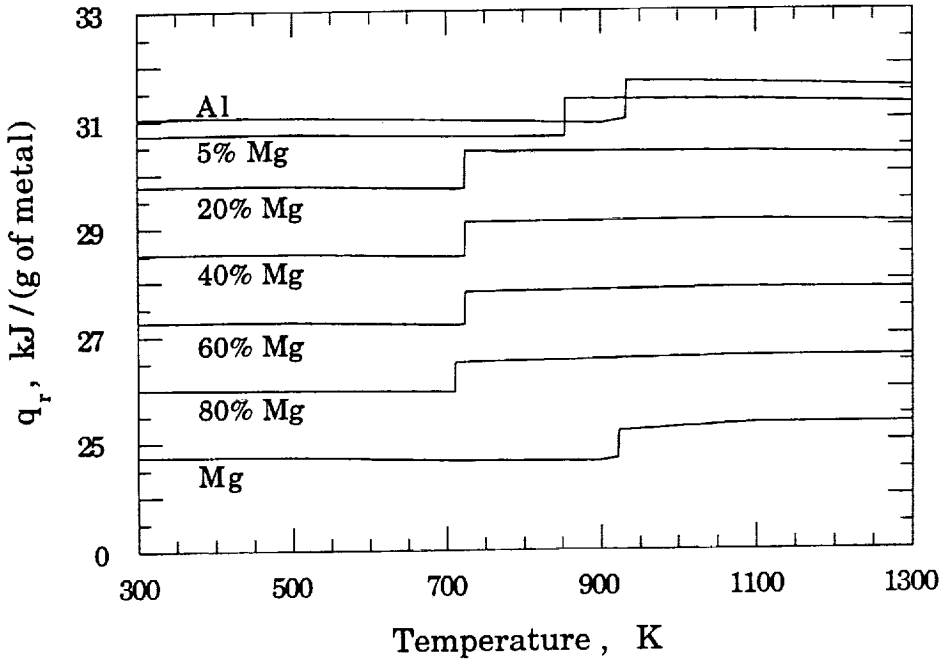

Fig. 3.14: Calculated specific heat of reaction as a function of alloy composition and temperature. The step increases are associated with the alloy solid/liquid phase change.

3.4.5 Al/Mg Alloy Boiling Point

The transition from heterogeneous to the detached (gas phase) reaction occurs at the metal boiling point for pure Mg and at the Al_2O_3 melting point for pure Al [38]. The present research seeks to determine the corresponding criterion for the transition to gas phase reaction of the Al/Mg alloys. It is evident that the variation in the alloy boiling point as a function of composition and pressure will play an important role in determining this transition criterion.

The vapor pressures of liquid Al and Mg below their normal boiling points as a function of temperature are given as [76]:

$$p_v^{Al} = 133.32 T^{-1.023}\, 10^{(12.36 - 16450/T)} \qquad 933\,K < T < 2767\,K \tag{3.36}$$

$$p_v^{Mg} = 133.32 T^{-1.41}\, 10^{(12.79 - 7550/T)} \qquad 923\,K < T < 1366\,K \tag{3.37}$$

where the calculated vapor pressure is in pascals. Assuming constant Al and Mg heats of vaporization, Q_v, the vapor pressure of the pure metals can be calculated using the Clausius-Clapeyron equation [25]:

$$\ln\left(\frac{p}{p_o}\right) = -\frac{Q_v}{R_u}\left(\frac{1}{T} - \frac{1}{T_o}\right) \tag{3.38}$$

where p_o = 1 atm, T_o is the normal boiling point at 1 atm, and R_u is the universal gas constant. Substituting the known values of p_o, T_o, and Q_v (see Table 3.1), into Eq. (3.38) yields the following relations for the vapor pressure of Al and Mg at temperatures above their respective normal boiling temperatures:

$$p_v^{Al} = 3.250 \times 10^{10}\, e^{-(35081/T)} \qquad 2767\,K < T \tag{3.39}$$

$$p_v^{Mg} = 1.490 \times 10^{10}\, e^{-(16373/T)} \qquad 1376\,K < T \tag{3.40}$$

The vapor pressures of the Al/Mg alloys are easily calculated using Dalton's law of partial pressures:

$$p_v^{alloy} = a_{Al} p_v^{Al} + a_{Mg} p_v^{Mg} \tag{3.41}$$

where the partial molar quantities $a_i = p_i(\text{alloy}) / p_i(\text{pure metal})$ are assumed to be independent of temperature and are tabulated as functions of alloy content [81]. The coefficients, a_i, account for the fact that the partial pressure of an

element in solution is slightly different from that measured for the pure element.

The boiling point of a substance is defined as the temperature at which the vapor pressure of the liquid equals the external gas pressure [82]. Based on this definition, the calculated boiling point of Al/Mg alloy as a function of gas pressure is shown in Fig. 3.15. The dashed line represents the melting point of Al_2O_3 (~2300 K). Due to the large difference in the normal boiling points of Mg and Al (1366 K and 2767 K, respectively), alloys with Mg contents of more than 35% have boiling points very near that of pure Mg and remain below the melting temperature of Al_2O_3 for gas pressures as high as 34 atm. The curves shown in Fig. 3.15 are accurately described by a curve fit relation of the form:

$$(T_{bp})_{alloy} = A\,(p_g)^B \tag{3.42}$$

where A and B are constants and p_g is in atmospheres. The calculated constants A and B are presented in Table 3.2 as a function of alloy composition.

3.4.6 Permeability of Al/Mg Alloy Oxide Films

Insight into the promotion of the particle's heterogeneous surface reactions can be obtained by examining the variation in the protective nature of the alloy oxide film as a function of particle composition and temperature. An important measure of the protective nature of an oxide film is the volume ratio, Φ, which is defined as [14]:

$$\Phi \equiv \frac{V_{ox}}{V_m} \tag{3.43}$$

where V_{ox} is the oxide volume and V_m is the volume of metal from which it is formed. If $\Phi < 1$, the oxide film is considered non-protective since it cannot fill

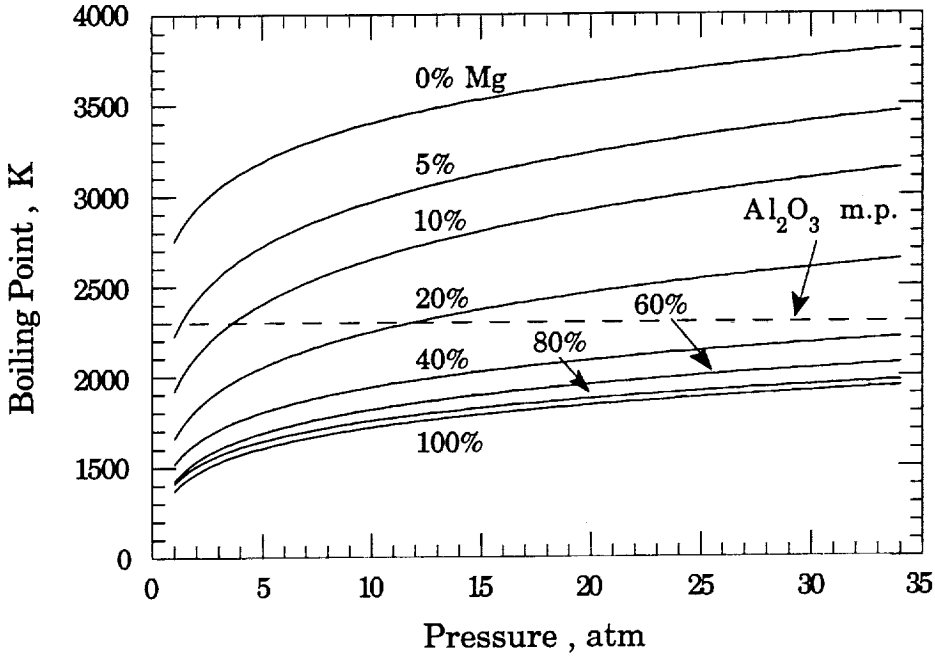

Fig. 3.15: Calculated Al/Mg alloy boiling point as a function of alloy composition and gas pressure. The curves are fit using a relation of the form $(T_{bp})_{alloy} = A(p_g)^B$, where the constants A and B are given in Table 3.1 and p_g is in atm.

Table 3.2: Constants used to calculate the Al/Mg alloy boiling point as a function of gas pressure. The constants are determined by fitting $(T_{bp})_{alloy} = A(p_g)^B$ to the calculated curves of Fig. 3.15.

	wt. % Mg in Alloy							
	0	5	10	20	40	60	80	100
A	2751	2226	1919	1659	1517	1424	1411	1371
B	.0923	.1250	.1405	.1323	.1069	.1060	.0950	.0985

the volume of space created by the metal consumed to form it. The resulting oxide film is porous. Conversely, if $\Phi > 1$, the oxide film is considered protective since its volume exceeds that of the metal from which it is formed.

It is generally stated that $\Phi_{Mg} = 0.81$ and $\Phi_{Al} = 1.28$ [14,42], indicating that Mg and Al have non-protective and protective oxide coatings, respectively. These statements are somewhat misleading due to the fact that the volume ratios are typically calculated at room temperature. The Al/Mg alloy density (see Figs. 3.12a and 3.12b), and therefore the alloy volume, is found to be a strong function of temperature. It follows that the Al/Mg alloy volume ratio may also be a function of temperature. This possibility will now be investigated.

The equation for the reaction of an arbitrary Al/Mg alloy with oxygen is given by:

$$[a]\mathbf{Al} + [b]\,\mathbf{Mg} + [c]\mathbf{O_2} \rightarrow [d]\,\mathbf{Al_2O_3} + [e]\,\mathbf{MgO} + [f]\,\mathbf{MgO{\bullet}Al_2O_3} \qquad (3.44)$$

where the bracketed terms are the stoichiometric coefficients. The double oxide is included here since its volume must be considered in the calculation of Φ. In order to determine the stoichiometric coefficients d, e, and f, a full equilibrium calculation of the reaction must be performed.

Figure 3.16 shows equilibrium oxide mole fractions, calculated with the NASA CEC program, plotted as a function of alloy composition. For these calculations, excess oxidizer is specified so that the equilibrium temperature of the products remain below 2000 K, similar to the pre-ignition particle temperatures. As Fig. 3.16 shows, the amount of each oxide formed is a strong function of alloy composition. At a Mg content of 30% in alloy, Al_2O_3 disappears completely, $MgO{\bullet}Al_2O_3$ reaches its maximum, and MgO just begins to form.

The stoichiometric coefficents of the reaction described by Eq. (3.44) are defined for each alloy composition, Al_aMg_b, by reading d, e, and f directly from Fig. 3.16 and noting that a = 2d + 3f, b = e + f, and 2c = 3d + e + 4f. The alloy volume ratio is then simply calculated from:

$$\Phi_{alloy} = \frac{[d]\overline{V}_{Al_2O_3} + [e]\overline{V}_{MgO} + [f]\overline{V}_{MgO\bullet Al_2O_3}}{[2d + e + 3f]\overline{V}_{alloy}} \tag{3.45}$$

where the molecular volumes are simply $\overline{V}_i = W_i / \rho_i$ and have units of cm^3/mole. The molecular volumes of the Al/Mg alloys are easily calculated using the densities of Figs. 3.12a and 3.12b and the calculated alloy molecular weights. The density of the three oxides, however, have yet to be determined.

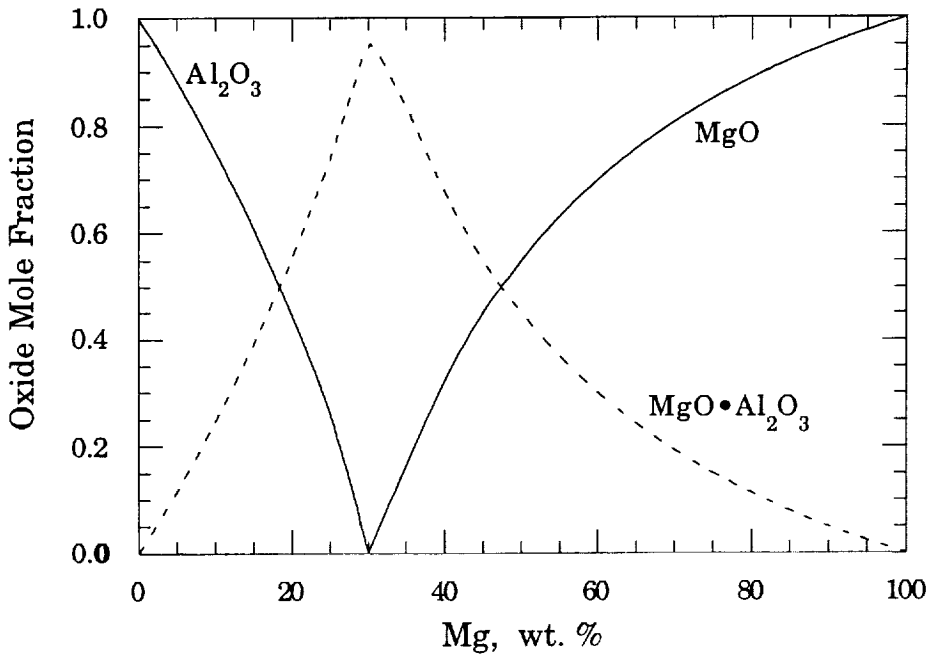

Fig. 3.16: Calculated mole fractions of Al_2O_3, MgO, and $MgO\bullet Al_2O_3$ formed as a function of alloy composition. Calculations used the NASA Gordon-McBride code and assumed equilibrium reactions.

The thermal linear expansion of both Al_2O_3 and MgO have been measured over the temperature range 300 K < T < 2200 K [79]. Based on the published data, it is possible to calculate the linear coefficient of expansion, α, for each oxide. Assuming $\beta = 3\alpha$ [83], where β is the volumetric coefficient of expansion, the value of β for each oxide is calculated to be $\beta_{Al_2O_3} = 2.7\text{x}10^{-5}$ K^{-1} and $\beta_{MgO} = 4.5\text{x}10^{-5}$ K^{-1} for T_o = 300 K. No published data on the thermal expansion of $MgO \bullet Al_2O_3$ is found, so it is assumed that $\beta_{MgO \bullet Al_2O_3} = (\beta_{Al_2O_3} + \beta_{MgO}) / 2 =$ 3.6x10-5 K^{-1}.

The variation in the molecular volumes of the oxides are then calculated using the following relation:

$$\overline{V}_i = \overline{V}_i^{\,o}\left[1 + \beta_i(T - T_o)\right] \tag{3.46}$$

where $\overline{V}_i^{\,o}$ are the molecular volumes at T_o = 300 K. Kubaschewski and Hopkins [14] give the following values for the oxide molecular volumes at T = 300 K:

$$\overline{V}^{\,o}_{Al_2O_3} = 25.60 \ \text{cm}^3/\text{mole}$$
$$\overline{V}^{\,o}_{MgO} = 11.25 \ \text{cm}^3/\text{mole}$$
$$\overline{V}^{\,o}_{MgO \bullet Al_2O_3} = 39.70 \ \text{cm}^3/\text{mole}$$

The calculated variation of the alloy volume ratio is plotted as a function of alloy composition and temperature in Fig. 3.17a. Φ_{alloy} is a nearly linear function of alloy composition. At room temperature, the volume ratio of the solid alloy varies from Φ_{Al} = 1.28 to Φ_{Mg} = 0.805 as is generally stated. The oxide film is predicted to become non-protective (Φ < 1) for Mg contents in excess of 60%. However, due to the substantial increase in volume associated with the solid/liquid phase change of the alloy, the curve corresponding to T = 1000 K is substantially lower than the room temperature curve. At T = 1000 K, the oxide

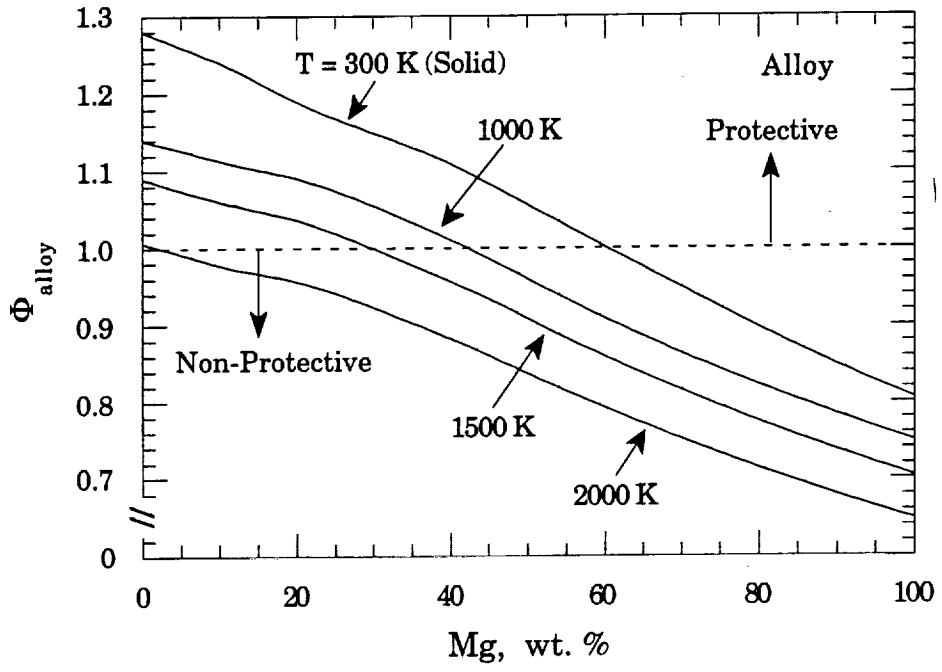

(a)

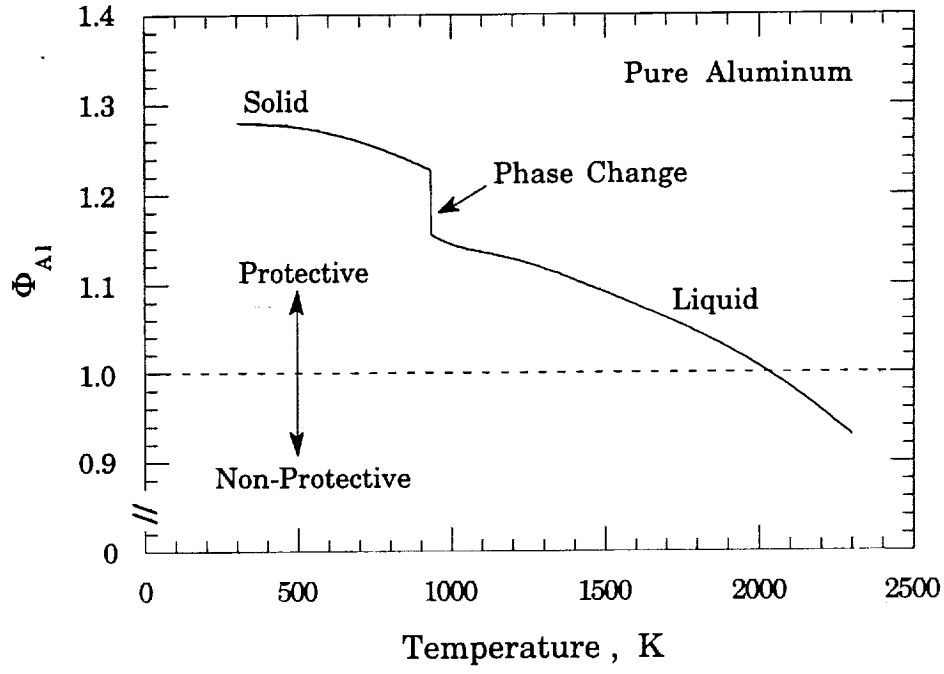

(b)

Fig. 3.17: Calculated variation of the Al/Mg alloy volume ratio as a function of temperature and alloy composition. a) Φ_{alloy} versus alloy composition and temperature. b) Φ_{Al} versus temperature.

film becomes non-protective at Mg contents as low as 40%. This trend is seen to continue with increasing temperature. Virtually all of the alloy compositions are predicted to have non-protective oxide films at temperatures above 2000 K.

It is interesting to consider the dependence of Φ_{Al} on temperature separately, as shown in Fig. 3.17b. The volume ratio drops slowly as the solid metal is heated to the melting point, where it drops to approximately $\Phi_{Al} = 1.5$ as the metal melts. The volume ratio of the liquid Al continues to drop until it reaches unity at a temperature of approximately 2030 K. Above this temperature, the Al_2O_3 oxide film is predicted to be non-protective. *This suggests that all of the Al/Mg alloy particles, including Al, will experience significant self heating due to the presence of surface reactions, at some point in the ignition process.*

The preceding calculations indicate that at elevated particle temperatures heterogeneous surface reactions will occur for all of the alloy compositions. It is also noted that Φ_{alloy} decreases with increasing temperature for all alloy compositions, indicating that the metal particle is expanding faster than the oxide film that surrounds it. This expansion will continuously crack the oxide film and open surface fissures that allow molten metal to react directly with the hot oxidizer. This fracturing of the oxide film will result in substantial particle self-heating, even for Al-rich alloy particles that possess initially protective oxide films.

3.5 SAMPLE CALCULATIONS

The particle heating/ignition delay problem is solved by writing Eqs. (3.7) and (3.20) in their finite difference form and numerically integrating in time (A detailed discussion of the numerical solution technique is included in Appendix

C). The equations are linearized by calculating the various parameters based on physical properties at the previous time step, which is valid for sufficiently small time step size (Δt = 0.01 μs for all calculations, see Appendix C). The numerical approach used here allows the use of gas tables containing the variable particle and variable gas properties discussed in the previous sections. The values of the model constants and thermophysical properties of the alloy particles assumed in the present investigation are summarized in Table 3.3. The values of the pre-exponential constants of the heterogeneous surface reactions are determined from the experimental data in Chapter 4.

Insight into the physics of the experimental technique can be gained by closely studying the results of the full convective ignition model. Figure 3.18 shows a representative calculated log-log t-x diagram for 20 μm Mg and 20% Mg alloy particles, showing the details of the near-wall region. The calculation assumes the knife blade is mounted 4 mm from the shock tube endwall and that the oxygen temperature and pressure are 2250 K and 17 atm. The calculation begins at time zero with the incident shock and particle locations coincident. The solid curves are the paths of the incident and reflected shock waves as well as the path of the 20% Mg alloy particles, and the dashed curve is the path of the Mg particles.

The calculation shows that the particles are accelerated behind the incident shock (region 2) for approximately 10 μs. After the passage of the reflected shock wave at 10 μs, the particles decelerate in the stagnant oxygen of region 5 as they move toward the endwall. The Mg and 20% Mg alloy particles are predicted to reflect from the endwall approximately 20 μs and 27 μs, respectively, after the time of shock reflection. The particle reflection times are slightly different because the heavier 20% Mg alloy particles are accelerated to a lower velocity than the less massive Mg particles by the shock induced flowfield.

The particles subsequently drift away from the endwall and ignite at a distance of approximately 10 mm from the endwall.

Table 3.3: Model parameters and thermophysical particle properties used in the numerical calculation of the alloy particle ignition delay time[a].

Model Parameter/ Particle Property		Value
$(A_1)_{Al}$	=	200 kg/m^2-s
$(A_1)_{Mg} = (A_1)_{alloy}$	=	400 kg/m^2-s
$(c)_p$	=	alloy and temperature dependent (Fig. 3.13a)
C_w	=	0.8
$(E_a)_p$	=	22,800 cal/mole
e	=	0.4
$(L_f)_{0\text{-}36.5\%\ Mg}$	=	397 kJ/kg (treated as an effective $(c)_p$, Fig. 3.13b)
$(L_f)_{36.5\text{-}67.7\%\ Mg}$	=	304 kJ/kg
$(L_f)_{67.7\text{-}100\%\ Mg}$	=	349 kJ/kg (treated as an effective $(c)_p$, Fig. 3.13b)
$(q_r)_p$	=	alloy and temperature dependent (Fig. 3.14)
$(T_{bp})_p$	=	alloy and pressure dependent (Fig. 3.15)
$(T_{mp})_{Al_2O_3}$	=	2300 K
$(T_{mp})_p$	=	alloy dependent (Fig. 3.11)
ε_p	=	0.9
ρ_p	=	alloy dependent (Fig. 3.12)

[a]The particle ignition delay time is modeled using real gas (oxygen) properties [9].

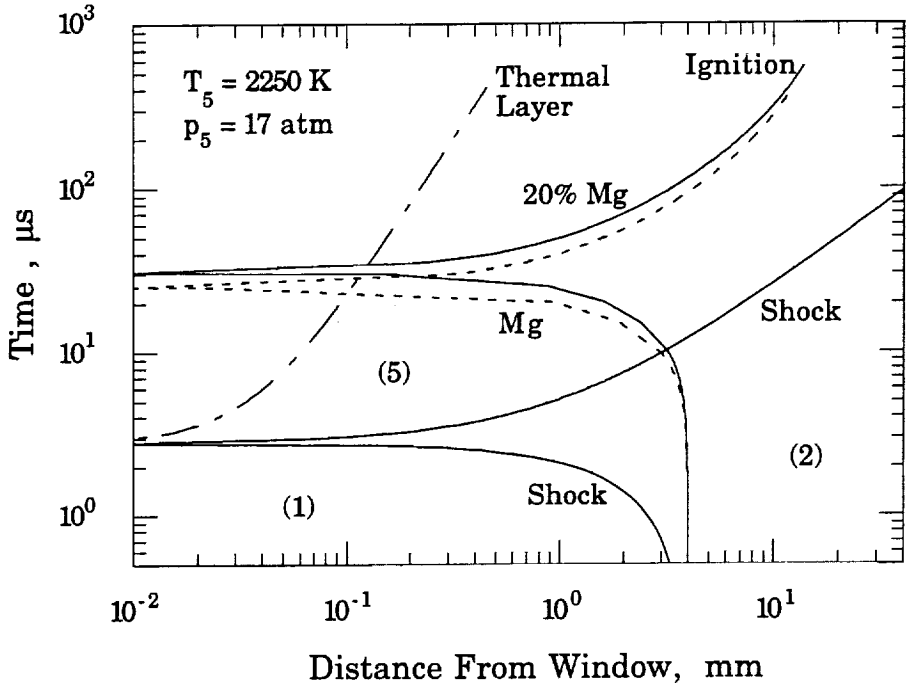

Fig. 3.18: Calculated t-x diagram for shock, particles (Mg and 20% Mg) and thermal layer. T_5 = 2250 K, p_5 = 17 atm, and d_{eff} = 20 mm. The knife blade is mounted 4 mm from the endwall (x_{kb} = 4mm).

Also shown in Fig. 3.18 is the growth of the endwall thermal layer as calculated from the analytical solution of Luikov [84], as described in Appendix C. The thermal layer height is taken to be the point at which the gas temperature reaches 99 percent of the experiment temperature. The calculations indicate that the particle spends approximately 10 μs inside the cooler gas of the endwall thermal layer, so that the effect on the experimentally measured ignition time is negligible.

Figure 3.19 shows the calculated particle velocities as a function of time corresponding to the trajectory calculations of Fig. 3.18. The Mg and 20% Mg particles are found to accelerate quickly behind the incident shock wave to maximum absolute velocities of 210 m/s and 160 m/s, respectively. The

difference between the magnitude of the accelerations is due to the difference in the particle densities, and therefore, the particle masses. The particle acceleration is reversed after passage of the reflected shock as the gas flow velocity is brought to rest, $v_5 \cong 0$. At the time of particle reflection, the incident particle velocities have slowed to approximately 180 m/s and 140 m/s for Mg and 20% Mg, respectively. The reflected particle velocities are approximately 70 m/s and 60 m/s for Mg and 20% Mg, respectively. At the time of particle ignition, both of the calculated particle velocities have slowed to about 10 m/s.

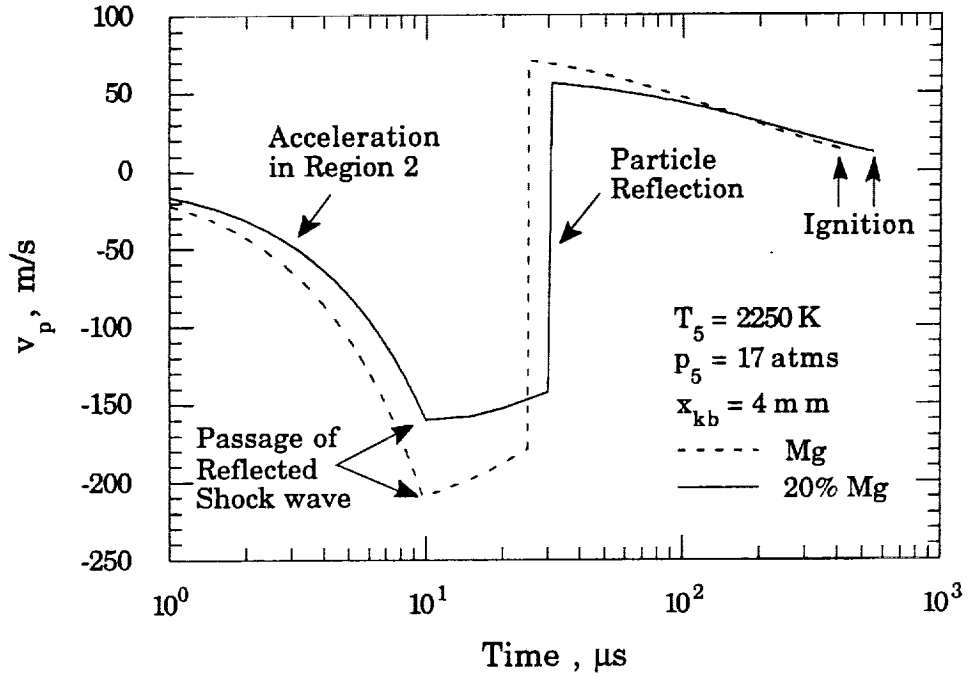

Fig. 3.19: Calculated particle velocities as a function of time for Mg and 20% Mg particles. Conditions correspond to those of Fig. 3.18.

Calculation of the particle drag coefficient and surface-averaged Nusselt number depends on accurate knowledge of the particle Mach and Reynolds numbers as functions of time. Figures 3.20a and 3.20b present the calculated Mach and Reynolds numbers as a function of time corresponding to the

calculated particle trajectories of Fig. 3-18. The calculations indicate that the particle Mach numbers range over two orders of magnitude for the conditions of this experiment. The Mach number is based on the local gas sonic velocity and the speed of the particle relative to the gas. The particle Mach number behind the incident shock wave is calculated to be $M_p \cong 1.8$ and is found to remain relatively constant.

After passage of the reflected shock wave, the increase in the sonic velocity of the gas and the substantially reduced relative particle velocity lowers the particle Mach number to $M_p \cong 0.15$. Reflection from the endwall further lowers M_p to about 0.08 and by the time of particle ignition the calculated Mach number has dropped to nearly 0.01. The calculations show that the particles will be heated to ignition and subsequently combusted in a low Mach number regime. The integrated Mach numbers for the Mg and 20% Mg particles are $\overline{M}_p \cong .043$ and .035, respectively.

The calculated particle Reynolds numbers presented in Fig. 3.20b vary from a maximum of $Re_p \cong 340$ behind the incident shock wave to a miniumum of $Re_p \cong 10$ at the time of particle ignition. The integrated particle Reynolds numbers for the Mg and 20% Mg particles are approximately 21 and 28, respectively. Therefore, the particles have relatively low Reynolds numbers during a majority of the ignition delay time.

Based on the particle kinematics discussed in Figs. 3.18, 3.19, 3.20a, 3.20b and the calculated real gas properties, the resulting particle drag coefficient and surface-averaged Nusselt numbers are presented in Fig. 3.21 plotted as a function of time. The particle drag coefficient in region 2 is $C_D \cong 1.4$ and remains constant until passage of the reflected shock wave. While in region 5 prior to the particle's reflection from the endwall, C_D drops to a constant value of

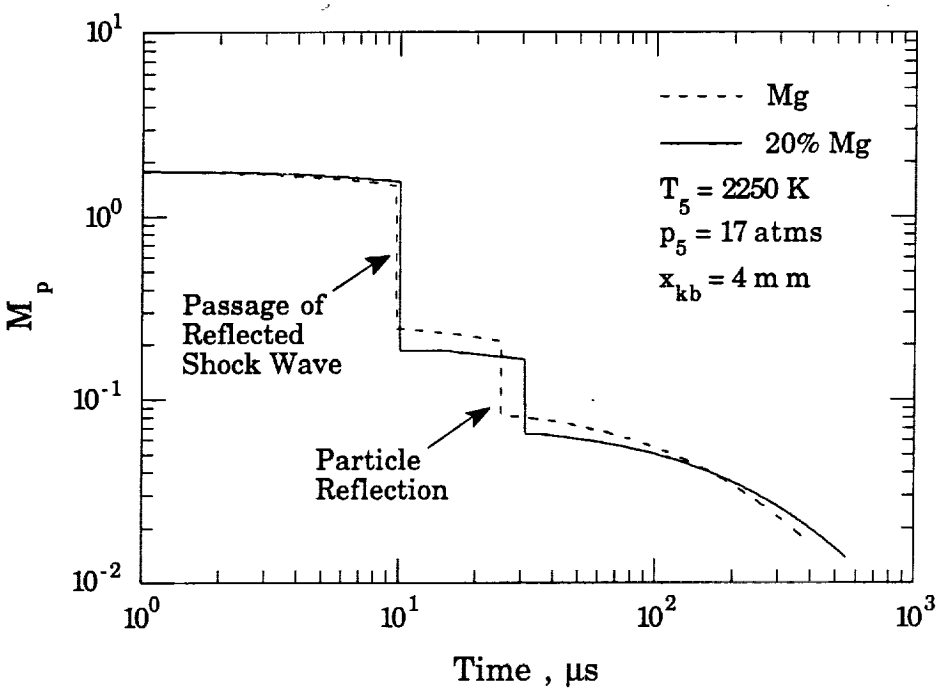

(a)

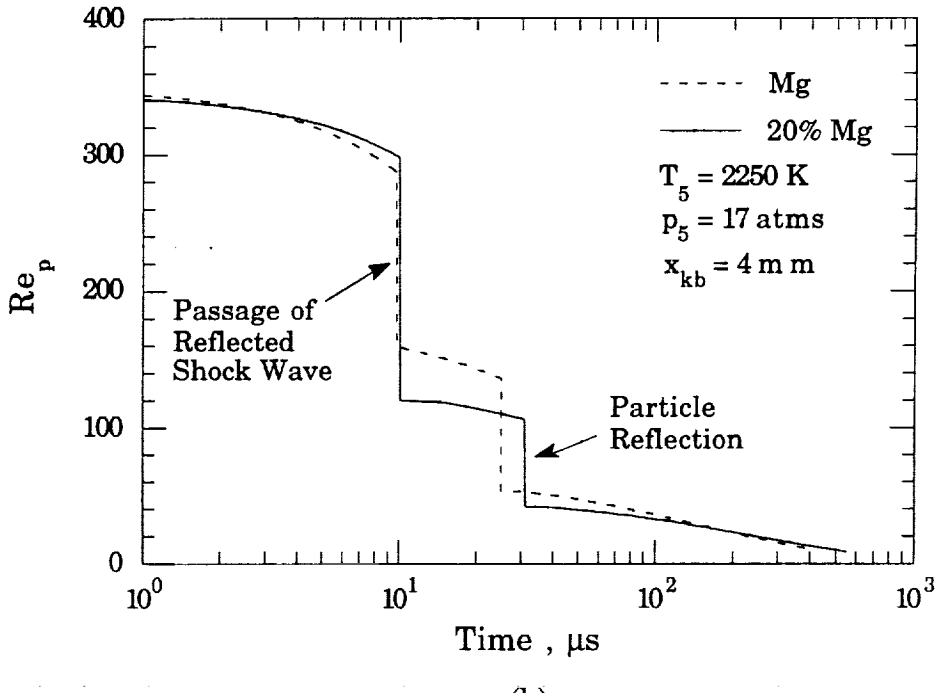

(b)

Fig. 3.20: Calculated particle Mach and Reynolds numbers as a function of time for Mg and 20% Mg particles. Conditions correspond to those of Fig. 3.18. a) M_p. b) Re_p.

C-3

approximately 1.0. After the particle reflects from the endwall, the drag coefficient jumps to about 1.8 and then steadily rises to the neighborhood of 4.0 as the particle slows substantially prior to ignition.

The calculated surface-averaged Nusselt numbers presented in Fig. 3.21 start at a value of $Nu_p \cong 10$. After the reflected shock passes, Nu_p drops slightly to approximately 8.0 and then is further reduced to $Nu_p \cong 5.0$ when the particles reflect from the endwall. Prior to ignition, the slowing of the particles reduce Nu_p further until it reaches a value of approximately 3.5. The resulting integrated values of the surface-averaged Nusselt numbers are 3.81 and 4.14 for Mg and 20% Mg particles, respectively.

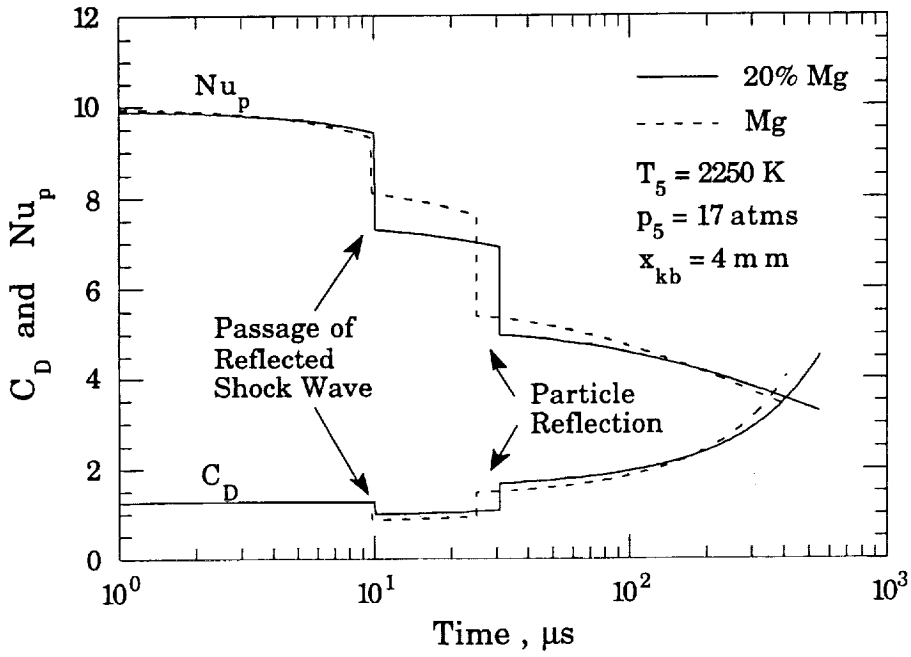

Fig. 3.21: Calculated particle drag coefficient and surface-averaged Nusselt number as a function of time for Mg and 20% Mg particles. Conditions correspond to those of Fig. 3.18.

Figure 3.22 shows the particle temperature time histories corresponding to the t-x calculations of Fig. 3-18. The calculations show that particle heating behind the incident shock is minimal. The results also clearly illustrate the different way in which the Mg and 20% Mg alloy particles melt. The Mg particle temperature rises to its melting point of 923 K and remains there until the particle has absorbed an amount of energy equal to its enthalpy of fusion. The temperature of the 20% Mg alloy particle rises to 723 K, where it remains while the particle absorbs an amount of energy equal to 11 percent of its enthalpy of fusion, then continues to rise until all of the alloy has melted.

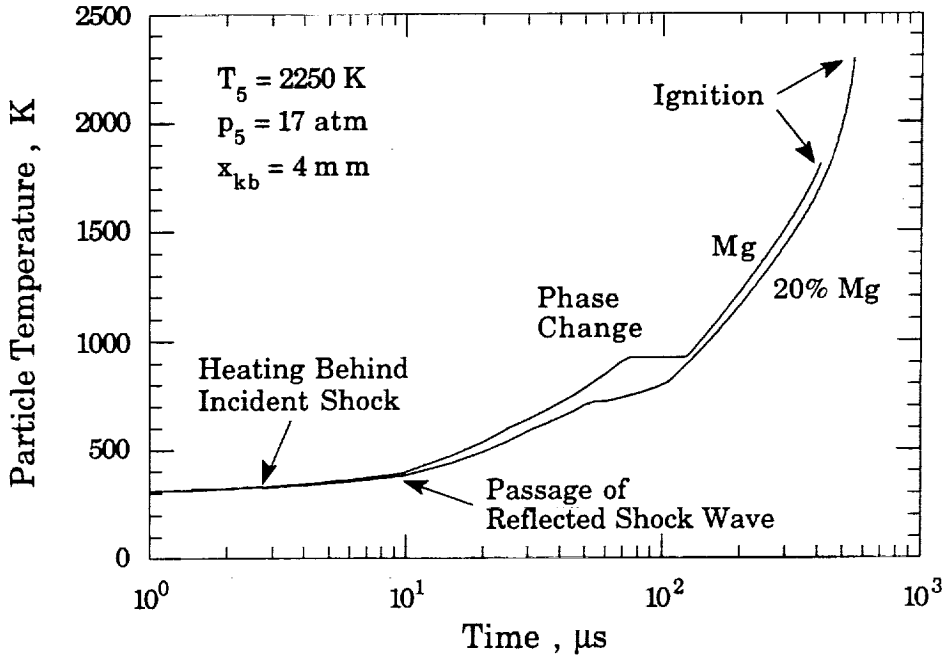

Fig. 3.22: Calculated particle temperature as a function of time for Mg and 20% Mg particles. Conditions correspond to those of Fig. 3.18.

After melting, both particle temperatures continue rising until the particles reach their respective ignition temperatures. With reference to the

particle reflection times shown in Fig. 3.18, the calculations indicate that the particles are at a temperature on the order of 600 K when they reflect from the endwall window. As previously stated, a coefficient of restitution of e = 0.4 is chosen based on the elevated particle temperature at the time of reflection. It will later be shown (see Fig. 4.9) that the magnitude of e does not significantly influence the conclusions drawn from the experiment and model.

The results of the experimental measurements are presented in the following chapter. The kinematic particle heating model is used to assess the developed knife blade mounting technique and to analyze the experimental results. The sensitivity of the ignition model to the choice of the model parameters is also investigated.

CHAPTER 4: RESULTS AND DISCUSSION

4.1 VALIDATION OF KNIFE BLADE MOUNTING TECHNIQUE

A fundamental assumption of the knife blade particle mounting technique is that the alloy particles do not interact with each other while being heated or combusted. The experiment is designed to study individual particle ignition and burning rather than group ignition and combustion. The possibility of group particle interactions is investigated by studying Mg powders with bimodal size distributions.

Figure 4.1 shows the results of the bimodal experiments. The dashed and solid curves in Fig. 4.1 correspond to bimodal size distributions composed of 20-25/30-38 μm and 20-25/38-45 μm diameter particles, respectively. The 20-25 μm size distribution has a measured mean diameter of 21.5 μm. The 30-38 μm and 38-45 μm diameter size distributions were not analyzed to determine the mean sizes. In both tests, the particles are mounted 8 mm from the endwall. The measured gas temperature and pressure corresponding to the dashed and solid curves are 2740 K, 16.5 atm and 2730 K, 16.2 atm, respectively.

Each of the light signals shown in Fig. 4.1 display two peaks, associated with the two distinct particle size distributions, as would be expected for particles which ignite and burn independently. As the bimodal size difference is increased the separation between the peaks of the light signals increases. The measured ignition delay times corresponding to the solid curve shown in Fig. 4.1 are 194 μs for the 20-25 μm particles and 685 μs for the 38-45 μm particles, yielding an ignition delay time ratio of 3.53. Assuming mean particle diameters of 21.5 μm and 41.5 μm, and gas conditions of 2750 K and 34 atm, the calculated ignition delay times are 194 μs and 662 μs. This yields a calculated ignition delay ratio of 3.41. The good agreement between the calculated and measured ignition

delay ratios supports the assumption of individual, rather than group, particle ignition and combustion.

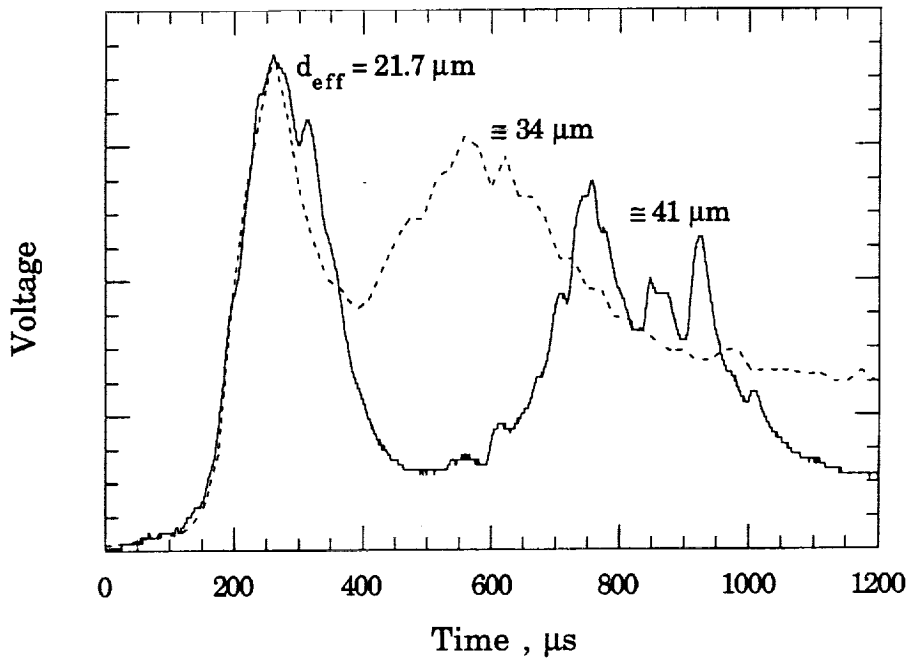

Fig. 4.1: Light signals of Mg powders with bimodal size distributions measured at x_{kb} = 8 mm. Dashed Curve: 20-25/30-38 μm mixture, T ≅ 2740 K, p ≅ 16.5 atm. Solid Curve: 20-25/38-45 μm mixture, T ≅ 2730 K, p ≅ 16.2 atm.

Additionally, the dashed curve in Fig. 4.1 yields an ignition delay time of 197 μs for the 20-25 μm particles. This value is in excellent agreement with the result obtained from the solid curve and indicates that the variation in the bimodal size distribution does not effect the ignition process.

The physics of the knife blade particle mounting technique is further investigated by studying the ignition of 21.5 μm Mg particles as a function of the knife blade mounting distance, x_{kb}. Figure 4.2 compares the measured and calculated ignition delay times of the Mg particles as a function of knife blade mounting distance. The experimental data represents measurements for

which the knife blade mounting distance ranged from x_{kb} = 2 mm to 29.5 mm. The experimental conditions corresponding to the plotted data are given in Table 4.1. The mean of the experimentally measured temperatures and pressures is 2684 K and 16.2 atm with standard deviations of 47 K and 1.1 atm. The ignition delay time calculations assumed an oxygen temperature and pressure of 2675 K and 16.0 atm.

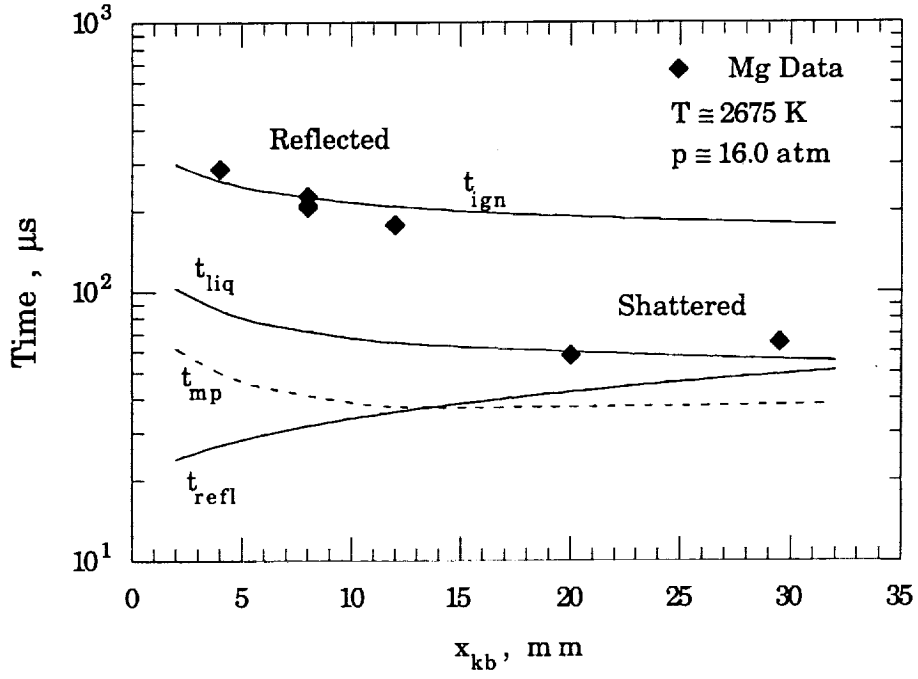

Fig. 4.2: Measured particle ignition delay time as a function of knife blade mounting distance.

The ignition delay times measured at knife blade mounting distances of 12 mm or less are clearly associated with the calculated ignition delay time, t_{ign}, plotted in Fig. 4.2 for comparison. However, as x_{kb} is increased from 12 mm to 20 mm, the measured ignition delay time drops precipitously from 177 μs to 58 μs and differs substantially from the calculated value. As the knife blade mounting

distance is further increased to 29.5 mm, the measured ignition delay time increases only slightly to 65 μs.

Also plotted in Fig. 4.2 are curves corresponding to the calculated times at which the Mg particles reflect from the endwall (t_{refl}), reach the melting point of Mg (t_{mp} = 923 K), and become molten (t_{melt}). The time has been plotted on a log scale in Fig. 4.2 so that the relationship between these three curves are clearly shown. It is evident that at knife blade mounting distances in excess of 20 mm, the measured ignition delay times are associated with these three curves.

Table 4.1: Measured ignition delay times for Mg particles as a function of knife blade mounting distance at T ≅ 2684 K and p ≅ 16.2 atm.

Shot #	x_{kb} (mm)	T_1 (K)	p_1 (psia)	M_{s_i}	T_5 (K)	p_5 (atm)	t_{ign} (μs)
108	4.0	301	1.18	4.93	2730	16.6	285
72	8.0	309	1.41	4.80	2690	18.5	226
103	8.0	308	1.18	4.87	2730	16.1	205
111	8.0	303	1.18	4.81	2650	15.6	210
115	8.0	307	1.18	4.75	2630	15.2	209
109	12.0	302	1.18	4.89	2700	16.3	177
114	20.0	306	1.18	4.74	2610	15.1	58
107	29.5	303	1.18	4.93	2740	16.5	65

Referring to Fig. 4.2, the calculated particle reflection time increases with x_{kb}, while the time required to reach the melting point and to become molten decreases as x_{kb} is increased. At x_{kb} > 13.5 mm, the heating model predicts that the particle will reach the melting point of Mg before the particle reflects from

the endwall. At x_{kb} = 30 mm, the time at which the particle reflects is nearly as large as the time required for the particle to become molten. Therefore, it is believed that the measured ignition times at x_{kb} = 20 mm and 29.5 mm are the result of the particles becoming "soft" before reflecting from the endwall, resulting in particle shattering or splattering and subsequent ignition of the small particle fragments. At knife blade mounting distances of less than 12 mm, the particles remain intact as they reflect from the endwall and continue to be heated to the point of ignition.

The shattering of the particles is further supported by comparing the measured light signals shown in Fig. 4.3. The signals correspond to the nominal ignition measurement taken at x_{kb} = 12 mm and the splattered ignition measurement taken at x_{kb} = 29.5 mm. The light signal measured at 29.5 mm is found to rise very abruptly and has an uncharacteristically narrow signal width, both of which are consistent with a reduced mean particle diameter.

Examination of the observation window, following the experiment in which x_{kb} = 29.5 mm, revealed a 16 mm diameter circular deposit of splattered particles. These deposits support the belief that the "soft" particles were splattered when they impacted the endwall, resulting in the expulsion of smaller particles which were then ignited. The splattering is believed to be similar to that of water droplets hitting a hard surface. Examination of the observation window after the nominal ignition experiment at x_{kb} = 12 mm revealed the presence of only a small number of individual particles, which is normally the case.

Based on these observations, it is evident that care must be taken to select a knife blade mounting distance which insures that the particles do not melt before reaching the window. Since a number of the particles are expected to be slowed by interactions with the knife blade boundary layer and wake, another

concern is the possibility that particles which stick to the window may experience a delayed ignition and interfere with the time delay measurements. To assess the possibility of particles igniting on the observation window, Luikov's solution [84] (see Appendix C) is used to calculate the surface temperature of the window over the range of experiment temperatures and pressures used in this investigation. The calculations used real oxygen properties and assumed room temperature values for the properties of the quartz observation window, which provide an upper limit on the calculated window temperature. The results of these calculations are shown in Fig. 4.4.

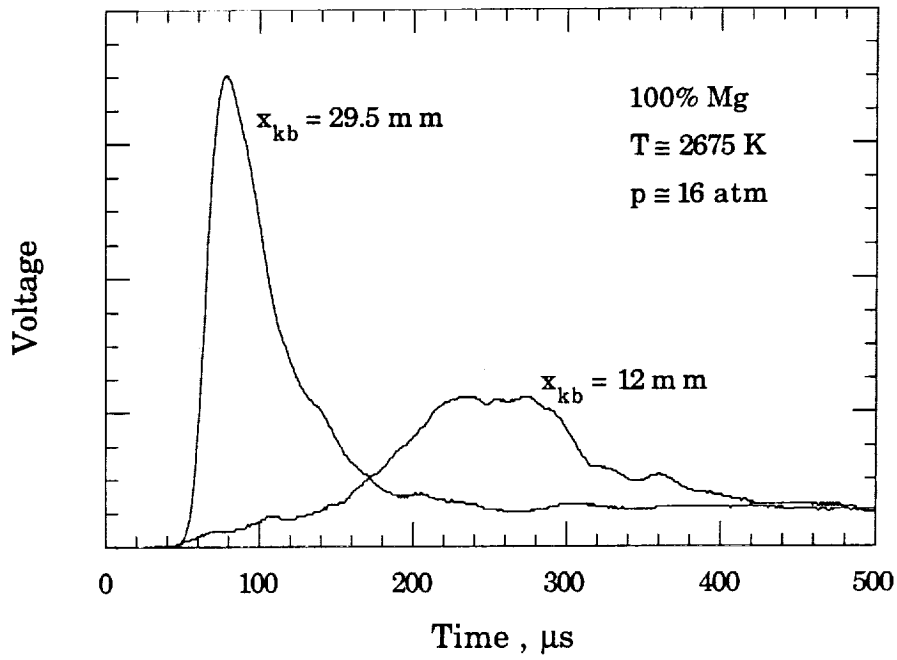

Fig. 4.3: Comparison of the measured light signals for non-splattered (x_{kb} = 12 mm) and splattered (x_{kb} = 29.5 mm) Mg particles. d_{eff} = 21.5 μm, T ≅ 2675 K, and p ≅ 16 atm.

Particles which stick to the observation window will be cooled to the temperature of the window's surface. Fig. 4.4 shows that the calculated window temperature will never exceed 400 K under the gas conditions of interest. Thus,

particles which stick to the window will be quenched and should never ignite. This phenomenon is supported experimentally. After each experiment, examination of the observation window usually showed a number of particles stuck to it. Microscopic examination indicates that these particles were unburnt. Driscoll et al. compensated for this cooling effect in their experiment by electrically heating their Al foil samples, which were mounted directly on the endwall [35].

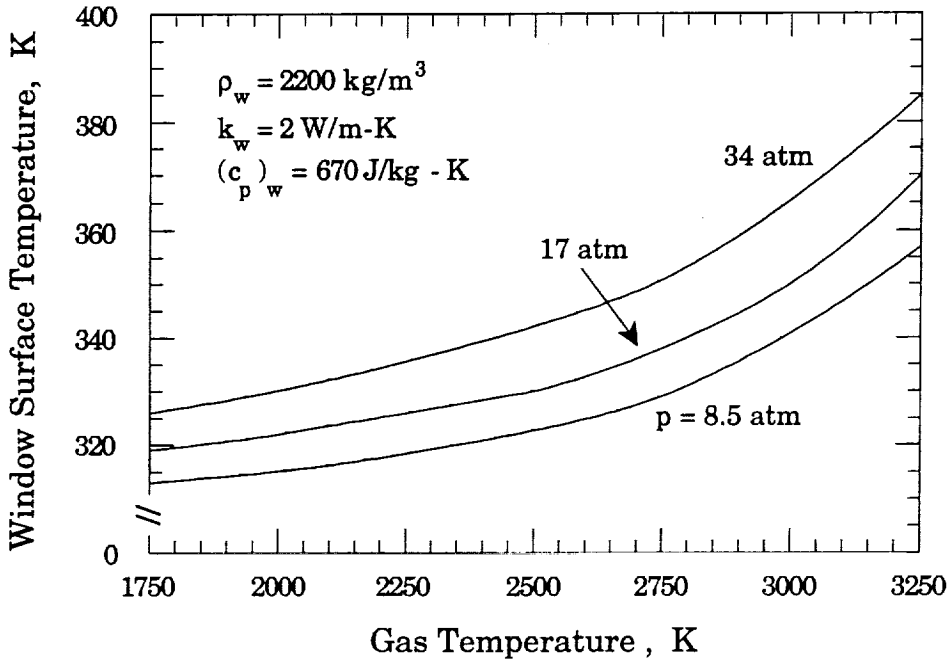

Fig. 4.4: Quartz window surface temperature as a function of gas temperature and pressure calculated using the analytical solution of Liukov.

Two experiments at 2250 K and 17 atm used 21.5 μm diameter, 40% Mg particles to specifically study this quenching phenomena. The particles were mounted directly on the window prior to the shot. The concussion of the shock reflection jarred many of the particles off the window, but those that remained were found to be unburnt and their appearance was identical to the particles

originally placed on the window. The particles which were jarred from the window were ignited, but showed a significant increase in their ignition delay times over particles ignited using the knife blade mounting technique under identical gas conditions. This is probably due to a combination of particle interaction with the endwall thermal layer and a reduction in the magnitude of the convective particle heat transfer coefficient.

The ignition delay time of 21.6 μm Al particles mounted directly on the endwall is also measured, and is compared with that measured for particles mounted on the knife blade 8 mm from the endwall. The gas temperature and pressure for these shots is approximately 3000 K and 17 atm. The measured ignition delay time for the particles initially mounted on the endwall is 1205 μs while two measurements made with the knife blade at 8 mm yield ignition delay times of 301 μs and 289 μs. The calculated ignition delay time at these gas conditions for a particle with zero velocity is 724 μs. The quadrupling of the measured ignition delay time can be accounted for by assuming the particles mounted on the endwall spend substantial time in the cool gas of the endwall thermal layer.

4.2 EFFECT OF GAS TEMPERATURE ON IGNITION DELAY TIME

The first series of ignition delay time measurements are made for Al and Mg particles as a function of oxygen temperature with the pressure held constant. This set of data is used to determine the magnitudes of the pre-exponential constants for both Al and Mg. These empirically determined pre-exponential constants are then used to model the remaining experimental data.

The reflected gas temperatures and pressures presented here are equal to those calculated using the NASA Gordon-McBride program [9]. The ignition

delay time of the particle is most sensitive to the temperature of the oxidizing medium in which the particle is heated. Based on the analyses of Section 2.4.4, the maximum uncertainty in the calculated reflected shock temperature, resulting from the uncertainties in the measurement of M_{s_i}, T_1, and p_1, is $w_{T_5} \equiv \pm 15$ K (see Fig. 2.54). This small uncertainty in the experimental gas temperature has no significant effect on the conclusions drawn from the data.

As discussed in Section 2.4.4, an additional error associated with the calculated reflected shock temperature is that due to the non-ideal reflection of the incident shock wave, which may result in a reflected shock temperature that is either slightly lower or higher (~1 to 2%) than that calculated assuming ideal shock reflection. An accurate measurement of this error was beyond the scope of this research. However, since the calculations will constistently over or under-predict the actual temperature, the error will have no significant effect on the overall trend of the data presented.

4.2.1 Pure Al and Mg

Table 4.2 shows the results of 20 measurements of the ignition delay time of 21.5 μm Al and 21.6 μm Mg particles. The knife blade is mounted 8 mm from the shock tube endwall. The measured reflected gas temperatures (referred to as T_5 or T) for Mg have a range of 1780 K ≤ T ≤ 3130 K, and for Al a range of 2430 K ≤ T ≤ 3280 K. The experiment pressure (referred to as p_5 or p) is held constant for these measurements. The Mg pressure has a mean of 16.4 atm, with a standard deviation of 1.1 atm, and the Al pressure has a mean of 17.1 atm, with a standard deviation of 0.9 atm.

Figure 4.5 displays the ignition delay time data of Table 4.2 plotted as a function of gas temperature. The Mg ignition delay time is found to be

Table 4.2: Measured ignition delay and combustion time of Mg and Al particles as a function of oxygen temperature. x_{kb} = 8 mm.

Shot #	Mg (wt. %)	T_1 (K)	p_1 (psia)	M_{s_i}	T_5 (K)	p_5 (atm)	t_{ign} (μs)	t_b (μs)
64	0	300	1.46	4.55	2430	17.0	549	312
65	0	300	1.41	4.64	2500	17.0	607	297
60	0	300	1.41	4.71	2560	17.7	606	206
110	0	304	1.18	4.70	2570	14.8	518	613
61	0	301	1.18	4.93	2720	16.6	396	319
102	0	307	1.18	4.89	2730	16.3	434	-
90	0	311	1.18	5.03	2860	17.5	365	-
58	0	300	1.05	5.30	2970	17.6	301	374
59	0	300	1.05	5.36	3010	18.1	289	248
66	0	300	.83	5.86	3270	17.8	197	317
62	0	301	.81	5.89	3280	17.5	209	214
71	100	309	2.58	3.67	1780	16.8	826	249
73	100	306	2.06	3.95	1980	16.4	577	264
68	100	308	2.05	4.01	1990	16.9	595	242
74	100	304	1.83	4.21	2180	17.2	520	259
115	100	307	1.18	4.75	2630	15.2	209	238
111	100	303	1.18	4.81	2650	15.6	210	161
72	100	309	1.41	4.80	2690	18.5	226	189
130	100	308	1.18	4.87	2730	16.1	205	204
70	100	310	.83	5.51	3130	15.3	142	228

significantly less than that of Al. Also shown in the figure are solid and dashed curves corresponding to ignition model calculations, with and without surface oxidation, respectively. For all model calculations presented, the model parameters are e = 0.4, ε_p = 0.9, C_w = 0.8, and $(E_a)_{Mg} = (E_a)_{Al}$ = 22,800 cal/mol (corresponding to the published activation energy of Al [74]). The calculations use real oxygen properties over the temperature range 1750 K ≤ T ≤ 3250 K and assume an experiment pressure of 17 atm.

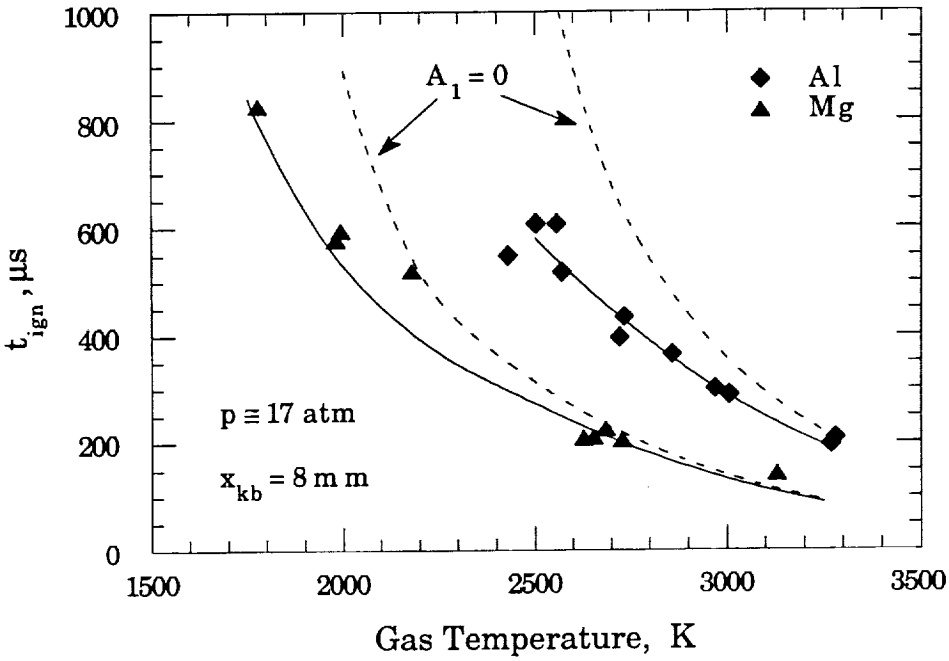

Fig. 4.5: Measured and calculated ignition delay time versus gas temperature for Al and Mg particles at p ≅ 17.0 atm. The solid curves assume $(A_1)_{Mg}$ = 400 kg/m^2-s and $(A_1)_{Al}$ = 200 kg/m^2-s. The dashed curves assume no heterogeneous reaction. The knife blade is mounted 8 mm from the endwall (x_{kb} = 8 mm).

The solid curves in Fig. 4.5 are calculated assuming a linear heterogeneous surface reaction. The empirical pre-exponential constant for Al is $(A_1)_{Al}$ = 200 kg/m^2-s, and is determined by fitting the experimental data at

T = 2500 K. The empirical pre-exponential constant for Mg is $(A_1)_{Mg}$ = 400 kg/m^2-s, and is determined by fitting the experimental data at T = 1750 K. The model correctly predicts the overall trend of the data. Note that as the gas temperature is increased, the reacting and non-reacting calculations converge as the convective heat transfer rate becomes dominant.

The calculations assume that the onset of detached (gas phase) combustion for Mg occurs at the Mg boiling point (1812 K at 17 atm), and for Al at the Al_2O_3 melting point (2300 K). The dashed curves in Fig. 4.5 correspond to calculations made assuming there is no heterogeneous reaction (A_1 = 0) to contribute to particle heating. Elimination of particle self heating from the model is found to cause a significant over-prediction of the ignition delay time for both metals at the lower gas temperatures. Without self heating the calculated ignition delay time is infinite at 1812 K for Mg and 2300 K for Al, in contradiction to the data.

Two values of the Mg surface reaction activation energy are given in the literature: 23,700 and 50,500 cal/mole [14]. For the higher value, the pre-exponential constant is increased to $(A_1)_{Mg} = 2.7 \times 10^6$ kg/m^2-s, but the calculated ignition delay time is not significantly changed. The result of the Mg calculation (dashed curve) with $(E_a)_{Mg}$ = 50,500 cal/mole is plotted in Fig. 4.6, along with the corresponding Mg data and the result of the standard ignition model with $(E_a)_{Mg}$ = 22,800 cal/mole (solid curve). The calculations show that for the gas conditions and particle sizes being investigated, different values of $(E_a)_{Mg}$ do not significantly change the result of the ignition time delay calculation.

For Al, the surface reaction is also modeled assuming a parabolic oxidation law [74]. The calculations assume an initial oxide thickness of 0.004 μm [14] and an empirically determined parabolic pre-exponential constant of

$(A_1)_{Al}$ = 7.0 x 10^{-6} kg/m-s. The result of the parabolic Al calculation (dot-dashed curve) is plotted in Fig. 4.6, along with the corresponding Al data and the result of the linear calculation (solid curve). The calculated parabolic ignition delay time is nearly identical to that calculated assuming a linear heterogeneous reaction rate. This result is in agreement with Merzhanov [12], who states that the high-temperature oxidation of Al in oxygen is independent of oxide thickness to 0.5 μm, and the model of Gurevich et al. [85] which assumes the oxidation rate depends on the oxide film structure and temperature, but not its thickness.

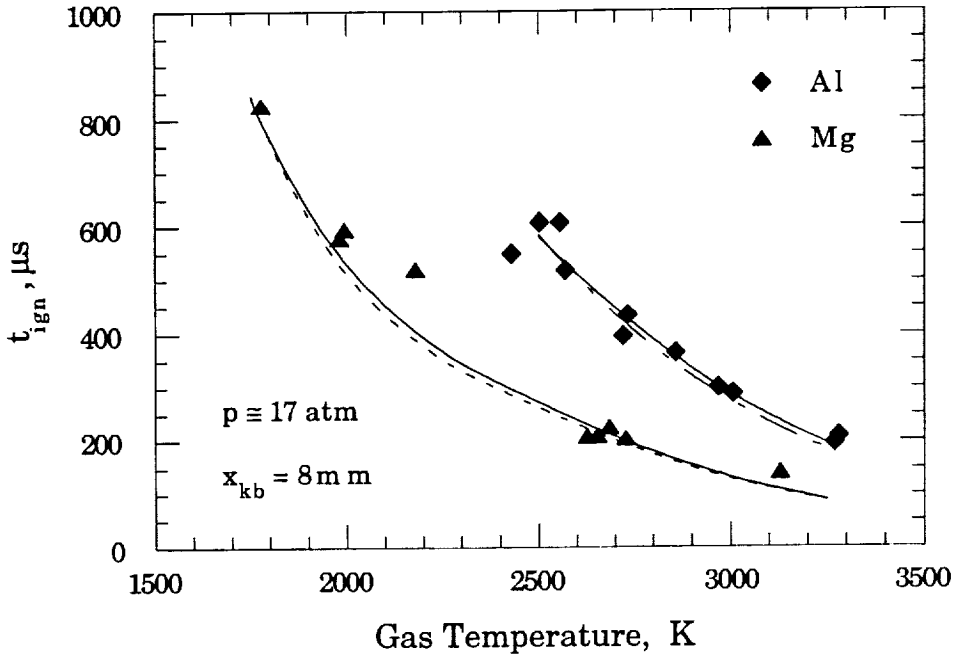

Fig. 4.6: Measured and calculated ignition delay time versus gas temperature for Al and Mg particles at p ≅ 17.0 atm. The solid curves correspond to those of Fig. 4.5. The dashed curve assumes a linear oxidation law for Mg with $(E_a)_{Mg}$ = 50,500 cal/mole and $(A_1)_{Mg}$ = 2.7x10^6 kg/m^2-s. The dot-dashed curve assumes a parabolic oxidation law for Al with $(A_1)_{Al}$ = 7.0x10^{-6} kg/m-s and $(E_a)_{Al}$ = 22,800 cal/mole.

Based on these calculations a linear reaction rate is assumed here and the activation energies of both Al and Mg and their alloys are chosen to be equal, so that variations in the pre-exponential constant can be compared directly.

The accuracy of any particle ignition model depends on how accurately one knows the thermoconductivity of the oxidizing atmosphere. NASA's Gordon-McBride program [9] calculates two thermal conductivities at each temperature and pressure of interest, an equilibrium value and a frozen value. When a gas is dissociated, the equilibrium conductivity is always larger than the frozen value. The reason for this is that if local chemical equilibrium exists, the composition of the gas will vary with temperature and concentration gradients will form. The concentration gradients then result in the transport of chemical enthalpy by molecular diffusion [86].

Figure 4.7a shows the calculated equilibrium and frozen thermal conductivities for oxygen as a function of temperature at the three experiment pressures investigated, 8.5 atm, 17.0 atm, and 34.0 atm. The frozen conductivities all lie on the same linearly varying curve, independent of pressure. The equilibrium conductivities diverge from the frozen value at a temperature of approximately 2000 K. As the temperature increases, the equilibrium conductivity increases significantly in a nonlinear fashion. The magnitude of the equilibrium conductivity is found to be inversely related to the pressure, as is the degree of dissociation of the gas. At T = 3000 K, the equilibrium conductivity at p = 8.5 atm is three times greater than the corresponding frozen conductivity.

Svehla states that the thermal conductivity of all reacting systems will lie somewhere between the nonreacting frozen state and a state of chemical equilibrium [86]. The exact value of the thermal conductivity will be determined by the kinetics of the various reactions involved. Since each physical system is

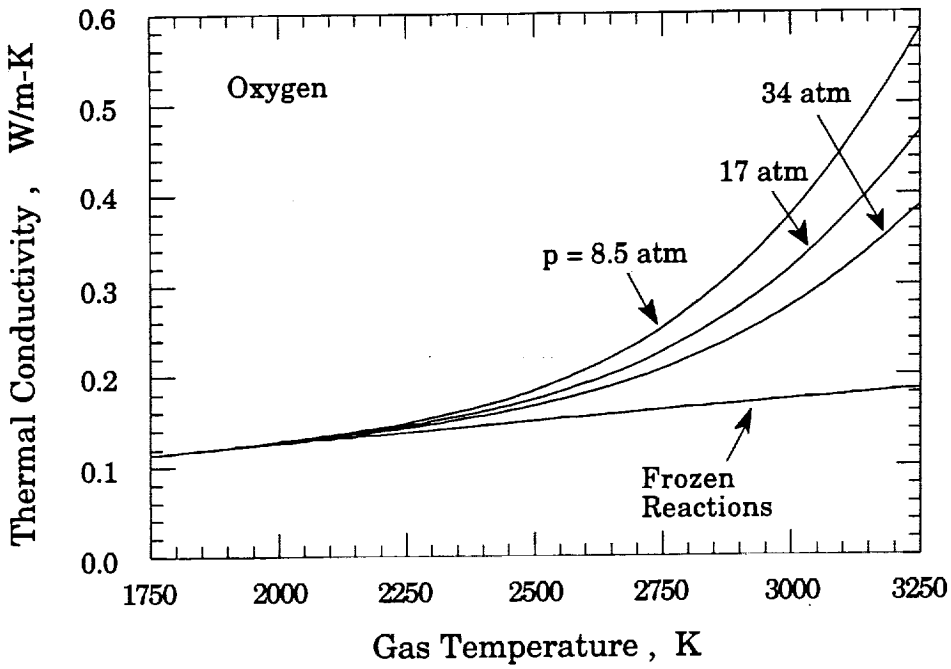

(a)

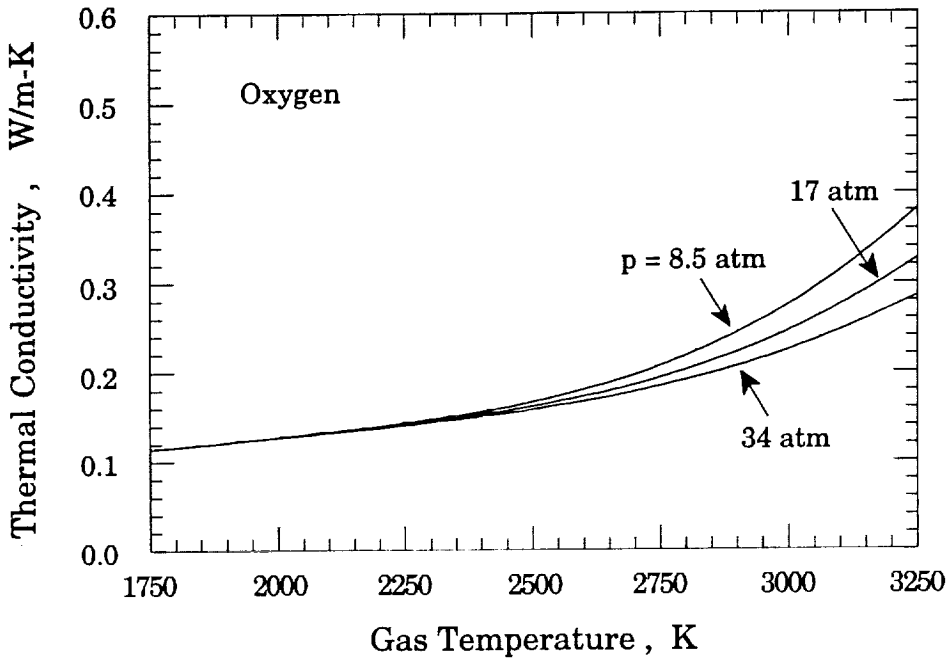

(b)

Fig. 4.7: Calculated oxygen thermal conductivity as a function of gas temperature and pressure. a.) Equilibrium and frozen conductivities. b.) Average conductivities used in ignition model.

different, it is impossible to determine a generalized thermal conductivity. Consequently, an average thermal conductivity is used in all of the model calculations presented in this work, unless stated otherwise. Figure 4.7b presents the averaged thermal conductivity for oxygen as a function of temperature and pressure. The average is simply computed as $\overline{k_g} = \frac{1}{2}\left[(k_g)_e + (k_g)_f\right]$, where $\overline{k_g}$, $(k_g)_e$, and $(k_g)_f$ are the average, equilibrium, and frozen thermal conductivities, respectively.

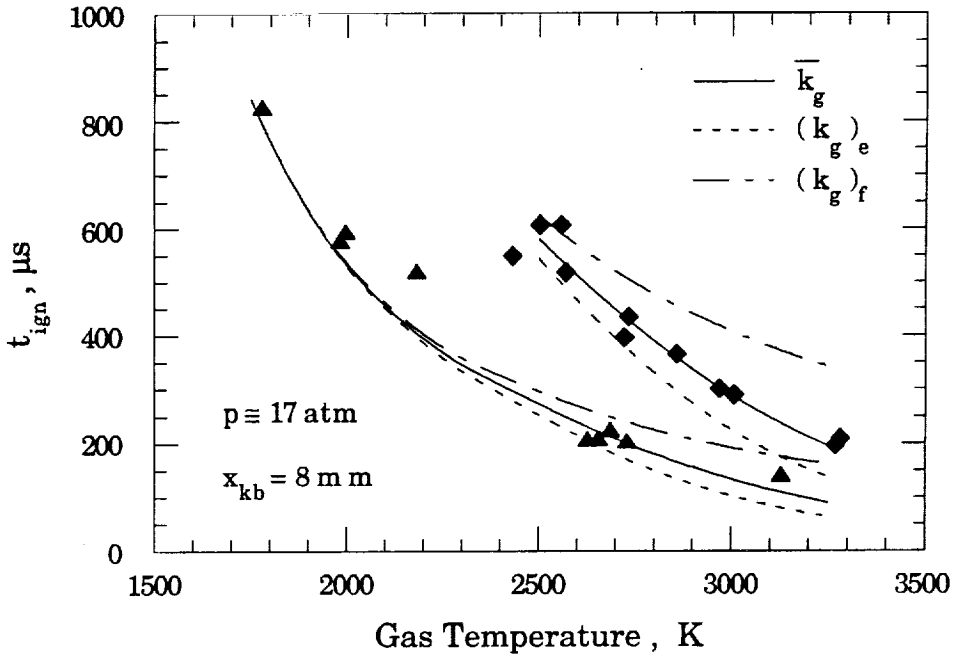

Fig. 4.8: Effect of the assumed oxygen thermal conductivity on the calculated ignition delay time of Mg and Al particles. The dashed, dot-dashed, and solid curves are calculated assuming equilibrium, frozen, and an average thermal conductivity, respectively.

The effect of k_g on ignition delay is shown in Fig. 4.8, which shows the measured Al and Mg ignition delay times as a function of gas temperature, plotted along with the predicted times calculated assuming averaged,

equilibrium, and frozen values of the oxygen thermal conductivity. For both Al and Mg, the averaged thermal conductivity is found to fit the data accurately, while the equilibrium and frozen conductivities underpredict and overpredict t_{ign}, respectively. The error in the predicted t_{ign} increases with gas temperature, as is expected. Since heat transfer becomes the dominant particle heating mechanism at the higher gas temperatures, and the choice of the surface reaction pre-exponential constant becomes less significant, the calculations indicate that an averaged conductivity is indeed the appropriate choice.

The effect of the choice of the various ignition model parameters, e, C_w, and A_1 on the ignition delay time predictions will now be investigated. Figures 4.9, 4.10, and 4.11 compare the measured t_{ign} of Al particles versus gas temperature with calculations made assuming various values of the ignition model parameters. The Al data corresponds to that presented in Table 4.2 and Fig. 4.5.

Figure 4.9 shows the variation in the ignition delay time of Al calculated assuming e = 0.2, 0.4, and 0.6. The results indicate that the predicted ignition delay time is only mildly dependent on the choice of e. The overall trend of the predicted ignition delay time is unaffected by the choice of e, indicating that an uncertainty in the choice of e will only result in a slight change in the empirically determined A_1. The general conclusions drawn from the ignition model will not be altered.

The wake coefficient, C_w, represents the drag deficit experienced by the particle during acceleration behind the incident shock due to the presence of the knife blade oblique shocks, boundary layer, and wake (see Chapter 3). Figure 4.10 shows the results of Al t_{ign} predictions calculated assuming C_w = 0.6, 0.8, and 1.0. The calculated ignition delay time is found to be an extremely weak

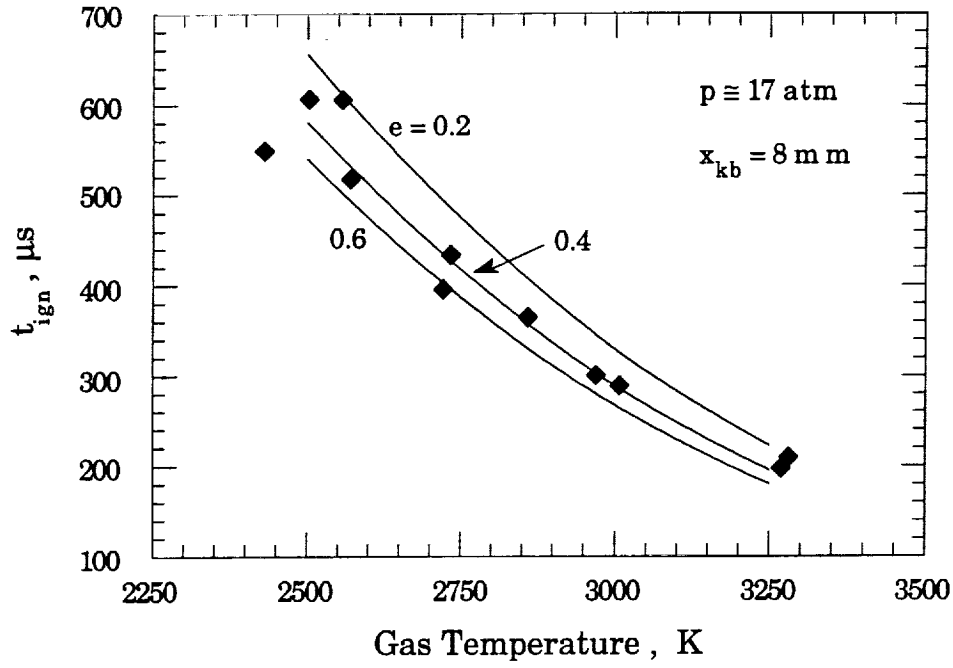

Fig. 4.9: Effect of the particle coefficient of restitution, e, on the calculated Mg and Al particle ignition delay time versus gas temperature. Calculations assume p = 17 atm and x_{kb} = 8 mm.

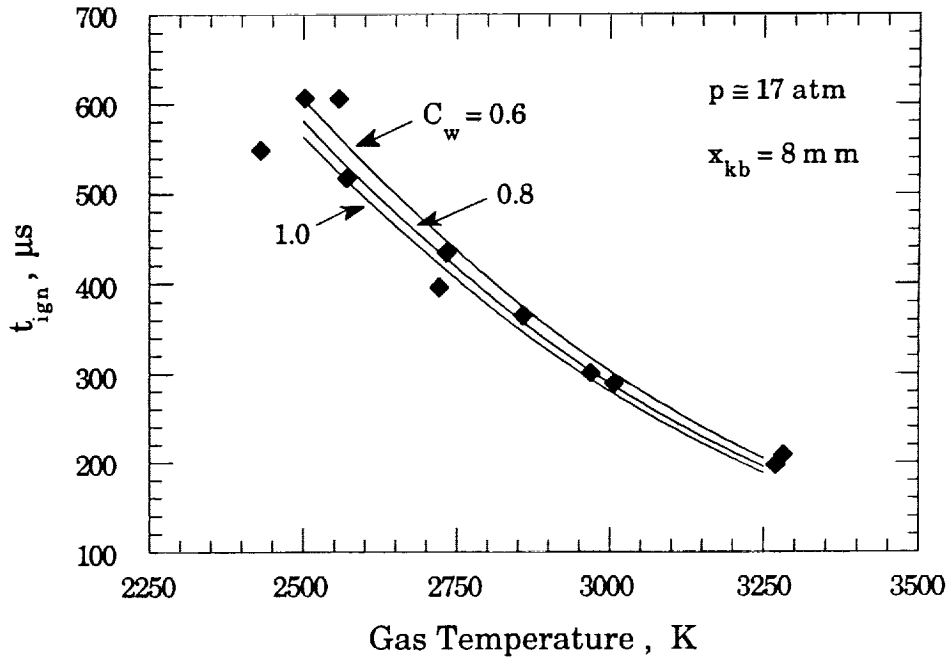

Fig. 4.10: Effect of the knife blade wake coefficient, C_w, on the calculated Mg and Al particle ignition delay time versus gas temperature. Calculations assume p = 17 atm and x_{kb} = 8 mm.

function of the wake coefficient. Therefore, C_w = 0.8 was chosen as the standard value for all of the model calculations presented.

Figure 4.11 shows the effect which variations in the magnitude of the pre-exponential constant $(A_1)_{Al}$ has on the calculated Al ignition delay time. At the highest gas temperature, T = 3250 K, convective heat transfer dominates and the variation in t_{ign} due to variations in $(A_1)_{Al}$ are small. However, as the gas temperature is decreased, the heterogeneous reaction's contribution to particle heating becomes increasingly important. At the lowest temperature of about T = 2500 K, the calculated ignition delay time becomes very sensitive to the magnitude of $(A_1)_{Al}$. Thus, the empirically determined $(A_1)_{Al}$ and $(A_1)_{Mg}$ are fit to the lowest temperature data available, since this provides the most sensitive determination of the pre-exponential constant.

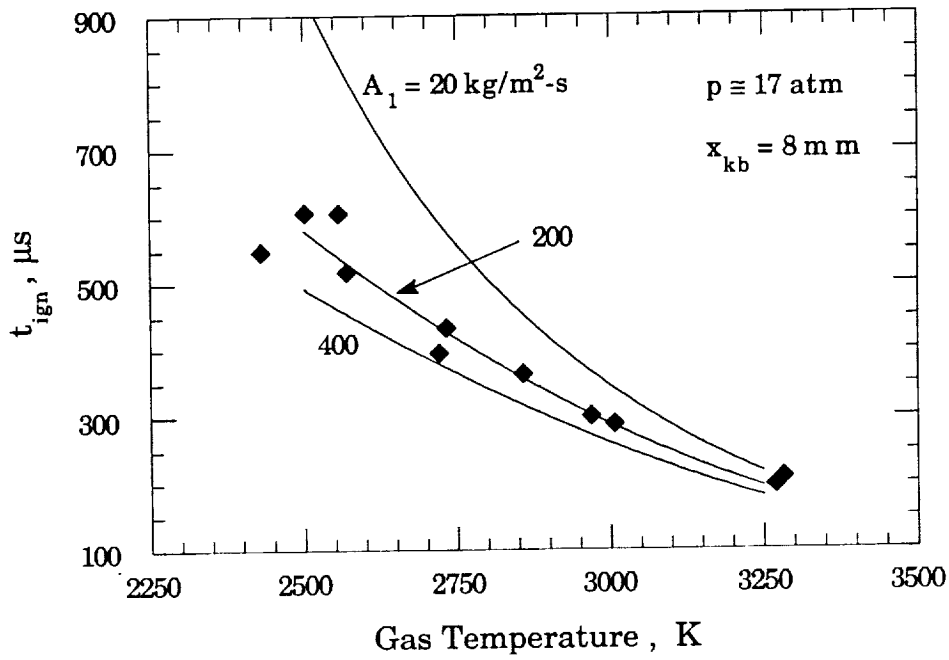

Fig. 4.11: Effect of the heterogeneous reaction pre-exponential constant, A_1, on the calculated Mg and Al particle ignition delay time versus gas temperature. The calculations assumed p = 17 atm and x_{kb} = 8 mm.

Further insight into the physics of the Al and Mg particle ignition processes, and the knife blade mounting technique, are obtained by closely examining the results of the ignition model calculations. The results presented in Figs. 4.12 thru 4.18 are based on the calculations first presented in Fig. 4.5.

Shown in Figs. 4.12a and 4.12b are the calculated t_{refl}, t_{mp}, and t_{melt} as a function of experiment temperature for Mg and Al. The Mg and Al particles are predicted to reflect from the endwall at approximately t_{refl} = 40 μs and 35 μs, respectively. It is interesting to note that t_{refl} is predicted to be nearly independent of the gas temperature, and therefore independent of the incident shock Mach number, which ranges from $3.7 \leq M_{s_i} \leq 5.8$.

The particles are predicted to reflect from the window prior to reaching their melting points at gas temperatures up to 2900 K for Mg and 3000 K for Al. The particles are never predicted to melt prior to reflection. Although the ignition delay time of Al is measured at a gas temperature near 3300 K, and that of Mg near 3100 K (see Fig. 4.5), the particles do not appear to experience the splattering type of ignition discussed in section 4.1. If they had splattered at these temperatures, the measured ignition delay times would have been substantially reduced to near that of the particle reflection times, which are on the order of 50 μs.

The solid curves shown in Fig. 4.13 are the calculated mass fraction of the particle oxidized by heterogeneous reaction at the time of ignition, as a function of temperature. It is found that less than two percent of the particle's initial mass is consumed by heterogeneous reaction prior to ignition, which is quite reasonable. The oxidized mass fraction of the Mg particle is predicted to be a nonlinear function of the gas temperature, while the oxidized mass fraction for Al is predicted to vary in a nearly linear manner. As expected, the oxidized

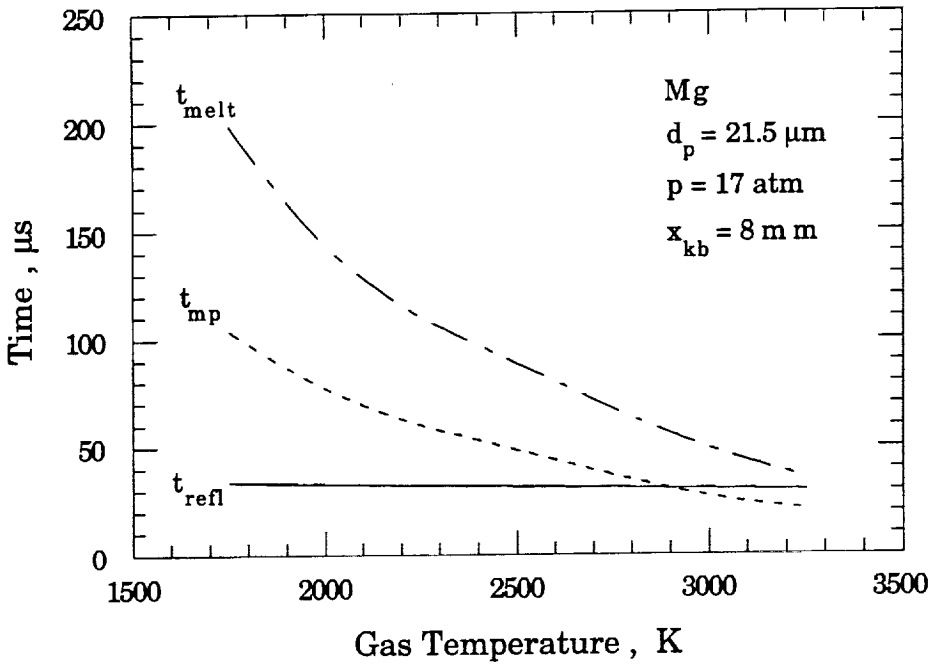

(a)

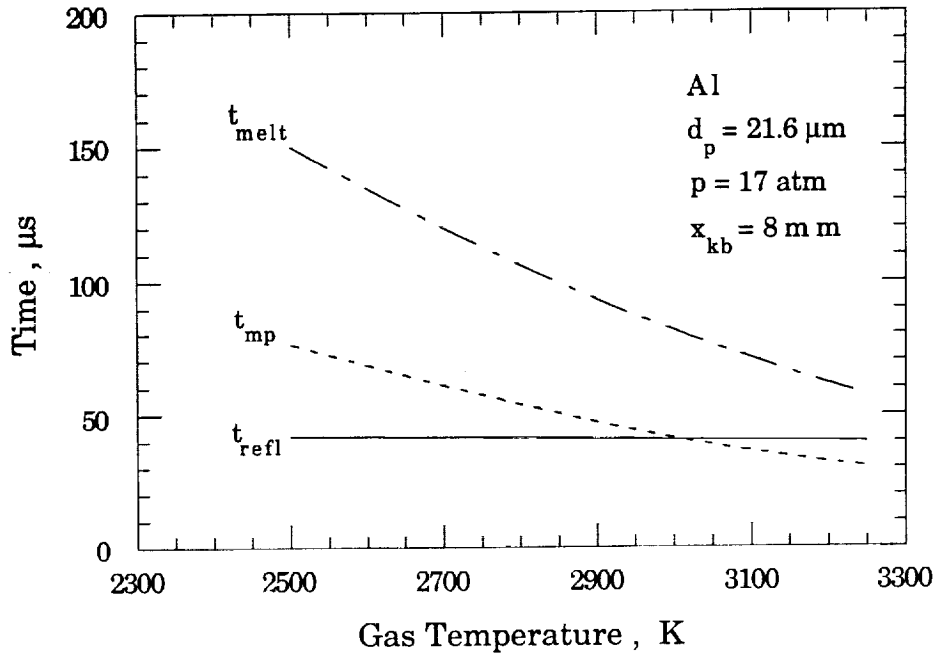

(b)

Fig. 4.12: Calculated times of particle reflection, onset of softening, and melting as a function of gas temperature. The calculations assume p = 17 atm and x_{kb} = 8 mm. a) 21.5 μm diameter Mg particles. b) 21.6 μm diameter Al particles.

mass fraction is inversely related to the gas temperature, since the rate of convective heat transfer becomes dominant at higher gas temperatures.

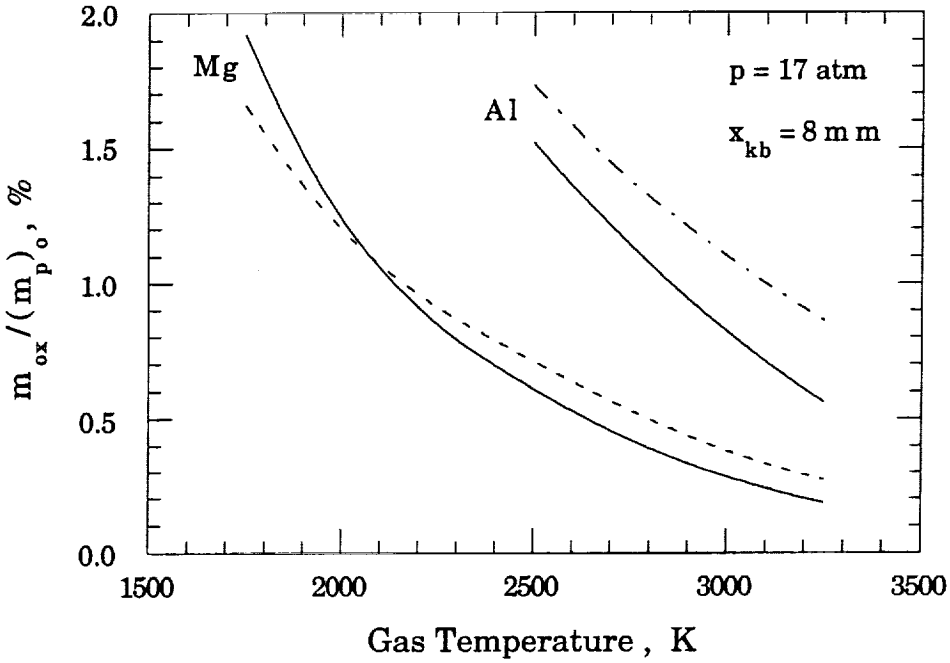

Fig. 4.13: Mg and Al oxidized particle mass fraction versus gas temperature calculated assuming p = 17 atm and x_{kb} = 8 mm. The solid curves correspond to the calculations shown in Fig. 4.6. The dashed curve assumes $(E_a)_{Mg}$ = 50,500 cal/mole and $(A_1)_{Mg}$ = 2.7x10^6 kg/m^2-s. The dot-dashed curve assumed a parabolic oxidation rate for Al.

The dashed curve in Fig. 4.13 corresponds to a Mg calculation with the larger heterogeneous reaction activation energy and pre-exponential constant of 50,500 cal/mole and 2.7x10^6 kg/m^2-s, respectively (refer to Fig. 4.6 and related discussion). Once again, the choice of $(E_a)_{Mg}$ does not significantly change the conclusions drawn from the results of the model calculations. The dashed-dot curve in Fig. 4.13 was calculated assuming a parabolic relation for the Al heterogeneous reaction (refer to Fig. 4.6 and related discussion). Although the mass fraction oxidized by the parabolic reaction is predicted to be slightly greater

than that of the linear reaction, both curves have nearly identical slopes and the resulting conclusions are not altered. It is believed that these results bolster the choice of a linear form for the heterogeneous reaction rate and associated parameters.

If it is assumed that the heterogeneous reaction occurs uniformly over the surface of the particle, it is possible to define an oxide penetration depth, δ_{ox}, as being equal to the difference between the initial radius of the metal (neglecting oxide thickness) and the radius of the metal at the time of ignition; $\delta_{ox} = r_i - r_{ign}$. Figure 4.14 shows the oxide penetration depth of the Mg and Al particles plotted as a function of the gas temperature. The calculations are based on a constant, room temperature metal density. As is expected, the oxide penetration depth follows the same trend as the oxidized mass fraction. The predicted maximum penetration depths are 0.070 μm for Mg and 0.055 μm for Al, and represent a change in radius of only 0.65 percent and 0.51 percent, respectively. The calculations indicate that, even in the most extreme cases, the calculated depths of oxide penetration are minimal.

The calculated fraction of energy supplied to heat the particles by the heterogeneous surface reaction is shown in Fig. 4.15. The reaction energy fraction is defined as:

$$\eta_{ox} = e_{ox} / (e_{ht} + e_{ox}) \tag{4.1}$$

where e_{ox} is the total energy produced by the heterogeneous reaction and e_{ht} is the total energy transferred to the particle through convective heat transfer. The model predicts that less than 1% of the total energy transferred to the particle and produced by reaction is lost radiatively (see Fig. 4.42 and related discussion), even though a relatively high particle emissivity, $\varepsilon_p = 0.9$, was chosen based on

the work of Brewster and Taylor [37]. The calculations predict that approximately 21 percent of the total energy needed to ignite the Mg particle at T = 1750 K is produced by the heterogeneous reaction. If the gas temperature is increased to T = 3250 K, this number drops to only 2 percent. Similarly, approximately 18 percent of the Al particle's ignition energy is produced by heterogeneous reactions at T = 2500 K, and only 6 percent at T = 3250 K.

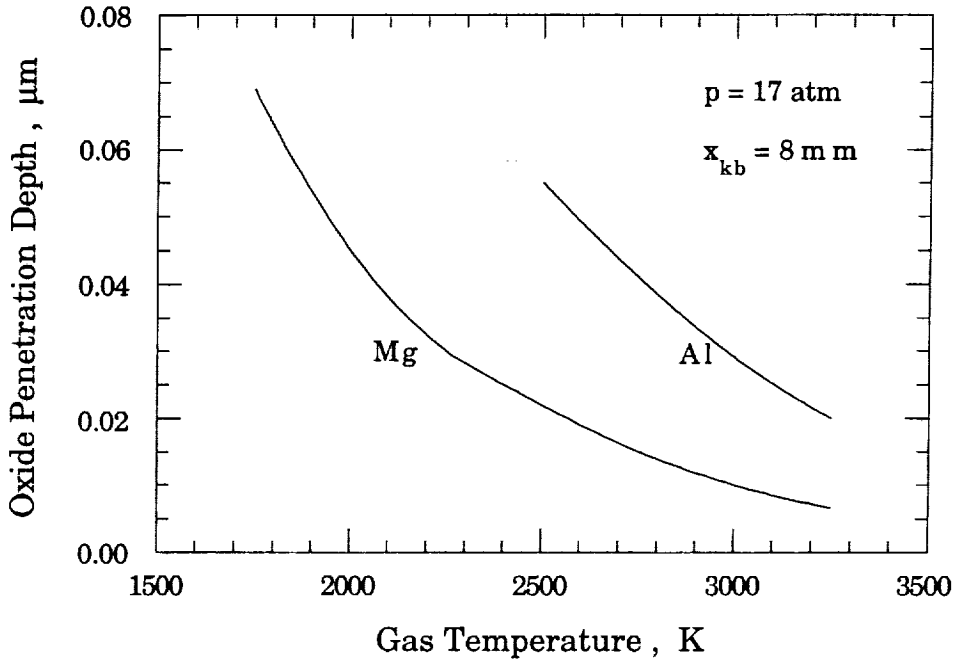

Fig. 4.14: Calculated Mg and Al oxide penetration depth versus gas temperature calculated assuming p = 17 atm and x_{kb} = 8 mm. The corresponding ignition delay time calculations are shown in Fig. 4.5.

The experimental measurement of the ignition delay time of the Mg and Al particles as a function of temperature is made while holding the gas pressure and knife blade mounting distance constant. Since the incident shock Mach number has to be varied in order to produce the temperatures of interest,

the conditions behind the incident shock are also varied. This variation in v_2, ρ_2, T_2, and p_2, results in a variation in the particle velocities. Therefore, it is important that the impact of this velocity variation on the rate of particle heating be assessed.

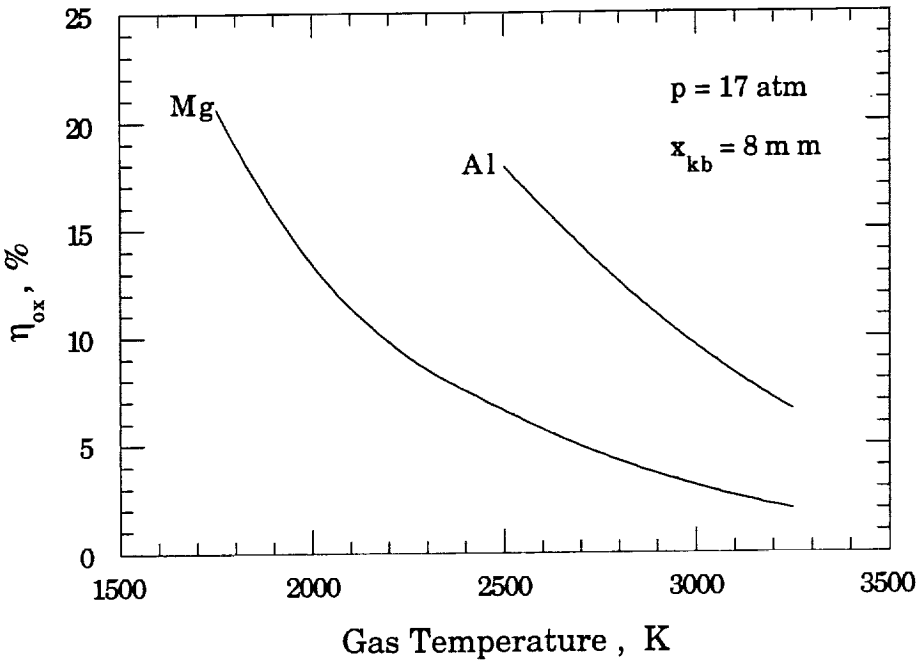

Fig. 4.15: Mg and Al reaction energy fraction versus gas temperature calculated assuming p = 17 atm and x_{kb} = 8 mm. The corresponding ignition delay time calculations are shown in Fig. 4.5.

Figure 4.16 shows the time-integrated particle Reynolds number, $\overline{Re_p}$, calculated for the Mg and Al particles as a function of gas temperature. For the Mg particles, the time-integrated Reynolds numbers are calculated to range from $\overline{Re_p}$ = 42 at T = 1750 K to $\overline{Re_p}$ = 74 at T = 3250 K, and deviates only slightly from a linear relationship. The Al particles are calculated to have $\overline{Re_p}$'s which vary linearly from $\overline{Re_p}$ = 38 at T = 2500 K to $\overline{Re_p}$ = 46 at T = 3250 K. The difference

in the magnitude of the two curves is due to the fact that the Al/Mg particle mass ratio is 1.55. The acceleration, and thus the velocity, of the lighter Mg particles in region 2 is about 1.55 times that of the heavier Al particles. The ratio of the two curves at any gas temperature , which is equal to the ratio of the time-integrated particle velocities, is approximately 1.6 and correlates well with the Al/Mg particle mass ratio.

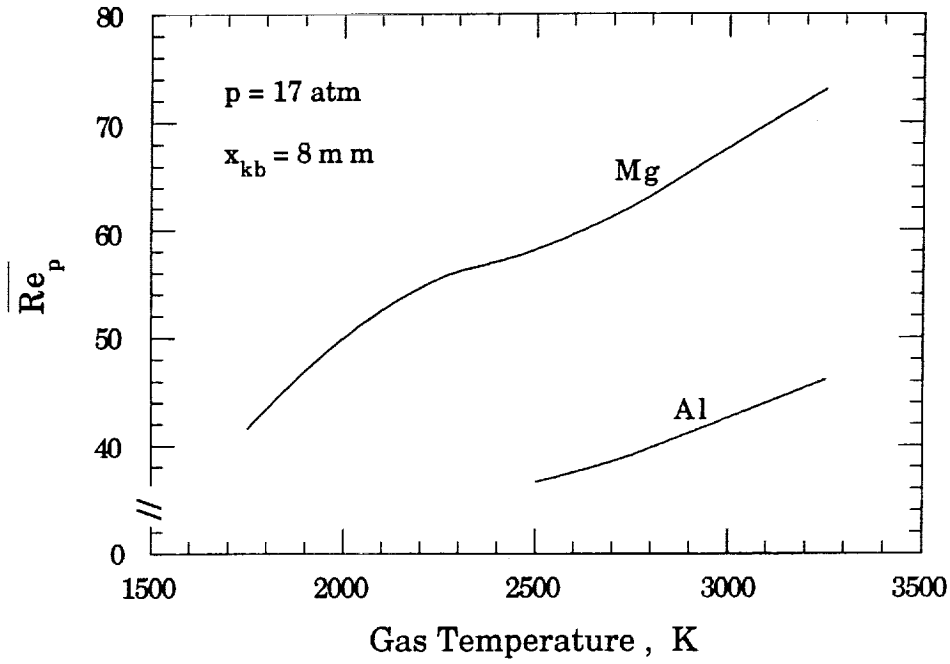

Fig. 4.16 Mg and Al time-integrated particle Reynolds number versus gas temperature calculated assuming p = 17 atm and x_{kb} = 8 mm. The corresponding ignition delay time calculations are shown in Fig. 4.5.

The corresponding time-integrated surface-averaged Nusselt numbers, $\overline{Nu_p}$, are plotted as a function of gas temperature in Fig. 4.17. Due to the dependence of Nu_p on the particle Reynolds number, $\overline{Nu_p}$ exhibits the same general trend as that shown by $\overline{Re_p}$ in the previous figure. However, since the dependence of the surface-averaged Nusselt number on the particle Reynolds

number is basically of the form $Nu_p = A + B(Re_p)^{0.55}$ (see Eq. (3.23)), the magnitude of the variation in $\overline{Nu_p}$ is substantially less than that of $\overline{Re_p}$. For Mg, the value of $\overline{Nu_p}$ increases from 4.52 at T = 1750 K to 5.47 at T = 3250 K, an increase of 21 percent. Over the same temperature range, $\overline{Re_p}$ increases by 76 percent. For Al, the particle surface-averaged Nusselt numbers and particle Reynolds numbers are predicted to increase by 7 percent and 21 percent, respectively, over the range of gas temperatures investigated.

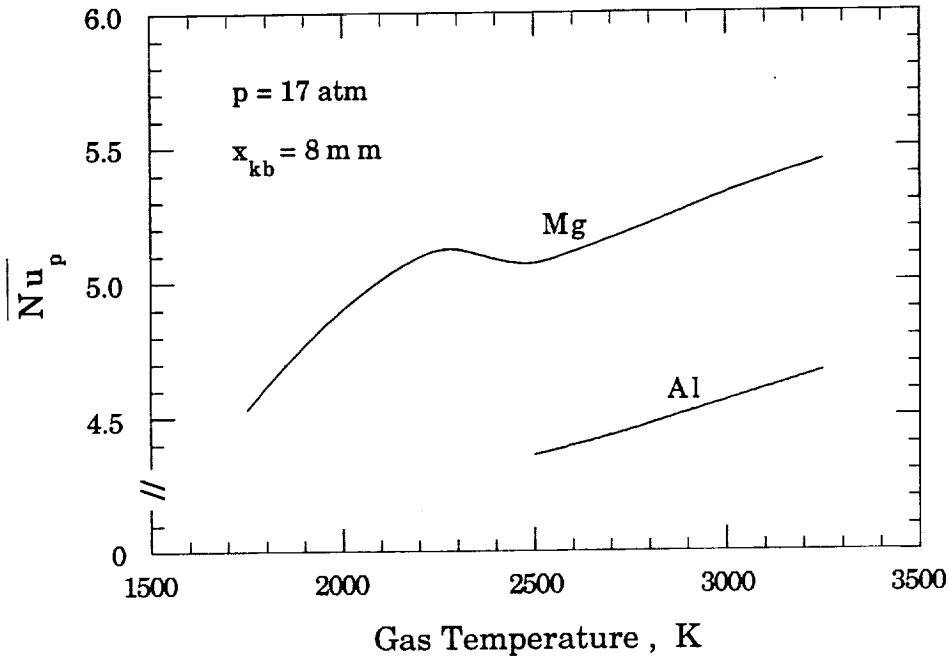

Fig. 4.17: Mg and Al time-integrated particle surface-averaged Nusselt number versus gas temperature calculated assuming p = 17 atm and x_{kb} = 8 mm. The corresponding ignition delay time calculations are shown in Fig. 4.5.

Figure 4.18 shows the time-integrated Biot number for the Mg and Al particles, where $\overline{Bi} = \frac{1}{6}(k_g/k_p)\overline{Nu_p}$, plotted versus gas temperature. The calculations use the room temperature thermal conductivity of Mg and Al and the averaged real thermal conductivity of oxygen. The error associated with

using the lumped capacitance energy balance is small if $\overline{Bi} \leq 0.1$ [62]. The calculations show that for the gas conditions and particle characteristics investigated here, the maximum time-integrated Biot number is never larger than $\overline{Bi} = 0.002$. Therefore, the lumped capacitance energy balance used in the formulation of the particle heating model is well suited to the analysis of the measurements of this investigation.

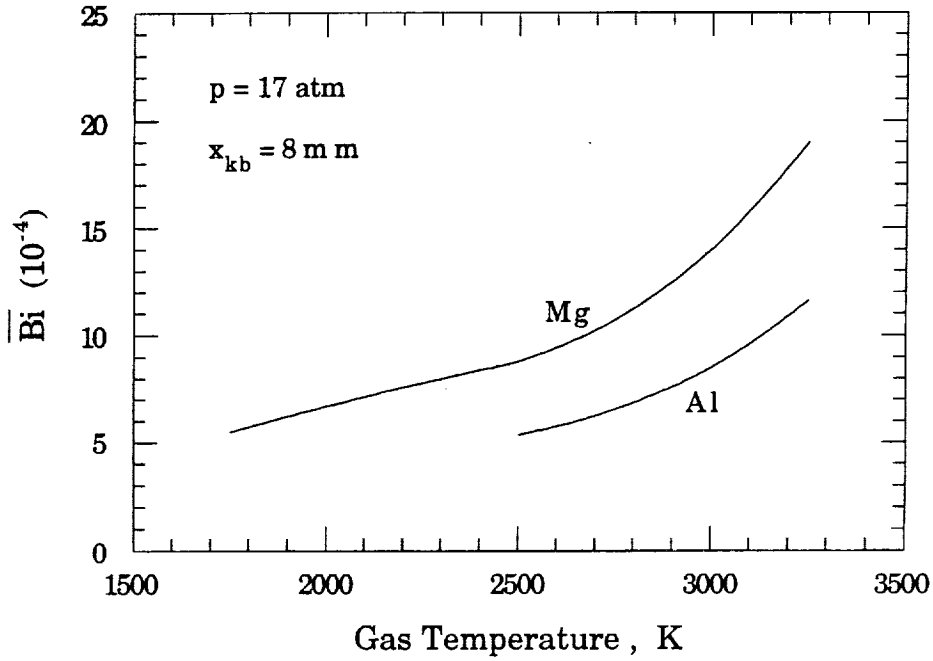

Fig. 4.18: Mg and Al time-integrated particle Biot number versus gas temperature calculated assuming p = 17 atm and x_{kb} = 8 mm. The corresponding ignition delay time calculations are shown in Fig. 4.5.

4.2.2 20% Mg and 60% Mg Alloy

The variation of the particle ignition delay time at two alloy compositions will now be compared to that of the pure metals. Table 4.3 shows the results of 15 measurements of the ignition delay time, tabulated for 20% Mg and 60% Mg

alloy particles, with mean particle diameters of 21.2 μm and 21.6 μm, respectively. The knife blade is mounted at x_{kb} = 8 mm from the shock tube endwall. The measured experiment temperature has a range of 2000 K ≤ T ≤ 3050 K for 20% Mg and 1978 K ≤ T ≤ 3015 K for 60% Mg. The experiment pressure is held constant for these measurements. The 20% Mg pressure has a mean of 17.2 atm, with a standard deviation of 0.6 atm, and the 60% Mg pressure has a mean of 16.8 atm, with a standard deviation of 0.6 atm.

Table 4.3: Measured ignition delay and combustion time of 20% Mg and 60% Mg alloy particles as a function of oxygen temperature. x_{kb} = 8 mm.

Shot #	Mg (wt. %)	T_1 (K)	p_1 (psia)	M_{s_i}	T_5 (K)	p_5 (atm)	t_{ign} (μs)	t_b (μs)
83	20	308	2.06	3.99	2000	17.0	801	364
85	20	305	1.69	4.29	2250	16.7	435	388
87	20	307	1.69	4.39	2350	17.7	449	304
88	20	309	1.39	4.62	2540	16.6	366	184
82	20	308	1.41	4.63	2550	17.0	414	134
86	20	308	1.18	4.93	2770	16.6	269	256
91	20	310	1.18	5.04	2860	17.6	232	200
84	20	307	1.06	5.37	3050	18.4	183	194
78	60	304	2.06	3.96	1980	16.5	624	302
75	60	306	1.61	4.36	2320	16.6	471	183
76	60	304	1.44	4.52	2430	16.3	372	140
175	60	296	1.18	4.94	2700	16.7	280	160
79	60	306	1.18	4.89	2730	16.3	258	132
80	60	307	1.05	5.28	3000	17.5	175	156
77	60	306	1.05	5.32	3020	17.8	171	160

Figure 4.19 shows the measured ignition delay time data of Table 4.3 plotted as a function of gas temperature. The dashed curves are the calculated Al and Mg curves from Fig. 4.5. The experimental data show that the ignition time of the 20% and 60% Mg alloy particles is closer to that of pure Mg than pure Al. The solid curves correspond to the calculated ignition delay times for the alloys and are in good agreement with the experimental data.

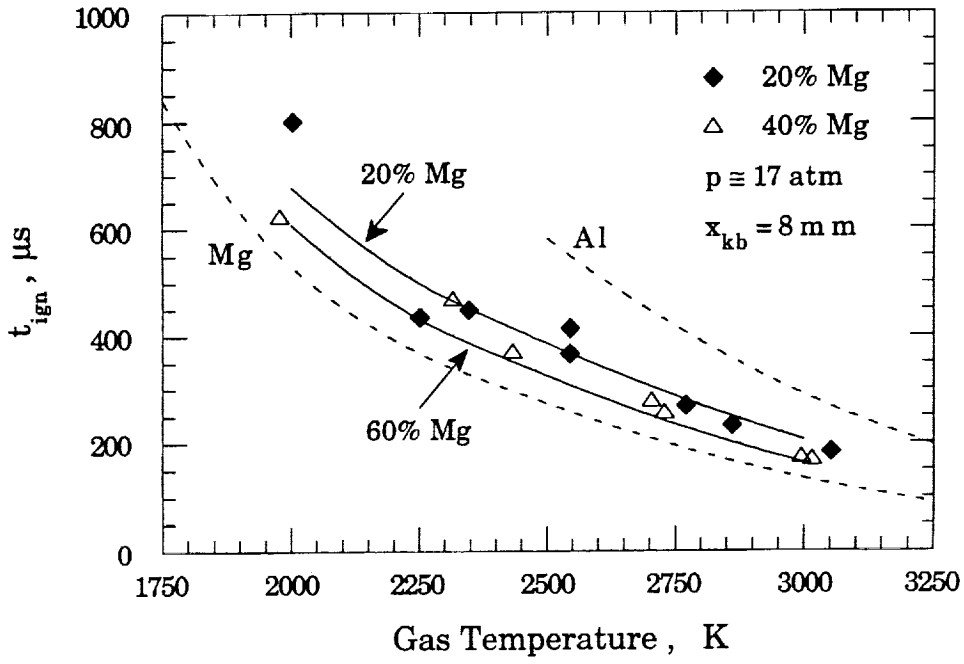

Fig. 4.19: Measured and calculated ignition delay time versus gas temperature for 20% and 60% Mg particles at p = 17 atm. The solid curves assume $(A_1)_{alloy}$ = 400 kg/m^2-s. The dashed curves correspond to the calculated Mg and Al ignition delay times of Fig. 4.5. The knife blade is mounted 8 mm from the endwall.

The alloy calculations assume that the heterogeneous reaction pre-exponential constant is equal to that of pure Mg:

$$(A_1)_{20\%\ Mg} = (A_1)_{60\%\ Mg} = (A_1)_{Mg} = 400\ kg/m^2\text{-}s$$

and that the alloy ignition temperature (corresponding to the onset of detached, gas phase combustion) is equal to the alloy boiling point or the melting point of Al_2O_3, whichever is lower. The ignition model indicates (see Fig. 4.25 and related discussion in section 4.3) that the most accurate prediction of the ignition delay time as a function of alloy composition is obtained when the pre-exponential constant of the alloy is taken to be equal to that of pure Mg.

These findings are consistent with the calculation of the Al/Mg alloy volume ratio, Φ (see Fig. 3.17), which indicates that the Al oxide film remains protective to significantly higher temperatures than that of the alloys. In addition, at p = 17 atm the boiling point of the 20% Mg alloy is calculated to be 2413 K, which is greater than the melting point of Al_2O_3. Since it is assumed that the ignition temperature is the lower of T_{bp} or $(T_{mp})_{Al_2O_3}$, the ignition temperature of the 20% Mg alloy is taken to be equal to that of pure Al, 2300 K.

Although the Al and 20% Mg alloy particles must rise to the same temperature to ignite, the 20% Mg alloy particle will experience a greater degree of self heating, due to the fact that its oxide film will become non-protective at a lower temperature than that of Al (see Fig. 3.17). In the case of the 60% Mg alloy, its ignition delay time is reduced by the combination of a low volume ratio and an ignition temperature (equal to its boiling point at 17 atm) of only 1922 K, substantially below that of the melting point of Al_2O_3.

Figures 4.20 thru 4.23 compare the results of calculations corresponding to the predicted ignition delay times of the 20% Mg and 60% Mg alloy particles presented in Fig. 4.19, and those of the Mg and Al particles presented in Fig. 4.5. In all of these figures, the solid curves represent the results of the alloy calculations, and the dashed curves, the results of the pure metal calculations.

Figure 4.20 compares the calculated mass fraction of the particles oxidized by heterogeneous reactions as a function of gas temperature. The

calculated curves all exhibit the same general trend, an inverse relationship to the gas temperature, but differ substantially in magnitude. If the calculated mass fraction is examined as a function of alloy composition at a single

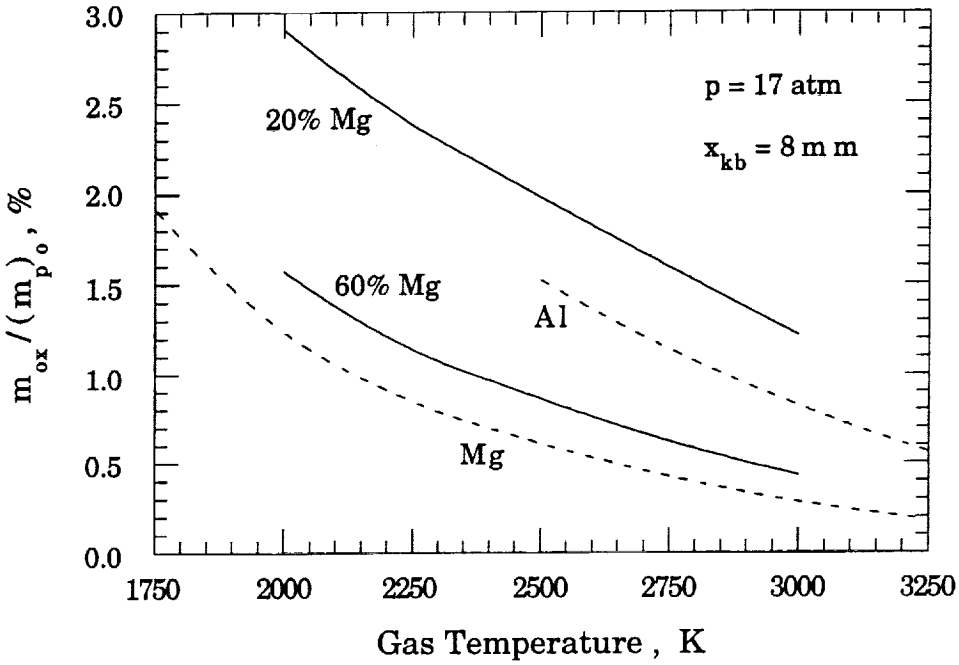

Fig. 4.20: Calculated oxidized particle mass fraction versus gas temperature corresponding to the calculated ignition delay times presented in Fig. 4.19.

temperature, the variation of the oxidized mass fraction is non-monotonic. The 20% Mg alloy particles, rather than the Al particles, are predicted to have the largest oxidized mass fraction at a given gas temperature. At T = 2750 K, the oxidized mass fraction rises from 1.15 percent for pure Al to 1.60 percent for 20% Mg, and then drops rapidly to 0.62 percent and 0.42 percent for 20% Mg and pure Mg, respectively. The oxidized mass fraction increases with decreasing Mg content due to the increase in the alloy boiling point.

The corresponding calculated oxide penetration depths are plotted versus gas temperature in Fig. 4.21. The depth of oxide penetration for the 20% Mg particles is predicted to vary linearly over the range of gas temperatures investigated, as it does for Al, with a maximum penetration of 0.10 μm. For the 60% Mg alloy particles, the oxide penetration depth is predicted to vary non-linearly, in a manner similar to the Mg particles, with a maximum depth of 0.06 μm.

Presented in Fig. 4.22 are the calculated reaction energy fractions (Eq. (4.1)) for the alloys and metals plotted as a function of the gas temperature. The reaction energy fractions are predicted to follow the same general trends as the curves of the previous two figures. The magnitude of the reaction energy fraction for the 20% Mg alloy particles is found to be substantially greater than that of the other alloys, with a maximum value of 35 percent at T = 2000 K.

Figure 4.23 shows the time-integrated surface-averaged Nusselt number as a function of temperature for the four particle compositions tested. The variation in the time-integrated Nusselt number of the alloy particles is quite similar to that of the pure Mg particles. For the 20% Mg alloy particles, $\overline{Nu_p}$ ranges from 4.73 at T=2000 K to 4.85 at T = 3000 K, an increase of 2.6 percent. For the 60% Mg alloy particles, $\overline{Nu_p}$ increases by 6.2 percent from a value of 4.83 at T = 2000 K to 5.13 at T = 3000 K. The interesting local minimum in $\overline{Nu_p}$, which occurs at a gas temperature of approximately 2500 K, is likely due to the nonlinear relationship between the particle acceleration in region 2 and the varying incident shock Mach number.

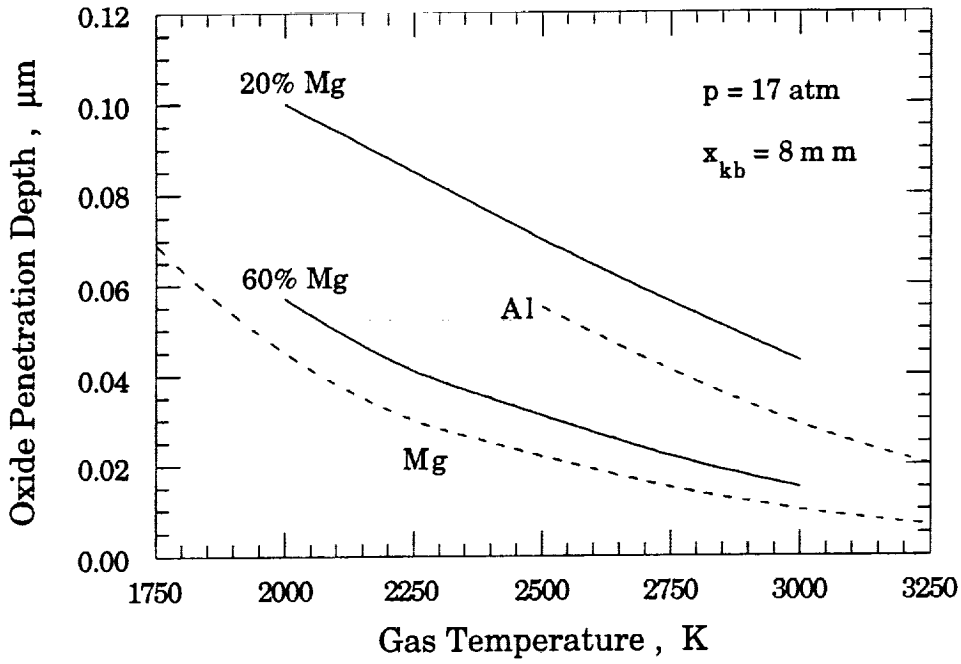

Fig. 4.21: Calculated oxide penetration depth versus gas temperature corresponding to the calculated ignition delay times presented in Fig. 4.19.

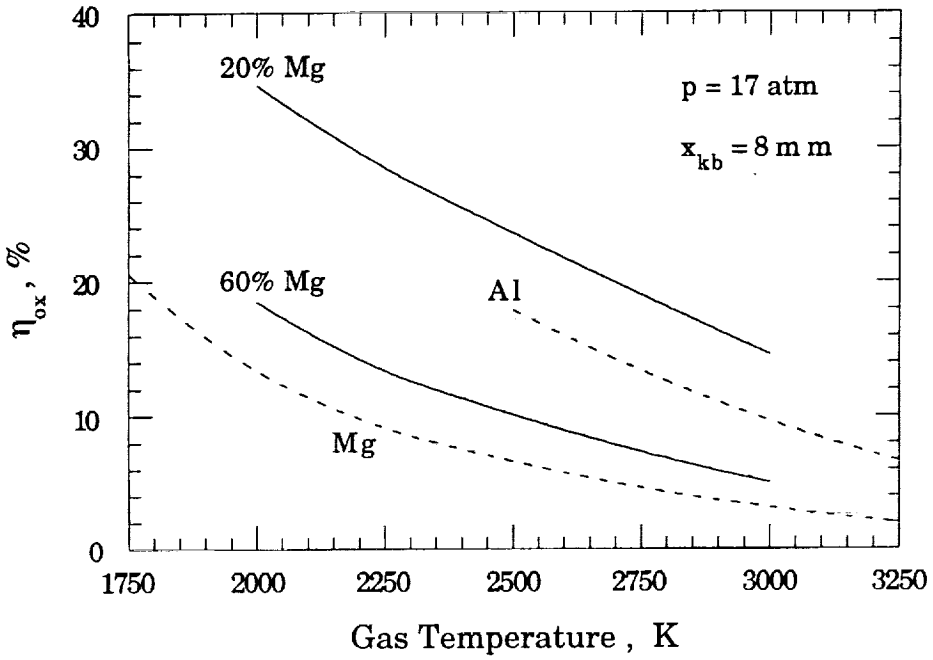

Fig. 4.22: Calculated reaction energy fraction versus gas temperature corresponding to the calculated ignition delay times presented in Fig. 4.19.

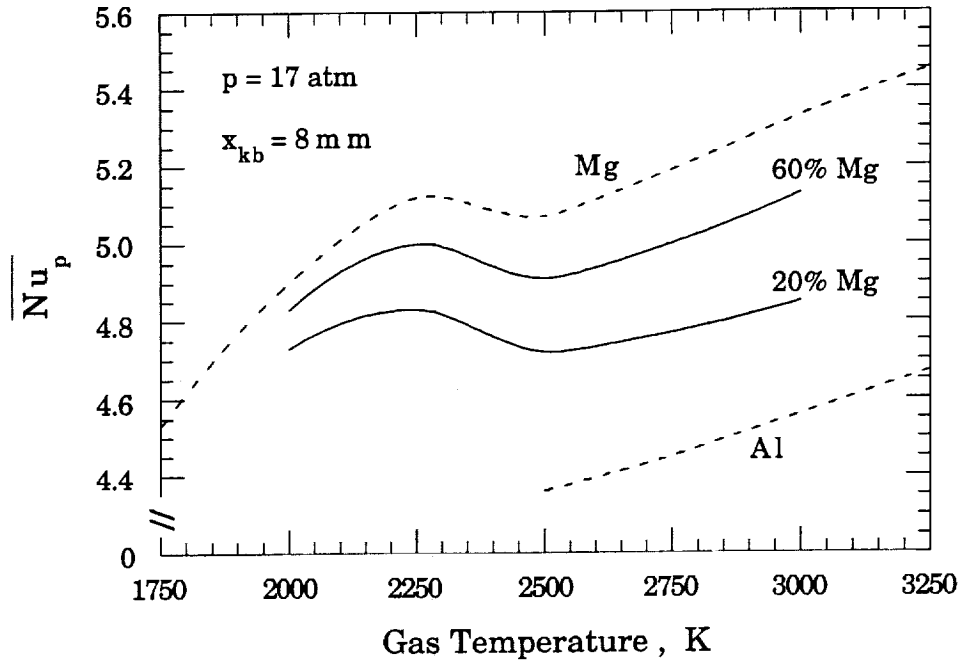

Fig. 4.23: Calculated time-integrated surface-averaged Nusselt number versus gas temperature corresponding to the calculated ignition delay times presented in Fig. 4.19.

4.2.3 Effect of Knife Blade Mounting Distance on the Ignition Delay Time of Pure Al

The effect of the knife blade mounting distance on the measured ignition delay time of the 21.6 μm Al particles is now investigated. Table 4.4 shows the results of 20 measurements of t_{ign} as a function of gas temperature for the Al particles mounted at distances of 2 mm and 4 mm. The measured experiment temperature has a range of 2450 K ≤ T ≤ 3000 K, for x_{kb} = 2 mm, and 2240 K ≤ T ≤ 3150 K for x_{kb} = 4 mm. The experiment pressure was held constant for these measurements. The x_{kb} = 2 mm data has a mean pressure of 16.9 atm, with a standard deviation of 0.8 atm, and the x_{kb} = 4 mm data has a mean pressure of 16.7 atm, with a standard deviation of 0.7 atm.

Table 4.4: Measured ignition delay and combustion time of Al particles as a function of temperature and knife blade mounting distance.

Shot #	x_{kb} (wt. %)	T_1 (K)	p_1 (psia)	M_{s_i}	T_5 (K)	p_5 (atm)	t_{ign} (μs)	t_b (μs)
136	2	305	1.41	4.53	2450	16.0	836	491
135	2	304	1.18	4.89	2720	16.3	568	189
140	2	296	1.05	5.15	2840	16.4	541	227
143	2	300	1.05	5.24	2930	17.2	481	332
138	2	298	1.05	5.32	2970	17.8	440	416
137	2	302	1.05	5.33	3000	17.9	470	322
245	4	298	1.63	4.33	2240	16.4	795	552
237	4	300	1.63	4.33	2250	16.4	786	424
144	4	301	1.41	4.50	2390	15.8	647	-
147	4	300	1.41	4.59	2460	16.6	644	356
148	4	300	1.36	4.75	2590	17.4	578	665
149	4	300	1.27	4.89	2700	17.6	523	286
271	4	297	1.14	4.94	2710	16.1	550	610
145	4	302	1.18	4.90	2710	16.4	581	489
146	4	298	1.18	4.99	2750	17.2	527	385
272	4	300	1.14	5.02	2790	16.8	508	446
273	4	299	1.14	5.05	2800	17.1	434	220
139	4	297	1.05	5.16	2860	16.5	420	306
141	4	294	1.05	5.34	2960	18.0	314	-
150	4	297	.81	5.67	3150	15.9	261	309

The ignition delay time measurements of Table 4.4 are plotted in Fig. 4.24 as a function of gas temperature. Also included in the figure are solid curves corresponding to the predicted ignition delay times for the Al particles assuming x_{kb} = 2 mm and 4 mm, and a dashed curve corresponding to the predicted t_{ign} at x_{kb} = 8 mm (see Fig. 4.5). The magnitude of the experimentally-measured ignition delay time is found to be inversely related to the knife blade mounting distance. As the knife blade mounting distance is decreased, the duration of particle exposure to the high velocity flow in region 2 is also reduced. This results in a reduction in the particle velocity and the rate of convective heat transfer, which increases t_{ign}.

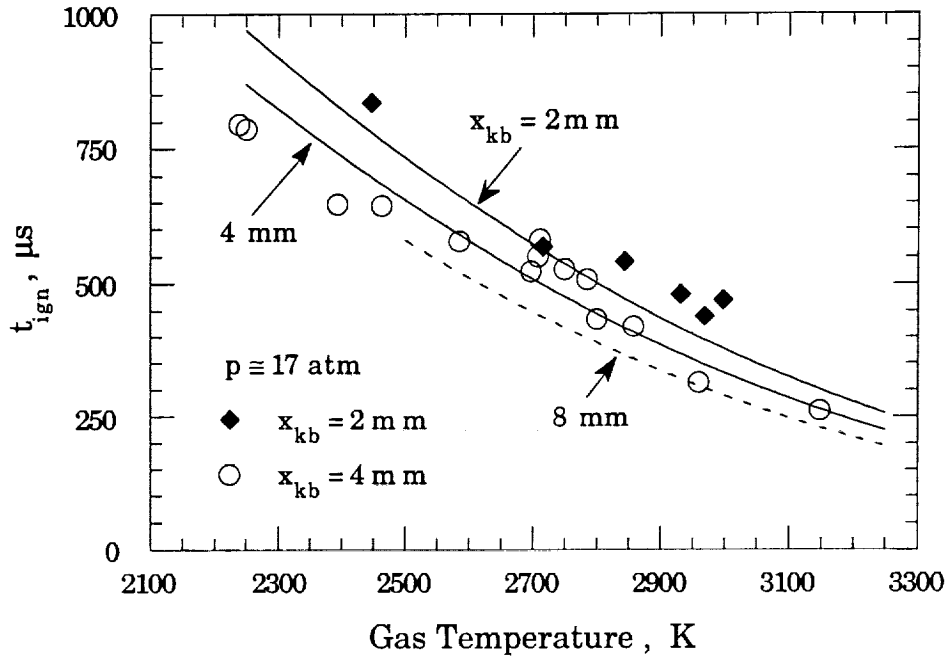

Fig. 4.24: Measured and calculated Al ignition delay time versus gas temperature as a function of knife blade mounting distance. Calculations assume d_p = 21.6 μm and p = 17 atm.

The model predictions agree well with the experimental data at x_{kb} = 4 mm and 8 mm (see Fig. 4.5). As the knife blade distance is reduced to 2 mm, the model underpredicts the ignition delay time by 10 to 15 percent. The underprediction at smaller knife blade mounting distances is probably due to the particle acceleration losses associated with particle-particle interactions, the knife blade boundary layer and wake, and an increased particle residence time within the endwall thermal layer. For example, the particle acceleration time, $t_{acc} \cong x_{kb}\ (1/v_{s_i} + 1/v_{s_r})$, is calculated to vary from 22.4 μs at x_{kb} = 8 mm to 5.6 μs at x_{kb} = 2 mm, for gas conditions of T = 2750 K and p = 17 atm. It is believed that the associated losses may become increasingly important as the acceleration time decreases, due to an increase in the fraction of the acceleration period in which the particles are in contact with the knife blade, as well as with each other. These results were considered when determining the appropriate knife blade mounting distances at each gas pressure.

4.3 EFFECT OF ALLOY COMPOSITION ON IGNITION DELAY TIME

The following section presents the results of investigations of the ignition and combustion of the Al/Mg alloy particles as a function of their composition, under constant experiment conditions. The measurements are taken at gas temperatures of T ≅ 2225 K and 2775 K for each of three gas pressures; p ≅ 8.5 atm, 17 atm, and 34 atm. The knife blade mounting distance is held constant at x_{kb} = 8 mm, 4 mm, and 3 mm for gas pressures of 8.5 atm, 17 atm, and 34 atm, respectively. The knife blade mounting distance is varied with gas pressure in an attempt to produce time-integrated particle Nusselt numbers which do not vary substantially over the range of gas conditions investigated.

Data is presented for 0, 5, 10, 20, 40, 60, 80, and 100 weight percent Mg alloys with various effective particle diameters (see Table 2.1). In order to clarify the trends in the experimental data, it is useful to normalize the ignition and combustion times to a single particle diameter. Fox et al. [34] point out that the particle ignition time scales as $t_{ign} \sim (d_p)^{n_i}$, where n_i is between 1.45 and 2, depending on the degree of convective heating. Wilson and Williams [18] state that Al particle combustion times scale as $t_b \sim (d_p)^{n_b}$, where n_b is between 1.5 and 2. The experimental data of Prentice [17], for Al particles burning in oxygen/argon mixtures, yields a burn rate exponent of approximately $n_b = 1.8$, and is equal to the exponent assumed in the empirical Al combustion rate model developed by Hermsen [87].

Using the ignition model developed here, n_i is numerically calculated as a function of the particle composition for all experimental gas temperatures and pressures, and varies between 1.70 and 1.91. The experimental ignition delay and combustion times have therefore been normalized to a particle diameter of $d_p = 20\ \mu m$, assuming $n_i = n_b = 1.8$. The normalization used the following relation:

$$(t)_{20\ \mu m} = (t)_{d_{eff}} \left(\frac{20\ \mu m}{d_{eff}} \right)^{1.8}$$

where $(t)_{d_{eff}}$ is the measured ignition delay or combustion time, and $(t)_{20\ \mu m}$ is the normalized value. Assuming a constant exponent in the normalization introduces a maximum error of less than 1% into the normalized values.

4.3.1 Alloy Ignition at 8.5 atm

Tables 4.5 and 4.6 present the measured ignition delay and combustion times of the alloy particles as a function of their composition at $p \cong 8.5$ atm for

two gas temperatures, T ≅ 2220 K and 2800 K, respectively. The knife blade is mounted 8 mm from the endwall in all cases. The measurements of Table 4.5 have a mean Mach number, temperature, and pressure of 4.32, 2220 K, and 8.4 atm, with standard deviations of 0.03, 20 K, and 0.1 atm. The measurements of Table 4.6 have a mean Mach number, temperature, and pressure of 5.10, 2800 K, and 9.0 atm, with standard deviations of 0.03, 20 K, and 0.2 atm.

The ignition delay data of Tables 4.5 and 4.6 are normalized and plotted in Fig. 4.25 as a function of alloy composition. At both gas temperatures, the ignition delay time of pure Mg and of the Mg alloys is significantly reduced below that of pure Al, by the addition of as little as 10% Mg in alloy. The results of the measurements at both gas temperatures exhibit a slight increase in ignition time as the percentage of Al is increased, and display an abrupt rise at Al percentages greater than 90%. The addition of as little as 20% Mg to Al is found to reduce the ignition delay time by approximately 30 percent at T ≅ 2225 K, and by approximately 20 percent at T ≅ 2775 K.

The ignition of the pure Al particles at 2225 K occurs after the quasi-steady reflected shock conditions have ceased to exist. However, the particle heating model predicts that the majority of the particle heating occurs during the quasi-steady test time, and the subsequent heating occurs in a gas environment generally described by a gradually rising pressure. If it is assumed that the pressure rise is due to isentropic compression waves, the corresponding rise in the gas temperature can be estimated to be about 5%, or an average increase of 60 K. This rise in the gas temperature and pressure has a negligible effect on the overall trend shown in Fig. 4.25.

The solid curves shown in Fig. 4.25 correspond to the calculated ignition delay times of 20 μm alloy particles assuming x_{kb} = 8 mm, a gas pressure of 8.5 atm, and gas temperatures of 2225 K and 2775 K. The pre-exponential

Table 4.5: Measured ignition delay and burn times of the alloy particles as a function of composition at T ≅ 2225 K and p ≅ 8.5 atm. p_1 = .843 psia and x_{kb} = 8 mm for all measurements.

Shot #	Mg (wt. %)	T_1 (K)	M_{s_i}	T_5 (K)	p_5 (atm)	t_{ign} (μs)	t_b (μs)
215	0	297	4.30	2210	8.4	1172	261
221	0	297	4.37	2260	8.7	1106	469
208	5	297	4.31	2210	8.4	677	416
210	5	297	4.35	2250	8.6	784	247
211	5	297	4.29	2200	8.3	770	349
212	10	297	4.29	2200	8.3	785	251
213	10	298	4.35	2250	8.6	712	218
234	10	298	4.29	2200	8.3	879	142
235	10	301	4.31	2230	8.4	711	266
214	20	298	4.32	2230	8.5	792	223
222	20	299	4.30	2220	8.4	726	411
209	40	297	4.33	2230	8.5	628	264
216	40	298	4.35	2250	8.6	600	450
217	40	298	4.30	2210	8.4	763	268
226	40	297	4.27	2180	8.2	829	162
218	60	298	4.33	2240	8.5	613	273
223	60	299	4.30	2210	8.3	635	307
219	80	299	4.33	2240	8.5	533	340
224	80	297	4.35	2250	8.6	543	150
220	100	297	4.34	2240	8.6	526	305
225	100	298	4.28	2190	8.3	546	189

Table 4.6: Measured ignition delay and burn times of the alloy particles as a function of composition at T ≅ 2775 K and p ≅ 8.5 atm. p_1 = .584 psia and x_{kb} = 8 mm for all measurements.

Shot #	Mg (wt. %)	T_1 (K)	M_{s_i}	T_5 (K)	p_5 (atm)	t_{ign} (μs)	t_b (μs)
177	0	298	5.08	2790	8.8	519	244
181	0	297	5.00	2730	8.5	534	240
178	5	296	5.14	2810	9.1	385	410
182	5	299	5.12	2820	9.0	377	285
179	10	297	5.13	2820	9.1	297	282
183	10	299	5.07	2790	8.8	368	160
184	10	297	5.10	2800	8.9	353	253
186	20	297	5.13	2820	9.1	370	268
207	20	294	5.11	2780	9.0	391	215
228	40	297	5.11	2800	9.0	377	168
232	40	297	5.06	2770	8.8	291	353
233	40	298	5.13	2820	9.1	341	239
229	60	297	5.11	2800	9.0	395	188
231	60	299	5.13	2820	9.1	358	217
227	80	296	5.12	2800	9.0	337	196
230	80	298	5.10	2800	8.9	317	150
180	100	298	5.11	2800	9.0	279	145
185	100	298	5.12	2810	9.0	267	219

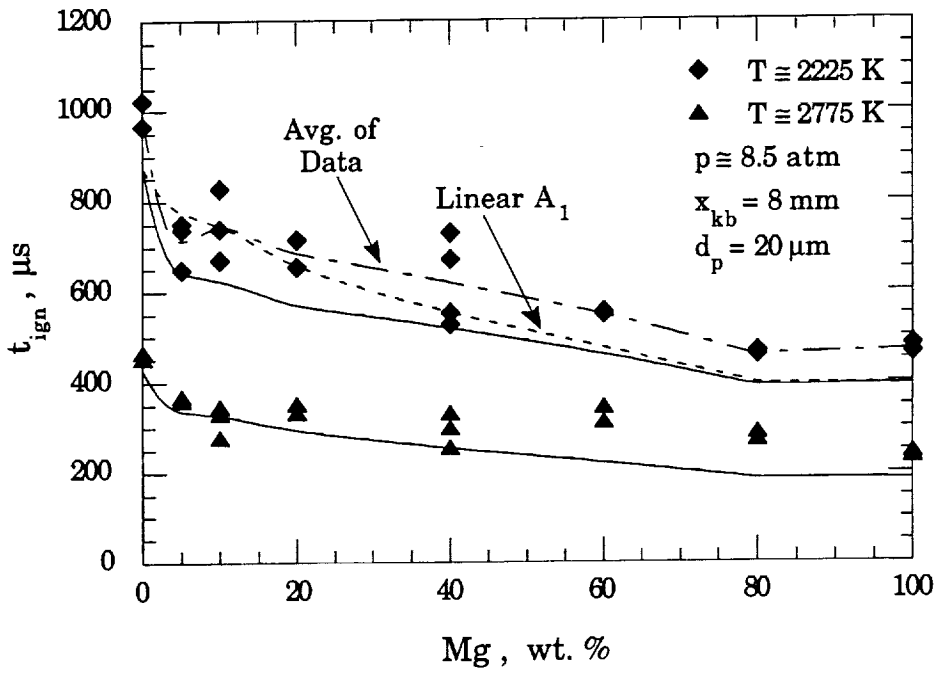

Fig. 4.25: Measured (symbols) and calculated (solid curves) ignition delay time versus alloy composition as a function of temperature at p ≅ 8.5 atm. Measured ignition delay times are normalized to a particle diameter of 20.0 μm assuming $t_{ign} \sim d_p^{1.8}$. The dashed curve is calculated with a linearly varying A_1. The dot-dashed curve is the average of the data at T ≅ 2225 K.

constants of the alloys are assumed to be equal to that of pure Mg, $(A_1)_{alloy} = (A_1)_{Mg}$ = 400 kg/m^2-s. Although the predicted ignition times are slightly below the experimental data, the overall trends are quite similar. The dash-dot curve in Fig. 4.25 is produced from the average, at each composition, of the 2225 K data, and the predicted and measured trends are found to be in excellent agreement. The calculated Mg particle Knudsen numbers are Kn = .012 at T = 2225 K and Kn = .016 at T = 2775 K, indicating that the flow is slightly rarefied at these conditions (see Fig. 3.5). This rarefaction may be one source of the model's underprediction, possibly reducing the heterogeneous reaction rate.

The dot-dashed curve in Fig. 4.25 corresponds to calculations made for an alloy heterogeneous pre-exponential constant which varies linearly from Mg to

Al; $(A_1)_{alloy} = 200 + 200Y_{Mg}$ kg/m^2-s. If this linear variation is assumed, the ignition delay times are predicted to slowly rise from the Mg value to the Al value without the characteristic rapid increase at Al contents in excess of 90%. This slow variation in t_{ign} contradicts the data, and bolsters the choice of an alloy pre-exponential constant, $(A_1)_{alloy}$, that is constant and equal to that of Mg.

Calculations of the ignition delay time are also made with the assumption that the heterogeneous reactions do not contribute to the particle heating ($A_1 = 0$). The result of these calculations are plotted as the dashed curves in Figure 4.26, along with the measured and calculated results presented in Fig. 4.25. At a gas temperature of T = 2225 K, the non-reacting calculations are found to tend toward infinity as the Mg content is reduced. This is because the ignition temperature of the alloy exceeds that of the gas at a Mg content of approximately 20%.

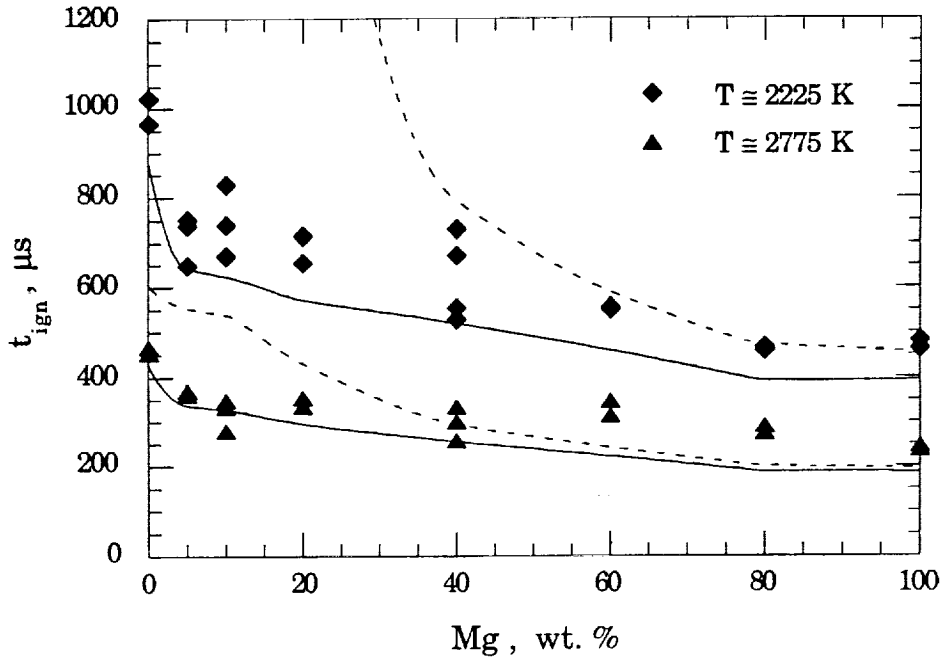

Fig. 4.26: Comparison of the alloy particle ignition delay time calculated with (solid curves) and without (dashed curves) heterogeneous reaction.

The results of the non-reacting calculations, at T = 2775 K, agree with the reacting calculations at Mg contents above 40%. However, they are found to substantially overpredict the ignition delay times for Mg contents below 40%. It is apparent that the heterogeneous reaction must be included in any model developed to accurately predict the ignition delay times of Al/Mg alloy particles.

The predicted mass fraction of the particle oxidized by the heterogeneous reaction is plotted as a function of alloy composition in Fig. 4.27. The calculations correspond to the solid curves presented in Fig. 4.25, with d_p = 20 μm, x_{kb} = 8 mm, p = 8.5 atm, and T = 2225 K and 2775 K. The solid curves are calculated assuming $(A_1)_{alloy} = (A_1)_{Mg}$, and the dashed curve is calculated assuming $(A_1)_{alloy}$ varied linearly with composition at T = 2225 K.

The calculations indicate that the oxidized mass fractions are highly nonlinear functions of alloy composition, and that their magnitudes are a strong function of the gas temperature. At both gas temperatures, the oxidized mass fraction rises steeply from an Al value to a peak at approximately 10% Mg. As the percentage of Mg is increased further, the oxidized mass fraction decreases until the curve plateaus for Mg contents in excess of 75%. The curve corresponding to the linearly varying $(A_1)_{alloy}$ differs only slightly from that calculated assuming a constant $(A_1)_{alloy}$. The linear calculation predicts only a slight rise in the oxidized mass fraction as the Mg content is increased, followed by the characteristic drop and plateau. The basic variation of the oxidized mass fraction with alloy composition is found to be dependent on the particle's physical characteristics, e.g. T_{ign}, rather than the variation of $(A_1)_{alloy}$.

Figure 4.27 also indicates that increasing the gas temperature from 2225 K to 2775 K nearly halves the predicted oxidized mass fraction at all alloy compositions. The reason for this is that the heterogeneous reaction proceeds at a rate which is dependent upon the particle temperature. Therefore, the mass

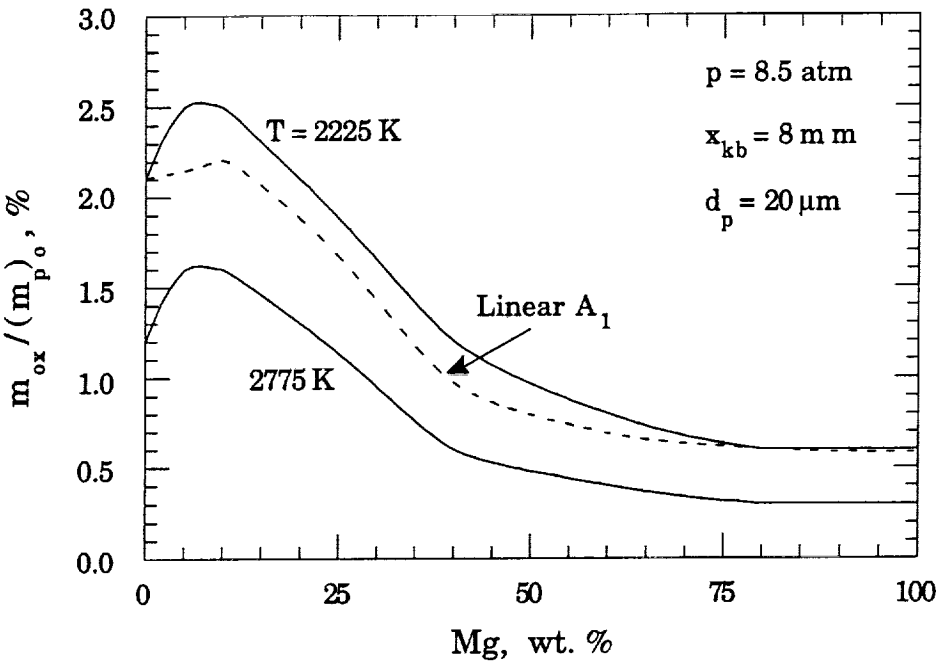

Fig. 4.27: Calculated oxidized particle mass fraction as a function of alloy composition corresponding to the conditions of Fig. 4.25. The dashed curve assumes a linearly varying A_1.

of the particle oxidized will be inversely proportional to the rate of change of the particle temperature, dT_p/dt. At the higher gas temperature, the rate of convective heat transfer is increased substantially, increasing dT_p/dt, and reducing the mass fraction of the particle which is oxidized by the heterogeneous reaction.

Figure 4.28 presents the calculated reaction energy fraction, $\eta_{ox} = e_{ox} / (e_{ht} + e_{ox})$, plotted as a function of alloy composition. The curves presented in Fig. 4.28 correspond to the solid curves shown in the two preceding figures. The variation of the reaction energy fraction with alloy composition is found to be virtually identical to that of the oxidized mass fraction.

At a gas temperature of 2225 K, 25 percent of the energy required to ignite the pure Al particles is provided by the heterogeneous reaction. The predicted reaction energy fraction rises to 31 percent at Mg contents of 5 - 10%, then drops

to a minimum of approximately 7 percent for pure Mg. The same trend is predicted at a gas temperature of 2775 K, with η_{ox} peaking at approximately 20 percent and falling to a minimum of 3 percent. The substantial increase in the fraction of energy provided by the heterogeneous reaction to the heating energy of the alloy particles, with decreasing Mg content, is due to the combined effect of an increasing alloy heat of reaction and alloy ignition temperature.

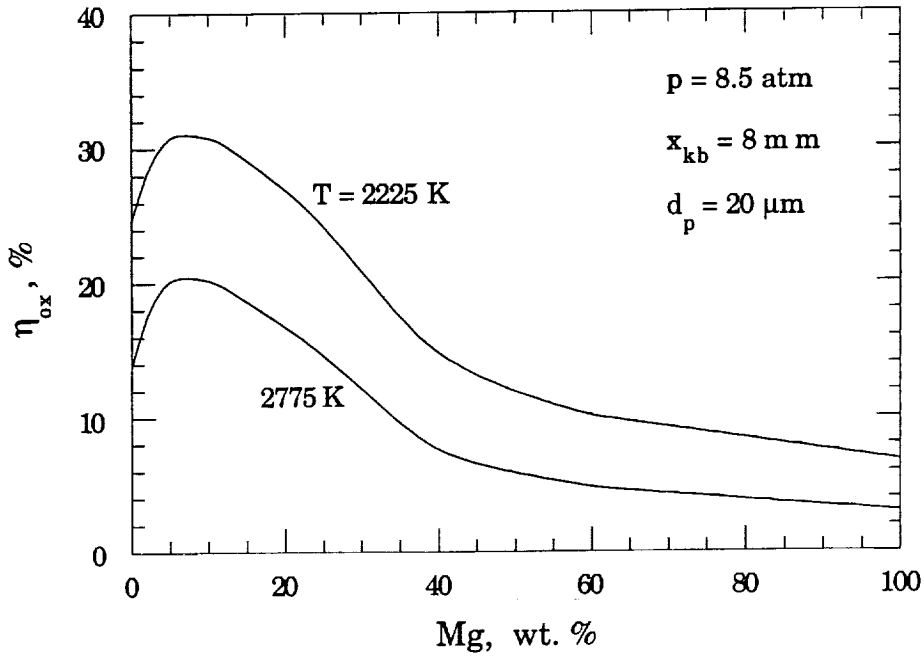

Fig. 4.28: Calculated reaction energy fraction as a function of alloy composition corresponding to the conditions of Fig. 4.25.

The trends exhibited in Figs. 4.27 and 4.28 can, in part, be explained by the dependence of the alloy ignition temperature, T_{ign}, on the alloy composition. Shown in Fig. 4.29 is the calculated alloy boiling point versus weight percent Mg at gas pressures of p = 8.5, 17.0, and 34.0 atm. The dashed curve is the temperature at which the Al_2O_3 protective film melts, $(T_{mp})_{Al_2O_3}$ = 2300 K. The

ignition temperature for each alloy is assumed to be equal to the alloy boiling point or the melting point of Al_2O_3, whichever is lower:

$$(T_{ign})_{alloy} = Min[(T_{bp})_{alloy}, (T_{mp})_{Al_2O_3}] \tag{4.2}$$

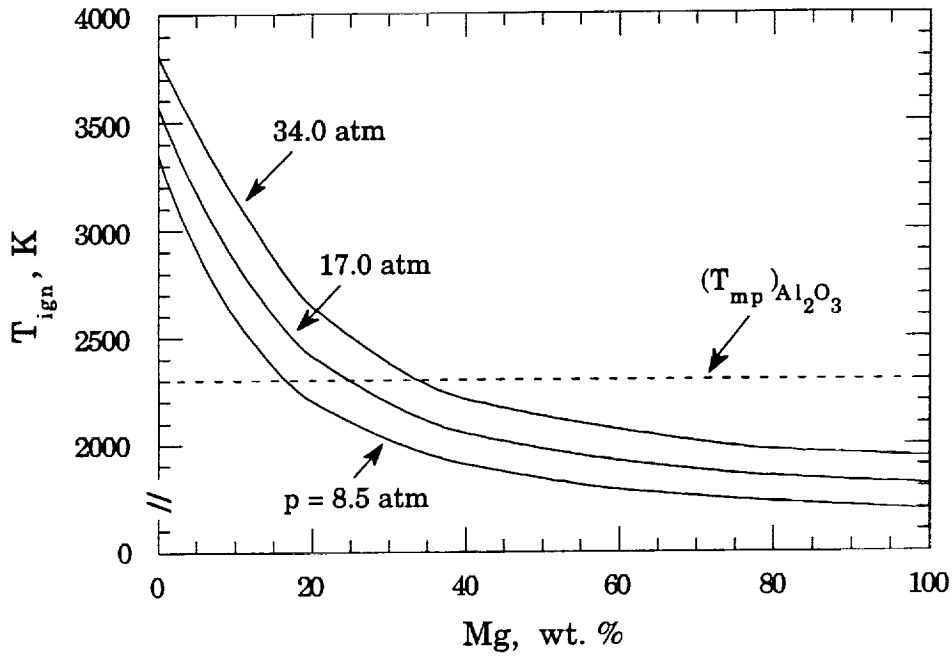

Fig. 4.29: Calculated Al/Mg alloy ignition temperature versus alloy composition as a function of gas pressure. The dashed curve corresponds to the melting temperature of Al_2O_3, which is taken to be the upper limit of the alloy ignition temperature.

Based on this assumption, Fig. 4.29 indicates that at p = 8.5 atm, the alloy ignition temperature rises from 1700 K for pure Mg to 2300 K at 17% Mg. Therefore, the oxidized mass fractions and reaction energy fractions at p = 8.5 atm rise as the alloy ignition temperature rises. Alloys with Mg contents of less than 17% are expected to ignite at the same temperature, $(T_{mp})_{Al_2O_3}$ = 2300 K, and the oxidized mass and reaction energy fractions are

expected to level off. The relative drop in the oxidized mass and reaction energy fractions for pure Al is due to the lower pre-exponential constant of Al, which substantially increases the ignition delay time, and the magnitude of the total heat transferred to the particle from the gas.

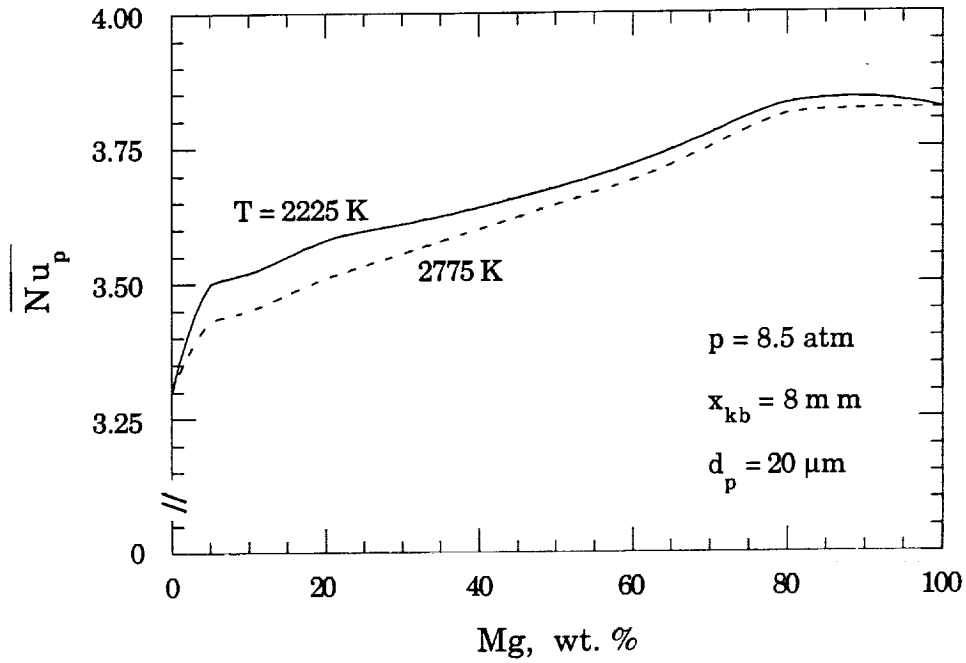

Fig. 4.30: Time-integrated surface-averaged particle Nusselt number as a function of alloy composition corresponding to the solid curves of Fig. 4.25.

Since the particle masses are a function of their alloy composition, and the particle diameters are nearly equal, the acceleration of the particles in the high-speed flow induced by the incident shock wave will be a function of alloy composition. The resulting particle velocity variation will affect the rate of convective heat transfer to the particles. Figure 4.30 shows the time-integrated surface-averaged Nusselt number, $\overline{Nu_p}$, plotted as a function of Mg content corresponding to the calculations of Figs. 4.25 to 4.28. The calculated $\overline{Nu_p}$'s are

found to be only weakly dependent upon the gas temperature. $\overline{Nu_p}$ is predicted to decrease approximately 9 percent from 3.82 for pure Mg to about 3.5 for 5% Mg. $\overline{Nu_p}$ then drops to 3.3 for pure Al since the significantly longer Al ignition delay time allows the particle to decelerate to a lower velocity than the alloy particles. The calculated variation of approximately 9 percent in the alloy $\overline{Nu_p}$ is significantly less than the variation in the measured ignition delay times, and therefore, does not alter the resulting conclusions.

4.3.2 Alloy Ignition at 17 atm

The effect of ambient gas temperature, at $p \cong 17.0$ atm, on the ignition delay time of the alloy particles as a function of composition is shown in Fig. 4.31. The corresponding measurements are presented in Table 4.7. The knife blade is mounted 4 mm from the endwall in all cases. The lower temperature measurements of Table 4.7 have a mean Mach number, temperature, and pressure of 4.33, 2240 K, and 16.4 atm, with standard deviations of 0.03, 20 K, and 0.3 atm. The higher temperature measurements of Table 4.7 have a mean Mach number, temperature, and pressure of 5.06, 2800 K, and 17.1 atm, with standard deviations of 0.03, 20 K, and 0.3 atm.

The measured ignition delay times shown in Fig. 4.31 are found to have the same general dependence on the alloy composition as was obtained at $p \cong 8.5$ atm. The measured t_{ign} is found to decrease substantially as the Mg fraction is increased from zero to approximately 20% Mg. At a gas temperature of $T \cong 2225$ K, t_{ign} decreases from its Al value of approximately 700 μs to approximately 550 μs at 10% Mg, and then remains nearly constant as the Mg content is increased further.

Table 4.7: Measured ignition delay and burn times of the alloy particles as a function of composition at p ≅ 17.0 atm. x_{kb} = 4 mm for all measurements.

Shot #	Mg (wt. %)	T_1 (K)	M_{s_i}	T_5 (K)	p_5 (atm)	t_{ign} (μs)	t_b (μs)
T ≅ 2225 K, p_1 = 1.63 psia							
237	0	300	4.33	2250	16.4	786	421
245	0	298	4.33	2240	16.4	795	553
238	5	298	4.32	2230	16.3	664	244
246	5	299	4.33	2240	16.4	706	261
239	10	299	4.34	2250	16.5	515	275
247	10	299	4.30	2220	16.1	580	238
256	10	296	4.36	2250	16.7	560	178
240	20	298	4.30	2220	16.1	655	249
248	20	297	4.33	2230	16.4	644	236
241	40	298	4.33	2240	16.4	542	209
249	40	298	4.34	2250	16.5	534	173
242	60	296	4.39	2280	17.0	509	262
252	60	296	4.34	2240	16.5	501	226
243	80	297	4.30	2210	16.1	530	157
253	80	297	4.33	2230	16.4	511	137
244	100	297	4.35	2250	16.6	442	221
254	100	297	4.28	2200	16.0	533	139
257	100	297	4.29	2200	16.0	501	165
T ≅ 2775 K, p_1 = 1.14 psia							
272	0	300	5.02	2790	16.8	508	446
273	0	299	5.05	2800	17.1	434	220
275	20	296	5.07	2800	17.2	330	144
274	100	299	5.09	2830	17.4	258	298

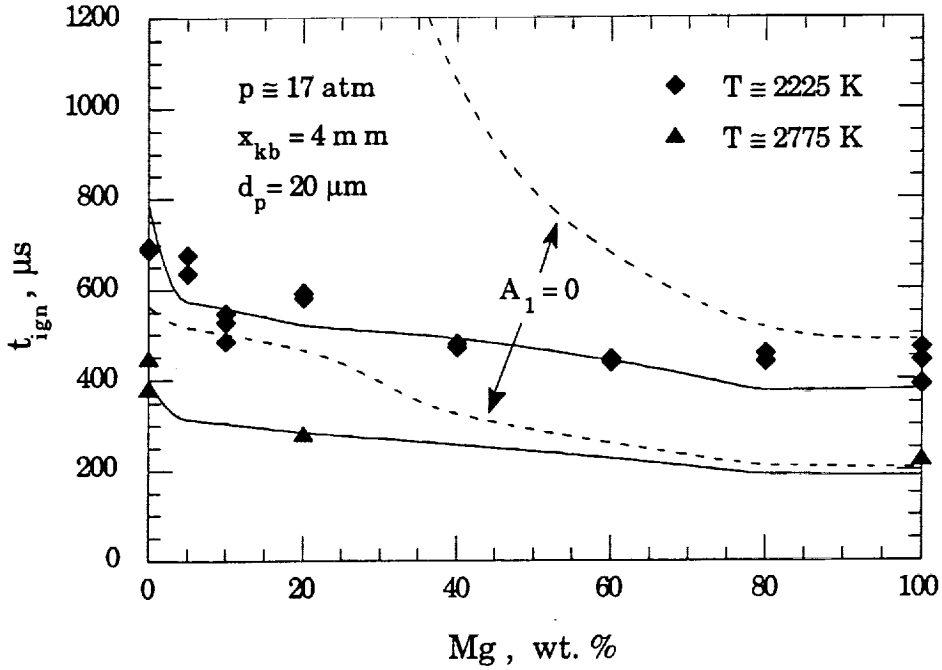

Fig. 4.31: Measured and calculated ignition delay time versus alloy composition as a function of temperature at p ≅ 17 atm. Measured ignition delay times are normalized to a particle diameter of 20.0 μm assuming $t_{ign} \sim d_p^{1.8}$. The solid and dashed curves correspond to calculations with and without heterogeneous reaction, respectively.

The data corresponding to T ≅ 2775 K plotted in Fig. 4.31 indicates that t_{ign} decreases from approximately 400 μs at pure Al to approximately 275 μs at 20% Mg, and then decreases further to approximately 220 μs at pure Mg. The addition of as little as 20% Mg to Al is again found to reduce the ignition delay time by nearly 30 percent, from that of pure Al, for both gas temperatures.

The solid and dashed curves plotted in Fig. 4.31 correspond to model calculations with and without a heterogeneous reaction, respectively. The solid curves are in excellent agreement with the experimental data. As is expected, neglecting the contribution of the heterogeneous reaction to the particle heating results in an overprediction of t_{ign} for particles with low Mg content. Since the

alloy ignition temperature approaches 2225 K at approximately 27% Mg (see Fig. 4.29), the error is particularly severe at a gas temperature of $T \cong 2225$ K.

Figures 4.32, 4.33, and 4.34 show the calculated oxidized mass fraction, reaction energy fraction, and time-integrated particle Nusselt number, plotted as a function of alloy composition. All of the calculations correspond to the solid curves presented in Fig. 4.31. The predicted oxidized mass and reaction energy fractions are found to rise from their Al value to a plateau, which stretches from 5% Mg to approximately 20% Mg. As was predicted at p = 8.5 atm (see Figs. 4.28 and 4.29 and the related discussion), the plateau is caused by the fact that the alloy ignition temperature increases with decreasing Mg content until it reaches the melting point of Al_2O_3 at approximately 25% Mg, and then remains constant as shown in Fig. 4.29. At Mg contents above 20%, the oxidized mass and reaction energy fractions decrease with increasing Mg content, and are well correlated with the decrease in the alloy ignition temperature.

The variation of the calculated $\overline{Nu_p}$, as a function of alloy composition at p = 17.0 atm (Fig. 4.34), is similar to that predicted at p = 8.5 atm. A comparison of the calculations presented in Figs. 4.30 and 4.34 indicate that the overall magnitude of $\overline{Nu_p}$ at p = 17.0 atm is approximately 10 percent greater than that predicted at p = 8.5 atm. This increase in $\overline{Nu_p}$ accounts for the slight reduction in the measured and predicted ignition delay times at the corresponding gas temperatures, when the gas pressure is doubled. Figure 4.34 indicates that $\overline{Nu_p}$ decreases only 7 percent from pure Mg to 5% Mg. $\overline{Nu_p}$ then drops another 6 percent from 5% Mg to pure Al, due to the Al particle's substantially longer ignition delay time. This predicted variation in $\overline{Nu_p}$ does not change the conclusions drawn from these measurements.

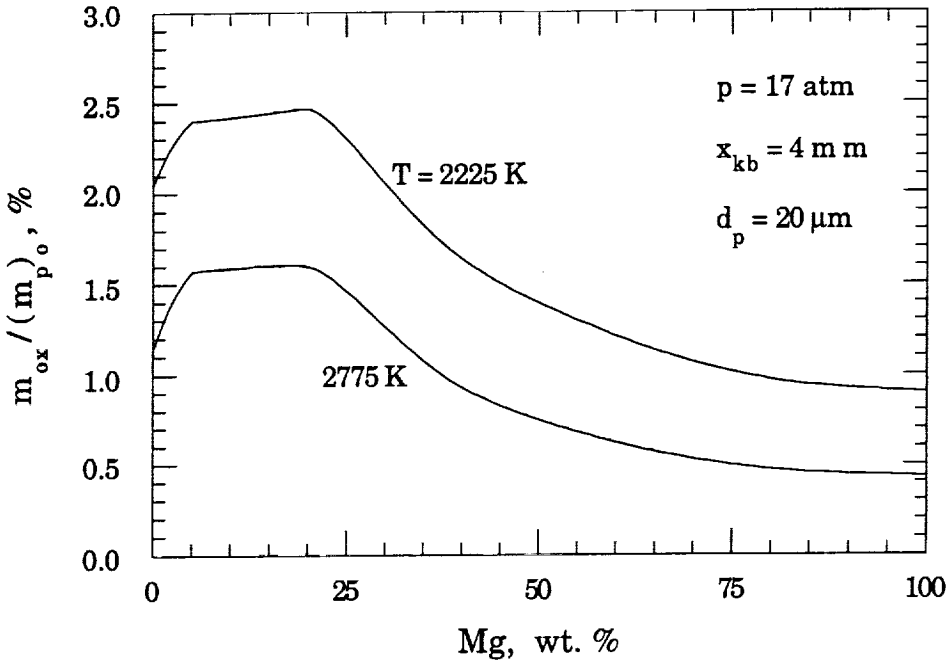

Fig. 4.32: Calculated oxidized particle mass fraction as a function of alloy composition corresponding to the conditions of Fig. 4.31.

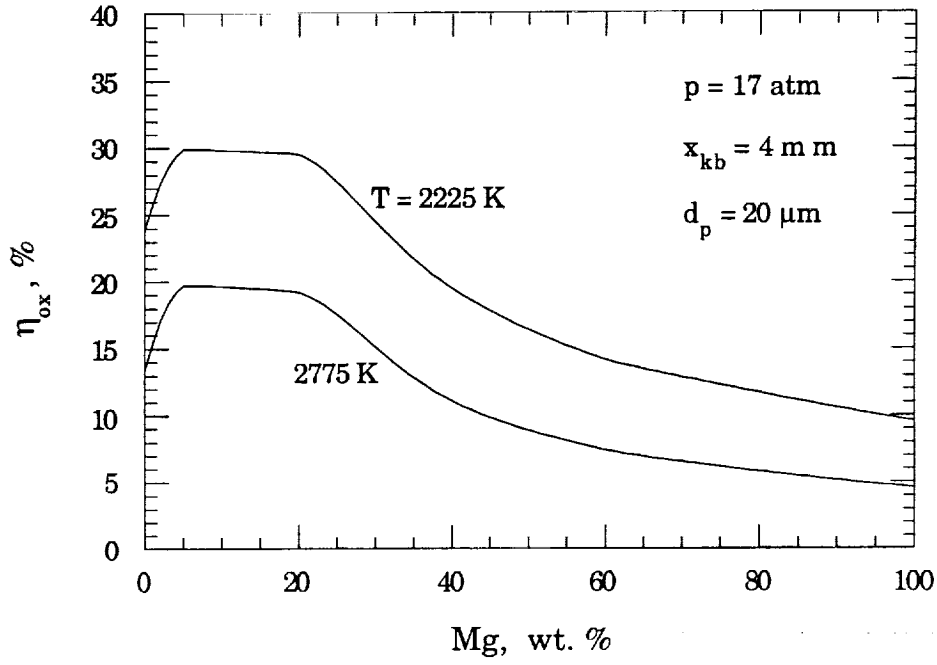

Fig. 4.33: Calculated reaction energy fraction as a function of alloy composition corresponding to the conditions of Fig. 4.31.

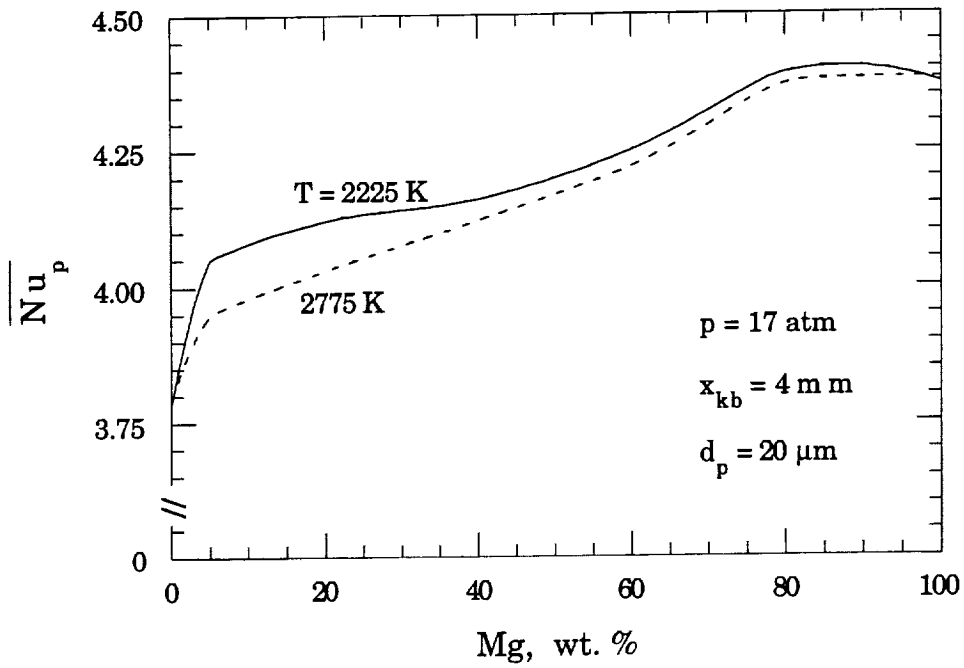

Fig. 4.34: Time-integrated surface-averaged particle Nusselt number as a function of alloy composition corresponding to the solid curves of Fig. 4.31.

4.3.3 Alloy Ignition at 34 atm

The ignition delay time of the alloy particles as a function of composition at p ≅ 34.0 atm and T ≅ 2225 K and 2775 K is shown in Fig. 4.35. The corresponding measurements are presented in Table 4.2. The knife blade is mounted 3 mm from the endwall in all cases. The lower temperature measurements of Table 4.2 have a mean Mach number, temperature, and pressure of 4.31, 2220 K, and 33.7 atm, with standard deviations of 0.02, 20 K, and 0.4 atm. The higher temperature measurements of Table 4.2 have a mean Mach number, temperature, and pressure of 5.01, 2780 K, and 34.1 atm, with standard deviations of 0.06, 50 K, and 1.0 atm.

The measured ignition delay times shown in Fig. 4.35 are again found to have the same general dependence on the alloy composition as was obtained at

$p \cong 8.5$ atm and 17 atm. The measured t_{ign} is found to decrease significantly as the Mg fraction is increased from pure Al to approximately 20% Mg. At a gas temperature of $T \cong 2225$ K, t_{ign} decreases from its Al value of approximately 550 μs to approximately 440 μs at 10% Mg, and then decreases slowly to 360 μs as the composition is increased to 100% Mg. The data corresponding to $T \cong 2775$ K indicates that t_{ign} decreases from approximately 320 μs at pure Al, to approximately 200 μs at 20% Mg, and then decreases further to approximately 150 μs at pure Mg. The addition of as little as 20% Mg to Al reduces the ignition delay time by nearly 30 percent from that of pure Al at both gas temperatures investigated.

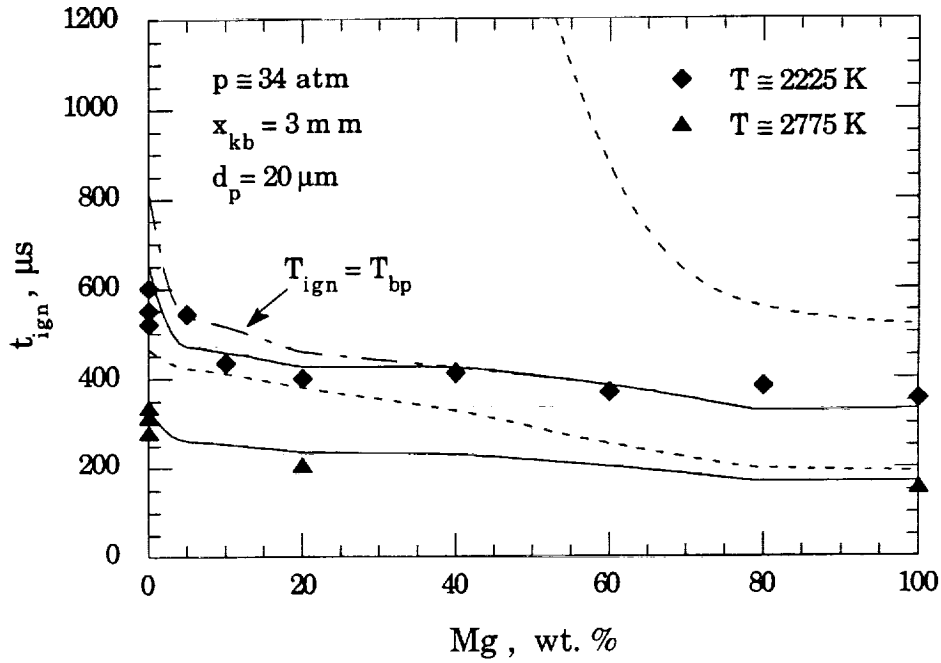

Fig. 4.35: Measured and calculated ignition delay time versus alloy composition as a function of temperature at $p \cong 34$ atm. Measured ignition delay times are normalized to a particle diameter of 20.0 μm assuming $t_{ign} \sim d_p^{1.8}$. The solid and dashed curves correspond to calculations with and without heterogeneous reaction, respectively. The dot-dashed curve is calculated assuming $T_{ign} = T_{bp}$.

Table 4.8: Measured ignition delay and burn times of the alloy particles as a function of composition at p ≅ 34.0 atm. x_{kb} = 3 mm for all measurements.

Shot #	Mg (wt. %)	T_1 (K)	M_{s_i}	T_5 (K)	p_5 (atm)	t_{ign} (μs)	t_b (μs)
T ≅ 2225 K, p_1 = 3.38 psia							
260	0	298	4.32	2240	34.0	596	319
269	0	298	4.28	2200	33.1	688	278
270	0	298	4.29	2200	33.3	631	332
264	5	297	4.28	2200	33.2	568	216
265	10	297	4.33	2230	34.1	461	203
266	20	294	4.34	2220	34.3	444	229
267	40	297	4.31	2220	33.7	468	201
262	60	298	4.32	2230	33.9	423	173
268	80	298	4.29	2200	33.3	445	133
263	100	296	4.33	2230	34.0	404	213
T ≅ 2775 K, p_1 = 2.32 psia							
277	0	298	4.92	2720	32.5	384	250
278	0	297	5.09	2840	35.4	320	216
279	0	296	5.02	2780	34.2	357	217
281	20	298	5.03	2800	34.4	242	127
280	100	297	5.01	2780	34.1	181	163

The solid and dashed curves in Fig. 4.35 correspond to model calculations with and without a heterogeneous reaction, respectively. The solid curves are in excellent agreement with the experimental data. Neglecting the contribution of the heterogeneous reaction to the particle heating results in the expected

overprediction of t_{ign} for particles with low Mg contents. At a gas pressure of 34 atm, the alloy ignition temperature approaches 2225 K at an alloy composition of approximately 39% Mg (see Fig. 4.29). Therefore, as that composition is approached, the ignition delay time will approach infinity asymptotically for a gas temperature of T = 2225 K, if particle self-heating is neglected.

The dot-dashed curve in Fig. 4.35 is calculated assuming the particle ignition temperature is equal to the alloy boiling point, $T_{ign} = T_{bp}$, even if T_{bp} exceeds the melting point of Al_2O_3. The result of this calculation does not differ substantially from that of the standard calculation, however, the solid curve clearly predicts the trend in the experimental measurements more accurately for particles containing less than 20% Mg.

The solid curves plotted in Figs. 4.36 and 4.37 are the calculated oxidized mass and reaction energy fraction plotted as a function of alloy composition, and correspond to the solid curves presented in Fig. 4.35. The predicted oxidized mass and reaction energy fractions are found to rise from their Al value to a plateau which stretches from 5% Mg to approximately 40% Mg. As shown previously, the termination of this plateau is associated with the alloy composition at which the ignition temperature drops below the Al_2O_3 melting point. At Mg contents above 40%, the oxidized mass and reaction energy fractions decrease with increasing Mg content, and are related to the decrease in the alloy ignition temperature. It is interesting to note that the magnitudes of the oxidized mass and reaction energy fractions, at given alloy compositions, are nearly independent of the gas pressure.

The dash-dotted curve in Figs. 4.36 and 4.37 correspond to the ignition delay time calculation which assumes $T_{ign} = T_{bp}$. Although this assumption has only a small effect on the calculated t_{ign}, the effect it has on the calculated

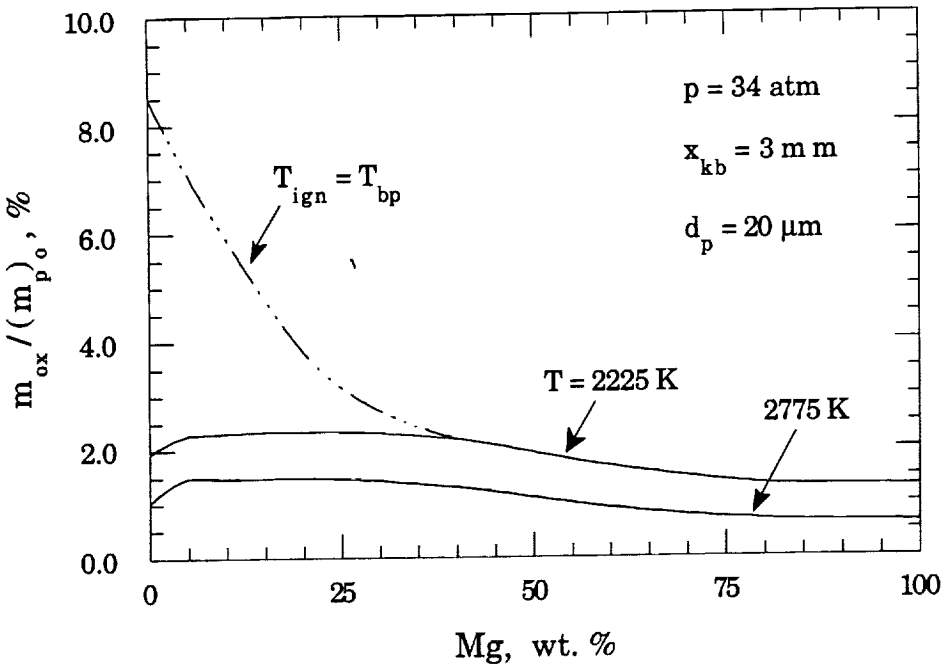

Fig. 4.36: Calculated oxidized particle mass fraction as a function of alloy composition corresponding to the conditions of Fig. 4.35.

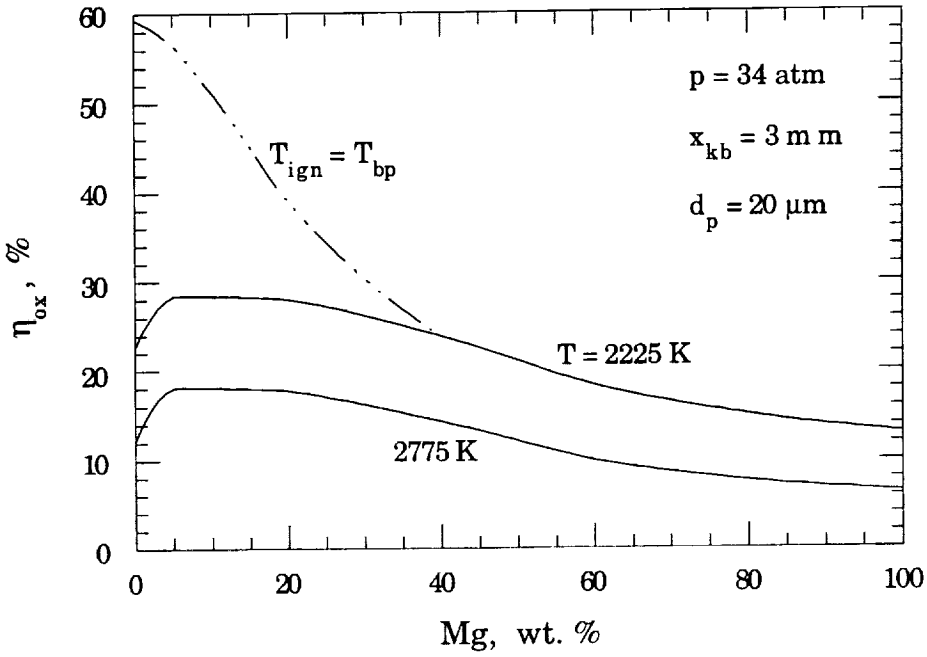

Fig. 4.37: Calculated reaction energy fraction as a function of alloy composition corresponding to the conditions of Fig. 4.35.

oxidized mass and reaction energy fractions is substantial. For example, if $T_{ign} = T_{bp}$, the 5% Mg oxidized mass and reaction energy fractions are increased by a factor of 3.3 and 2.0, respectively. The variation of these results with alloy composition is clearly associated with the variation of the alloy boiling point at p = 34 atm, as shown in Fig. 4.29.

The variation of the calculated $\overline{Nu_p}$ at p = 34.0 atm, shown in Fig. 4.38 plotted as a function of alloy composition, is similar to that predicted at p = 8.5 atm and 17.0 atm. A comparison of the calculations presented in Figs. 4.34 and 4.38 indicate that the overall magnitude of $\overline{Nu_p}$, at p = 34.0 atm, is approximately 30 percent greater than that predicted at p = 17.0 atm. Figure 4.38 indicates that $\overline{Nu_p}$ decreases approximately 8 percent from pure Mg to 5% Mg. $\overline{Nu_p}$ then drops another 7 percent, from 5% Mg to pure Al, due to the

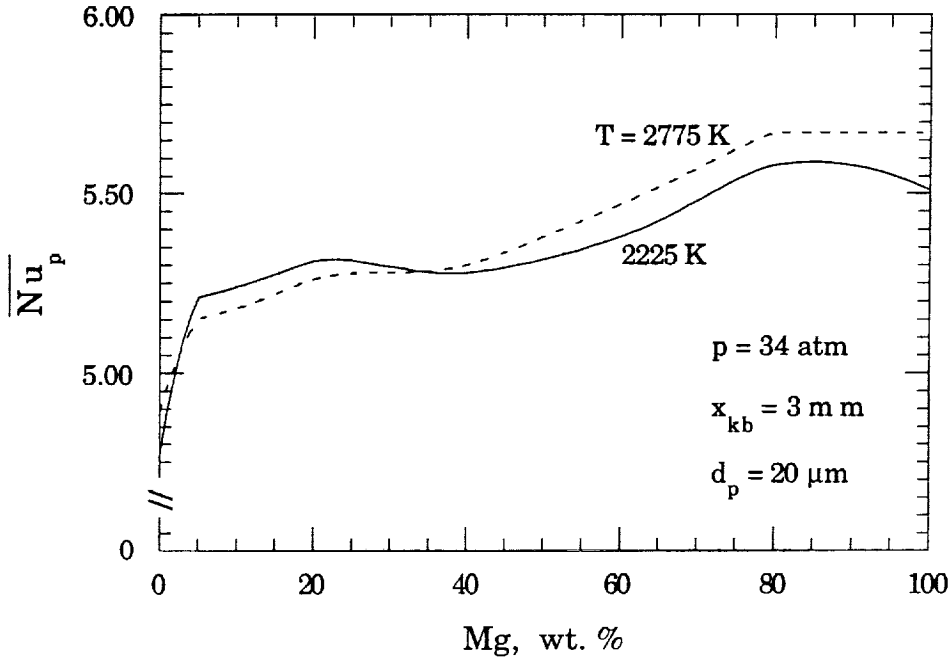

Fig. 4.38: Time-integrated surface-averaged particle Nusselt number as a function of alloy composition corresponding to the solid curves of Fig. 4.35.

longer relative ignition delay time of the Al particles. This variation in the time-integrated particle Nusselt number is believed to have no effect on the conclusions drawn from the experimental measurements and model calculations.

4.4 RATE OF ENERGY PRODUCTION AND TRANSFER DURING THE PARTICLE PRE-IGNITION HEATING PERIOD

Further insight into the ignition process of the Al/Mg alloy particles can be obtained by comparing the temporal history of the rate of particle energy production. Figure 4.39 shows the calculated rate of energy transferred to the particle convectively, $\dot{q}_c$, and produced by the particle's heterogeneous reaction, $\dot{q}_r$, as a function of time for a 20 μm diameter, pure Mg particle. The oxygen atmosphere is assumed to be at a temperature of T = 2225 K. The solid and dashed curves correspond to gas pressures and knife blade mounting distances of 8.5 atm, 8 mm and 34 atm, 3 mm, respectively.

Figure 4.39 indicates that the high convective heating rates, $O\{10^8$ W/m$^2\}$, are found to fluctuate for a short period of time as the particle is heated in the high velocity gas in region 2, decelerated in region 5 while drifting toward the endwall, and then reflected from the endwall. After particle reflection, $\dot{q}_c$ is predicted to decrease monotonically as the particle temperature rises. On the other hand, the rates of energy produced through the heterogeneous reaction are found to rise from essentially zero to approximately 5 x 10^4 W/m^2, at which point it remains constant as the particle melts. The magnitude of $\dot{q}_r$ then continues to rise exponentially with increasing particle temperature. At the time of ignition, which is indicated by the open circles, $\dot{q}_r \cong \dot{q}_c$ at p = 8.5 atm and $\dot{q}_r > \dot{q}_c$ at p = 34 atm. This difference is due to the fact that the Mg ignition

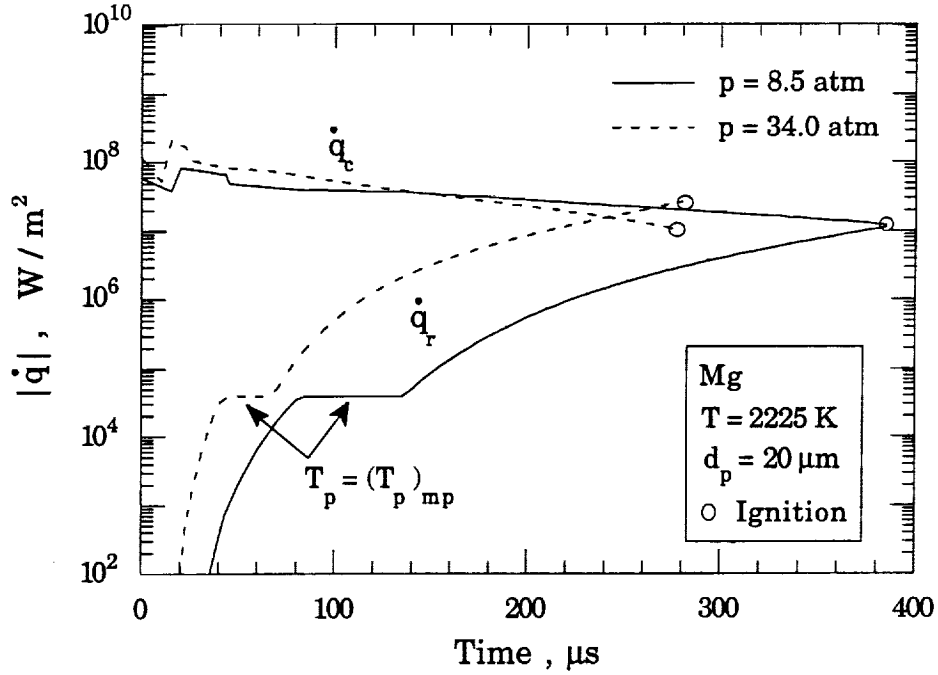

Fig. 4.39: Time dependence of the rate of energy transferred to a Mg particle convectively ($\dot{q}_c$) and produced by the heterogeneous reaction ($\dot{q}_r$) as a function of gas pressure.

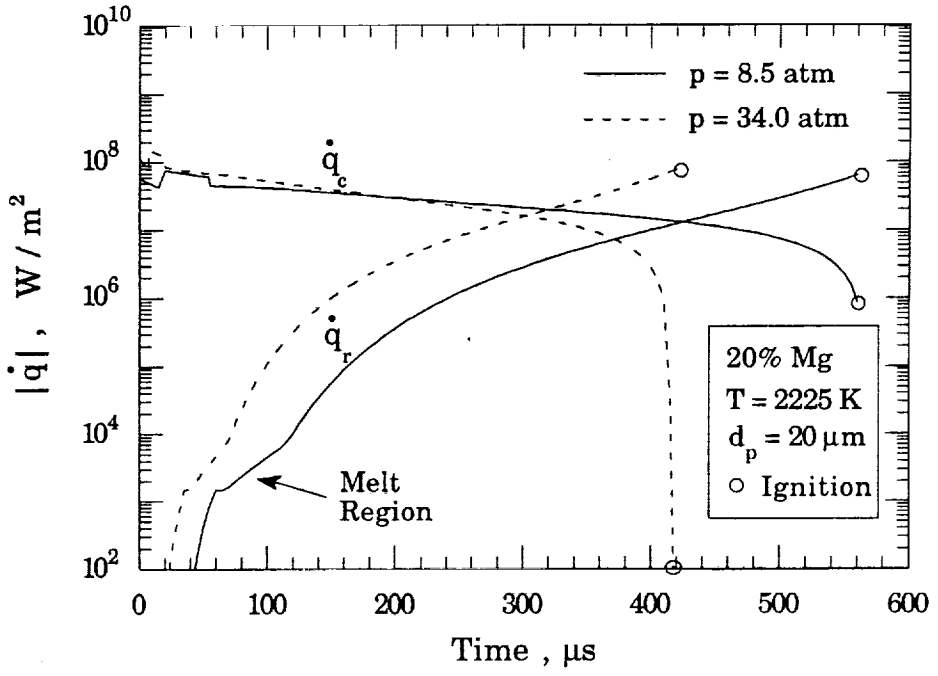

Fig. 4.40: Time dependence of the rate of energy transferred to a 20% Mg particle convectively ($\dot{q}_c$) and produced by the heterogeneous reaction ($\dot{q}_r$) as a function of gas pressure.

temperature, equal to the Mg boiling point, rises from $(T_{ign})_{Mg}$ = 1690 K at p = 8.5 atm to $(T_{ign})_{Mg}$ = 1940 K at p = 34.0 atm.

For comparison, Fig. 4.40 presents $\dot{q}_c$ and $\dot{q}_r$ as a function of time for a 20 μm diameter, 20% Mg particle. The experiment conditions are identical to those assumed in Fig. 4.39. The overall trends of the curves are similar to those for pure Mg. The high Al content of the 20% Mg particle results in an ignition temperature which is substantially higher than that of pure Mg, $(T_{ign})_{20\%\ Mg}$ = 2200 K at p = 8.5 atm and $(T_{ign})_{20\%\ Mg}$ = 2300 K at p = 34 atm. At the time of particle ignition, the solid curves (8.5 atm) indicate that $\dot{q}_r$ is two orders of magnitude greater than $\dot{q}_c$. At p = 34 atm, the ignition temperature of the 20% Mg particles exceed the temperature of the gas. The solid curves show that, as the particle temperature rises above the gas temperature, $\dot{q}_c$ drops below zero and energy is convectively transferred from the particle to the gas. The subsequent ignition of the particle is accomplished solely through self-heating of the particle by the heterogeneous reaction.

Figure 4.41 clearly shows the effect that the gas temperature has on the time dependence of $\dot{q}_c$ and $\dot{q}_r$ for a 20 μm diameter, 20% Mg particle. The calculations assumed a gas pressure of p = 34.0 atm and x_{kb} = 3 mm. The dashed and solid curves correspond to gas temperatures of T = 2225 K and T = 2775 K, respectively. The calculated rate of convective heat transfer never drops to zero for a gas temperature of T = 2775 K, while $\dot{q}_c$ becomes an energy loss at T = 2225 K, as was discussed in the previous paragraph. Although the calculated $\dot{q}_r$ reaches the same magnitude at the time of particle ignition for both gas temperatures, the integral of $\dot{q}_r$ is substantially larger at the lower gas temperature, due to the corresponding reduction in dT_p/dt. Since the oxidized particle mass fraction is proportional to the integral of $\dot{q}_r$, Fig. 4.41 clearly shows why it is a strong function of the gas temperature.

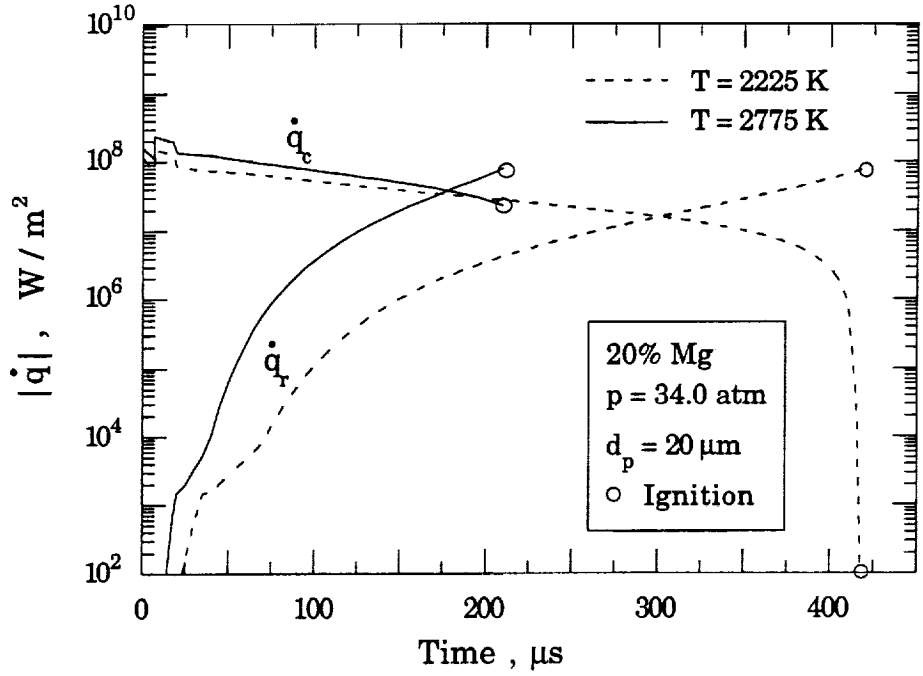

Fig. 4.41: Time dependence of the rate of energy transferred to a 20% Mg particle convectively ($\dot{q}_c$) and produced by the heterogeneous reaction ($\dot{q}_r$) as a function of gas temperature.

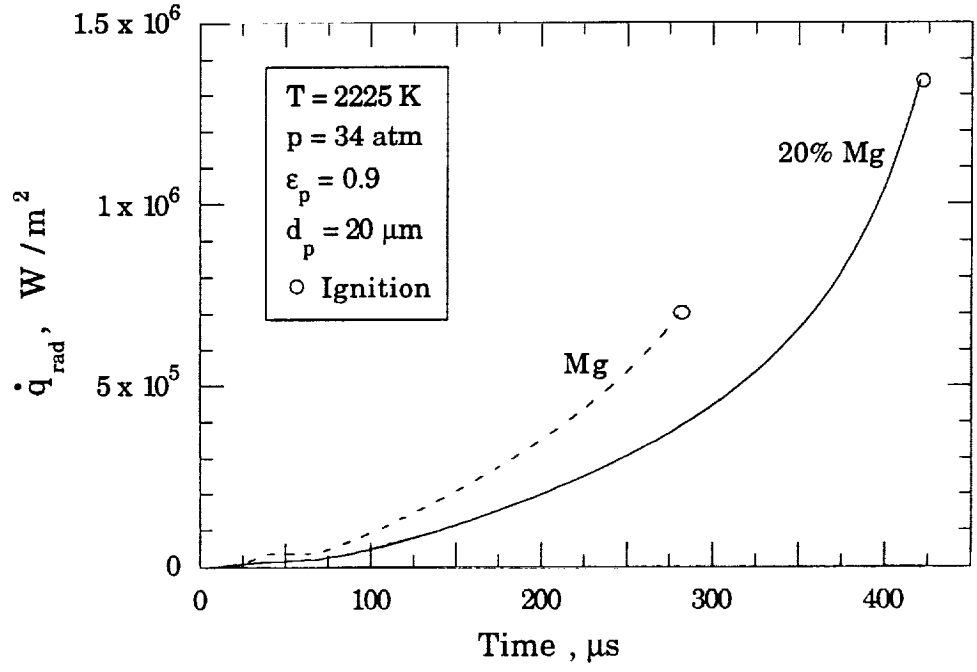

Fig. 4.42: Time dependence of the rate of energy lost radiatively by the Mg and 20% Mg particles. The calculations assume $\varepsilon_p = 0.9$.

The calculated rate of radiative energy loss, $\dot{q}_{rad}$, as a function of time, for Mg and 20% Mg particles is shown in Fig. 4.42. The calculations assume that $\varepsilon_p = 0.9$, T = 2225 K, p = 34 atm, and $x_{kb} = 3$ mm. At the time of particle ignition, $\dot{q}_{rad}$ has increased from ~0 to 7 x 10^5 W/m^2 and 1.3 x 10^6 W/m^2 for Mg and 20% Mg, respectively. The difference in the magnitudes of $\dot{q}_{rad}$ at t_{ign} is due to the difference in the particle ignition temperatures. The magnitude of $\dot{q}_{rad}$ is always calculated to be at least two orders of magnitude smaller than those of $\dot{q}_c$ or $\dot{q}_r$. The integrated fraction of energy lost radiatively is always less than two percent of the total energy transferred to the particle convectively and produced by the heterogeneous reaction.

4.5 EFFECT OF O_2 PRESSURE ON THE PREDICTED ALLOY IGNITION DELAY TIME

Figure 4.43 presents the result of calculations performed to assess the effect of gas pressure on the variation of t_{ign} with alloy composition. The calculations are performed assuming the particles are stationary relative to the oxygen atmosphere, $|v_p - v_g| = 0$, so that the surface-averaged Nusselt number does not vary with alloy composition. Calculations are performed for gas pressures of p = 8.5 atm, 34.0 atm, and 136 atm, to cover the range of operating rocket motor chambers. The gas temperature and particle diameter are assumed to be T = 2500 K and $d_p = 20$ μm. The curves in Fig. 4.43 indicate that the dependence of t_{ign} on alloy composition is relatively insensitive to the gas pressure. Raising the gas pressure by a factor of 16 has little effect on the ignition delay time of particles containing less than 30% Mg. The ignition delay times of particles with greater than 30% Mg are predicted to increase slightly with increasing gas pressure, due to the rising particle ignition temperature.

The ignition delay time of pure Mg is predicted to increase by 20 percent if the gas pressure is increased from 8.5 atm to 136 atm.

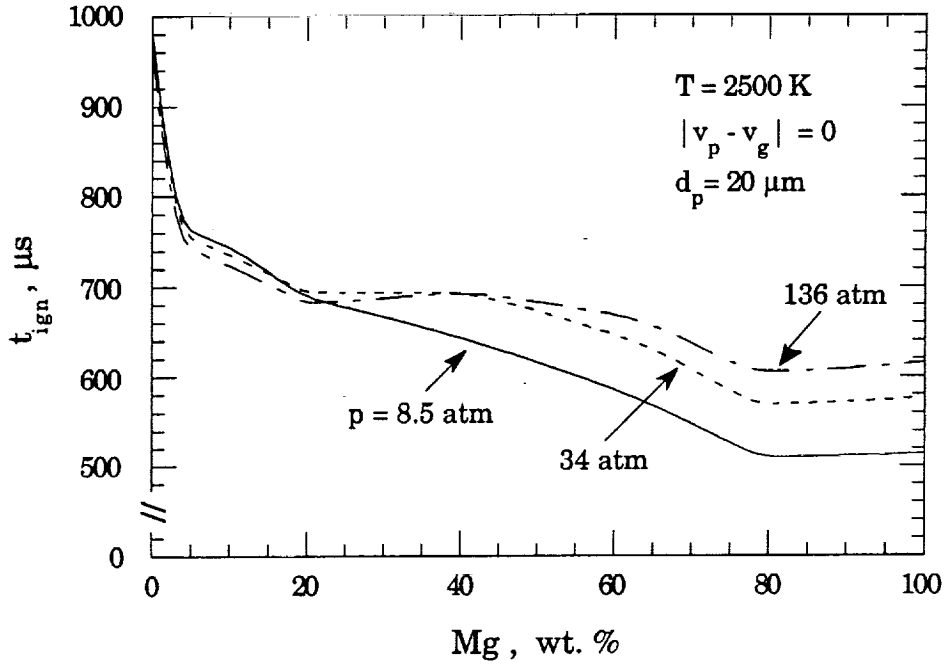

Fig. 4.43: Effect of gas pressure on the calculated Al/Mg alloy particle ignition delay time in quiescent oxygen at T = 2500 K.

4.6 MEASURED ALLOY PARTICLE COMBUSTION TIME

As was discussed in Section 2.1, the particle combustion time, t_b, is taken to be equal to the difference between the first and last times at which the magnitude of the photodiode signal equals half of its peak value (see Fig. 2.3). This measurement will be valid only if the decay time of the broadband emissions from the condensed phase oxide products is small compared to the measured particle burn time.

The size of the condensed oxide products produced during combustion is uncertain, but the majority of the particles are believed to be less than 1 μm

diameter [1,28,88]. Using the kinematic particle heating model developed here, the calculated radiative emission decay time for condensed Al_2O_3 is dominated by conduction to the gas and is < 2 μs for a 1 μm particle. This calculation assumes a spherical particle, an initial oxide temperature of 5000 K, T_{O_2} = 2775 K, p_{O_2} = 17 atm, ε_{ox} = 0.9, and c_{ox} = 1.47 kJ/kg, and a Nusselt number of 2. The decay time is taken to be the time required for the emissive power to drop to half of its initial value, which corresponds to a final oxide temperature of 4200 K. Since the particle burn times are in excess of 100 μs, oxide radiation does not significantly affect the measurement of t_b.

4.6.1 Effect of Gas Temperature on Alloy Particle Combustion

The measured burn times of Al, Mg, 20% Mg, and 60% Mg alloy particles as a function of gas temperature at p ≅ 17 atm are shown in Fig. 4.44. The measurements have been normalized to d_p = 20 μm assuming n_b = 1.8 (see section 4.3). The raw data is presented in Tables 4.2 and 4.3 along with the corresponding ignition delay times.

Figure 4.44a shows the measured burn times of pure Mg and Al particles, plotted along with their corresponding best-fit linear curves. The Mg data is well behaved, while the Al data is quite scattered. The burn time of the Mg particles is found to be nearly independent of gas temperature, decreasing only slightly from approximately 220 μs at T ≅ 1750 K to 200 μs at T ≅ 3150 K. Although the Al particle burn time data is scattered, it is clearly higher than that of the Mg particles. The best fit linear curve for Al indicates that its burn time decreases from ~300 μs to ~240 μs, for gas temperatures of 2500 K and 3300 K, respectively.

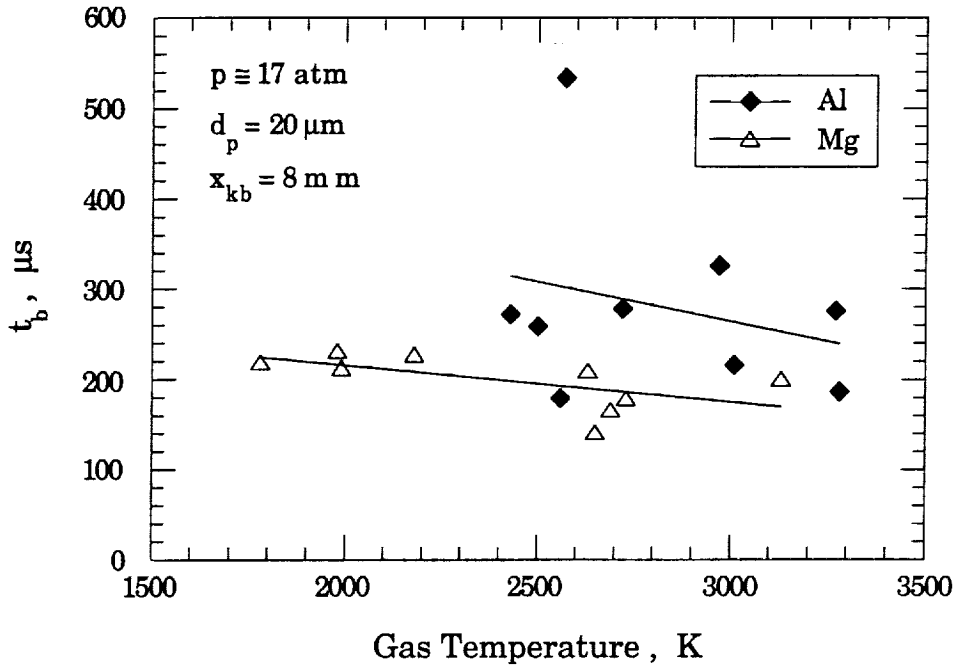

(a)

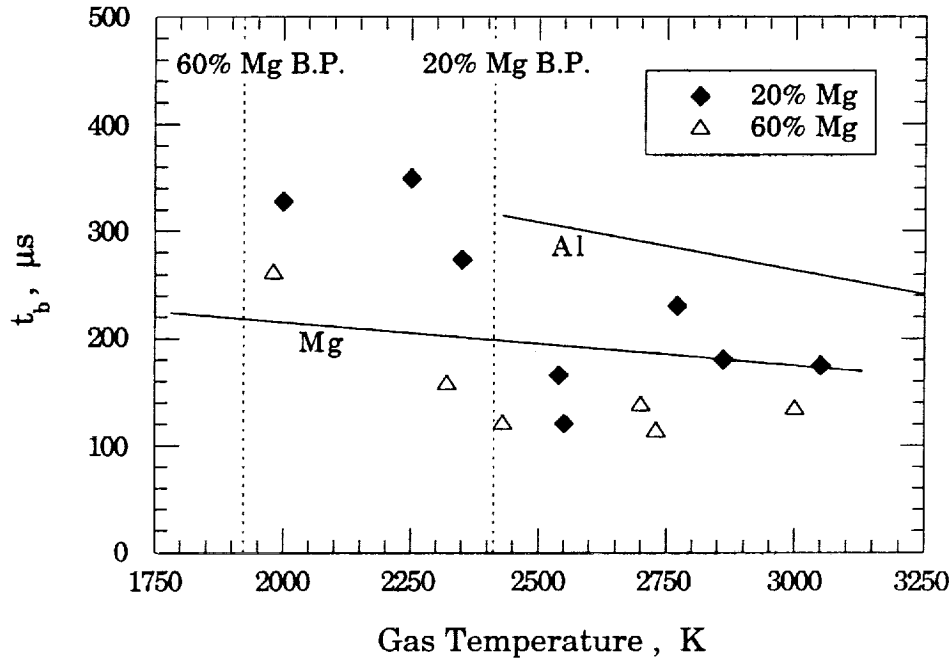

(b)

Fig. 4.44: Measured particle combustion time as a function of gas temperature. a) Al and Mg particles, solid curves are linear fits. b) 20% Mg and 60% Mg alloy particles, solid curves are the linear fits of Fig. 4.44a.

Figure 4.44b presents the measured burn times of the 20% Mg and 60% Mg alloy particles as a function of gas temperature. The solid curves correspond to the linear fits for Al and Mg shown in Fig. 4.44a. For a Mg content of 60%, the particle burn time is nearly independent of gas temperature, and is found to be less than even that of pure Mg.

Although the 20% Mg particle burn time data is more scattered than that measured using the pure Mg and 60% Mg particles, a very interesting trend is observed. At lower gas temperatures, the burn times of the 20% Mg particles are on the order of 300 μs. As the gas temperature is increased, the burn time suddenly drops to approximately 200 μs, and then remains fairly constant. This sudden drop in burn time is roughly correlated with the boiling point (~2420 K) of the 20% Mg alloy particles, as indicated by the vertical dashed curve in Fig. 4.44b. The boiling point (~1920 K) of the 60% Mg particles is also shown in the figure, and is just slightly below the temperature corresponding to the measured burn time that appears be uncharacteristically long.

Figure 4.45 presents a compilation of the Al particle burn times, measured as a function of temperature, for various knife blade mounting distances. The measurements have been normalized to d_p = 20 μm and the raw data is presented in Tables 4.2 and 4.4. As is generally the case for Al particles, the burn time data is quite scattered, particularly at the lower gas temperatures. The solid curve in Fig. 4.45 is a best fit linear curve of all the data presented. The best fit curve indicates that the Al burn time decreases with increasing temperature from ~400 μs at T ≅ 2250 K to ~240 μs at T ≅ 3250 K.

The scatter in the measurements of Fig. 4.45 is attributed to a slowly falling photodiode signal. It is believed that the data points that lie above 500 μs in Fig. 4.45 are obvious anomalies that should be neglected. The source of these erroneous signals is unknown. A possible explanation may be the erratic

trajectories of Al particles, caused by the jetting and fragmentation known to accompany Al particle combustion [28], which may result in a large number of particles impinging on the observation window. The particles may then continue to burn in a slower, heterogeneous manner, due to the low window temperature. If these particles lie in the photodiode focal region, a slowly falling signal could result.

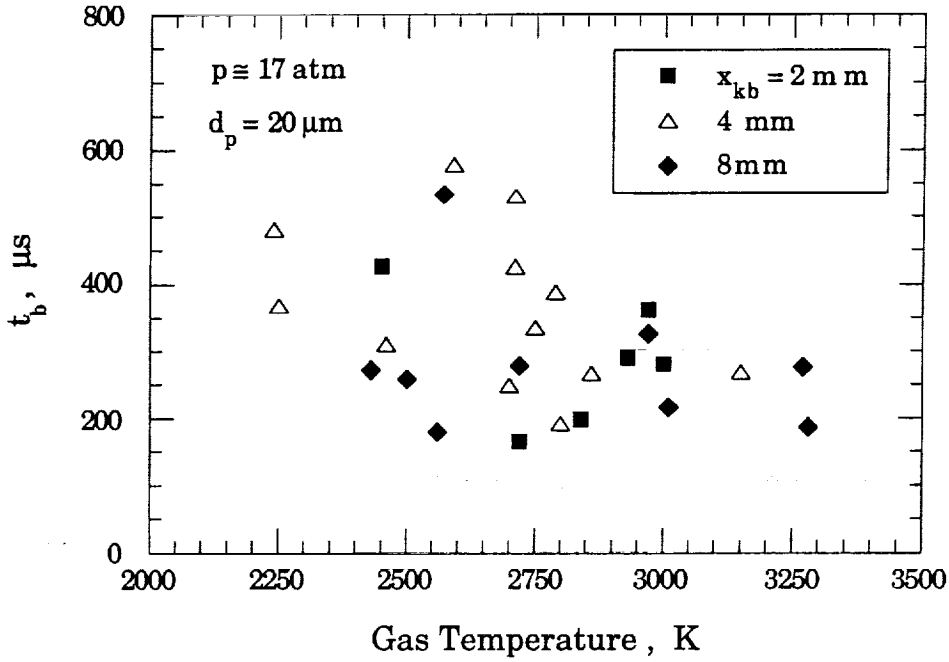

Fig. 4.45: Measured Al particle burn time versus gas temperature and knife blade mounting position.

4.6.2 Effect of Alloy Composition on Particle Combustion

Shown in Fig. 4.46 are the measured particle burn times, normalized to d_p = 20 µm, plotted as a function of alloy composition. The gas conditions for these measurements are p ≅ 8.5 atm and T ≅ 2225 K and 2775 K. The raw data is presented in Tables 4.5 and 4.6 and corresponding to the ignition delay times

plotted in Fig. 4.25. The solid curve is a best fit third order polynomial of all the data presented. Although the data exhibit substantial scatter at both gas temperatures, the best fit curve indicates that the measured particle burn time decreases in a nearly linear fashion from approximately $t_b \cong 270$ μs for Al to $t_b \cong 180$ μs for Mg, a reduction of 33 percent. The gas temperature is found to have a negligible effect on the measured particle combustions times.

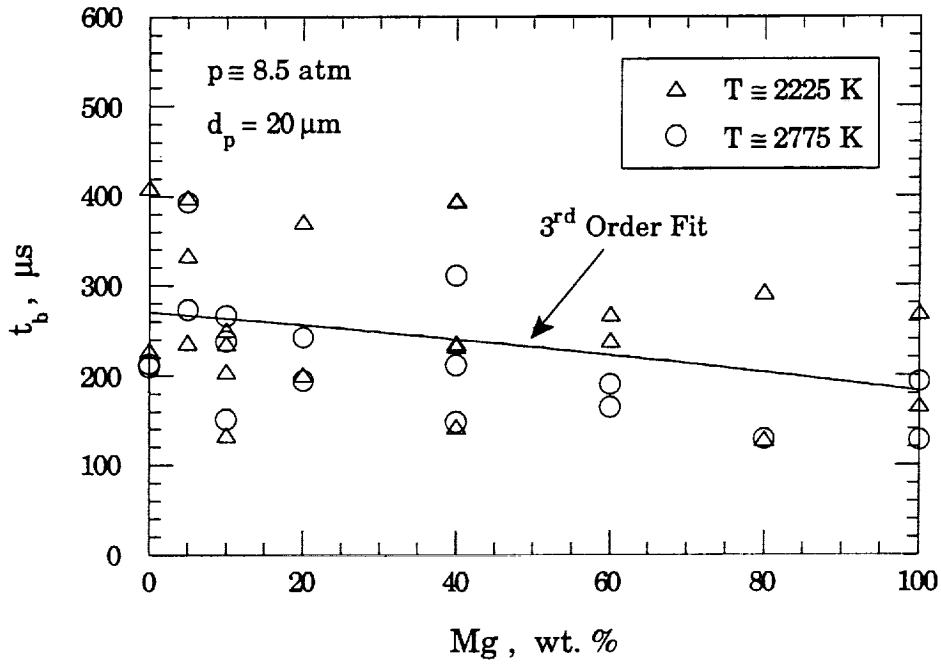

Fig. 4.46: Measured particle burn time versus alloy composition at p ≅ 8.5 atm corresponding to the ignition delay times presented in Fig. 4.25. The burn times are normalized to a particle diameter of 20.0 μm.

The particle burn times, normalized to $d_p = 20$ μm, corresponding to the data presented in Figs. 4.31 and 4.35 are plotted in Fig. 4.47 as a function of alloy composition. The gas conditions for these measurements were T ≅ 2225 K and 2775 K at each pressure of p ≅ 17.0 and 34.0 atm. The raw data is presented in Tables 4.7 and 4.2. The data presented in Fig. 4.47 shows little scatter, and the

solid curve is a third order polynomial which has been fit to all of the data points presented. The curve fit indicates that the combustion time of the particles decreases from $t_b \cong 275$ μs for pure Al to $t_b \cong 170$ μs for pure Mg, a reduction of 38 percent. The variation of the burn time is a nonlinear function of the particle alloy composition. With the addition of as little as 20% Mg, the combustion time is reduced to near that of pure Mg.

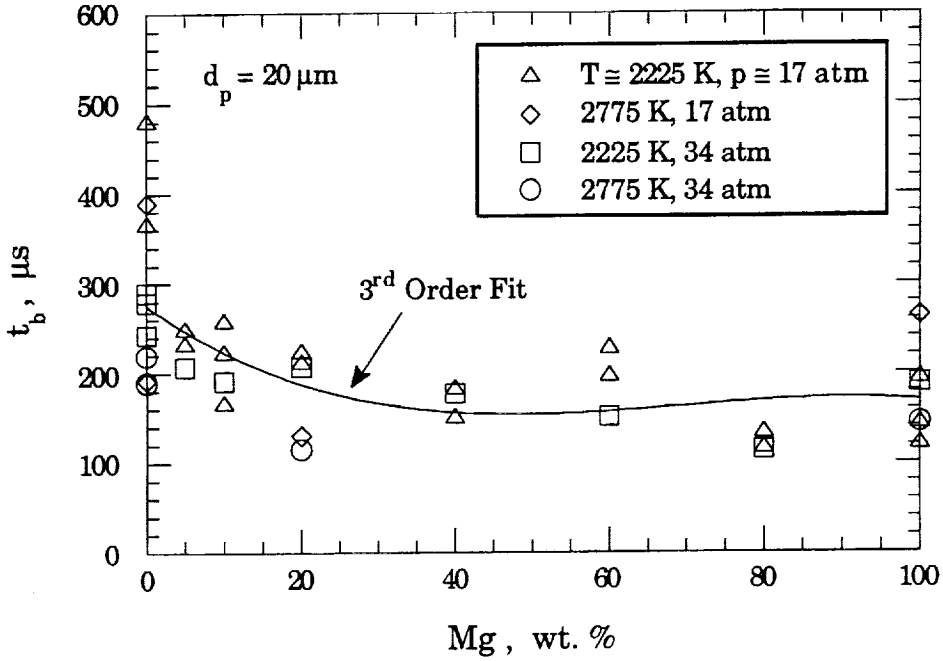

Fig. 4.47: Measured particle burn time versus alloy composition at p ≅ 17 and 34 atm corresponding to the ignition delay times presented in Figs. 4.25 and 4.31. The burn times are normalized to a particle diameter of 20.0 μm.

4.7 COMPARISON OF MEASURED Al AND Mg BURN TIMES WITH PUBLISHED EXPERIMENTAL AND THEORETICAL VALUES

For the gas conditions used in this experiment, high oxygen concentration and high gas temperatures, the Al/Mg alloy particles are expected to burn in a detached flame (vapor phase), diffusion limited manner

[1,18,23,28,42,43]. As discussed in Chap. 1, the combustion of metal particles is generally treated analytically in a quasi-steady-state manner. However, the results of these models are in qualitative, rather than quantitative, agreement with experiments [26]. The quasi-steady-state combustion model developed by Brzustowski and Glassman predicts burn times of $t_b \cong 800$ μs and 400 μs for 20 μm Al and Mg particles burning in pure oxygen, respectively [24]. Qualitatively, the analytic model predicts the burn time of Mg to be 50 percent shorter than that of Al. This is in general agreement with the measurements shown in Figs. 4.46 and 4.47, which indicate a burn time reduction of approximately 40 percent.

The analytically-predicted burn times are found to be substantially longer than those measured in this experiment. A fundamental assumption of the quasi-steady-state combustion model is that the particle is at rest relative to the oxidizing atmosphere, and therefore, convective heat and mass transfer to the burning particle is ignored. The particles of this experiment are predicted to have velocities on the order of 10 m/s at the time of ignition (see Fig. 3.19). Although the particle Reynolds numbers are quite low, convective effects can be significant [24], and could possibly account for the increased burn rates measured in this experiment.

Wilson and Williams [18] measured the burn rate of stationary 50 μm Al particles to be $\beta = 15 \times 10^{-3}$ cm^2/s in pure oxygen at room temperature and pressures to 5 atm. Using this result and the relation $t_b = (d_p)^{1.8}/\beta$, the corresponding burn time for a 20 μm Al particle is calculated to be 920 μs, which is substantially longer than the value measured here. Prentice measured the burn times of 300-450 μm diameter Al particles in a 20% oxygen/argon atmosphere at a pressure of 0.93 atm [17]. Larson states that it is generally accepted that the burn rate of Al particles is proportional to the sum of the

oxidizer mole fractions raised to the 0.9 power [89], which is consistent with the results of Wilson and Williams [18]. Assuming this dependence of the burn rate on the oxidizer mole fraction and assuming $t_b = (d_p)^{1.8}/\beta$, the burn rate of Al in pure oxygen based on the data of Prentice is estimated to be $\beta \cong 3.0 \times 10^{-2}$ cm^2/s. This rate yields a calculated burn time of $t_b \cong 460$ μs for a 20 μm Al particle and is found to be approximately twice that of the Al measurements of this experiment.

Hermsen [87] has proposed an empirical model for the Al particle combustion rate which has the form:

$$(d_p)^{1.8} = (d_p)_o^{1.8} - \beta t \qquad (4.3)$$

where $\beta = 8.3314 \times 10^{-5} R_k (A_k)^{0.9} p^{0.27}$ cm$^{1.8}$/s

A_k = mole percent of oxidizer, %

p = gas pressure, psia

$(d_p)_o$ = initial particle diameter, cm.

The factor R_k is an empirically determined constant, which is a correction to the burning rate used to account for the difference between the gas environments which exist in laboratory experiments and operating rocket chambers. For the non-convective, low blackbody temperature environment of a laboratory experiment, it is suggested that a value of $R_k = 1$ be used. For the convective, high blackbody temperature environment of a rocket chamber, the appropriate value of R_k was determined to be 2.7 [87].

Assuming $d_o = 20$ μm (.002 cm), $A_k = 100$, and p = 8.5 atm (125 psia), Hermsen's model predicts Al particle burn times of $t_b \cong 450$ μs and 170 μs for $R_k = 1$ and 2.7, respectively. The measured Al particle burn times measured here

are found to be bracketed by these two limiting values, and are nearer to the value associated with the convective environment of an operating rocket chamber.

The relatively short combustion times measured here may also be due to particle fragmentation, which may be caused by superheating of the particles above their boiling points [16,42,43,90]. Macek [28] states that Al particle combustion becomes increasingly uneven as the mole fraction of oxygen and the gas temperature are increased, resulting in particle fragmentation. Gordon [90] reported that the combustion of small Mg particles, $d_p < 44$ μm, is always characterized by fragmentation. Breiter et al. [42] and Popov et al. [43] found that Al/Mg alloy particles fragmented when burned in atmospheres which were representative of the gas products of a solid propellant, and proposed a superheating mechanism to explain the phenomena. Therefore, the high oxygen concentration, high gas temperature, and small particle sizes used in this investigation are believed to promote the fragmentation of the combusting Al, Mg, and Al/Mg alloy particles, resulting in substantially reduced combustion times.

CHAPTER 5: CONCLUSIONS AND RECOMMENDATIONS

5.1 CONCLUSIONS

The ignition and combustion of ~20 μm diameter Al/Mg alloy particles in a high temperature and pressure, oxygen-rich atmosphere has been experimentally investigated. The measurements were made in the reflected shock region near the endwall of a shock tube using a novel particle mounting technique that results in individual, rather than group, particle ignition and combustion. The ignition results have been successfully modeled using real particle and gas properties and a one-dimensional kinematic description of the particle motion.

Based on experimental measurements and results of the ignition model, the following conclusions concerning the ignition of Al/Mg alloy particles in a hot, high pressure, oxygen atmosphere are drawn:

1) Due to the small diameter and high thermal conductivity of the alloy particles, the particle temperature is isothermal and the *simple lumped capacitance energy equation accurately models the transient heating problem involved in the particle ignition process.* The accuracy of the solution appears only to be limited by the precision of the specified rates of heat transfer, energy production, and energy loss.

2) *As little as 10% Mg in alloy reduces the particle ignition delay time substantially over that of pure Al at all of the pressures tested.* At a pressure of 8.5 atm, the ignition delay time continues to decrease considerably as the Mg content is increased further. Although the latter effect is also observed at pressures of 17 and 34 atm, it is less pronounced.

3) *The contribution of heterogeneous surface reactions to the particle heating rate is significant at lower temperatures for all particle*

compositions, including pure Al. As the temperature of the gas is increased, the contribution of the heterogeneous reaction is reduced due to the high rate of heat transfer from the gas to the particle. Near ignition, the heating rate due to heterogeneous surface reaction is comparable to that due to convection. At gas temperatures above 3000 K, the heterogeneous reactions can be neglected when calculating the ignition delay time of particles with diameters on the order of 20 μm.

4) A simple, constant coefficient, Arrhenius type reaction rate is used to model the complicated processes (i.e., fracturing of the oxide film due to particle expansion, etc.) associated with the particle's heterogeneous surface reaction. This simple reaction model predicts that *the pre-exponential constant (and, therefore, the rate of reaction) of the Al/Mg alloy particles is equal to that of pure Mg for alloys containing more that 10 weight percent Mg.*

5) *Transition from the heterogeneous reaction to the detached gas-phase reaction occurs when the heated particle reaches either the alloy boiling point or the melting point of Al_2O_3, whichever is lower. Therefore, the alloy particle ignition temperatures are pressure dependent.*

The generally accepted criterion for Al ignition (melting of the oxide film) and Mg ignition (boiling of the metal) have been confirmed. To the author's knowledge, the corresponding criteria for alloy ignition presented here are the first published.

Breiter et al. [42] reported that the ignition delay times of Al/Mg alloy particles, measured in the combustion products of a burning solid propellant, exhibit a minimum at an alloy content of approximately 70 weight percent Mg. No such trend is found for the ~20 μm diameter Al/Mg alloy particles burned in an oxygen-rich atmosphere.

The results presented here are limited to the case of Al/Mg alloy particle ignition in oxygen. For conditions of reduced oxygen concentrations, and in the presence of water vapor, the complexity of the particle ignition processes require modification to the analyses presented here, as shown by Megli [46].

Calculations performed as part of this research indicate that the protective nature of the particle oxide layer is a strong function of the composition and temperature of the Al/Mg alloy particle (see Fig. 3.17). The oxide to metal volume ratio, Φ, decreases monotonically from that of pure Al to that of pure Mg. At room temperature, the oxide film remains impermeable ($\Phi > 1$) to a Mg content of approximately 60%. As the particle temperature is increased, Φ decreases for all particle compositions. At T = 1000 K, the Mg content at which the oxide film becomes permeable drops to only 40% by weight. Even the oxide film formed on a pure Al particle becomes non-protective at temperatures above ~2000 K. *These results indicate that significant particle self-heating can occur for any Al/Mg alloy composition, as has been verified experimentally as part of this investigation.*

The combustion times of ~20 μm diameter Al/Mg alloy particles have been measured in oxygen, as a function of gas temperature and pressure, and alloy composition. The following general conclusions can be drawn from the experimental results:

1) For gas temperatures ranging from 1700 K to 3300 K, and at a pressure of ~17 atm, the burn times of Mg, Al, and 60% Mg alloy particles are mildly dependent on the gas temperature. The burn times decrease slightly with increasing temperature. Under these same gas conditions, the burn times of 20% Mg alloy particles are scattered, but the results suggest that a significant reduction (~30%) in burn time occurs as the gas temperature is increased above the alloy's boiling

point. Of the four alloys investigated, particles containing 60% Mg have the shortest overall burn times.

2) At an oxygen pressure of 8.5 atm and temperatures of approximately 2220 K and 2800 K, the particle burn times are found to decrease linearly with increasing Mg content. A third order polynomial curve fit of the data yields particle burn times ranging from 270 μs to 180 μs for pure Al and Mg, respectively.

3) At oxygen pressures of 17 atm and 34 atm, the measured burn times decrease in a nonlinear fashion with increasing Mg content. A third order polynomial curve fit of the data yields a minimum burn time of 150 μs at an alloy composition of ~40% Mg. Consistent with the burn times measured at 8.5 atm, the curve fit of the higher pressure data yields burn times of 275 μs and 175 μs for Al and Mg, respectively. Over the pressure range tested, the results indicate that the particle burn times are nearly independent of pressure.

4) Measured burn times of pure Al and Mg particles are significantly shorter than the measured and calculated (assuming vapor-phase combustion) burn times reported in the literature. The combustion times of the Al particles are in agreement with those calculated using Hermsen's empirical Al burning rate model if the empirical constant, R_k, is taken to be 2.7. This value of R_k is representative of a convective flow environment.

The observed decrease in particle burn time with increasing Mg content is in general agreement with the results obtained by Ozerov and Yurinov [45], for Al/Mg alloy particles *burning in water vapor*. However, Ozerov and Yurinov reported that the particle burn times increased with increasing pressure, whereas the present results indicate the burn times are independent of pressure. This difference may be due to the properties of the oxidizers used in each investigation.

5.2 RECOMMENDATIONS FOR FUTURE RESEARCH

Important information concerning the ignition and combustion characteristics of small diameter Al/Mg alloy particles has been revealed. *The results indicate that, based on the overall particle ignition and combustion time, the optimum alloy composition for use in an Al/Mg-LOX rocket engine is approximately 20% Mg.* At this composition, the overall ignition and combustion time is significantly less than that of pure Al. Therefore, the slight reduction in motor specific impulse, due to a slightly lower heat of reaction, may be offset by a substantial increase in the particle combustion efficiency.

Several critical issues remain unresolved. The performance of rocket motors that burn metallized propellants suffer from two-phase flow losses due to the formation of condensed phase combustion products. An important area of research would be to investigate the dependence of oxide composition on the Mg content of the alloy particle. The agglomeration characteristics of the various oxides formed by the Al/Mg/O_2 reaction (Al_2O_3, MgO, and $MgO \bullet Al_2O_3$) need to be quantified. It would be extremely desirable to tailor the alloy composition to produce smaller size oxide particles that do not readily agglomerate. Thus, further research in this area is also required.

The mechanism responsible for the "explosive" combustion of Al/Mg alloy particles, observed by Breiter et al. [42] and Popov et al. [43], may also play an important role in reducing the size of condensed phase products. This possibility should be carefully investigated.

Theoretically, the specific impulse of a metal/LOX rocket engine can be increased significantly by injecting small amounts of hydrogen into the combustion chamber of the rocket engine [80]. Characterizing the impact of

hydrogen on the ignition and combustion processes of the metal particles would provide a fruitful area of investigation.

APPENDIX A: THEORETICAL Al/Mg-LOX ROCKET PERFORMANCE

A.1 IDEAL ROCKET PERFORMANCE

This section is intended to be a cursory review of the fundamental operation and performance of a liquid propellant rocket engine. For further information, the reader is referred to the works of Sutton [7] and Hill and Peterson [8].

Figure A.1 shows a simplified schematic diagram of a liquid propellant rocket engine. The propellant system consists of a liquid oxidizer and fuel that are typically stored in separate tanks. The propellants are injected into the head-end of the thrust chamber and react to form hot, high-pressure gases which are accelerated through the converging-diverging nozzle to high velocity. The change in the velocity of the gas, from nearly zero in the chamber, $v_c \sim 0$, to the supersonic exhaust velocity, u_e ~O{1000 m/s}, imparts momentum to the rocket system.

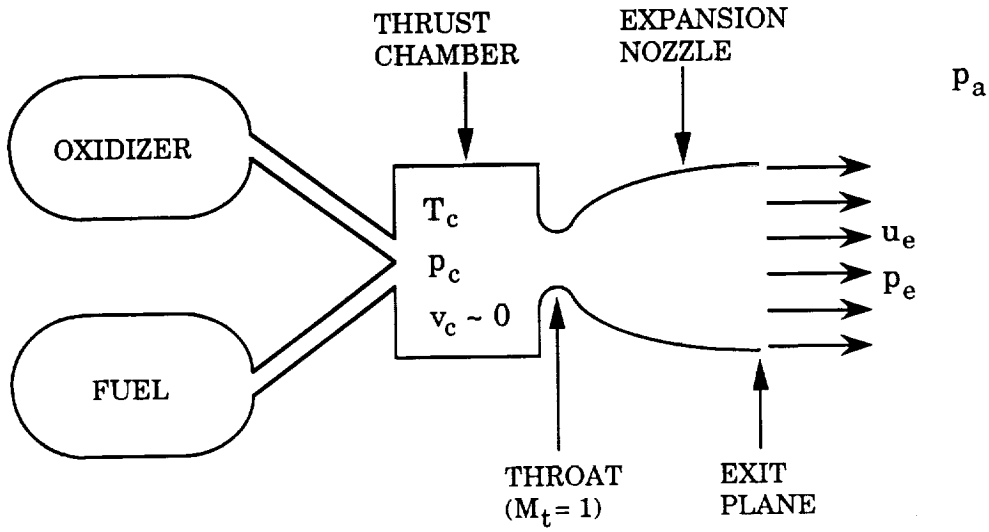

Fig. A.1: Simplified schematic diagram of a liquid propellant rocket engine.

Assuming the rocket engine is operating steadily and the exhaust gases have a uniform velocity, the thrust produced by the rocket engine is simply expressed as:

$$F_T = \dot{m}\, u_e + (p_e - p_a)A_e \tag{A.1}$$

where F_T is the thrust, $\dot{m}$ the propellant mass flow rate, p_e the exit pressure, p_a the ambient pressure of the surroundings, and A_e is the area of the nozzle exhaust. An important measure of the efficiency of a rocket engine is the specific impulse, which is defined as the thrust per unit weight flow rate of propellant:

$$I = \frac{F_T}{\dot{m}\, g_o} = \frac{u_e}{g_o} + \frac{(p_e - p_a)A_e}{\dot{m}\, g_o} \tag{A.2}$$

where g_o is the acceleration of gravity at sea level. It is convenient to define an equivalent exhaust velocity as [8]:

$$u_{eq} = u_e + \frac{(p_e - p_a)A_e}{\dot{m}} \tag{A.3}$$

This reduces the thrust and specific impulse relations, Eqs. (A.1) and (A.2), to the following relatively simple forms:

$$F_T = \dot{m}\, u_{eq} \tag{A.4}$$

and

$$I_{sp} = \frac{u_{eq}}{g_o} \tag{A.5}$$

respectively. The units of specific impulse are generally given in seconds.

Assuming constant propellant flow $\dot{m}$, the change in the velocity of a rocket can be expressed as [7]:

$$\Delta v = v_f - v_o = u_{eq} \ln\left(\frac{m_o}{m_f}\right) \tag{A.6}$$

where v_f is the final velocity, v_o the initial velocity, m_o the initial mass of the rocket, and m_f is the final rocket mass. The final rocket mass is simply defined as $m_f = m_o - \dot{m}t_b = m_o - m_p$, where t_b is the engine burn time and m_p is the total propellant mass. Substituting Eq. (A.5) into Eq. (A.6) and solving for the mas ratio, MR, yields the following relation:

$$MR \equiv \frac{m_f}{m_o} = e^{-\Delta v/u_{eq}} = e^{-\Delta v/(I_{sp} g_o)} \tag{A.7}$$

Equation (A.7) shows the exponential dependence of MR on the specific impulse of the rocket engine, since the velocity change (Δv) for a given mission is a constant. The final mass of the rocket includes the useful payload, m_u, plus the mass of the propulsion system (thrust chamber, propellant feed system, tankage), guidance system, etc. Clearly, it is desirable to increase the I_{sp} to maximize MR, and thus m_u. For example, the velocity change required for a transfer from low earth orbit (LEO) to low lunar orbit (LLO) is approximately 4170 m/s [91]. For rocket engine specific impulses of 250 s and 300 s, the calculated mass ratios are 0.183 and 0.243, respectively. The following section will discuss the ideal performance of an Al/Mg-LOX rocket engine, calculated using the NASA Gordon-McBride program [9].

A.2 CALCULATED PERFORMANCE OF AN Al/Mg-LOX ROCKET ENGINE

The results presented here were calculated using the rocket performance section of the NASA Gordon-McBride program [9]. The program makes the following assumptions when calculating the various parameters: one-dimensional form of the continuity, energy, and momentum equations; zero velocity in the combustion chamber; complete, adiabatic combustion; isentropic

expansion; homogeneous mixing; ideal gas law; and zero temperature and velocity lags between condensed and gaseous species. The program calculates both equilibrium and frozen performance. Equilibrium calculations assume the composition of the gas attains equilibrium instantaneously during expansion, while the frozen calculations assume the composition remains fixed at the composition of the combustion chamber.

Figures A.2 - A.5 (and Fig. 1.1) show the results of calculations for an Al/Mg-LOX rocket engine performed assuming a chamber pressure of p_c = 1000 psia, a nozzle expansion ratio of $\varepsilon = A_e/A_t = 77.5$, where A_t is the throat area, and equilibrium gas composition. In addition, the propellant system is assumed to consist of a metal-LOX slurry mixture. Therefore, the oxygen and metal are assumed to enter the combustion chamber at a temperature equal to the normal boiling point of liquid oxygen, $(T_{bp})_{LOX}$ = 90.18 K. At this temperature, the specified reference enthalpies of the constituents are -3102 cal/mole, - 981 cal/mol, and -1056 cal/mole for O_2, Al, and Mg, respectively.

Figures A.2 and 1.1 show the Al/Mg-LOX vacuum specific impulse ($p_a = 0$) plotted as a function of Al/Mg alloy composition and oxidizer to fuel mass ratio (O/F), respectively. Note that at O/F ratios of 0.88 and 0.66 for pure Al and pure Mg, respectively, the reactants are in stoichiometric proportion and will react to form only solid products, prohibiting their expansion through the nozzle. Although these stoichiometric ratios represent the theoretical limit of operation of an Al/Mg-LOX rocket, the practical limit will undoubtedly occur at O/F ratios significantly higher than these, since the presence of a sufficient excess of oxygen is required to carry and accelerate the condensed oxide products through the rocket nozzle.

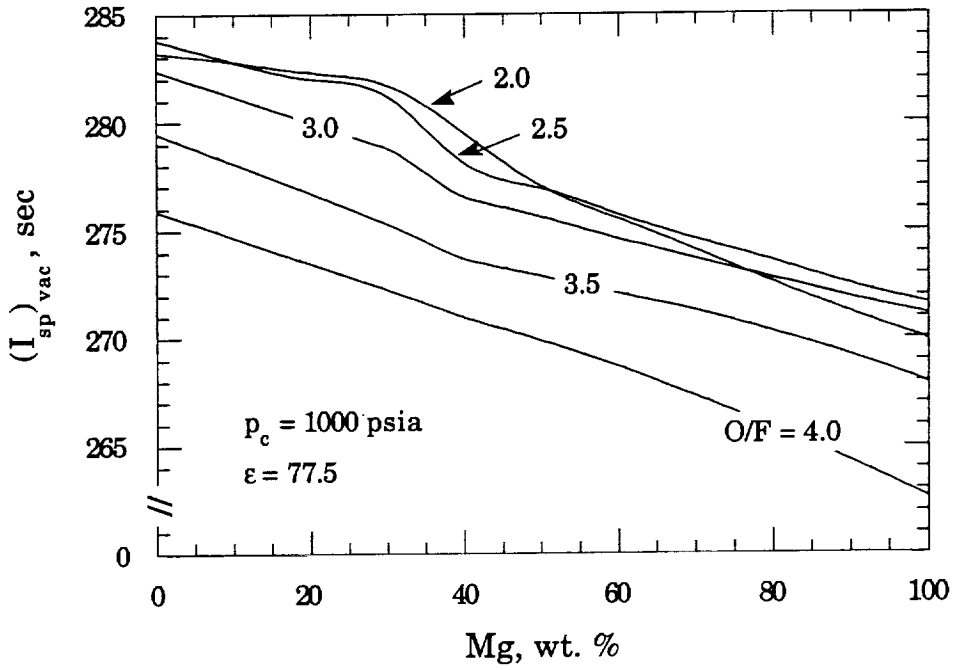

Fig. A.2: Calculated vacuum specific impulse of an Al/Mg-LOX rocket engine as a function of alloy composition for various O/F ratios.

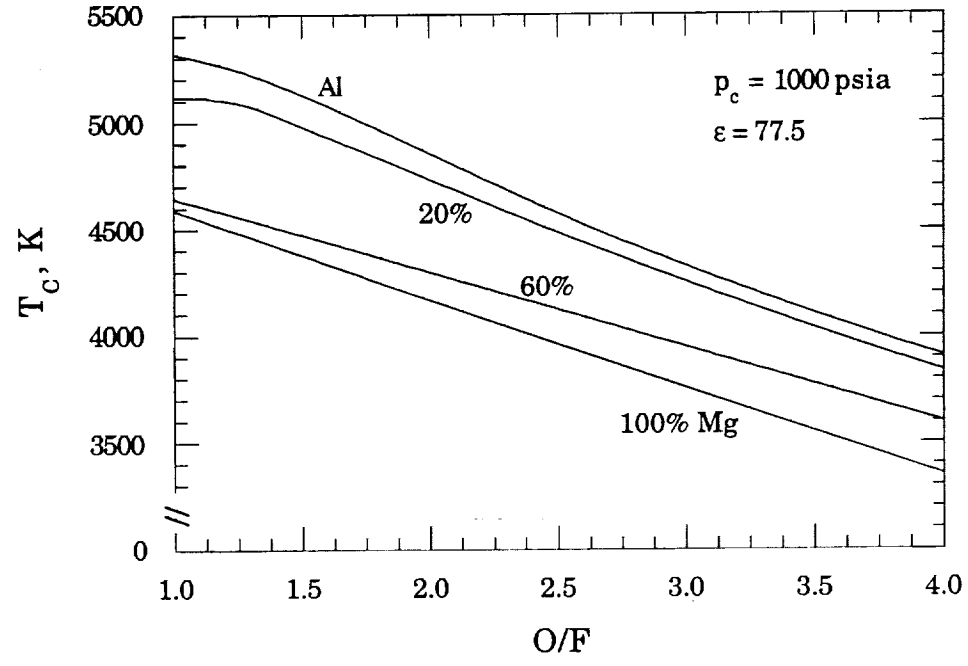

Fig. A.3: Calculated chamber temperature of an Al/Mg-LOX rocket engine as a function of O/F ratio and alloy composition.

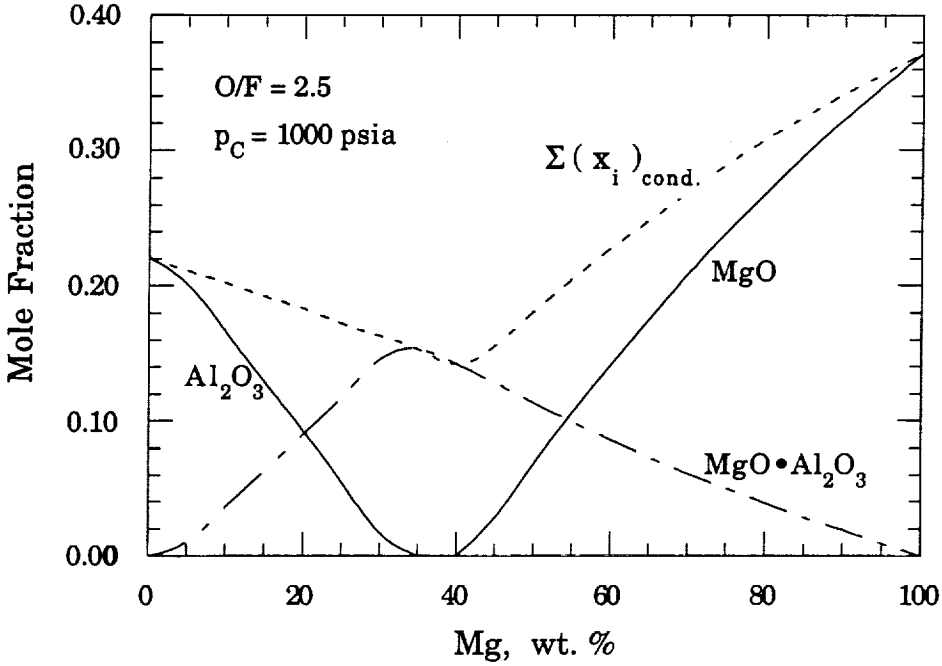

Fig. A.4: Calculated mole fractions of the condensed species produced by an Al/Mg-LOX rocket engine.

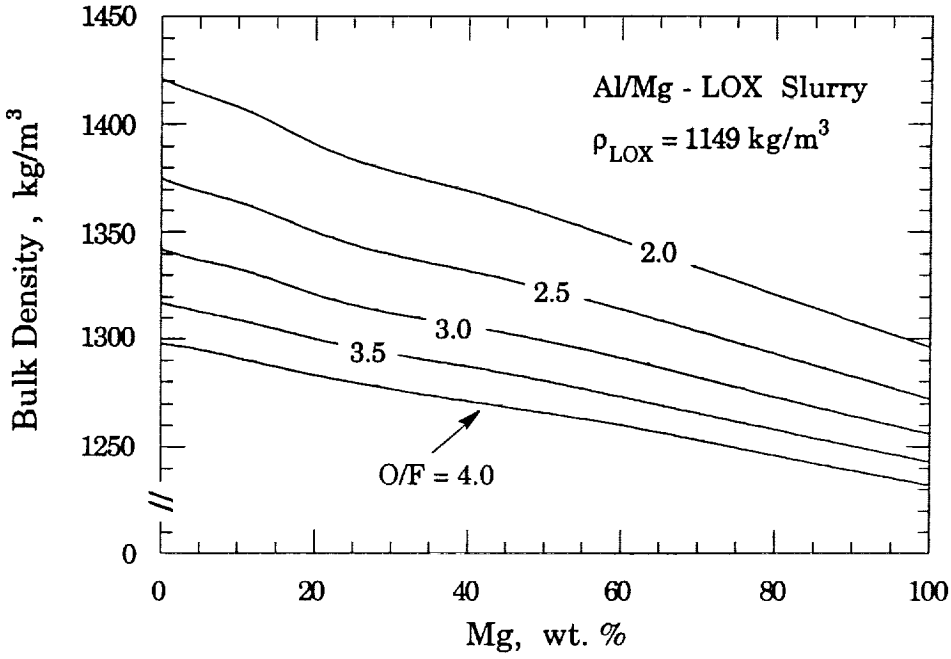

Fig. A.5: Calculated bulk density of an Al/Mg-LOX slurry propellant plotted as a function of alloy composition.

The results of the ideal vacuum specific impulse calculations show that the overall maximum specific impulse occurs for a pure Al-LOX rocket engine operating at an O/F ratio of approximately 2.4. As the Mg content of the alloy is increased to approximately 40%, the maximum $(I_{sp})_{vac}$ is lowered slightly and the optimum O/F ratio is lowered to approximately 1.4. As the Mg content of the alloy is increased further, the maximum $(I_{sp})_{vac}$ decreases further while the optimum O/F ratio is shifted to higher values. For pure Mg, the maximum vacuum specific impulse has dropped by approximately 12.5 seconds from that of pure Al and the optimum O/F ratio has increased to ~2.7.

Figure A.3 shows the calculated chamber temperature of the Al/Mg-LOX rocket engine plotted as a function of O/F ratio for several alloy compositions. The results indicate that the chamber temperature decreases in a nearly linear manner with increasing O/F ratio for each alloy composition. T_c is also found to decrease with increasing Mg content. The chamber temperature corresponding to the maximum ideal specific impulse for pure Al at O/F $\cong$ 2.4 is approximately 4650 K, which is quite high. This high chamber temperature can be significantly lowered by increasing the O/F ratio, with only a slight corresponding decrease in the vacuum specific impulse, as shown in Fig. 1.1.

Figure A.4 shows the mole fraction of the condensed oxide products (based on all species present in the chamber) as a function of alloy composition for an O/F ratio of 2.5. The mole fraction of Al_2O_3 decreases in a linear manner from ~0.22 for pure Al to zero for a Mg content of 35%. The double oxide, $MgO \bullet Al_2O_3$, reaches a peak of ~0.15 at a Mg content of ~35% and decreases to zero as the Mg content is decreased to 0% or increased to 100%. The mole fraction of MgO increases from zero at 40% Mg to the maximum condensed oxide mole fraction of ~0.37 for pure Mg.

The dashed curve in Fig. A.4 corresponds to the sum of all the condensed oxide mole fractions, $\sum (x_i)_{cond}$. The total mole fraction of the condensed oxide products is found to have a minimum at ~35% Mg, at which point the only oxide produced is $MgO \bullet Al_2O_3$. These trends may prove to be important when considering the two-phase flow losses that are associated with the agglomeration of the condensed oxide products. These losses are not considered in these calculations.

Another important characteristic of a rocket propellant is its density, since the size of the propellant tanks are a driving factor in the design of a rocket system. Figure A.5 shows the calculated bulk density of the Al/Mg-LOX slurry propellant plotted as a function of Mg content for several O/F ratios. The propellant bulk density is defined as [80]:

$$\rho_{bulk} = (1 + O/F) \left[\frac{1}{\rho_{alloy}} + \frac{O/F}{\rho_{LOX}} \right]^{-1} \qquad (A.8)$$

where $\rho_{LOX} = 1.149$ g/m^3 and the alloy density is obtained from Fig. 3.12. The bulk density is found to decrease linearly with increasing Mg content. At a given alloy composition, the bulk density decreases in a non-linear manner with increasing O/F ratio.

When considering the results presented above, it should be remembered that although real-gas effects are included, several important non-ideal losses, such as those due to two-phase flow, have not been considered.

APPENDIX B: IDEAL AND NON-IDEAL SHOCK TUBE THEORY

B.1 DESCRIPTION OF THE FLOWFIELD IN A SHOCK TUBE WITH A REDUCTION IN AREA AT THE DIAPHRAGM

This section is intended as a brief overview of the flowfield physics required to describe the complex flow phenomena existing in a shock tube that has a reduction in area at the diaphragm section. It is assumed that the reader is familiar with the ideal theory of simple constant-area shock tubes. Those who would like additional information on basic shock tube theory, are referred to several complete works on the subject by Glass et al. [92], Bradley [48], and Gaydon and Hurle [93].

The basic shock tube consists of a constant cross-sectional area tube that has a diaphragm separating high and low pressure sections of gas, referred to as the driver and driven sections, respectively. After the diaphragm is burst, either naturally or mechanically [48], the high pressure gas rapidly expands into the driven section producing a shock wave. It has been experimentally established that if all other initial conditions are equal, a shock tube that has a reduction in area, from the driver to driven section at the diaphragm, will produce a stronger shock wave than that of a tube with constant cross-sectional area [3,4]. This results from the fact that a steady expansion of the driver gas converts thermal energy to kinetic energy more efficiently than does an unsteady expansion [94].

Figure B.1 describes the unsteady flowfield of a shock tube that has a reduction in area at the diaphragm section. A t-x diagram of the unsteady wave system is shown in Fig. B.1a and the corresponding shock tube geometry is shown in Fig. B.1b. The driven section endwall is arbitrarily located at $x = x_{ew} = 0$, the diaphragm section at x_d, and the driver section head-end at x_{he},

as shown in Fig. B.1a. The horizontal dashed curves in the t-x diagram denote two finite time intervals, t_1 and t_2, after the time of diaphragm rupture (t = 0). Figures B.1c, B.1d, and B.1e show the velocity, pressure, and temperature variation inside the shock tube at times t = 0 (thick dashed curve), t_1 (thick solid curve), and t_2 (thin solid curve).

At time t=0, the shock tube flow velocity, u, is everywhere zero and the temperature is uniform and equal to that of the room (~300 K). Initially, the pressure in the shock tube rises discontinuously across the diaphragm from the low driven pressure in region 1 to the high driver pressure in region 4. Each region of the flowfield is denoted by a number in parentheses, ( ). After the diaphragm ruptures, the wave system shown in Fig. B.1a is established.

The flow in region 4 is accelerated to a subsonic velocity, u_{3a}, by a centered expansion wave that propagates toward the head-end of the shock tube. R_h and R_t in Fig. B.1a refer to the head and tail of the expansion wave, respectively. The flow temperature and pressure decrease through the expansion wave to values of T_{3a} and p_{3a}. When the gas in region 3a reaches the converging section of the shock tube, it is accelerated through a steady subsonic expansion until the flow Mach number reaches unity at the outlet of the convergent section, the location of which is denoted as 3b in Figs. B.1a and B.1b. Therefore, $M_{3b} = 1$ and $|u_{3b}| = a_{3b}$.

As the gas enters the driven section of the shock tube, it is accelerated further to a supersonic velocity, u_3, as it passes through another unsteady expansion wave that is propagating toward the head-end of the shock tube. The temperature and pressure of the driver gas have now dropped to T_3 and p_3, respectively. It is interesting to note that the head of this expansion wave is fixed at the outlet of the convergent section. This is due to the fact that the wave

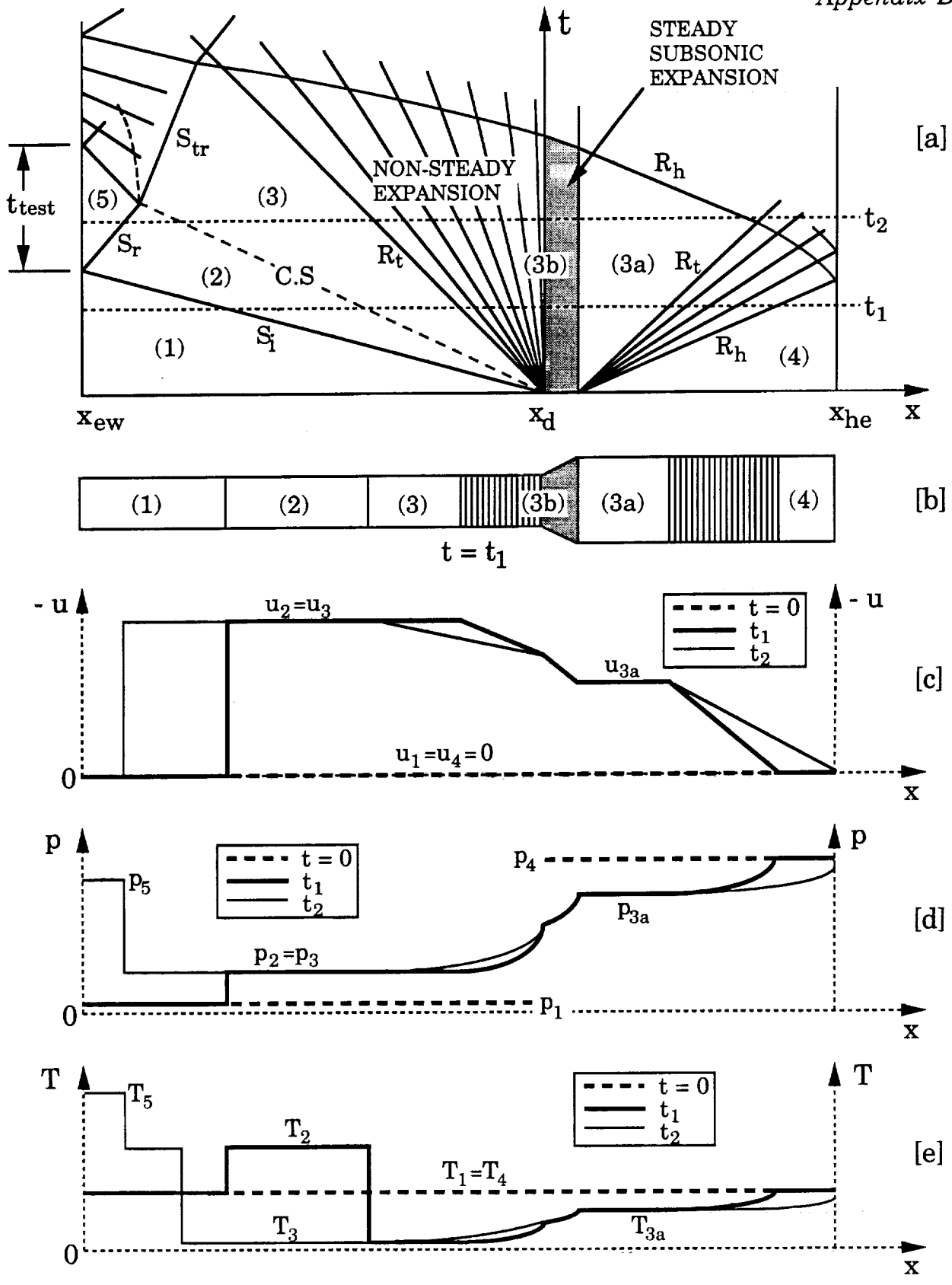

Fig. B.1: Description of the flowfield of a shock tube with a reduction in cross-sectional area at the diaphragm.

speed, u_w, at any point within an expansion wave is given by $u_w = a + u$ (for a rightward moving wave), where a and u are the local sound speed and velocity of the fluid, respectively [67]. Therefore, the head of the expansion fan is fixed at location 3b, since $-u_{3b} = a_{3b}$, yielding $u_{R_h} = 0$. Similarly, the tail of the expansion wave (denoted by R_t) moves toward the endwall of the driven section since $|u_3| > a_3$ (since $M_3 > 1$) and $u_{R_t} = a_3 + u_3 < 0$.

The supersonic flow in region 3 drives the low pressure gas in region 1 like a piston and produces an incident shock wave, S_i, which races toward the endwall of the shock tube. The incident shock wave compresses and heats the gas in region 1 to p_2 and T_2, respectively. The shock wave also accelerates the gas to a high velocity, u_2.

The interface between the flow through which the incident shock wave has passed (denoted as region 2) and the flow which has passed through both of the expansion waves and the convergent section (denoted as region 3) is called the contact surface (C.S.). The motion of the contact surface is shown as the large dashed curve in Figs. B.1a and B.1b. The contact surface marks the boundary between the fluids which were initially on either side of the diaphragm. Neglecting diffusion, the gas in regions 2 and 3 do not mix. The fluid velocities and pressures in regions 2 and 3 are necessarily equal, thus $u_2 = u_3$ and $p_2 = p_3$. The temperatures (see Fig. B.1e) and densities of the fluid in regions 2 and 3 are generally not equal.

When the incident shock wave reaches the endwall, it is reflected as another normal shock wave. The strength of the reflected shock wave, S_r, is just sufficient to bring the flow in region 2 to rest, as is required by the condition that the net flow at the endwall must be zero [93]. The reflected shock wave increases the temperature and pressure of the gas from T_2 to T_5 and from p_2 to p_5, respectively, and the flow velocity is reduced to zero, $u_5 = 0$.

The reflection of the incident shock wave from the endwall marks the beginning of the test conditions of interest here. The reflected shock continues to move toward the head-end of the shock tube until it meets the contact surface. The interaction of the reflected shock wave and the contact surface is an extremely complicated phenomena [48]. It may result in the production of two shock waves, a shock wave and an expansion wave, or two expansion waves. In each case, one wave is transmitted into region 3 and the other is "refracted" back toward the endwall. The reflected shock test conditions in region 5 end when this refracted wave arrives at the endwall, as shown in Fig. B.1a.

In a special case in which the gas properties in regions 2 and 3 are carefully adjusted, the reflected shock wave passes through the contact surface and reflects only a Mach wave, which does not effect the gas conditions at the endwall [48]. This "tailored" operation of the shock tube can increase the duration of the quasi-steady reflected shock conditions by as much as an order of magnitude, but the available range of the reflected gas conditions are severely limited unless a mixture of driver gases are employed (typically H_2 and He) or the driver gas is heated in some manner [96].

The shock tube flowfield discussed above corresponds to the specific case applicable to the experiment conditions employed in this research. Depending on the initial conditions of the gases in the driven and driver sections, the flowfield of the shock tube can differ significantly from that presented here. For example, it is possible that the flow velocity in region 3 may be subsonic, in which case the driven section expansion wave shown in Fig. B.1a would not be present [95]. For a complete discussion of the flowfields that are possible for a shock tube with a reduction in cross-sectional area at the diaphragm, the reader is referred to the article by Alpher and White [95].

C-4

B.2 SUMMARY OF FLUID DYNAMIC RELATIONS AND ITERATION METHOD USED TO PREDICT THE SHOCK TUBE PERFORMANCE

The following section will present the various fluid dynamic relations used to solve the complicated shock tube flowfield discussed in section B.1. The derivation of the various relations from the governing equations for non-steady, one-dimensional flows will be omitted here. The reader is referred to the report by Glass et al. [92] or the books by Bradley [48] and Gaydon and Hurle [93] if further information is required.

The variation of the gas conditions through the expansion (rarefaction) waves between regions 3 and 3b and 3a and 4 (see Fig. B.1a) is isentropic and is governed by the Riemann invariant [48]:

$$u - \frac{2a}{\gamma - 1} = \text{constant} \tag{B.1}$$

Noting that the velocity in region 4 is zero, $u_4 = 0$, the velocity and speed of sound in regions 3a and 4 are simply related by:

$$a_4 = a_{3a} - \frac{\gamma_4 - 1}{2} u_{3a} \tag{B.2}$$

Note that once the speed of sound in a given region has been determined, the temperature in that region can immediately be calculated from the ideal gas law using:

$$a = \sqrt{\gamma R T} \Rightarrow T = \frac{a^2}{R\,T} \tag{B.3}$$

Since the flow is isentropic, the pressure ratio across the expansion wave is related by:

$$\frac{p_4}{p_{3a}} = \left(\frac{a_4}{a_{3a}}\right)^{\frac{2\gamma_4}{\gamma_4 - 1}} \tag{B.4}$$

Using a similar analysis and noting that $u_{3b} = a_{3b}$, the conditions between regions 3 and 3b are related by:

$$a_{3b} = \frac{\gamma_4 - 1}{\gamma_4 - 3} u_3 + \frac{2}{\gamma_4 - 3} a_3 \tag{B.5}$$

$$\frac{p_{3b}}{p_3} = \left(\frac{a_{3b}}{a_3}\right)^{\frac{2\gamma_4}{\gamma_4 - 1}} \tag{B.6}$$

Regions 3a and 3b are related using the results of a quasi-one-dimensional analysis of the steady, isentropic flow in a duct with slowly varying cross-section [97]. Noting that $M_{3b} = 1$ and assuming the shock tube has a contraction ratio of A_4/A_1, the Mach number in region 3a can immediately be calculated from the following transcendental equation [97]:

$$\frac{1}{M_{3a}}\left[1 + \frac{(\gamma_4 - 1)}{2}(M_{3a})^2\right]^{\frac{\gamma_4 + 1}{2(\gamma_4 - 1)}} = \frac{A_4}{A_1}\left(\frac{(\gamma_4 + 1)}{2}\right)^{\frac{\gamma_4 + 1}{2(\gamma_4 - 1)}} \tag{B.7}$$

Using the isentropic flow relations, the pressures and sound speeds in regions 3a and 3b can immediately be related by calculating the ratio [97]:

$$\frac{p_{3a}}{p_{3b}} = \left(\frac{a_{3a}}{a_{3b}}\right)^{\frac{2\gamma_4}{(\gamma_4 - 1)}} = \left[\frac{2}{(\gamma_4 + 1)}\left(1 + \frac{(\gamma_4 - 1)}{2}(M_{3a})^2\right)\right]^{-\frac{\gamma_4}{(\gamma_4 - 1)}} \tag{B.8}$$

Equations (B.2) - (B.8) can be used to accurately describe the isentropic flow of the driver gas. The driver section flowfield is coupled to the driven section flowfield through the conditions that exist across the contact surface:

$$u_2 = u_3 \tag{B.9}$$

$$p_2 = p_3 \tag{B.10}$$

Treating the gas in regions 1 and 2 as ideal allows the flow velocity in region 2 to be expressed in terms of the incident shock Mach number, M_{s_i}, the constant ratio of specific heats, γ_1, and the incident shock pressure ratio, p_2/p_1, as follows [48]:

$$u_2 = u_3 = \frac{a_1}{\gamma_1}\left(\frac{p_2}{p_1} - 1\right)\left[\frac{\frac{2\gamma_1}{\gamma_1 + 1}}{\frac{p_2}{p_1} + \frac{\gamma_1 - 1}{\gamma_1 + 1}}\right]^{\frac{1}{2}} \tag{B.11}$$

where the incident shock pressure ratio is given by [93]:

$$\frac{p_2}{p_1} = \frac{2\gamma_1 (M_{s_i})^2 - (\gamma_1 - 1)}{(\gamma_1 + 1)} \tag{B.12}$$

The goal of this analysis is the development of a method that can be used to specify the driver to driven pressure ratio, p_4/p_1, required to produce a set of desired reflected shock conditions, T_5 and p_5. Since the solution will proceed from the known values of T_5 and p_5, it is convenient to express these variables in terms of M_{s_i}, T_1, and p_1. If the gas is once again assumed to be ideal, T_5 and p_5 can be expressed as follows [93]:

$$T_5 = T_1 \frac{\left[2(\gamma_1 - 1) M_{s_i}^2 + (3 - \gamma_1)\right]\left[(3\gamma_1 - 1) M_{s_i}^2 - 2(\gamma_1 - 1)\right]}{(\gamma_1 + 1)^2 M_{s_i}^2} \tag{B.13}$$

$$p_5 = p_1 \left[\frac{2\gamma_1 M_{s_i}^2 - (\gamma_1 - 1)}{(\gamma_1 + 1)}\right]\left[\frac{(3\gamma_1 - 1) M_{s_i}^2 - 2(\gamma_1 - 1)}{(\gamma_1 - 1) M_{s_i}^2 + 2}\right] \tag{B.14}$$

After choosing T_5, noting that T_1 is fixed at the temperature of the room, and determining g_1 for the gas of interest, Eq. (B.13) is a transcendental equation that can be solved iteratively for M_{s_i}. Once M_{s_i} has been calculated and p_5 has been chosen, the initial pressure of the driven gas, p_1, can be calculated explicitly from Eq. (B.14).

Real gas effects (i.e., dissociation of polyatomic gases, variable specific heats, etc.) are easily included in the analysis presented above. The monatomic helium driver gas employed in this research clearly expands isentropically, so the analysis described in Eqs. (B.2) - (B.8) is appropriate. However, due to the high gas temperatures produced by the incident and reflected shock waves, the oxygen driven gas needs to be treated in a non-ideal manner. The NASA Gordon-McBride program [9] is used to calculate the real gas conditions behind the incident and reflected shock waves. The required inputs for the Gordon-McBride program are the composition of the driven gas, M_{s_i}, T_1, and p_1. The program calculates all of the required shock parameters, such as u_2 and p_2, based on equilibrium or frozen gas compositions.

A computer program was developed that solves the coupled shock tube flowfield. The solution method employs an iterative technique that solves Eqs. (B.2) - (B.14), and runs the NASA Gordon-McBride program as a subroutine, to calculate the required initial driver and driven pressures, p_4 and p_1, given the desired reflected shock temperature and pressure, T_5 and p_5. The details of the iterative technique are as follows:

1) Choose T_5, p_5, and T_1 (typically, $T_1 = T_4 = 300$ K).

2) If the driven gas is treated as ideal, Eq. (B.13) is solved iteratively for M_{s_i}, which is then substituted into Eq. (B.14) to calculate p_1 explicitly.

   If the driven gas is treated as real, the NASA Gordon-McBride program is run in an iterative manner until the correct M_{s_i} and p_1 are determined. A double iteration is performed in which M_{s_i} and p_1 are varied until the calculated T_5 and p_5 are equal to the target values.

3) If the driven gas is treated as ideal, p_2 and u_2 are calculated using Eqs. (B.12) and (B.11), respectively.

If the driven gas is treated as real, p_2 and u_2 are obtained directly from the output of the NASA Gordon-McBride program.

4) A value for a_3 is assumed.

5) Noting that $u_3 = u_2$, Eq. (B.5) is used to calculate a_{3b}.

6) Using the known contraction ratio, A_4/A_1, Eq. (B.7) is solved iteratively for M_{3a}.

7) Equation (B.8) is solved explicitly for a_{3a}.

8) u_{3a} is calculated from $u_{3a} = a_{3a}M_{3a}$ and a_4 is calculated from Eq. (B.2).

9) T_4 is calculated from $T_4 = \dfrac{(a_4)^2}{\gamma_4 R_4}$.

10) If the T_4 calculated in step 9 does not equal the known value of $T_4 = T_1 = 300$ K, a new a_3 is assumed and the calculation procedure is continued by returning to step 4.

If the calculated T_4 is equal to $T_4 = T_1 = 300$ K, the required driver pressure is calculated by noting that $p_3 = p_2$ and:

$$p_4 = \frac{p_4}{p_{3a}} \frac{p_{3a}}{p_{3b}} \frac{p_{3b}}{p_3} p_3 \tag{B.15}$$

where the pressure ratios in Eq. (B.15) are calculated from Eqs. (B.4), (B.6), and (B.8).

The calculated shock tube parameters can now be used to estimate the reflected shock test time, t_{test}. A relation for t_{test} can be developed by examining the t-x diagram in Fig. B.1a. Assuming the shock tube flowfield develops instantaneously at the time of diaphragm rupture (t = 0) and a driven section tube length of l_1, the time at which the incident shock wave reflects from the endwall can be written as:

$$t_{s_i} = \frac{l_1}{v_{s_i}} = \frac{l_1}{a_1 M_{s_i}} \tag{B.16}$$

The position of the reflected shock wave for $t > t_{s_i}$ is given by:

$$x_{s_r} = v_{s_r}(t - t_{s_i}) \tag{B.17}$$

where the reflected shock velocity, v_{s_r}, is obtained from the real gas solution of the Gordon-McBride program or calculated explicitly assuming an ideal gas from [93]:

$$v_{s_r} = v_{s_i}\left(\frac{2 + \frac{2}{\gamma_1 - 1}\frac{p_1}{p_2}}{\frac{\gamma_1 + 1}{\gamma_1 - 1} - \frac{p_1}{p_2}}\right) \tag{B.18}$$

The position of the contact surface is given by:

$$x_{c.s.} = l_1 + u_2 t \tag{B.19}$$

The time at which the reflected shock wave and the contact surface collide, $t_{s\text{-}c}$, is found by equating Eqs. (B.17) and (B.19):

$$t_{s\text{-}c} = l_1\left[\frac{1}{v_{s_r}} + \frac{1}{v_{s_i}}\left(1 + \frac{u_2}{v_{s_i}}\right)\right] \tag{B.20}$$

The location of the contact surface at the time it collides with the reflected shock wave is simply determined by substituting Eq. (B.20) into Eq. (B.19):

$$x_{s\text{-}c} = l_1\left\{1 + u_2\left[\frac{1}{v_{s_r}} + \frac{1}{v_{s_i}}\left(1 + \frac{u_2}{v_{s_i}}\right)\right]\right\} \tag{B.21}$$

If $\gamma_1\rho_1 < \gamma_3\rho_3$ and $(\gamma_1+1)\rho_1 < (\gamma_3+1)\rho_3$, the wave reflected from the interaction of the shock wave and the contact surface will always be a shock wave [48]. This condition is satisfied for all of the reflected shock conditions investigated here. The strength of the shock wave reflected from the contact surface is not easily determined. Therefore, it will be assumed that the shock created by the interaction of the reflected shock and the contact surface travels at

the speed of sound in region 5. The maximum reflected test time is then simply expressed as:

$$(t_{test})_{max} = \frac{x_{s-c}}{a_5} + \frac{x_{s-c}}{a_5} = l_1\left(\frac{1}{v_{s_r}} + \frac{1}{a_5}\right)\left\{1 + u_2\left[\frac{1}{v_{s_r}} + \frac{1}{v_{s_i}}\left(1 + \frac{u_2}{v_{s_i}}\right)\right]\right\} \qquad (B.22)$$

Equation (B.22) indicates that the length of the test time available in the reflected shock region is directly proportional to the length of the driven section, l_1. This will only hold if the driver section is of sufficient length to insure that the head of the expansion wave, after reflecting from the head-end of the driver section, does not reach the contact surface before the reflected shock wave does. If the driver section is too short, the reflected expansion wave will adversely effect the reflected shock conditions, and may even overtake the incident shock wave before it reaches the shock tube endwall.

B.3 COMPARISON OF PREDICTED AND MEASURED SHOCK TUBE PERFORMANCE

Figure B.2 compares the predicted and experimentally measured shock tube performance. The shock tube dimensions were presented in Fig. 2.19. The driver gas is He and the driven gas is a mixture of 98.6% O_2 / 1.4% N_2. The shock tube has a driver diameter of 6.377" and a driven diameter of 3.500", yielding a contraction ratio of $A_4/A_1 = 3.32$. The initial temperature of the driven and driver gases are $T_1 = T_4 \cong 300$ K for all measurements. The calculations assume the driven gas is O_2 and the initial temperatures are $T_1 = T_4 = 300$ K. The incident and reflected shock parameters are calculated for a real gas using the NASA Gordon-McBride program [9].

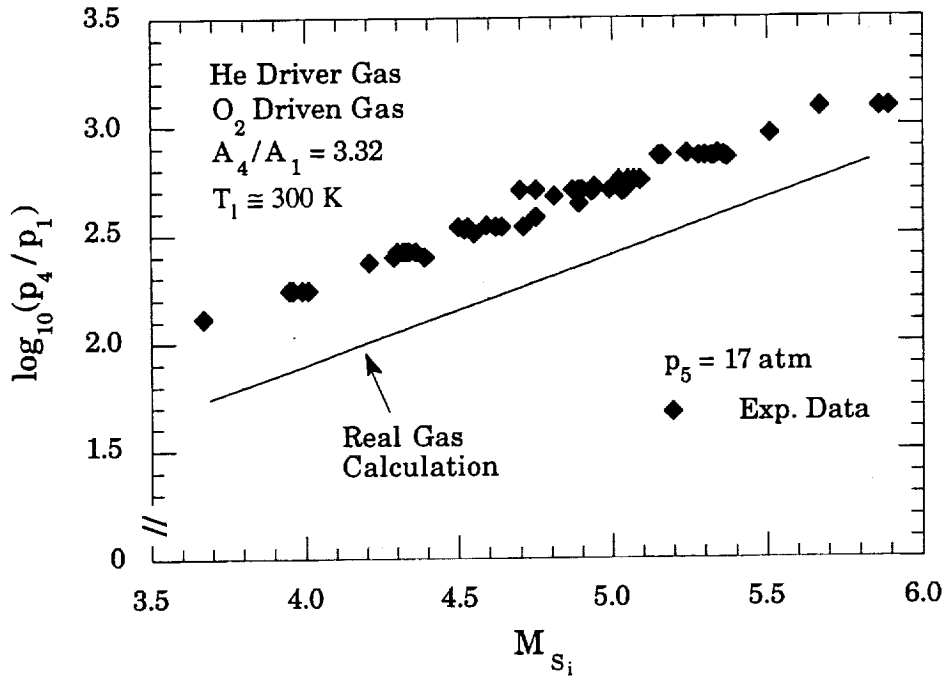

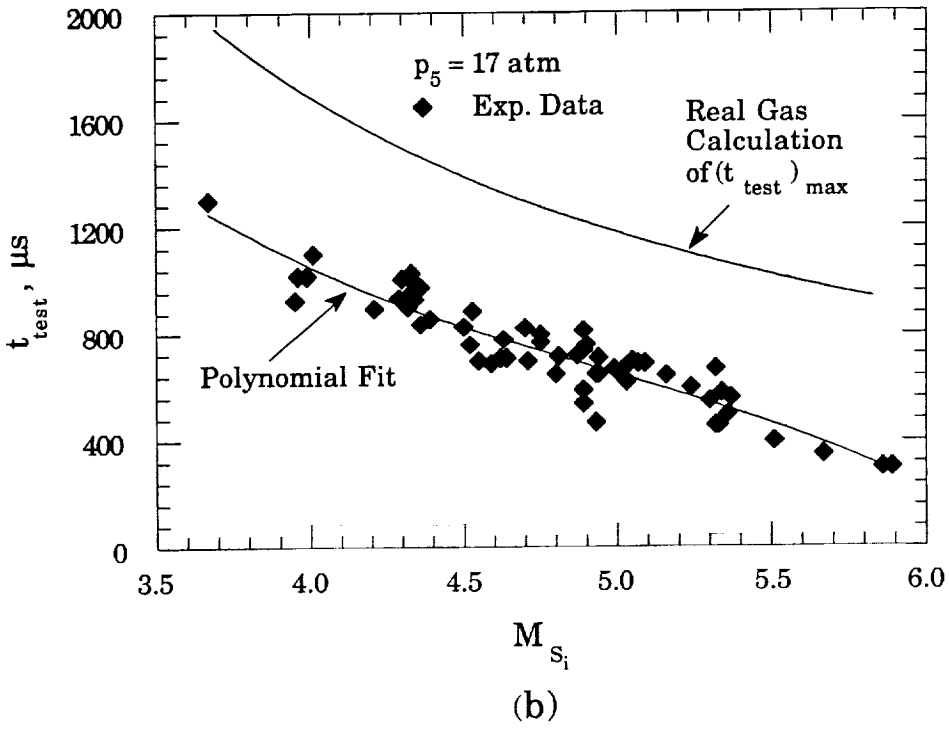

Fig. B.2: Comparison of measured and calculated shock tube performance. a) Shock tube pressure ratio versus incident shock Mach number at p_5 = 17 atm. b) Experimental test time versus incident shock Mach number at p_5 = 17 atm.

Figure B.2a compares the predicted and measured driver to driven pressure ratio, p_4/p_1, as a function of incident shock Mach number, M_{s_i}. The calculations and measurements correspond to a reflected shock pressure of $p_5 = 17$ atm. The trend in the calculated and measured results are in excellent agreement. The measurements lie above the predictions, as is typical for most shock tubes [98]. The fact that the slope of the predicted and measured performance curves are in excellent agreement allows the actual shock tube performance to be estimated precisely after a single shock tube firing. This is done by plotting the single measured data point and drawing a line through it that is parallel to the predicted curve, thus allowing the correct pressure ratio to be estimated [98]. This technique was found to work extremely well as part of this investigation.

The measured reflected shock test time is compared with the predicted maximum test time, $(t_{test})_{max}$, in Fig. B.2b. The results are plotted as a function of M_{s_i} for a reflected shock pressure of $p_5 = 17$ atm. The overall trend of the calculated and measured test times are in good agreement. The measured test times are less than the predicted $(t_{test})_{max}$, which is expected.

The discrepancies between the measured and calculated results shown in Fig. B.2 are undoubtedly related to non-ideal behavior of a real shock tube that is not included in the analysis presented in section B.2. For instance, non-ideal diaphragm rupturing will result in mixing at the contact surface and delay the formation of the incident shock wave. The analysis assumes instantaneous shock formation and neglects the shock attenuation that results from the boundary-layer that is formed on the shock tube wall in the high-speed region of flow induced by the incident shock wave.

APPENDIX C: NUMERICAL SOLUTION OF THE IGNITION MODEL

C.1 FINITE DIFFERENCE FORMS OF THE PARTICLE EQUATIONS OF MOTION AND THE PARTICLE ENERGY EQUATION

The one-dimensional particle equations of motion, Eqs. (3.15) and (3.20), and the particle energy equation, Eq. (3.7), are written in their differenced forms using a simple forward difference [99] as follows:

$$v_p^{n+1} = v_p^n - \frac{3}{8}\frac{\rho_g^n}{r_p\,\rho_p} C_W^n C_D^n \left|v_g^n - v_p^n\right| (v_g^n - v_p^n)\Delta t \tag{C.1}$$

$$x_p^{n+1} = x_p^n + v_p^n\,\Delta t \tag{C.2}$$

$$T_p^{n+1} = T_p^n + \left\{ -\frac{3}{2}\frac{k_g^n}{\rho_p\, c^n\, r_p^2}(Nu_p^n)(T_p^n - T_g) + \frac{3}{\rho_p\, c^n\, r_p}\left[q_r^n k_s^n - \varepsilon_p \sigma\left((T_p^n)^4 - T_b^4\right)\right]\right\}\Delta t \tag{C.3}$$

where the superscript "n+1" refers to the new time level, the superscript "n" refers to the previous time level, and Δt is the constant time step at which the integration proceeds. Equations (3.7), (3.15), and (3.20) are nonlinear first order differential equations. Their respective finite difference forms have been linearized by simply lagging the nonlinear terms on the RHS of the equations by one time step, i.e., the value of v_p, x_p, and T_p at the new time level, n+1, are calculated using parameters taken from the previous time level, n.

The particle location, velocity, and temperature are calculated by stepping the solution of Eqs. (B.1) - (B.3) forward in time, at finite time intervals of length Δt. By definition, $t^{n+1} = t^n + \Delta t$. The temperature dependent particle specific heat, the real gas properties in regions 2 and 5 of the shock tube, and the tabulated constants used to calculated the particle drag coefficient (see Eq. 3.16)) are numerically interpolated from data tables that are accessed by the developed

computer program. The numerical integration of Eqs. (B.1) - (B.3) proceed until the specified particle ignition temperature is reached.

C.2 ACCURACY OF THE NUMERICAL SOLUTION

The accuracy of the numerical method used to solve the governing equations of the kinematic particle ignition model is examined. The numerically calculated particle ignition delay time will first be compared with the exact solution given in Eq. (3.11). In order to make a direct comparison, the same assumptions that were made in the derivation of Eq. (3.11) must be applied to the numerical calculation. Therefore, it is assumed that the particle has a constant specific heat and is at rest in a hot, quiescent gas. In addition, both radiative losses and the contribution of heterogeneous reaction to the particle self-heating are neglected. These assumptions are easily satisfied numerically by setting:

$$Nu_p^{n+1} = Nu_p^n = \text{constant} = 2$$

$$\varepsilon_p = 0$$

$$A_1 = 0$$

Since the heat transfer is assumed constant, this calculation will uncouple the particle energy and kinematic equations, allowing the accuracy of the numerical solution of the energy equation to be assessed independently.

The analytical and numerical calculations of the ignition delay time will be performed for a 20 μm diameter Al particle in oxygen at 2750 K and 17 atm. The following thermophysical constants are used in the calculation:

$$d_p = 20\ \mu m$$

$$\rho_{Al} = 2.700\ g/cm^3$$

c_{Al} = 1.177 kJ/kg-K
$(L_f)_{Al}$ = 397 kJ/kg
$(T_m)_{Al}$ = 933 K
$(T_{ign})_{Al}$ = 2300 K
T_o = 300 K
T_{O_2} = 2750 K
k_{O_2} = 0.22 W/m-K

The exact solution yields an ignition delay time of:

$$t_{ign}^{exact} = 880.9\ \mu s$$

The numerically calculated ignition delay time is shown in Fig. C.1 plotted as a function of the numerical time step size, Δt. The exact solution is also plotted as the horizontal dashed line for reference. The symbols in Fig. C.1 indicate the discrete time step sizes at which t_{ign} is calculated. As Δt is decreased from 1 μs to 0.1 μs, the calculated t_{ign} drops to a value of approximately 881.2 μs, which is in excellent agreement with the analytical value of 880.9 μs. As Δt is decreased further, the calculated t_{ign} remains nearly constant until Δt is reduced to below 0.005 μs, at which point the numerically calculated t_{ign} begins to increase rapidly. Based on this calculation, the nominal time step size is chosen to be Δt_o = 0.01 μs, and is indicated by the vertical line in Fig. C.1.

An identical set of numerical calculations are now performed with the addition of a variable, temperature-dependent, particle specific heat. The temperature dependent Al specific heat is incorporated into the numerical solution by interpolating the tabulated values corresponding to the curve of c_{Al} plotted in Fig. 3.13a. The result of these calculations are plotted in Fig. C.2 as a function of Δt. A corresponding analytical solution is not performed due to the

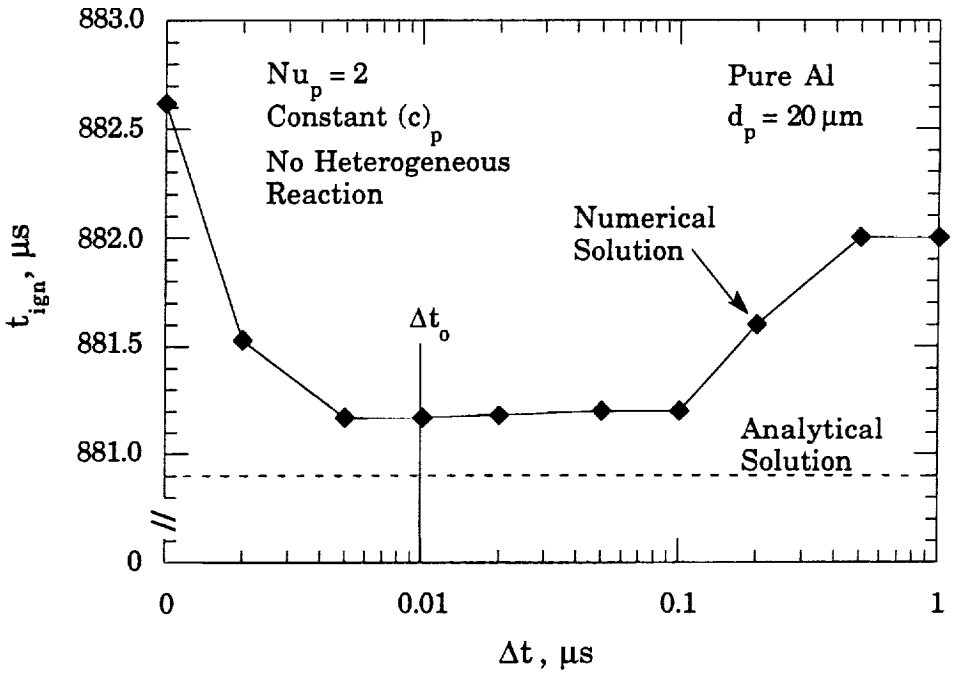

Fig. C.1: Comparison of the numerically calculated particle ignition delay time with an analytical solution.

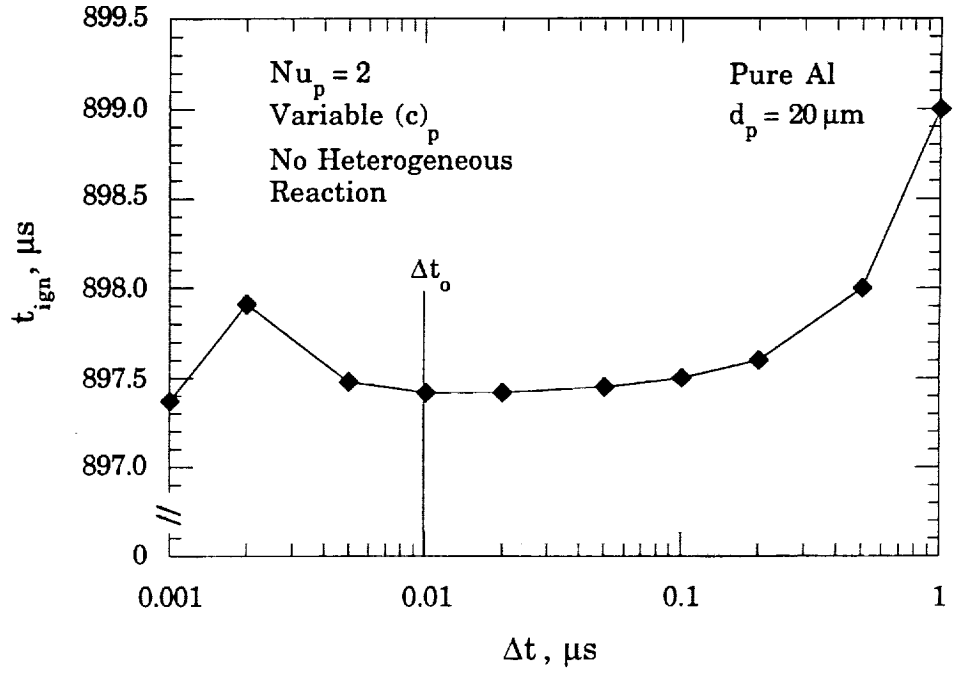

Fig. C.2: Numerically calculated ignition delay time of an Al particle, with a temperature-dependent specific heat, plotted as a function of the time step size Δt.

inclusion of the time-dependent specific heat. As the time step is reduced, t_{ign} again decreases until a stable solution is obtained for time step sizes ranging from approximately 0.05 μs to 0.005 μs, yielding $t_{ign} \cong 897.4$ μs. If the time step size is decreased further, the solution becomes unstable and yields erroneous ignition delay times. The nominal time step size, $\Delta t_o = 0.01$ μs, is indicated by the vertical line in Fig. C.2.

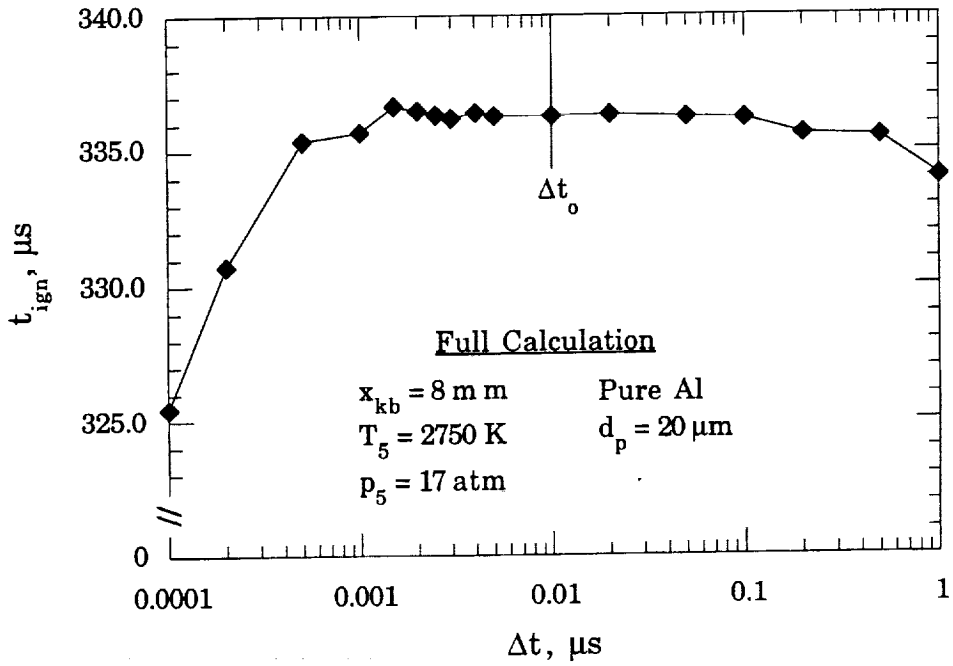

Fig. C.3: Effect of time step size on the full numerical calculation of the particle ignition delay time. The nominal step size used in the model calculations is denoted by Δt_o.

The effect of the time step size on the accuracy of the full numerical solution is assessed by calculating the ignition delay time of an Al particle initially mounted 8 mm from the endwall. The particle and gas properties are those listed above, with the additional assumption of variable Al specific heat, $\varepsilon_p = 0.9$, and $A_1 = 200$ kg/m^2-s. Fig. C.3 shows the results of these calculations plotted as a function of Δt. A stable solution of $t_{ign} \cong 336$ μs is obtained for time

step sizes ranging from 0.1 μs to 0.005 μs. As Δt is decreased further, the solution again becomes unstable, and the calculated t_{ign} plummets to 325 μs at Δt = 0.0001 μs.

C.3 CALCULATION OF THE ENDWALL THERMAL LAYER AND THE SURFACE TEMPERATURE OF THE OBSERVATION WINDOW

Figure C.4a shows the temperature field that will exist in the region of the endwall observation window just prior to the reflection of the incident shock wave ($t = 0^-$). The surface of the endwall window is located at x = 0. The oxygen is assumed to fill the region of space defined by $0^+ \leq x_{O_2} \leq \infty$. The quartz observation window is assumed to fill the region of space defined by $\infty \leq x_w \leq 0^-$. Both the window and the oxygen are initially at room temperature (~300 K).

Figure C.4b shows the temperature field that will exist immediately after the shock wave has reflected off the endwall ($t = 0^+$). The temperature of the quartz window remains at 300 K while the temperature of the oxygen has been suddenly increased to the reflected shock temperature, T_5, which is generally in excess of 1700 K for the conditions of this experiment. The temperature field in the oxygen and window at any later time will be determined by the transient conduction of heat from the hot gas to the cool window.

Due to the relatively short test times (~ 1 ms) characteristic of the reflected shock technique, the oxygen and window material can be treated as if they are infinitely thick. Therefore, the problem reduces to that of two semi-infinite rods with different initial temperatures and thermal conductivities, the ends of which are brought into contact at time t = 0. The analytical solution to this problem has been obtained by Luikov [84].

The transient heat conduction problem can now be specified mathematically. The heat equation in each region is simply:

$$\frac{\partial}{\partial t} T_{O_2}(x\,,\,t) = \alpha_{O_2} \frac{\partial^2}{\partial x^2} T_{O_2}(x\,,\,t) \qquad (t > 0\,;\, x > 0) \tag{C.4}$$

$$\frac{\partial}{\partial t} T_w(x\,,\,t) = \alpha_w \frac{\partial^2}{\partial x^2} T_w(x\,,\,t) \qquad (t > 0\,;\, x < 0) \tag{C.5}$$

where the thermal diffusivity is defined as $\alpha_i = k_i / (\rho_i\, c_i)$. The appropriate boundary conditions are given by:

$$T_{O_2}(0^+ \le x \le \infty\,,\,0) = T_5 \tag{C.6}$$

$$T_w(-\infty \le x \le 0^-\,,\,0) = T_1 = 300\ \text{K} \tag{C.7}$$

$$\frac{\partial}{\partial t} T_{O_2}(+\infty\,,\,t) = \frac{\partial}{\partial t} T_w(-\infty\,,\,t) = 0 \tag{C.8}$$

$$T_{O_2}(0^+\,,\,t) = T_w(0^-\,,\,t) \tag{C.9}$$

$$\frac{\partial}{\partial t} T_{O_2}(0\,,\,t) = -\left(\frac{k_w}{k_{O_2}}\right) \frac{\partial}{\partial t} T_w(0\,,\,t) \tag{C.10}$$

Luikov obtained the following solution to the mathematical problem specified by Eqs. (C.4) - (C.10) [84]:

$$T_{O_2}(x\,,\,t) = T_1 + \frac{K_\epsilon}{1 + K_\epsilon}\left[1 + \frac{1}{K_\epsilon}\,\text{erf}\left(\frac{x}{2\sqrt{\alpha_{O_2} t}}\right)\right](T_5 - T_1) \tag{C.11}$$

and

$$T_w(x\,,\,t) = T_1 + \frac{K_\epsilon}{1 + K_\epsilon}\,\text{erf}\left(\frac{|x|}{2\sqrt{\alpha_w t}}\right)(T_5 - T_1) \tag{C.12}$$

where the constant K_ϵ is defined as:

$$K_\epsilon = \left[\frac{k_{O_2}\, \rho_{O_2}\, (c_p)_{O_2}}{k_w\, \rho_w\, c_w}\right]^{\frac{1}{2}} \tag{C.13}$$

The transient temperature distributions defined by Eqs. (C.11) and (C.12) are shown schematically in Fig. C.4c. At time t = 0, the temperature of the oxygen and window are T_5 and T_1, respectively. An important result is the fact that the temperature at x = 0 (the surface of the window) instantaneously adjusts to a temperature, T_s, which remains constant for all time t as the temperature distributions in the gas and solid vary about x = 0. Setting x = 0 in Eqs. (C.11) or (C.12) yields the following expression for the constant surface temperature of the window:

$$T_s = T_1 + \frac{K_\varepsilon}{1 + K_\varepsilon}(T_5 - T_1) \tag{C.14}$$

Equation (C.14) shows that for $K_\varepsilon << 1$, the temperature of the window surface approaches T_1. For $K_\varepsilon >> 1$, the window surface temperature approaches T_5. For the typical conditions of interest here (hot oxygen and a quartz window), $K_\varepsilon << 1$ and $T_s \cong T_1$ (see Fig. 4.4).

Figure C.4c shows the temperature distribution corresponding to several finite times labeled as t_1, t_2, t_3, and t_4. After an infinite time, the temperature everywhere will equal T_s, as shown by the dashed line. The height of the endwall thermal layer δ_t (see Fig. 3.18), defined as the distance from the endwall at which the oxygen temperature reaches $0.99T_5$, can be determined by setting $x = \delta_t$ and $T_{O_2}(x, t) = T_{O_2}(\delta_t, t) = 0.99\ T_5$ in Eq. (C.11). The thermal layer height is then given by:

$$\delta_t = 2\,\eta\sqrt{\alpha_{O_2}\,t} \tag{C.15}$$

where the constant η is determined from the following transcendental equation:

$$\mathrm{erf}[\eta] = \left[\frac{0.99T_5 - T_1}{T_5 - T_1}\right](1 + K_\varepsilon) - K_\varepsilon \tag{C.16}$$

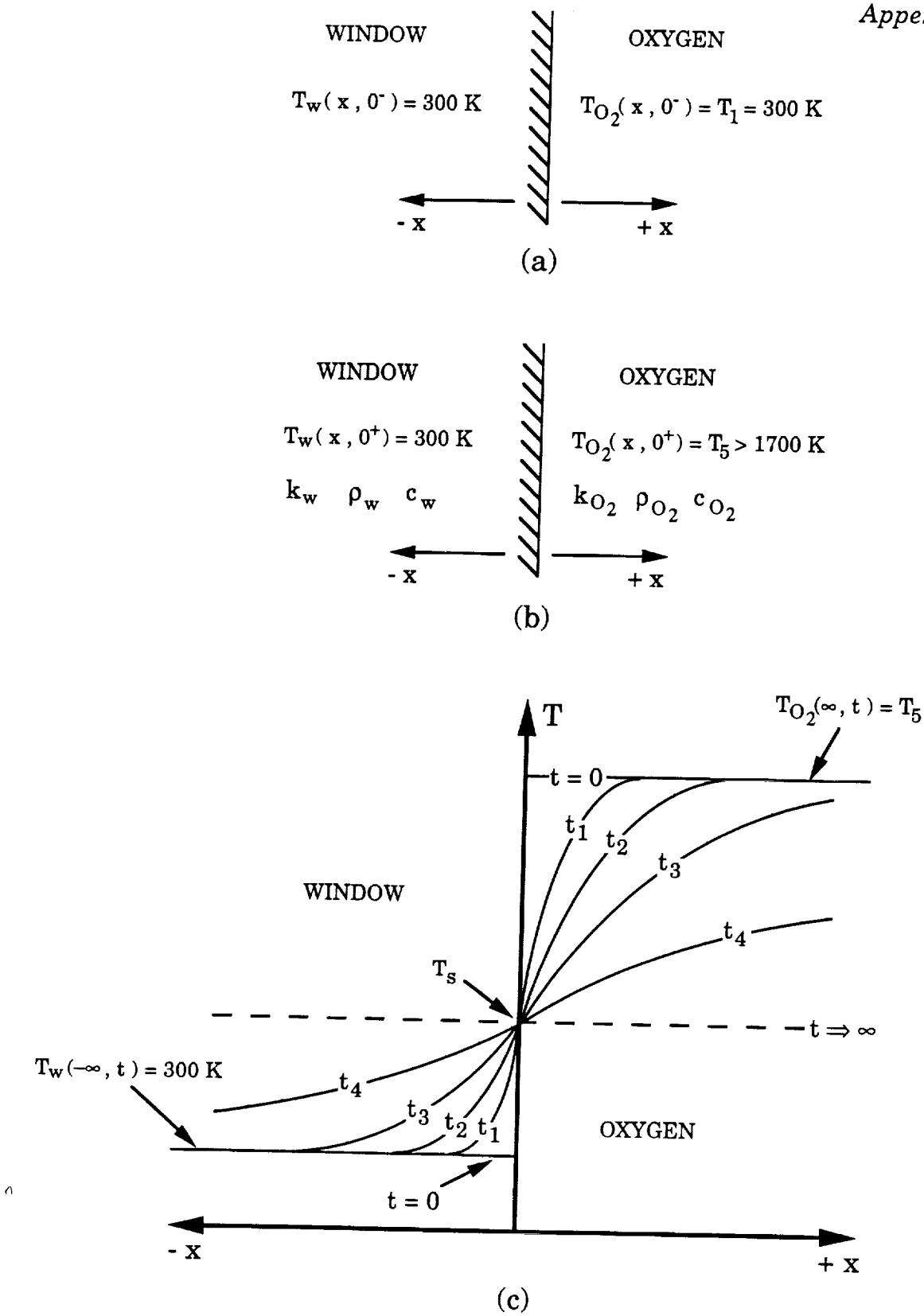

Fig. C.4: Description of observation window heat transfer. a) Temperature prior to shock reflection. b) Temperature immediately following shock reflection. c) Transient temperature field.

LIST OF REFERENCES

1. Price, E. W., "Combustion of Metallized Propellants," In *Fundamentals of Solid Propellant Combustion*, Progress in Astronautics and Aeronautics Series (K. K. Kuo and M. Summerfield, Eds.), AIAA, New York, Vol. 90, pp. 479-514, 1984.

2. Doll, D. W. and Lund, G. K., "Magnesium-Neutralized Propellant," *Journal of Propulsion and Power*, Vol. 8, No. 6, pp. 1185-1191, 1992.

3. Pinns, M. L., Olson, W. T., Barnett, H. C., and Breitwieser, R., "NACA Research on Slurry Fuels," NACA TR-1388, August 15, 1958.

4. Rapp, D. C. and Zurawski, R. L., "Characterization of Aluminum/RP-1 Gel Propellant Properties," NASA TM 100951, July, 1988.

5. Linne, D. L. and Meyer, M. L., "Technical Prospects for Utilizing Extraterrestrial Propellants for Space Exploration," NASA TM 105263, October, 1991.

6. Meyer, M. L., "Design Issues for Lunar In Situ Aluminum/Oxygen Propellant Rocket Engines," NASA TM 105433, February, 1992.

7. Sutton, G. P., *Rocket Propulsion Elements: An Introduction to the Engineering of Rockets*, Sixth ed., John Wiley & Sons, Inc., New York, 1992.

8. Hill, P. G. and Peterson, C. R., *Mechanics and Thermodynamics of Propulsion*, Addison-Wesley Publishing Co., Menlo Park, 1965.

9. Gordon, S. and McBride, B. J., "Computer Program for Calculation of Complex Chemical Equilibrium Compositions, Rocket Performance, Incident and Reflected Shocks, and Chapman-Jouguet Detonations," NASA SP-273, March, 1976.

10. Wickman, J. H., Oberth, A. E., and Mockenhaupt, J. D., "Lunar Base Spacecraft Propulsion With Lunar Propellants," AIAA Paper 86-1763, AIAA 22nd Joint Propulsion Conference, Huntsville, 1986.

11. Frolov, Y. V., Pokhil, P. F., and Logachev, V. S., "Ignition and Combustion of Powdered Aluminum in High-Temperature Gaseous Media and in a Composition of Heterogeneous Condensed Systems," *Combustion, Explosion, and Shock Waves*; Vol. 8, No. 2, pp. 168-187, 1972.

12. Merzhanov, A. G., "Thermal Theory of Metal Particle Ignition," *AIAA Journal*, Vol. 13, No. 2, pp. 209-215, 1975.

13. Fox, T. W., TeVelde, J. A., and Nicholls, J. A., "Shock Wave Ignition of Metal Powders," *Proceedings of the 1976 Heat Transfer and Fluid Mechanics Institute*, Heat Transfer and Fluid Mechanics Institute, Univ. of California, Davis, pp. 241-256, 1976.

14. Kubaschewski, O. and Hopkins, B. E., *Oxidation of Metals and Alloys*, Second ed., Butterworths, London, 1967.

15. Drew, C. M., Gordon, A. S., and Knipe, R. H., "Study of Quenched Aluminum Particle Combustion," In *Heterogeneous Combustion*, Progress in Astronautics and Aeronautics Series (H. G. Wolfhard, I. Glassman, and L. Green Jr., Eds.), AIAA, New York, Vol. 15, pp. 16-39, 1964.

16. Friedman, R. and Macek, A., "Ignition and Combustion of Aluminum Particles in Hot Ambient Gases," *Combustion and Flame*; Vol. 6, pp. 9-19, 1962.

17. Prentice, J. L., "Combustion of Pulse-Heated Single Particles of Aluminum and Beryllium," *Combustion Science and Technology*; Vol. 1, No. pp. 385-398, 1970.

18. Wilson, R. P. and Williams, F. A., "Experimental Study of the Combustion of Single Aluminum Particles in O_2/Ar," *Thirteenth Symposium (International) on Combustion*, Vol. 13, The Combustion Institute, pp. 833-845, 1971.

19. Markstein, G. H., "Analysis of a Dilute Diffusion Flame Maintained by Heterogeneous Reaction," In *Heterogeneous Combustion*, Progress in Astronautics and Aeronautics Series (H. G. Wolfhard, I. Glassman, and L. Green Jr., Eds.), AIAA, New York, Vol. 15, pp. 177-202, 1964.

20. Markstein, G. H., "Combustion of Metals," *AIAA Journal*, Vol. 1, No. 3, pp. 550-562, 1963.

21. Pokhil, P. F., Belyayev, A. F., Frolov, Yu. V., Logachev, V. S., and Korotkov, A. I., *Combustion of Powdered Metals in Active Media*, U.S. Air Force Translation, FTD-MT-24-551-73, 1972.

22. Breiter, A. L., Mal'tsev, V. M., and Popov, E. I., "Models of Metal Ignition," *Combustion, Explosion, and Shock Waves*; Vol. 13, No. 4, pp. 475-485, 1977.

23. Brzustowski, T. A. and Glassman, I., "Vapor-Phase Diffusion Flames in the Combustion of Magnesium and Aluminum: I. Analytical Developments," In *Heterogeneous Combustion*, Progress in Astronautics and Aeronautics Series (H. G. Wolfhard, I. Glassman, and L. Green Jr., Eds.), AIAA, New York, Vol. 15, pp. 75-116, 1964.

24. Brzustowski, T. A. and Glassman, I., "Vapor-Phase Diffusion Flames in the Combustion of Magnesium and Aluminum: II. Experimental Observations in Oxygen Atmospheres," In *Heterogeneous Combustion*, Progress in Astronautics and Aeronautics Series (H. G. Wolfhard, I. Glassman, and L. Green Jr., Eds.), AIAA, New York, Vol. 15, pp. 117-158, 1964.

25. Kuo, K. K., *Principles of Combustion*, John Wiley & Sons, New York, 1986.

26. Kuehl, D. K., "Ignition and Combustion of Aluminum and Beryllium," *AIAA Journal*, Vol. 3, No. 12, pp. 2239-2247, 1965.

27. Prentice, J. L., "On the Combustion of Single Aluminum Particles," *Combustion and Flame*; Vol. 9, No. 2, pp. 208-210, 1965.

28. Macek, A., "Fundamentals of Combustion of Single Aluminum and Beryllium Particles," *Eleventh Symposium (International) on Combustion*, The Combustion Institute, Berkeley, California, pp. 203-217, 1967.

29. Belyaev, A. F., Frolov, Yu. V. and Korotkov, A. I., "Combustion and Ignition of Finely Dispersed Aluminum," *Combustion, Explosions, and Shock Waves*; Vol. 4, No. 3, pp. 182-185, 1968.

30. Gurevich, M. A., Lapkina, K. I., and Ozerov, E. S., "Ignition Limits of Aluminum Particles," *Combustion, Explosions, and Shock Waves*; Vol. 6, No. 2, pp. 154-157, 1970.

31. Glassman, I., "Combustion of Metals: Physical Considerations," In *Solid Propellant Rocket Research*, Progress in Astronautics and Aeronautics Series (M. Summerfield, Ed.), AIAA, New York, Vol. 1, pp. 253-258, 1960.

32. Keshavan, R. and Brzustowski, T. A., "Ignition of Aluminum Particle Streams," *Combustion Science and Technology*; Vol. 6, No. 4, pp. 203-209, 1972.

33. Law, C. K. and Williams, F. A., "Combustion of Magnesium Particles in Oxygen-Inert Atmospheres," *Combustion and Flame*; Vol. 22, No.3, pp. 383-405, 1974.

34. Fox, T. W., Rackett, C. W., and Nicholls, J. A., "Shock Wave Ignition of Magnesium Powders," *Shock Tube and Shock Wave Research*, Vol. 11, University of Washington Press, Seattle, pp. 262-268, 1977.

35. Driscoll, J. F., Nicholls, J. A., Patel, V., Shahidi, B. K., and Liu, T. C., "Aluminum Combustion at 40 Atmospheres Using a Reflected Shock Wave," *AIAA Journal*, Vol. 24, No. 5, pp. 856-858, 1984.

36. Driscoll, J. F., Nicholls, J. A., Patel, V., Shahidi, B. K., and Liu, T. C., "Shock Tube Study of the Ignition and Combustion of Aluminum," AIAA Paper 84-1201, AIAA 20th Joint Propulsion Conference, Cincinnati, 1984.

37. Brewster, M. Q. and Taylor, D. M., "Radiative Properties of Burning Aluminum Droplets," *Combustion and Flame*; Vol. 72, pp. 287-299, 1988.

38. Boiko, V. M., Lotov, V. V., and Papyrin, A. N., "Ignition of Gas Suspensions of Metallic Powders in Reflected Shock Waves," *Combustion, Explosion, and Shock Waves*; Vol. 25, No. 2, pp. 193-199, 1989.

39. Steinberg, T. A. and Wilson, D. B., "The Combustion Phase of Burning Metals," *Combustion and Flame*; Vol. 91, pp. 200-208, 1992.

40. Fassell, W. M., Papp, C. A., Hildenbrand, D. L., and Sernka, R. P., "The Experimental Nature of the Combustion of Metallic Powders," In *Solid Propellant Rocket Research*, Progress in Astronautics and Aeronautics Series (M. Summerfield, Ed.), AIAA, New York, Vol. 1,pp. 259-270, 1960.

41. Murray, J. L., "Al-Mg (Aluminum-Magnesium)," In *Phase Diagrams of Binary Magnesium Alloys* (A. A. Nayeb-Hashemi, and J. B. Clark, Eds.), ASM International, Metals Park, Vol. 17-34, 1988.

42. Breiter, A. L., Kashporov, L. Ya., Mal'tsev, V. M., Pokhol, P. F., Popov, E. I., Pepekin, V. I., and Stasenko, A. G., "Combustion of Individual Aluminum-Magnesium Alloy Particles in the Flame of an Oxidizer-Fuel Mixture," *Combustion, Explosion, and Shock Waves*; Vol. 7, No. 2, pp. 186-190, 1971.

43. Popov, E. I., Kashporov, L. Ya., Mal'tsev, V. M., and Breiter, A. L., "Combustion Mechanism of Aluminum-Magnesium Alloy Particles," *Combustion, Explosion and Shock Waves*; Vol. 9, No. 2, pp. 204-208, 1973.

44. Lasheras, J. C., Fernandez-Pello, A. C., and Dryer, F. L., "Experimental Observations on the Disruptive Combustion of Free Droplets of Multicomponent Fuels," *Combustion Science and Technology*; Vol. 22, pp. 195-209, 1980.

45. Ozerov, E. S. and Yurinov, A. A., "Combustion of Particles of Aluminum-Magnesium Alloys in Water Vapor," *Combustion, Explosions and Shock Waves*; Vol. 13, No. 6, pp. 778-780, 1977.

46. Megli, T. W., "Aluminum-Magnesium Particle Ignition in Shocked Mixtures of Water Vapor and Argon," M.S. Thesis, University of Illinois at Urbana-Champaign, 1993.

47. Seeker, W. R., Wegener, D. C., Lester, T. W., and Merklin, J. F., "Single Pulse Shock Tube Studies of Pulverized Coal Ignition," *Seventeenth Symposium (International) on Combustion*, Vol. 17, The Combustion Institute, Leeds, pp. 155-166, 1978.

48. Bradley, J. N., *Shock Waves in Chemistry and Physics*, John Wiley & Sons Inc., New York, 1962.

49. Strehlow, R. A. and Cohen, A., "Limitations of the Reflected Shock Technique for Studying Fast Chemical Reactions and Its Application to the Observation of Relaxation in Nitrogen and Oxygen," *The Journal of Chemical Physics*; Vol. 30, No. 1, pp. 257-265, 1959.

50. Roberts, T. A. and Burton, R. L., "Piezoelectric Pressure Transducer Technique for Oxidizing Atmospheres," *Review of Scientific Instruments*; Vol. 63, No. 7, pp. 3787-3788, 1992.

51. Holman, J. P., *Experimental Methods for Engineers*, McGraw-Hill, New York, 1984.

52. Mark, H., "The Interaction of a Reflected Shock Wave With the Boundary Layer in a Shock Tube," *Journal of the Aeronautical Sciences,*, Vol. 24, No. 4, pp. 304-306, 1957.

53. Skinner, G. B., "Limitations of the Reflected Shock Technique for Studying Fast Chemical Reactions," *The Journal of Chemical Physics*; Vol. 31, No. 1, pp. 268-269, 1959.

54. Brabbs, T. A., Zlatarich, S. A., and Belles, F. E., "Limitations of the Reflected-Shock Technique for Studying Fast Chemical Reactions," *The Journal of Chemical Physics*; Vol. 33, No. 1, pp. 307-308, 1960.

55. Strehlow, R. A. and Cohen, A., "Initiation of Detonation," *Physics of Fluids*; Vol. 5, No. 1, pp. 97-101, 1962.

56. Strehlow, R. A. and Case, C. T., "Limitations of the Reflected Shock Technique for Studying Fast Chemical Reactions," *Journal of Chemical Physics*; Vol. 35, No. 4, pp. 1506-1507, 1961.

57. Rudinger, G., "Comments on the Strehlow and Case Letter," *Journal of Chemical Physics*; Vol. 35, No. 4, p. 1507, 1961.

58. Mirels, H. and Braun, W. H., "Non-Uniformities in Shock-Tube Flow Due to Unsteady-Boundary-Layer Action," NACA TN 4021, May, 1957.

59. Palmer, H. B., McHale, E. T., and Starkey, G. R., "Note on Reflected Shock Conditions in a Single-Pulse Tube," *Proceedings of the Fifth International Shock Tube Symposium*, U.S. Naval Ordnance Laboratory, Silver Spring, Maryland, pp. 557-570, 1965.

60. Cohen, A. and Decker, L., "Shock Tube Ignition of Nitrocellulose," *Proceedings of the Twelfth International Symposium on Shock Tubes and Waves*, The Magnes Press, Jerusalem, pp. 514-523, 1980.

61. Gurevich, M. A., Ozerov, E. S., and Yurinov, A. A., "Effect of an Oxide Film on the Inflammation Characteristics of Aluminum," *Combustion, Explosion, and Shock Waves*; Vol. 14, No. 4, pp. 448-451, 1978.

62. Incropera, F. P. and DeWitt, D. P., *Fundamentals of Heat and Mass Transfer*, John Wiley & Sons, New York, 1985.

63. Pehlke, R. D., Jeyarajan, A., and Wada, H., "Summary of Thermal Properties for Casting Alloys and Mold Materials," University of Michigan NTIS-PB83-211003, December, 1982.

64. Walsh, J. M., "Drag Coefficient Equations for Small Particles in High Speed Flows," *AIAA Journal*, Vol. 13, No. 11, pp. 1526-1528, 1975.

65. Bailey, A. B. and Hiatt, J., "Sphere Drag Coefficients for a Broad Range of Mach and Reynolds Numbers," *AIAA Journal*, Vol. 10, No. 11, pp. 1436-1440, 1972.

66. Zarin, N. A., "Measurement of Non-Continuum and Turbulence Effects on Subsonic Sphere Drag," NASA CR-1585, June, 1970.

67. Liepmann, H. W. and Roshko, A., *Elements of Gasdynamics*, John Wiley & Sons, Inc., New York, 1957.

68. Schlichting, H., *Boundary-Layer Theory*, McGraw-Hill Book Company, New York, 1968.

69. Brach, R. M., *Mechanical Impact Dynamics*, John Wiley & Sons, New York, 1991.

70. Ageev, N. V., *Handbook of Binary Metallic Systems*, Israel Program for Scientific Translations, Jerusalem, 1959.

71. Sonntag, R. E. and Van Wylen, G. J., *Introduction to Thermodynamics*, John Wiley & Sons, New York, 1982.

72. Weast, R. C., *Handbook of Chemistry and Physics*, CRC Press, Inc., Boca Raton, 1988.

73. Schaaf, S. A. and Chambre, P. L., "Flow of Rarefied Gases," In *Fundamentals of Gas Dynamics* (H.W. Emmons, Ed.), Princeton University Press, Princeton, Vol. 3, 1958.

74. Reynolds, W. C., "Investigation of Ignition Temperature of Solid Metals," NASA D-182, October, 1959.

75. Anon., *JANAF Thermochemical Data*, Dow Chemical Co., Midland, 1985.

76. Brandes, E. A., *Smithells Metals Reference Book*, Sixth ed., Butterworths, London, 1983.

77. Raynor, G. V., *The Physical Metallurgy of Mg and Its Alloys*, Pergamon Press, New York, 1959.

78. Hatch, J. E., *Aluminum: Properties and Physical Metallurgy*, American Society for Metals, Metals Park, 1984.

79. Anon., *Thermophysical Properties of High Temperature Solid Materials; Volume 4: Oxides and Their Solutions and Mixtures* (Y. S. Touloukian, Ed.), MacMillen Co., New York, 1967.

80. Zurawski, R. L., "Current Evaluation of the Tripropellant Concept," NASA TP 2602, June, 1986.

81. Hultgren, R., Desai, R. D., Hawkins, D. T., Gleiser, M., and Kenneth, K. K., *Selected Values of the Thermodynamic Properties of Binary Alloys*, American Society for Metals, Metals Park, 1973.

82. Mortimer, C. E., *Chemistry; A Conceptual Approach*, Fourth ed., D. Van Nostrand Co., New York, 1979.

83. Tipler, P. A., *Physics*, Worth Publishers, Inc., New York, Vol. 1., 1982.

84. Luikov, A. V., *Analytical Heat Diffusion Theory* (J. P. Hartnett, Ed.), Academic Press, New York, 1968.

85. Gurevich, M. A., Ozerova, G. E., and Stepanov, A. M., "Heterogeneous Ignition of an Aluminum Particle in Oxygen and Water Vapor," *Combustion, Explosion, and Shock Waves*; Vol. 6, No. 3, pp. 291-297, 1970.

86. Svehla, R. A., "Estimated Viscosities and Thermal Conductivities of Gases at High Temperatures," NASA TR-132, 1962.

87. Nickerson, G. R., Coats, D. E., Dang, A. L., Dunn, S. S., Berker, D. R., Hermsen, R. L., and Lamberty, J. T., "The Solid Propellant Rocket Motor Performance Prediction Computer Program (SPP)," AFAL-TR-87-078, Version 6.0, 1987.

88. Parry, D. L. and Brewster, M. Q., "Optical Constants of Al2O3 Smoke in Propellant Flames," *Journal of Thermophysics and Heat Transfer*; Vol. 5, No. 2, pp. 142-149, 1991.

89. Larson, R. S., "Prediction of Aluminum Combustion Efficiency in Solid Propellant Rocket Motors," *AIAA Journal*, Vol. 25, No. 1, pp. 82-91, 1987.

90. Gordon, D. A., "Combustion Characteristics of Metal Particles," In *Solid Propellant Rocket Research*, Progress in Astronautics and Aeronautics Series (M. Summerfield, Ed.), AIAA, New York, Vol. 1, pp. 271-278, 1960.

91. Linne, D. L. and Meyer, M. L., "A Compilation of Lunar and Mars Exploration Strategies Utilizing Indigenous Propellants," NASA TM-105262, January, 1992.

92. Glass, I. I., Martin, W., and Patterson, G. N., "A Theoretical and Experimental Study of the Shock Tube," University of Toronto, UTIA Report No. 2, November, 1953.

93. Gaydon, A. G. and Hurle, I. R., In *The Shock Tube in High-Temperature Chemical Physics*, Reinhold Publishing Corp., New York, 1963.

94. Resler, E. I., Lin, S. C., and Kantrowitz, A., "The Production of High Temperature Gases in Shock Tubes," *Journal of Applied Physics*; Vol. 23, No. 12, pp. 1390-1399, 1952.

95. Alpher, R. A. and White, D. R., "Flow in Shock Tubes With Area Change at the Diaphragm Section," *Journal of Fluid Mechanics*; Vol. 3, pp. 457-470, 1958.

96. Wittliff, C. E., Wilson, M. R., and Hertzberg, A., "The Tailored-Interface Hypersonic Shock Tunnel," *Journal of the Aerospace Sciences*; Vol. 26, No. 4, pp. 219-228, 1959.

97. Shapiro, A. H., *The Dynamics and Thermodynamics of Compressible Fluid Flow*, John Wiley and Sons, New York, Vol. 1, 1953.

98. Brabbs, T. A. and Belles, F. E., "Contact-Surface Tailoring in Real Shock Tubes," NASA TN D-3043, August, 1965.

99. Press, W. H., Flannery, B. P., Teukolsky, S. A., and Vetterling, W. T., *Numerical Recipes: The Art of Scientific Computing*, Cambridge University Press, Cambridge, 1989.